Advances in Experimental Medicine and Biology 737

Martin Wolf · Hans Ulrich Bucher
Markus Rudin · Sabine Van Huffel
Ursula Wolf · Duane F. Bruley
David K. Harrison *Editors*

Oxygen Transport to Tissue XXXIII

Springer

ADVANCES IN EXPERIMENTAL MEDICINE AND BIOLOGY

For further volumes:
http://www.springer.com/series/5584

Martin Wolf · Hans Ulrich Bucher
Markus Rudin · Sabine Van Huffel
Ursula Wolf · Duane F. Bruley
David K. Harrison
Editors

Oxygen Transport to Tissue XXXIII

Springer

Editors
Martin Wolf
Division of Neonatology
University Hospital Zurich
Zurich, Switzerland

Hans Ulrich Bucher
Division of Neonatology
University Hospital Zurich
Zurich, Switzerland

Markus Rudin
Institute for Biomedical Engineering
University of Zurich/ETHZ
Zurich, Switzerland

Sabine Van Huffel
Department of Electrical Engineering
Katholieke Universiteit Leuven
Leuven-Heverlee, Belgium

Ursula Wolf
Institute of Complementary
Medicine KIKOM
University of Bern
Imhoof Pavillon, Inselspital
Bern, Switzerland

Duane F. Bruley
Synthesizer Inc.
Ellicott City, MD, USA

David K. Harrison
Institute of Cellular Medicine
Newcastle University
Newcastle upon Tyne, UK

ISSN 0065-2598
ISBN 978-1-4614-1565-7 e-ISBN 978-1-4614-1566-4
DOI 10.1007/978-1-4614-1566-4
Springer New York Dordrecht Heidelberg London

Library of Congress Control Number: 2011941895

Preface

The 38th annual ISOTT conference was held on the Monte Verità in Southern Switzerland from 18th to 23rd of July 2010. The beautiful Mediterranean surrounding and the pleasant weather contributed to an excellent conference.

The highly interdisciplinary scientific program covered all aspects of oxygen transport from air to the cells, organs, and organisms; instrumentation and methods to sense oxygen and clinical evidence. It consisted of 10 invited keynote lectures, 81 abstracts and attracted 89 registered participants (19 students) from 14 countries. The spirit of ISOTT was alive due to an interested, prestigious and actively contributing audience, which very well attended the oral presentations and poster sessions and consequently lively discussions occurred at a high scientific level, in an atmosphere of enthusiasm and mutual interest.

To promote young researchers, students profited from a reduced registration fee, eight travel grants were given to young researches and each session was chaired by one senior and one young scientist. The constructive and stimulating interaction between experts in the field and students was one of the highlights of the conference.

Additionally to the scientific sessions, participants continued discussions during a hike to the Cardada and Cima della Trosa or during an evening on the patio while enjoying a beautiful view on Lago Maggiore and live music ably improvised by participants of the conference. Participants intensively used this opportunity to connect to and learn from each other, to form friendships, and to generate new ideas and collaborations. Thus, it was a truly successful meeting.

Zurich, Switzerland — Martin Wolf

Acknowledgments

Sponsors

As President of the 2010 Conference of the International Society on Oxygen Transport to Tissue, held from July 18 to 23 at Centro Stefano Franscini in Ascona, Switzerland, I would like to gratefully acknowledge the support of our sponsors:

Centro Stefano Franscini, ETH Zurich

Swiss National Science Foundation

Zurich Center for Imaging Science and Technology (CIMST)

Swiss Academy of Medical Sciences

HAMAMATSU

Hamamatsu Photonics

CASMED®
FOR WHAT'S VITAL

CASMED

artinis

Artinis Medical Systems

Contributors

In addition, I would like to thank those who helped make this meeting a success: Martin Biallas, Reto Kofmehl, Felix Scholkmann, Ivo Trajkovic, in particular Paolo Demaria, who excellently took care of the administrative and organizational side of the conference and the superb staff of the Centro Stefano Franscini.

Reviewers

The editors would like to thank the following experts, who scientifically reviewed the papers:

Reviewer	Institution
Zareen Bashir	University of Manchester, UK
Alexander Caicedo Dorado	Catholic University Leuven, Belgium
Giuseppe Cicco	University of Bari, Italy
Sebastiano Cicco	University of Bari, Italy
Clare Elwell	University College London, UK
Simon Faithfull	San Diego, USA
Artur Fournel	Heinrich Heine University, Duesseldorf, Germany
Thomas Gisler	University of Constance, Germany
David Harrison	Newcastle University, UK
Jack Honeysett	University College London, UK
Kyung Kang	University of Louisville, USA
Peter Keipert	Sangart Inc., San Diego, USA
Joseph LaManna	Case Western Reserve University, Cleveland, USA
Terence Leung	University College London, UK
Makii Muthalib	Queensland University of Technology, Bribane, Australia
Gunnar Naulaers	Catholic University Leuven, Belgium
Gerhard Pichler	Medical University of Graz, Austria
Michelle Puchowicz	Case Western Reserve University, Cleveland, USA
Joseph Rifkind	National Institute on Aging (NIH), Baltimore, USA
Kaoru Sakatani	Nihon University School of Medicine, Tokyo, Japan
Ilias Tachtsidis	University College London, UK
Eiji Takahashi	Saga University, Japan
Oliver Thews	University of Halle, Germany
Maureen Thorniley	University of Manchester, UK
Ivo Trajkovic	University Hospital Zurich, Switzerland
Sabine van Huffel	Catholic University Leuven, Belgium
Peter Vaupel	University Medical Centre, Mainz, Germany
David Wilson	University of Pennsylvania, Philapelphia, USA
Martin Wolf	University Hospital Zurich, Switzerland
Christopher Wolff	St. Bartholomew's & The Royal London Hospital, UK
Kurt Zaenker	University of Witten/Herdecke, Witten, Germany

Also, many thanks to the technical reviewers:
Laraine Visser-Isles (Rotterdam, The Netherlands)
Eileen Harrison (St Lorenzen, Italy)

Organization ISOTT 2010

Participants at ISOTT 2010.

Organizing Committee

Martin Wolf, University Hospital Zurich, Switzerland
Hans Ulrich Bucher, University Hospital Zurich, Switzerland
Markus Rudin, University of Zurich/ETHZ, Switzerland
Sabine Van Huffel, Katholieke Universiteit Leuven, Belgium
Ursula Wolf, University of Bern, Switzerland

ISOTT Officers and Executive Committee

Martin Wolf (President, Zurich, Switzerland)
Oliver Thews (Secretary, Halle, Germany)
Peter E. Keipert (Treasurer, San Diego, USA)
Duane F. Bruley (Knisely Award Committee, Ellicott City, USA)
John C. LaManna (Past President, Cleveland, USA)
William Welch (President-Elect, Washington, DC, USA)
Donald Buerk (Philadelphia, USA)
Arthur Fournell (Düsseldorf, Germany)
Lin Li (Philadelphia, USA)
Michelle A. Puchowicz (Cleveland, USA)
Hiromi Sakai (Tokyo, Japan)
Ludwig Schleinkofer (Munich, Germany)
Ilias Tachtsidis (London, UK)
Sabine Van Huffel (Leuven, Belgium)

Newly Elected Members of the Executive Committee

Clare Elwell (London, UK)
Ursula Wolf (Bern, Switzerland)

Conference Organization

Paolo Demaria www.demariaevent.ch

Awards

The Melvin H. Knisely Award

The Melvin H. Knisely Award was established in 1983 to honor Dr. Knisely's accomplishments in the field of the transport of oxygen and other metabolites and anabolites in the human body. Over the years, he has inspired many young investigators and this award is to honor his enthusiasm for assisting and encouraging young scientists and engineers in various disciplines. The award is to acknowledge outstanding young investigators. This award was first presented during the banquet

of the 1983 annual conference of ISOTT in Ruston, Louisiana. The award includes a Melvin H. Knisely plaque and a cash prize. Award recipients:

1983	Antal G. Hudetz (Hungary)
1984	Andras Eke (Hungary)
1985	Nathan A. Bush (USA)
1986	Karlfried Groebe (Germany)
1987	Isumi Shibuya (Japan)
1988	Kyung A. Kang (Korea/USA)
1989	Sanja Batra (Canada)
1990	Stephen J. Cringle (Australia)
1991	Paul Okunieff (USA)
1992	Hans Degens (The Netherlands)
1993	David A. Benaron (USA)
1994	Koen van Rossem (Belgium)
1995	Clare E. Elwell (UK)
1996	Sergei A. Vinogradov (USA)
1997	Chris Cooper (UK)
1998	Martin Wolf (Switzerland)
1999	Huiping Wu (USA)
2000	Valentina Quaresima (Italy)
2001	Fahmeed Hyder (Bangladesh)
2002	Geofrey De Visscher (Belgium)
2003	Mohammad Nadeem Khan (USA)
2004	Fredrick Palm (Sweden)
2005	Nicholas Lintell (Australia)
2007	Ilias Tachtsidis (UK)
2008	Kazuto Masamoto (Japan)
2009	Rossana Occhipinti (USA)
2010	Sebastiano Cicco (Italy)

The Dietrich W. Lübbers Award

The Dietrich W. Lübbers Award was established in honor of Professor Lübbers's long-standing commitment, interest, and contributions to the problems of oxygen transport to tissue and to the society. This award was first presented in 1994 during the annual conference of ISOTT in Istanbul, Turkey. Award recipients:

1994	Michael Dubina (Russia)
1995	Philip E. James (UK/USA)
1996	Resit Demit (Germany)

1997	Juan Carlos Chavez (Peru)
1998	Nathan A. Davis (UK)
1999	Paola Pichiule (USA)
2000	Ian Balcer (USA)
2001	Theresa M. Busch (USA)
2002	Link K. Korah (USA)
2003	James J. Lee (USA)
2004	Richard Olson (Sweden)
2005	Charlotte Ives (UK)
2006	Bin Hong (China/USA)
2007	Helga Blockx (Belgium)
2008	Joke Vanderhaegen (Belgium)
2009	Matthew Bell (UK)
2010	Alexander Caicedo Dorado (Belgium)

The Britton Chance Award

The Britton Chance Award was established in honor of Professor Chance's long-standing commitment, interest, and contributions to the science and engineering aspects of oxygen transport to tissue and to the society. This award was first presented in 2004 during the annual conference of ISOTT in Bari, Italy. Award recipients:

2004	Derek Brown (Switzerland)
2005	James Lee (USA)
2006	Hanzhu Jin (China/USA)
2007	Eric Mellon (USA)
2008	Jianting Wang (USA)
2009	Jessica Spires (USA)
2010	Ivo Trajkovic (Switzerland)

The Duane F. Bruley Travel Awards

The Duane F. Bruley Travel Awards were established in 2003 and first presented by ISOTT at the 2004 annual conference in Bari, Italy. This award was created to provide travel funds for student researchers in all aspects of areas of oxygen transport to tissue. The awards signify Dr. Bruley's interest in encouraging and supporting young researchers to maintain the image and quality of research associated with the society. As a co-founder of ISOTT in 1973, Dr. Bruley emphasizes cross-disciplinary research among basic scientists, engineers, medical scientists, and clinicians. His

pioneering work constructing mathematical models for oxygen and other anabolite/metabolite transport in the microcirculation, employing computer solutions, was the first to consider system nonlinearities, time dependence, including multidimensional diffusion, convection, and reaction kinetics. It is hoped that receiving the Duane F. Bruley Travel Award will inspire students to excel in their research and will assist in securing future leadership for ISOTT. Award recipients:

2004	Helga Blocks (Belgium), Jennifer Caddick (UK), Antonio Franco (Italy), Charlotte Ives (UK), Nicholas Lintell (Australia), Leonardo Mottola (Italy), Samin Rezania (USA/Iran), Ilias Tachtsidis (UK), Liang Tang (USA/China), Iyichi Sonoro (Japan)
2005	Robert Bradley (UK), Kathy Hsieh (Australia), Harald Oey (Australia), Jan Shah (Australia)
2006	Ben Gooch (UK), Ulf Jensen (Germany), Smruta Koppaka (USA), Daya Singh (UK), Martin Tisdall (UK), Bin Wong (USA), Kui Xu (USA)
2007	Dominique De Smet (Belgium), Thomas Ingram (UK), Nicola Lai (USA), Andrew Pinder (UK), Joke Vanderhaegen (Belgium)
2008	Sebastiano Cicco (Italy)
2009	Lei Gao (UK), Obinna Ndubuizu (USA), Joke Vanderhaegen (Belgium), Jianting Wang (USA)
2010	Zareen Bashir (UK), Martin Biallas (Switzerland), Takashi Eriguchi (Japan), Jack Honeysett (UK), Catalina Meßmer (USA), Tracy Moroz (UK), Yoshihiro Murata (Japan), Mark Muthalib (Australia)

Contents

Chapter 1
The History of ISOTT

Duane F. Bruley

1 History

This paper is an enhancement and extension of the presentations and papers prepared for the 1997 and 2006 of the *International Society on Oxygen Transport to Tissue* meetings [1, 2]. Similar to most successful research projects it was a serendipitous process. Therefore, it is important to step back and record the sequence of events that took place before this *special* society (ISOTT) was born. The original pioneers credited with the discovery of oxygen are first, Carl Wilhelm Scheele, a Swedish chemist who performed experiments in 1772 that demonstrated the presence of oxygen, and independently, Joseph Priestley, who conducted similar experiments in 1774. Antoine Lavoisier actually named the molecule (oxygen/oxygene) in 1775. Throughout the early years there have been many meetings related to oxygen transport in tissue and several societies that promoted sessions on the subject prior to the founding of a formal society.

The roots of ISOTT date back at least as far as Dr. Christian Bohr (1855–1911), for his pioneering work in respiratory physiology and to August Krogh (1847–1949), when his work conceptualizing the capillary-tissue cylinder for oxygen transport was awarded the Nobel Prize (1920). In my opinion, Krogh was the first tissue engineer because he quantified the physical system using mathematical modeling and calculated molecular transport and utilization in and around the microcirculation. Dr. Krogh studied under Dr. Bohr as his teaching assistant and continued his studies throughout his professional career. Dr. Melvin H. Knisely (1900–1975) served as Dr. Krogh's Post-Doctoral Fellow which propelled him on a career of studies related to blood agglutination in the capillaries and experimental research on the resulting tissue destruction and disease. Dr. Knisely has been cited as the first person to

D.F. Bruley (✉)
Synthesizer, Inc., 2773 Westminster Road, Ellicott City, MD 21043, USA
e-mail: bruley@umbc.edu

M. Wolf et al. (eds.), *Oxygen Transport to Tissue XXXIII*, Advances in Experimental Medicine and Biology 737, DOI 10.1007/978-1-4614-1566-4_1,

observe the pathological clumping of red and white cells, in vivo, at the capillary level [3]. He identified this phenomena as "blood sludging" and pointed out its negative impact on oxygen transport to the tissue and to the removal of toxic metabolic by-products.

Colleagues, on occasion, have told me that there were discussions regarding the possible establishment of a society on oxygen transport prior to 1973. If that is true, I was never a part of any of the discussions nor was I even contacted by a colleague to be part of such an effort. Also, I have been asked whether or not Dr. Knisely approached me to create a symposium in his honor or to form a society. Just for clarification, I never had any discussions related to the development of a symposium or a society with Dr. Knisely prior to gaining permission from Clemson to host a meeting at Clemson University in 1971.

My formal education was in traditional chemical, mechanical, and nuclear engineering. In the fall of 1962, I accepted a position as Assistant Professor of Chemical Engineering and Head Varsity Tennis coach at Clemson University in Clemson, South Carolina, USA. That fall a colleague, Dr. William Barlage, and I were discussing possible new research areas; thus, we decided to take a 500-mile round trip to the Medical College of South Carolina in Charleston, SC to see if there were problems involving "living systems" that we could apply our engineering skills to. Being traditional engineers neither of us had a formal education in the biological or life sciences and had studied only nonliving systems. To clarify, even though traditional engineers can make significant contributions to the engineering of living systems a new breed has evolved, the bioengineer, which represents the fifth traditional discipline of engineering [4]. A definition that I have frequently used for bioengineering is as follows: "Bioengineering is the application of engineering principles and fundamentals to engineering problems that *require* basic understanding of the biological and/or life sciences." This definition states that modern bioengineers must have a formal education that includes the biological and/or life sciences thus giving them insight into processes involved in living systems that would not be obvious to traditional engineers. This concept has a *foundation* in the principles upon which ISOTT was established.

On the second day of our visit to the Medical College and after several meetings, without success, we were standing outside of the Anatomy Department when Dr. Melvin H. Knisely (Head of the Department) appeared and introduced himself. After a brief discussion he invited us to lunch where he stated his interest in mathematical modeling and computer simulation of oxygen transport in the gray matter of brain. He was concerned about the viability of neurons under different pathological conditions and he thought that computer predication could be valuable.

This problem was of interest to me since I had recently completed my Ph.D. dissertation that included experimental and theoretical work on the thermal dynamics of a wetted-wall column [5]. My theoretical model consisted of a computer simulation of a coupled set of partial differential equations describing simultaneous heat and mass transfer in cylindrical coordinates. The equations contained terms for convection and conduction in two space dimensions and time and were solved using finite difference techniques via Fortran programming. We developed the *Direct Substitution*

Method for solving PDEs. This research fit perfectly with the description of the Krogh Capillary Tissue model and the problems associated with the solution of representative models that scientists and engineers around the world were then exploring to quantify the microcirculation. After a year of study to learn the necessary physiology and anatomy and the translation of two German articles, one by Opitz and Schneider [6] and the other by Thews [7] (help in translation was provided by Isabel Lockard and Elsie Tabor in Dr. Knisely's Laboratory) I derived a mathematical model, from basic principles (the Bruley Model), that was solved by various graduate students on digital, analog, and hybrid computers, for different anatomical and physiological conditions [8]. This research represented the first computer simulations of the microcirculation and a major step forward in quantitative analysis because computer simulation allowed investigation of the dynamic and nonlinear characteristics of the system.

These studies started in 1962 and we worked together until Dr Knisely's death in 1975. During that period, we published around 30 papers together regarding theoretical and experimental investigations of oxygen transport to tissue.

In 1968, Dr. Haim I. Bicher was recruited to our team because of his knowledge of blood agglutination and his expertise in the construction and use of oxygen microelectrodes. His contribution to our research effort allowed us to work back and forth between theory and experiment thus giving us the best possible research environment. We presented our work primarily at the European Microcirculation meetings and published in a variety of journals. It was then that we started to examine antiadhesive drugs in an attempt to prevent clotting and to reverse the consequences of blood agglutination [9]. This initial work has led to my current studies of Protein C, a blood factor that might be the ultimate anticoagulant/antithrombotic/anti-inflammatory/antiapoptotic for Protein C deficient patients, because there are little or no known side effects with the zymogen such as bleeding complications [10].

In 1971, our team attended a workshop on "oxygen supply" at The Max-Planck Institute in Dortmund, Germany. It was then that I decided to inquire about sponsoring a symposium at Clemson University to highlight our team work with Dr. Knisely's group at The Medical School of South Carolina. Immediately after I returned to the United States I asked Dr. Edwards, the President of Clemson University, for permission to host an oxygen transport to tissue symposium at Clemson University and with it honor Dr. Melvin H. Knisely for his many contributions to the field of microcirculation. In particular, I wanted to honor him for his development of the quartz rod crystal illumination technique that allowed him to visualize the sticking together of blood components, in vivo [3]. Dr. Knisely observed this phenomena in cases of malaria and over one hundred other disease states. He hypothesized that this condition leads to oxygen deprivation which could cause sickness and death. Permission was granted so I called Dr. Knisely's wife, Verona, to find out what she thought about it. After a short time Verona called back and said it was a good idea but she thought it would be better to have the symposium at The Medical College of South Carolina. With further discussion we decided to have a symposium at both campuses, with bus transportation in between. Both Dr. Edwards, President at Clemson University and Dr. McCord, President of The Medical School of South Carolina agreed to help fund the symposium.

When Dr. Bicher returned from an extended trip to Israel, I asked him if he would like to participate in setting up the symposium. He was anxious to do so and he then took responsibility for further arrangements at the Medical School while I handled all arrangements at Clemson University and the combined meeting. Together we obtained additional support from other companies and agencies to fund the meeting.

The intended purpose of the symposium was to promote interdisciplinary and cross-disciplinary research involving theoretical and experimental investigations for oxygen transport in tissue. It was to bring together life scientists and engineers in a single-session format to examine the many complex phenomena of normal tissue growth and maintenance, and tissue survival and repair under pathological conditions. This has remained the mission for ISOTT since its birth and is probably the precursor to what is defined as *Tissue Engineering* today.

After an intensive period of planning and preparation an initial meeting announcement was sent out to sample community interest. The results demonstrated enthusiasm far beyond projections and triggered Drs. Bruley and Bicher to consider the meeting as a launching pad for a very focused international society regarding oxygen transport to tissue. We presented our idea to several other investigators and then we decided that a formal society would be in the best interest of groups around the world to achieve research goals related to oxygen transport in tissue and that the Clemson/Charleston meeting would be an appropriate forum to formalize and begin an international society. We then decided on the name *International Society on Oxygen Transport to Tissue*, designed a society logo, assigned a mission, developed a charter, sketched the by-laws, contracted with Plenum Publishers to publish the meeting proceedings, and selected members to comprise an International Committee for the Clemson/Charleston meeting. The membership consisted of the following scientists and engineers:

Dr. Melvin H. Knisely, Charleston, USA	Dr. Duane F. Bruley, Clemson, USA
Dr. Haim I. Bicher, Charleston, USA	Dr. Gerhard Thews, Mainz, West Germany
Dr. Ian A. Silver, Bristol, England	Dr. Herbert J. Berman, Boston, USA
Dr. Britton Chance, Philadelphia, USA	Dr. Leland C. Clark, Jr., Cincinnati, USA
Dr. Lars-Erik Gelin, Goteborg, Sweden	Dr. Jurgen Grote, Mainz, West Germany
Dr. Manfred Kessler, Dortmund, Germany	Dr. Jose Strauss, Miami, USA
Dr. William J. Whalen, Cleveland, USA	Dr. Daniel D. Reneau, Ruston, USA

Drs. Bruley and Bicher solicited Dr. Melvin H. Knisely to serve as an honorary president of the society for the initial symposium. At the Clemson/Charleston meeting, ISOTT was founded, and the following slate of officers was elected:

- President-Elect – Dr. Gerhard Thews, Mainz, West Germany
- Secretary – Dr. Haim I. Bicher, Charleston, USA
- Treasurer – Dr. Ian A. Silver, Bristol, England

The first symposium of ISOTT surpassed all expectations and established a society that has continued to meet annually at various locations around the world. The registered participants numbered 267 and two volumes consisting of 133 papers

were published by Plenum Press in their "Advances in Experimental Medicine and Biology" series (Bicher and Bruley 1973; Bruley and Bicher 1973).

Society meetings have been held at the following locations under the leadership of the listed presidents:

1973	Clemson/Charleston, SC, USA	D.F. Bruley and H.I. Bicher
	Founding Meeting	M.H. Knisely (Honorary)
1974	Atlantic City, NJ, USA	D.F. Bruley and H.I. Bicher
	Group Meeting	M.H. Knisely (Honorary)
1975	Mainz, Germany	G. Thews (First Elected President)
1976	Anaheim, CA, USA	B. Chance
1977	Cambridge, UK	I.A. Silver
1978	Atlantic City, NJ, USA	J. Strauss
1979	La Jolla, CA, USA	J. Strauss
1980	Budapest, Hungary	A. Kovach
1981	Detroit, MI, USA	H. Bicher
1982	Dortmund, Germany	D. Lübbers
1983	Ruston, LA, USA	D.F. Bruley
1984	Nijmegen, The Netherlands	F. Kreuzer
1985	Raleigh, NC, USA	I.S. Longmuir
1986	Cambridge, UK	I.A. Silver
1987	Sapporo, Japan	M. Mochizuki
		C. Honig (Honorary)
1988	Ottawa, Canada	K. Rakusan
1989	Gottingen, Germany	J. Piper
1990	Townsville, Australia	M. McCabe
1991	Curacao, Dutch Antilles	W. Erdmann
1992	Mainz, Germany	P. Vaupel
1993	San Diego, CA, USA	P.D. Wagner
1994	Istanbul, Turkey	C. Ince
		K. Akpir (Honorary)
1995	Pittsburgh, PA, USA	E.M. Nemoto
1996	Dundee, Scotland	D.K. Harrison
1997	Milwaukee, WI, USA	A.G. Hudetz (25th Anniversary)
1998	Budapest, Hungary	A. Eke
1999	Hanover, NH, USA	H. Swartz
2000	Nijmegen, The Netherlands	B. Oeseburg
2001	Philadelphia, USA	D.F. Wilson
2002	Manchester, UK	M.S. Thorniley
2003	Rochester, USA	P. Okunieff
2004	Bari, Italy	G. Cicco
2005	Brisbane, Australia	D. Maguire
2006	Louisville, USA	K. Kang
2007	Uppsala, Sweden	P. Liss
2008	Sapporo, Japan	E. Takahashi
		M. Tamura (Honorary)
2009	Cleveland, USA	J. LaManna
2010	Ascona, Switzerland	M. Wolf

The 2011 meeting will be held in Washington, DC, where Dr. William Welch will serve as president. It is projected for 2012 that Dr. Sabine van Huffel will serve as president in Leuven, Belgium.

In 1983 at the Ruston, Louisiana meeting, Dr. Bruley initiated the first Melvin H. Knisely Award to a promising young investigator. This award was then approved and established by the Executive Committee to express the spirit and willingness of Dr. Knisely to work with and contribute to the growth of beginning scientists and engineers addressing the problems of oxygen transport to tissue. Dr. Bruley was then elected as the chairman of the "Melvin H. Knisely Award" selection committee and nominees have been reviewed each year with those selected being honored at the annual banquet.

The recipients, through the 2009 meeting in Cleveland, OH, USA are as follows:

1983 Antal G. Hudetz (Hungary)	1997 Chris Cooper (UK)
1984 Andras Eke (Hungary)	1998 Martin Wolf (Switzerland)
1985 Nathan A. Bush (USA)	1999 Huiping Wu (USA)
1986 Karlfried Groebe (Germany)	2000 Valentina Quaresima (Italy)
1987 Isumi Shibuya (Japan)	2001 Fahmeed Hyder (Bangladesh)
1988 Kyung A. Kang (Korea/USA)	2002 Geoffrey De Visscher (Belgium)
1989 Sanjay Batra (Canada)	2003 Mohammad Nadeem Khan (USA)
1990 Stephen J. Cringle (Australia)	2004 Frederick Palm (Sweden)
1991 Paul Okunieff (USA)	2005 Nicholas Lintell (Australia)
1992 Hans Degens (The Netherlands)	2006 No Awardee Selected
1993 David A. Benaron (USA)	2007 Ilias Tachtsidis (UK)
1994 Koen van Rossem (Belgium)	2008 Kazuto Masamoto (Japan)
1995 Clare E Elwell (UK)	2009 Rossana Occhipinti (USA)
1996 Sergei A. Vinogradov (USA)	

In 1994 a second Award to support travel for a young investigator was approved by the Executive Committee. The recipients of the "Dietrich W. Lübbers Award" are as follows:

1994 Michael Dubina (Russia)	2002 Lino K. Korah (USA)
1995 Philip E. James (UK/USA)	2003 James J. Lee (USA)
1996 Resit Demir (Germany)	2004 Richard Olson (Sweden)
1997 Juan Carlos Chavez (USA)	2005 Charlotte Ives (UK)
1998 Nathan A. Davis (UK)	2006 Bin Hong (China/USA)
1999 Paolo Pichiule (USA)	2007 Helga Blockx (Belgium)
2000 Ian Balcer (USA)	2008 Joke Vanderhaegen (Belgium)
2001 Theresa M. Busch (USA)	2009 Matthew Bell (UK)

The Britton Chance Award was established in 2003 in honor of Professor Chance's long-standing commitment, interest, and contributions to many aspects of oxygen transport to tissue and to the society. The award is to recognize outstanding

contributions to research by a young investigator to help support travel to the ISOTT meeting. The Britton Chance Awardees are as follows:

2004 Derek Brown (Switzerland)	2007 Eric Mellon (USA)
2005 James Lee (USA)	2008 Jianting Wang (USA)
2006 Hanzhu Jin (China/USA)	2009 Jessica Spires (USA)

The Duane F. Bruley Awards were established and were first presented by ISOTT at the 2004 annual meeting in Bari, Italy. They were established to support travel funds for student researchers in all areas of oxygen transport to tissue. The awards signify Dr. Bruley's interest in seeking young scientists and engineers to maintain the image and quality of research associated with the society. As a co-founder of ISOTT in 1973, Dr. Bruley emphasizes cross-disciplinary research among basic scientists, engineers, medical scientists, and clinicians. His pioneering work constructing mathematical models for oxygen and other anabolite/metabolite transport in the microcirculation, employing computer solutions, was the first to consider system nonlinearities, time dependence, including multidimensional diffusion, convection, and reaction kinetics. It is hoped that receiving the Duane F. Bruley Award will inspire students to excel in their research and will assist in securing future leadership for ISOTT. The Duane F. Bruley Awardees are as follows:

2004	2005	2006
Helga Blocks (Belgium)	Robert Bradley (UK)	Ben Gooch (UK)
Jennifer Caddick (UK)	Harald Oey (Australia)	Ulf Jensen (Germany)
Charlotte Ives (UK)	Kathy Hsieh (Australia)	Smruta Koppaka (USA)
Nicholas Lintell (Australia)	Jan Shah (Australia)	Daya Singh (UK)
Leonardo Mottola (Italy)	Martin Tisdall (UK)	Bin Wong (USA)
Samin Rezania (USA/Iran)		Kui Xu (USA)
Ilias Tachtsidis (UK)		
Liang Tang (USA/China)		
Iyichi Sonoro (Japan)		
Antonio Franco (Italy)		

2007	2008	2009
Dominique De Smet (Belgium)	Sebastiano Cicco (Italy)	Lei Gao (UK)
Thomas Ingram (UK)		Obinna Ndubuizu (USA)
Nicola Lai (USA)		Joke Vanderhaegen (Belgium)
Andrew Pinder (UK)		Jianting Wang (USA)
Joke Vanderhaegen (Belgium)		

As pointed out earlier the first society proceedings were published by Plenum Press (Bicher and Bruley 1973; Bruley and Bicher 1973). However, there has been some confusion about the total number of proceedings published due to different publishers' mistakes using two different names. Some of the first meeting proceedings were published under the Library of Congress Cataloging title of "International *Symposium* on Oxygen Transport to Tissue" rather than the official title of

"International *Society* on Oxygen Transport to Tissue." Since the two titles are listed separately the uninformed might not be aware of both sets of proceedings and some libraries do not have all of the volumes.

At the 25th Anniversary it was approved by the Executive Committee and the membership-at-large to proceed with arrangements to establish a journal for ISOTT with Plenum Press. The publications committee now consists of:

Duane F. Bruley, Chairman	Chris Cooper
Antal G. Hudetz	Joe C. LaManna
Kyung A. Kang	Hal Schwartz
David Harrison	Britton Chance

Many attempts to start a journal have failed for various reasons; however, we are still active and working with several publishers to develop a society journal. Because ISOTT remains small in numbers, by choice, most publishers do not feel a journal would be profitable.

The future of ISOTT will be determined by our young and new members, with the dedicated mentoring of our old time membership. It will be important to stay current with new technology and be flexible enough to embrace new directions in the area of oxygen transport to tissue. The vision of ISOTT members will be critical in guiding this very special international scientific and engineering society through the troubled waters created by politics and religion.

Acknowledgments Dr. Bruley acknowledges the assistance of Eileen Thiessen for the preparation of this paper and presentation.

References

1. Bruley DF (1998) The genesis of ISOTT. In: Hudetz AG, Bruley DF (eds) Oxygen transport to tissue XX. Plenum, New York, NY
2. Bruley DF (2008) ISOTT: roots, founding, and beyond. In: Kang KA, Harrison DK, Bruley DF (eds) Oxygen transport to tissue XXIX, vol 614, Advances in experimental medicine and biology. Springer, New York
3. Goro FW (1948) Blood sludge. Life Mag 24(22):49–59
4. Bruley DF (1992) Bioengineering: the fifth traditional engineering discipline. In: Erdmann W, Bruley DF (eds) Advances in experimental medicine and biology, vol 317. Plenum Press, New York, NY, pp 3–6
5. Bruley DF, Prados JW (1964) The frequency response analysis of a wetted wall adiabatic humidifier. AlChE J 11:612
6. Opitz E, Schneider M (1950) The oxygen supply of the brain and the mechanism of deficiency effects. Ergebnisse der Physiologie, Biologischem Chemic, und Experimentellen Pharmakologic 46:126–260
7. Thews G (1960) Oxygen diffusion in the brain. A contribution to the question of the oxygen supply of the organs. Pflugers Archiv 271:197–226
8. Artigue RS, Bruley DF (1983) The transport of oxygen, glucose, carbon dioxide and lactic acid in the human brain: mathematical models. Oxygen transport to tissue IV. Advances in experimental medicine and biology series, vol 159. \Plenum, New York

9. Bicher HI, Bruley DF, Knisely MH (1973) Anti-adhesive drugs and tissue oxygenation. In: Bruley DF, Bicher HI (eds) Advances in experimental medicine and biology, vol 37B. Plenum, Press, New York, NY, pp 657–667
10. Bruley DF, Drohan WN (1990) Protein C and related anticoagulants. In: Advances in applied biotechnology series, vol 11, Gulf Publishing Company (Portfolio Publishing Company), Woodlands, TX
11. Bicher HI, Bruley DF (eds) (1973) Oxygen transport to tissue – instrumentation, methods, and physiology, vol 37A, Advances in experimental medicine and biology. Plenum, New York, NY
12. Bruley DF, Bicher HI (eds) (1973) Oxygen transport to tissue – pharmacology, mathematical studies, and nematology, vol 37B, Advances in experimental medicine and biology. Plenum, New York

Part I
Brain Oxygenation

Chapter 2
Angioplasticity and Cerebrovascular Remodeling

Joseph C. LaManna

1 Introduction

To understand the phenomenon of angioplasticity it is useful to consider the primary function of the cerebral microcirculation as the timely delivery of substrate and oxygen, as well as the timely removal of the product of oxidative metabolism, i.e., carbon dioxide. The bulk delivery of substrate, in the case of the brain under normal conditions this is glucose, is described by its arterial concentration and the tissue blood flow. Even though there is a blood–brain barrier and a restricted aqueous pathway from the capillary to the parenchyma, and glucose is not very lipid soluble, the transport of glucose is, for the most part, not limiting for metabolism due to the presence of sufficient glucose transporters [1]. GLUT-1 at the blood–brain barrier facilitates diffusion across the endothelial cell membranes. The spatial distribution of glucose in the parenchyma is completely unknown, including the extracellular space and the possibility for differential cellular concentrations among the various cell types.

On the other hand, oxygen is transported by erythrocytes that contain hemoglobin. Arterial oxygen content depends on the concentration of hemoglobin and the blood oxygen tension, oxygen delivery on the content and the blood flow. There have been measurements and estimates of the spatial distribution of oxygen tensions in the parenchyma. There is some question remaining of the absolute values of oxygen tension and the shape of the distribution curve [2], but it seems to be agreed upon that there is distribution and that the oxygen tension is, on average, lower than

J.C. LaManna (✉)
Department of Physiology and Biophysics, Case Western Reserve University, Cleveland, OH, USA

Department of Neurology (BRB 525), Case Western Reserve University School of Medicine, 10900 Euclid Avenue, Cleveland, OH 44106-4938, USA
e-mail: joseph.lamanna@case.edu

M. Wolf et al. (eds.), *Oxygen Transport to Tissue XXXIII*, Advances in Experimental Medicine and Biology 737, DOI 10.1007/978-1-4614-1566-4_2,

the venous pO_2. Finally, the oxygen distribution is not constant with time, but varies with neuronal activity. When the neurons are activated, the blood flow and oxygen delivery to that locality are increased, so that transient capillary arterialization occurs and can be measured by the blood oxygen level dependent (BOLD) technique of functional magnetic resonance imaging (fMRI) [3].

2 The Cerebral Microcirculation

The spatial heterogeneity of brain oxygen tension is reflected in the spatial distribution of the microcirculation. Regional cerebral blood flow varies with the different regional metabolic activity as indicated by the correlation between CBF and CMRglu [4, 5] and CMRO2 [5, 6]. Thus, the structural distribution of capillaries, i.e., the capillary density, reflects the metabolic capacity of the tissue. Persistent changes in the patterns of neuronal activity will be reflected in changing capillary densities with some time constant that appears to be about 2 weeks. These relationships can be further appreciated as part of an overall organization of structure mapped to function. Whereas in the past the tendency was to view the structure as more or less fixed, the current view is changing to incorporate the idea that there is significant plasticity in local and regional brain function and that the functional plasticity is accompanied by structural plasticity.

3 Hypoxic Adaptation and Angiogenesis

In the late 1980s, we initiated a line of investigation into the brain microvascular acclimatization to prolonged hypoxia in rodents. The primary model exposed Wistar rats, 2–4 months of age, to hypobaric hypoxia (0.5 ATM, equivalent to an altitude of about 5,500 m) in modified Wright chambers [7, 8]. These and subsequent studies demonstrated a near doubling of the cortical capillary density in response to hypoxic exposure with a time course of 3 weeks which restores tissue oxygen levels [9]. A major angiogenesis mechanism responsible for hypoxia-induced increases in capillary density includes the hypoxia-inducible transcription factors HIF-1 and HIF-2 [10]. HIF-1 is found in all cells that have functional mitochondria and within the central nervous system HIF-2 is found primarily in astrocytes [11]. A wide list of genes have the hypoxic response element that is activated by these transcription factors including the angiogenesis molecule, vascular endothelial growth factor (VEGF), and the neuroprotective molecule, erythropoietin (EPO) [12].

The many systemic and central changes in response to prolonged hypoxia have been recently reviewed [13–15]. These acclimatizing responses are significantly attenuated with age [16].

4 Angioplasticity and Capillary Remodeling

Somewhat more surprising than hypoxia-induced angiogenesis was the finding that upon return to normoxia instead of persistent increases in capillary density there was rarefaction of the microcirculation back to prehypoxic exposure densities. This process was shown to be through activation of an intrinsic programmed cell death mechanism initiated by cyclooxynase-2 upregulation and prostaglandin PGE2 induction of angiopoietin-2 [17, 18]. This same pathway is also upregulated during hypoxia, but the difference between capillary growth or destruction is specified by the presence or absence of VEGF [19]. This led directly to the idea of angioplasticity which means that the structural arrangement of brain capillaries is continually and dynamically adjusted to take into account the balance between delivery of metabolic substrates and energy demands of neuronal activity.

An important implication of the angioplasticity hypothesis is that capillary density can be altered by manipulating the variables influencing delivery and metabolism. Indeed, it was shown that maintenance of rats on a ketogenic diet for 3 weeks or more induced angiogenesis and capillaries increased to densities comparable to those reached in prolonged hypoxia [20]. This effect is likely mediated through the HIF-1/COX-2 signaling pathways, activated because ketones induce an increase in cytoplasmic succinate concentrations leading to inhibition of prolyl hydroxylase which causes an accumulation of HIF-1 [21]. Rats on this ketogenic regimen have smaller infarcts when subjected to middle cerebral artery occlusion and show improved survival and recovery after cardiac arrest and resuscitation [21].

5 Angioplasticity Key Concepts

A number of key concepts can be gleaned from the series of studies summarized in this keynote address.

1. Brain tissue oxygen pressure is normally low and both spatially and temporally heterogeneously distributed.
2. Hypoxia induces capillary angiogenesis mediated by HIF-1 and VEGF.
3. Reoxygenation results in paring back of capillaries mediated by COX-2, PGE2, and ang-2 acting in the absence of growth factors.
4. The HIF-1 signaling system is attenuated in aging.

6 Conclusions

These concepts can be expanded to broader conclusions that include:

1. HIF-1/HIF-2-mediated vascular remodeling results in VEGF-induced angiogenesis and restoration of tissue oxygen levels.

2. Angiopoietin-2 likely participates in both angiogenesis and vascular regression and should be considered a "remodeling" molecule rather than an angiogenesis molecule.
3. Capillary regression during deacclimatization involves activation of intrinsic apoptotic mechanisms.
4. The structure of the neurovascular unit is continually adjusted with a response time on the order of a few weeks.
5. Disruption of the vascular remodeling process results in pathology, e.g., uncontrolled angiogenesis that occurs in arterio-venous malformations (AVMs) and tumors, or the ineffective angioplasticity with aging.
6. A ketogenic diet increases HIF-1 accumulation through increased succinate concentrations.
7. A ketogenic diet leads to angiogenesis without hypoxic trigger.
8. The signaling molecule HIF-1 is modulated by the cytoplasmic redox state.
9. A ketogenic diet "preconditions" the central nervous system and is neuroprotective.

Acknowledgments This work was supported by grants from the USA National Institutes of Health NS38632, HL092933 and NS062048.

References

1. Simpson IA, Carruthers A, Vannucci SJ (2007) Supply and demand in cerebral energy metabolism: the role of nutrient transporters. J Cereb Blood Flow Metab 27:1766–1791
2. Ndubuizu O, LaManna JC (2007) Brain tissue oxygen concentration measurements. Antioxid Redox Signal 9:1207–1219
3. Sanganahalli BG, Herman P, Blumenfeld H, Hyder F (2009) Oxidative neuroenergetics in event-related paradigms. J Neurosci 29:1707–1718
4. Sokoloff L (1981) Relationships among local functional activity, energy metabolism, and blood flow in the central nervous system. Fed Proc 40:2311–2316
5. Baron JC, Rougemont D, Soussaline F, Bustany P, Crouzel C, Bousser MG, Comar D (1984) Local interrelationships of cerebral oxygen consumption and glucose utilization in normal subjects and in ischemic stroke patients: a positron tomography study. J Cereb Blood Flow Metab 4:140–149
6. Leenders KL, Perani D, Lammertsma AA, Heather JD, Buckingham P, Healy MJ, Gibbs JM, Wise RJ, Hatazawa J, Herold S (1990) Cerebral blood flow, blood volume and oxygen utilization. Normal values and effect of age. Brain 113(Pt 1):27–47
7. LaManna JC, McCracken KA, Strohl KP (1989) Changes in regional cerebral blood flow and sucrose space after 3-4 weeks of hypobaric hypoxia (0.5 ATM). Adv Exp Med Biol 248:471–477
8. LaManna JC, Vendel LM, Farrell RM (1992) Brain adaptation to chronic hypobaric hypoxia in rats. J Appl Physiol 72:2238–2243
9. Lauro KL, LaManna JC (1997) Adequacy of cerebral vascular remodeling following three weeks of hypobaric hypoxia. Examined by an integrated composite analytical model. Adv Exp Med Biol 411:369–376
10. Chávez JC, Agani F, Pichiule P, LaManna JC (2000) Expression of hypoxic inducible factor 1α in the brain of rats during chronic hypoxia. J Appl Physiol 89:1937–1942

11. Chavez JC, Baranova O, Lin J, Pichiule P (2006) The transcriptional activator hypoxia inducible factor 2 (HIF-2/EPAS-1) regulates the oxygen-dependent expression of erythropoietin in cortical astrocytes. J Neurosci 26:9471–9481
12. LaManna JC, Chavez JC, Pichiule P (2007) Genetics and gene expression of glycolysis. In: Gibson GE, Dienel GA (eds) Brain energetics, integration of molecular and cellular processes, 3rd edn. Springer, Berlin, pp 771–788
13. LaManna JC (2007) Hypoxia in the central nervous system. Essays Biochem 43:139–152
14. Xu K, LaManna JC (2006) Chronic hypoxia and the cerebral circulation. J Appl Physiol 100:725–730
15. LaManna JC, Chavez JC, Pichiule P (2004) Structural and functional adaptation to hypoxia in the rat brain. J Exp Biol 207:3163–3169
16. Ndubuizu OI, Chavez JC, LaManna JC (2009) Increased prolyl 4-hydroxylase expression and differential regulation of hypoxia-inducible factors in the aged rat brain. Am J Physiol Regul Integr Comp Physiol 297:R158–R165
17. Pichiule P, LaManna JC (2002) Angiopoietin-2 and rat brain capillary remodeling during adaptation and de-adaptation to prolonged mild hypoxia. J Appl Physiol 93:1131–1139
18. Pichiule P, Chavez JC, LaManna JC (2004) Hypoxic regulation of angiopoietin-2 expression in endothelial cells. J Biol Chem 279:12171–12180
19. Dore-Duffy P, LaManna JC (2007) Physiologic angiodynamics in the brain. Antioxid Redox Signal 9:1363–1371
20. Puchowicz MA, Xu K, Sun X, Ivy A, Emancipator D, LaManna JC (2007) Diet-induced ketosis increases capillary density without altered blood flow in rat brain. Am J Physiol Endocrinol Metab 292:E1607–E1615
21. Puchowicz MA, Zechel JL, Valerio J, Emancipator DS, Xu K, Pundik S, LaManna JC, Lust WD (2008) Neuroprotection in diet-induced ketotic rat brain after focal ischemia. J Cereb Blood Flow Metab 28:1907–1916

Chapter 3
Cerebral Monitoring Using Near-Infrared Time-Resolved Spectroscopy and Postoperative Cognitive Dysfunction

Y. Kakihana, N. Okayama, A. Matsunaga, T. Yasuda, T. Imabayashi, M. Nakahara, N. Kiyonaga, K. Ikoma, T. Kikuchi, Y. Kanmura, M. Oda, E. Ohmae, T. Suzuki, Y. Yamashita, and M. Tamura

1 Introduction

Neuropsychological dysfunction after cardiac surgery is common (ranging from 33 to 83%) and is a significant cause of morbidity. Although many attempts have been made to establish predictors of postoperative neurological dysfunction, the etiology of neurological impairment after cardiac surgery remains unresolved. Early studies revealed that oxygen desaturation measured by jugular venous oxygen saturation ($SjvO_2$) during rewarming after cardiopulmonary bypass (CPB) was associated with cognitive dysfunction [1]. In contrast, other studies have suggested that the neurological outcome might be poorer in patients with a higher $SjvO_2$ during hypothermic CPB [2]. Therefore, the role of $SjvO_2$ as a predictor of cognitive dysfunction has been controversial.

Recently, near-infrared time-resolved spectroscopy (TRS), which is quite effective for the quantitative monitoring of tissue oxygenation, has been developed. Therefore, this study was conducted to investigate whether cerebral monitoring

Y. Kakihana, M.D., Ph.D. (✉) • N. Okayama • T. Yasuda • T. Imabayashi • M. Nakahara • N. Kiyonaga • K. Ikoma • T. Kikuchi
Division of Intensive Care Medicine, Kagoshima University Hospital, 8-35-1 Sakuragaoka, Kagoshima 890-8520, Japan
e-mail: kakihana@m3.kufm.kagoshima-u.ac.jp

A. Matsunaga • Y. Kanmura
Department of Anesthesiology and Critical Care Medicine, Kagoshima University, Kagoshima, Japan

M. Oda • E. Ohmae • T. Suzuki • Y. Yamashita
Central Research Laboratory, Hamamatsu Photonics K.K., Hamamatsu, Japan

M. Tamura
Hokkaido University, Sapporo, Japan

M. Wolf et al. (eds.), *Oxygen Transport to Tissue XXXIII*, Advances in Experimental Medicine and Biology 737, DOI 10.1007/978-1-4614-1566-4_3,

using TRS and parameters such as $SjvO_2$ and T-SO_2 was capable of predicting the incidence of postoperative cognitive dysfunction (POCD) after cardiac surgery requiring hypothermic CPB.

2 Methods

After obtaining institutional approval and informed consent, we studied ten patients undergoing valve replacements ($n=3$), coronary artery bypass grafts ($n=3$), or thoracic aortic surgery ($n=4$) requiring a CPB. Anesthesia was induced with midazolam, fentanyl, and vecuronium, and maintained with continuous infusion of propofol. Fentanyl and vecuronium were added as necessary. Rectal and pharyngeal temperatures were continuously monitored. A cannula was inserted into the left radial artery to monitor arterial pressure and to sample the arterial blood for blood gas analysis. A 5.5-Fr fiberoptic oximetry catheter (Opticath; Abbott Laboratories, North Chicago, IL) was inserted by retrograde cannulation via the right internal jugular vein to monitor the changes in the global cerebral oxygenation as $SjvO_2$. The TRS-10 (Hamamatsu Photonics K.K., Hamamatsu, Japan), consisting of a three-wavelength picosecond pulser (PLP; 759, 797, and 833 nm) as the light source and a photomultiplier tube (PMT) with a high speed and high sensitivity for time-resolved measurements, was attached to the left forehead to monitor changes in the regional cerebral oxygenation (T-SO_2). Hemodynamic variables and arterial and jugular venous blood gas analyses were obtained at the following time points (1) before CPB, (2) at 5 min after the onset of CPB, (3) before aorta clamping, (4) after aorta clamping, (5) during rewarming, (6) after aorta declamping, (7) at the end of rewarming, and (8) at the end of CPB.

To estimate the cerebral oxygenation state, the arterial oxygen content (CaO_2), jugular venous oxygen content ($CjvO_2$), the arteriojugular venous oxygen content difference (Ca-jvO_2), and the cerebral oxygen extraction ratio (COER) were calculated using the following equations: $CaO_2=(1.39\times Hb\times SaO_2)+0.0031\times PaO_2$, $CjvO_2=(1.39\times Hb\times SjvO_2)+0.0031\times PjvO_2$, Ca-$jvO_2=CaO_2-CjvO_2$, $COER=100\times$ Ca-jvO_2/CaO_2, where PaO_2, SaO_2, $PjvO_2$, and Hb are arterial oxygen pressure, arterial oxygen saturation, jugular venous oxygen pressure, and hemoglobin concentration, respectively. Cognitive function was assessed using the MMSE (Mini-Mental State Examination) 1–3 days before the operation and 7 days after the operation by a single investigator. Cognitive dysfunction was regarded as a change of 1 SD in performance from the preoperative assessment to the postoperative assessment [3]. In this study, "significant cognitive decline" was defined as present if, in any case, the difference in the score for a given test exceeded the preoperative SD for that test. Patients were then divided according to that criterion into a normal group and a decline group.

The variables of the decline and normal groups were compared using a Mann–Whitney *U*-test or a X^2 statistical analysis. To compare differences in cerebral hemodynamic variables between and within groups, a two-way analysis of variance with repeated measures followed by Fisher's protected least significant difference test was used. A *P* value less than 0.05 was considered statistically significant.

3 Results

Four of the ten cases developed POCD. Although no significant differences in PaO_2, $PaCO_2$, blood sugar, lactate, and hemoglobin concentration at each time point were observed between patients without POCD (normal group; $n=6$) and patients with POCD (decline group; $n=4$), the pharyngeal temperature during CPB was significantly lower in the decline group ($P<0.01$) (Table 3.1). No significant differences in Ca-jvO_2 were observed between the normal and decline groups, but the results suggested a tendency toward a lower cerebral oxygen extraction in the decline group. Figure 3.1 shows the changes in $SjvO_2$ and T-SO_2 during CPB between the normal and decline groups. The mean $SjvO_2$ and T-SO_2 values during surgery in the normal group were $60.5 \pm 9.7\%$ and $63.9 \pm 4.6\%$, respectively, and no significant difference was seen between these two values at each time point. In the decline group, however, significant differences between the mean $SjvO_2$ and T-SO_2 values were observed during surgery ($70.4 \pm 14.9\%$ [$SjvO_2$] vs. $62.8 \pm 5.6\%$ [T-SO_2], $P=0.0024$), and the $SjvO_2$ value was significantly higher than the T-SO_2 value during the rewarming period ($87.9 \pm 6.3\%$ vs. $65.0 \pm 5.3\%$, $P=0.0014$). Significant differences in the global–regional oxygenation differences (calculated by $SjvO_2$ minus T-SO_2) were observed in the decline group but not in the normal group (Fig. 3.2).

4 Discussion

The results of this study show that the incidence of postoperative cognitive decline was significantly associated with a high $SjvO_2$ and a tendency toward a lower cerebral oxygen extraction during hypothermic CPB. A lower P_{50} induced by hypothermia, which indicates a shift in the oxyhemoglobin dissociation curve to the left and an increased oxygen affinity to hemoglobin, would cause inadequate tissue oxygenation and a higher $SjvO_2$. Edelman and Hoffman [4] demonstrated arteriovenous shunting in cerebral circulation. Yoshitani et al. [3] and McCleary et al. [5] assumed that oxygenated blood was shunted to the venous side of the circulation because of the bypassing of the cerebral microcirculation, resulting in an increase in the $SjvO_2$ values. Nonpulsatile CPB results in cerebral capillary collapse, intravascular sludging, and vasodilation [6] and may lead to arteriovenous shunting. Therefore, arteriovenous shunting might induce a high $SjvO_2$ associated with inadequate tissue oxygenation and cognitive decline. Although a higher $SjvO_2$ was observed, T-SO_2 measured using TRS did not show a high value in the decline group. One possible reason is that differences may exist between global and regional cerebral oxygenation. If so, the monitoring of both $SjvO_2$ and T-SO_2 may be useful not only for detecting the occurrence of cognitive decline, but also for clarifying the mechanisms of neuropsychological dysfunction after cardiac surgery. However, these premises are speculative. In addition, this study is a preliminary study involving a small number of patients. To confirm the association between changes in global and regional cerebral oxygenation and cognitive dysfunction, further study is required.

Table 3.1 Physiologic variables in the normal ($n=6$) and decline ($n=4$) groups

Measurement time									
Variable	Group	(1)	(2)	(3)	(4)	(5)	(6)	(7)	(8)
PaO_2 (mm Hg)	Normal	247 ± 99	242.9 ± 1.3	284.5 ± 93.7	363.1 ± 110.4	391.4 ± 28.7	455.7 ± 103.4	304.8 ± 206.5	160.6 ± 51.2
	Decline	215 ± 64	313.1 ± 59.6	359.8 ± 69.1	406.2 ± 61.4	457.9 ± 57.3	372.2 ± 79.2	242.9 ± 233.1	238 ± 46.1
$PaCo_2$ (mm Hg)	Normal	35.5 ± 6	34.2 ± 0.3	32.6 ± 1.2	35.9 ± 2.6	38 ± 6.8	40.9 ± 2.4	40.9 ± 7	45.4 ± 2.2
	Decline	36.3 ± 5.5	33.4 ± 6.7	31.4 ± 3.9	32.9 ± 6.6	33.7 ± 5.5	33.9 ± 6.6	40.8 ± 8.8	42.6 ± 5.2
BS (m mol/dl)	Normal	125.3 ± 37.1	119.3 ± 6.5	202.6 ± 148.4	333.3 ± 217.1	240.3 ± 110.6	225.3 ± 102.6	210.3 ± 83.3	138.6 ± 48.7
	Decline	107 ± 30.2	141.7 ± 18	136.5 ± 20.7	227.2 ± 114.1	233.2 ± 136.1	292.2 ± 75.1	213 ± 38.2	183.2 ± 50
Hb (q/dl)	Normal	10.1 ± 5.8	7.3 ± 2.3	6.1 ± 1.1	6.6 ± 2.1	7.4 ± 3	7.8 ± 2.4	10.4 ± 1.7	9.6 ± 0.6
	Decline	10 ± 0.6	5.3 ± 1	5 ± 1.2	4.9 ± 1	5.1 ± 0.7	7.3 ± 2.4	9.2 ± 2.8	10.8 ± 1.7
Lactate (mol/l)	Normal	1.2 ± 0.3	1.3 ± 0.2	1.3 ± 0.2	1.4 ± 0.3	1.5 ± 0.2	1.8 ± 0.5	3.7 ± 2.2	2.3 ± 1
	Decline	1.2 ± 0.2	1.6 ± 0.5	1.7 ± 0.5	1.8 ± 0.5	1.7 ± 0.5	3.1 ± 1.4	2.8 ± 1.1	2.6 ± 1.4
Temperature (°C)	Normal	36.3 ± 0.6	36 ± 0.3	35.2 ± 0.5	33.5 ± 0.7	32.1 ± 0.6	30.8 ± 2.1	36 ± 0	36 ± 0
$Ca\text{-}ivO_2$ (Ml/dl)	Normal	7.6 ± 3.8	5.3 ± 1.5	4.3 ± 1.1	4.7 ± 1.4	4.4 ± 0.5	4.3 ± 0.6	5.8 ± 1.1	4.1 ± 0.9
	Decline	7.8 ± 1.6	3.8 ± 0.4	3.6 ± 0.7	3.1 ± 0.3	3.1 ± 0.3	2.3 ± 1.3	3.9 ± 1.2	5 ± 0.6
COER (%)	Normal	43.2 ± 20.6	48.4 ± 9.1	46 ± 6	45.6 ± 5.2	40.9 ± 13.2	36.9 ± 9.5	38.1 ± 6.2	29.7 ± 4.6
	Decline	53.5 ± 10.3	45 ± 3	449 ± 2.4	40.1 ± 8.7	37.3 ± 5.8	23.9 ± 18.1	32.1 ± 13.8	31.6 ± 5.3

Data are expressed as the mean ± S.D.

No significant differences between the two groups were observed, except for body temperature

Body temperature was significantly lower in the decline group ($P<0.01$)

Each variable was measured at the following points (1) before CPB, (2) at 5 min after the onset of CPB, (3) before aorta clamping, (4) after aorta clamping, (5) during rewarming, (6) after aorta declamping, (7) at the end of rewarming, (8) at the end of CPB. *BS* blood sugar, *Hb* hemoglobin concentration, *Ca-jvO*$_2$ arteriojugular venous oxygen content, *COER* cerebral oxygen extraction ratio

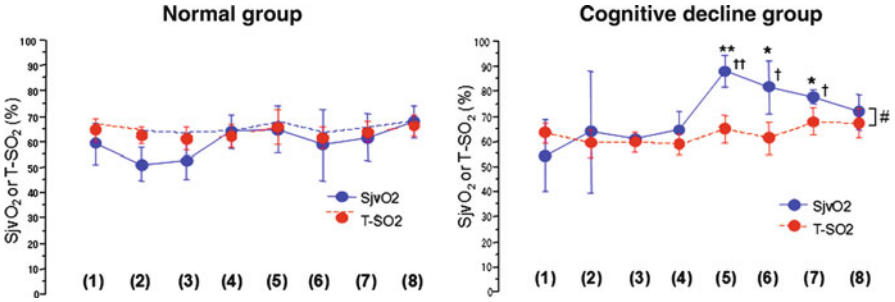

Fig. 3.1 Changes in $SjvO_2$ and $T\text{-}SO_2$ during CPB between the normal and decline groups. Significant differences between the $SjvO_2$ and $T\text{-}SO_2$ values were observed in the decline group but not in the normal group. *$SjvO_2$* jugular venous oxygen saturation; *$T\text{-}SO_2$* regional cerebral oxygenation

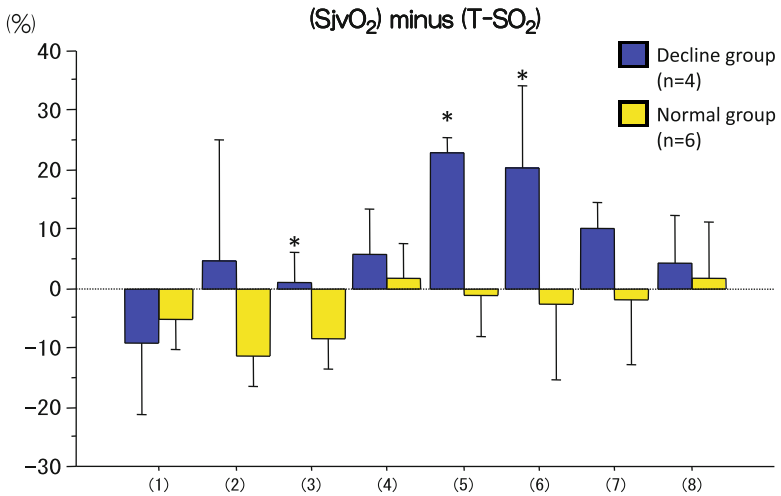

Fig. 3.2 Global–regional oxygen saturation differences. Significant differences in global–regional oxygenation (calculated by $SjvO_2$ minus $T\text{-}SO_2$) were observed in the decline group but not in the normal group. *$SjvO_2$* jugular venous oxygen saturation, *$T\text{-}SO_2$* regional cerebral oxygenation

5 Conclusions

Our results demonstrate a lack of agreement between $SjvO_2$ and $T\text{-}SO_2$ for the monitoring of cerebral oxygenation and the occurrence of postoperative cognitive decline. Therefore, we concluded that these two methods are not interchangeable, and that the monitoring of both $SjvO_2$ and $T\text{-}SO_2$ may be useful not only for detecting the occurrence of cognitive decline, but also for clarifying the mechanisms of neuropsychological dysfunction after cardiac surgery.

References

1. Croughwell ND, Newman MF, Blumenthal JA et al (1994) Jugular bulb saturation and cognitive dysfunction after cardiopulmonary bypass. Ann Thorac Surg 58:1702–1708
2. Murkin JM, Martzke JS, Buchan AM et al (1995) A randomized study of the influence of perfusion technique and pH management strategy in 316 patients undergoing coronary artery bypass surgery. II. Neurologic and cognitive outcomes. J Thorac Cardiovasc Surg 110:349–362
3. Yoshitani K, Kawaguchi M, Sugiyama N et al (2001) The association of high jugular bulb venous oxygen saturation with cognitive decline after hypothermic cardiopulmonary bypass. Anesth Analg 92:1370–1376
4. Edelman G, Hoffman WE (1999) Cerebral venous and tissue gases and arteriovenous shunting in the dog. Anesth Analg 89:679–683
5. McCleary AJ, Gower S, McGoldrick JP et al (1999) Does hypothermia prevent cerebral ischaemia during cardiopulmonary bypass? Cardiovasc Surg 7:425–431
6. Matsumoto T, Wolferth CC Jr, Perlman MH (1971) Effects of pulsatile and nonpulsatile perfusion upon cerebral and conjunctival microcirculation in dogs. Am Surg 37:61–64

Chapter 4
Comparison of the Kinetics of Pulmonary Oxygen Uptake and Middle Cerebral Artery Blood Flow Velocity During Cycling Exercise

Mikio Hiura, Norimitsu Kinoshita, Sigeki Izumi, and Tadashi Nariai

1 Introduction

At the onset of constant work rate exercise, pulmonary oxygen uptake ($\dot{V}O_2$) increases to transport oxygen from the atmosphere to working muscles. With respect to oxygen uptake by brain, the regional metabolic rate of oxygen ($rCMRO_2$) would also increase since the regional cerebral blood flow (rCBF) increases by 20–30% during exercise [1, 2]. $\dot{V}O_2$ kinetics at onset of constant work rate exercise is well established [3, 4], whereas there is no information on $rCMRO_2$ response during the on-transit phase of dynamic exercise. Although changes in $rCMRO_2$ could not be obtained during exercise, rCBF that contributes to $rCMRO_2$ could be estimated by middle cerebral artery blood flow velocity (MCA V_{mean}) using the transcranial Doppler (TCD) method. Considering that a change in cardiac output (CO) seems to be related with that in CBF [5], $\dot{V}O_2$, the product of CO and arterial–venous concentration difference for O_2, would be related to CBF. However, the role of $\dot{V}O_2$ in controlling CBF during exercise has not been investigated.

The purpose of the present study was to analyze the changes of $\dot{V}O_2$ and MCA V_{mean} as an index of rCBF in constant work rate exercise of moderate- and heavy-intensity constant work rate cycling exercise and to compare the kinetics of the two parameters during the transition from rest to exercise.

M. Hiura, M.D. (✉) • N. Kinoshita • S. Izumi
Faculty of Sports and Health Studies, Hosei University,
4342 Aihara-Town, Machida, Tokyo 194-0298, Japan
e-mail: phmikmd@hosei.ac.jp

T. Nariai
Department of Neurosurgery, Tokyo Medical and Dental University, Tokyo, Japan

M. Wolf et al. (eds.), *Oxygen Transport to Tissue XXXIII*, Advances in Experimental Medicine and Biology 737, DOI 10.1007/978-1-4614-1566-4_4,

2 Methods

Eight young volunteers (eight males; age 23.0 ± 2.9 year; height 1.71 ± 0.06 m; body mass 66.9 ± 10.9 kg), having given written informed consent, took part in this study. All subjects were healthy and none reported any history of diseases.

Subjects visited the laboratory on three occasions with a minimum of 2 days of recovery between each test and all tests were performed within 4 weeks. On the first visit, the subjects followed a ramp protocol with an increase in work rate (WR) of 25 W or 20 W/1 min, beginning from 25 W, for the determination of $\dot{V}O_{2peak}$, LT, and RC [4, 6] on an electromagnetically braked cycle ergometer (Lode Excalibur Sport, Groningen, The Netherlands). On the next two occasions, subjects performed two sets of 10-min constant workload of exercise bouts by cycle ergometer, with different intensities corresponding to the level of 10–20% below LT (moderate) and the level between LT and RC (heavy).

The subjects breathed through a facemask (Hans Rudolph, MO, USA) connected to an online gas analyzer (CPET; Cosmed, Rome, Italy). P_aCO_2 was estimated from measurements of the end-tidal pressure of CO_2 and V_T (in liters) using the equation described by Jones and colleagues [7] (eP_aCO_2). MCA V_{mean} was determined using TCD apparatus (Companion III, Nicolet Vascular, CO, USA). The proximal segment of the middle cerebral artery was insonated at a depth of 50–54 mm from the temporal bone depending on the position with the best signal-to-noise ratio [8]. MCA V_{mean} was determined as the time-averaged maximum velocity (TAV_{max}) that was calculated from the peak systolic and the end-diastolic velocity during each heart beat [9].

Breath-by-breath data from measurements of pulmonary gas exchange were linearly interpolated to 1-s intervals, time aligned, and ensemble averaged to yield a single profile, and then time averaged into 5-s bins to give a single response for each subject for subsequent analysis. MCA V_{mean} was also determined at 5-s intervals of TAV_{max}. On-transient phase II of $\dot{V}O_2$ [3, 4] and the corresponding response of MCA V_{mean} and eP_aCO_2 were investigated simultaneously with the same kinetics model. In the present study, the first 20 s of the ensemble dataset were removed as the time delay [10]. The remaining dataset was fitted to a monoexponential curve with a delay relative to the onset of exercise until 3 min when $\dot{V}O_2$ attains steady state in moderate-intensity exercise and until 2 min when the "slow component" of phase II occurs in heavy-intensity exercise [4, 11].

The responses were then modeled using a monoexponential of the form:

$$Y(t) = Y(0) + \mathrm{Amp}\left\{1 - e^{[-(t-\mathrm{TD})/\tau]}\right\}, 20 \le t \le 120 \text{ or } 180, \tag{4.1}$$

where $Y(t)$ represents the variable at any time (t), $Y(0)$ is the relevant baseline control value, Amp is the amplitude (i.e., increase in Y above baseline), τ is the time constant (i.e., the time taken to reach 63% of the total increase in Y above baseline), and TD is the time delay. The data were analyzed using the statistical package Prism

5.0 (GraphPad Software, CA, USA). Wilcoxon matched pairs test was used to compare the intensity differences. For comparison of τ within the intensity, one-way repeated measures of ANOVA followed by Tukey post hoc test was used. A Pearson's product moment correlation coefficient was used to determine relationships between appropriate variables. All data are presented as the mean ± SD. The level of statistical significance was set at $P < 0.05$.

3 Results

In the present study, moderate-intensity exercise represented 50 ± 6.6% $\dot{V}O_{2peak}$ at a work rate of 106 ± 28 W and heavy-intensity exercise represented 73 ± 4.8% $\dot{V}O_{2peak}$ at a work rate of 201 ± 44 W (Table 4.1). Figure 4.1 shows the time course of eP_aCO_2, MCA V_{mean}, and $\dot{V}O_2$. At the onset, response of MCA V_{mean} tracks that of $\dot{V}O_2$ whereas that of eP_aCO_2 seems to change more steeply. $\dot{V}O_2$ and MCA V_{mean} response for a representative subject (with the monoexponential model line of best fit) are shown in Fig. 4.2. A summary of the parameter estimates for the on-transient responses of $\dot{V}O_2$, MCA V_{mean}, and eP_aCO_2 in moderate and heavy intensity is presented in Table 4.1. Amplitude of $\dot{V}O_2$ in heavy-intensity exercise was significantly higher than moderate intensity, whereas that of MCA V_{mean} and eP_aCO_2 did not differ. The phase II $\dot{V}O_2$ time constant ($\tau\dot{V}O_2$) in moderate and heavy intensity were 21.7 ± 6.6 and 24.7 ± 8.4 s, respectively, and the corresponding MCA V_{mean} time constants (τMCA V_{mean}) were similar. The corresponding eP_aCO_2 time constants (τeP_aCO_2) in moderate and heavy intensity were significantly shorter than the other time constants in moderate and heavy intensity ($P < 0.05$). The goodness of fit for monoexponential response of $\dot{V}O_2$ was better than that of MCA V_{mean} and eP_aCO_2 as R values of 0.94 ± 0.03, 0.80 ± 0.11, and 0.73 ± 0.12, respectively ($P < 0.05$). Figure 4.3 shows the relationship between $\tau\dot{V}O_2$ and τMCA V_{mean} in moderate and heavy intensity.

Table 4.1 Summary of parameter estimates for the on-transient responses of pulmonary oxygen uptake ($\dot{V}O_2$), middle cerebral artery blood flow velocity (MCA V_{mean}), and the estimated arterial carbon dioxide tension (eP_aCO_2) in moderate and heavy intensity

	Moderate	Heavy
WR (W)	106 ± 28	201 ± 44[a]
% $\dot{V}O_{2peak}$	50 ± 6.6	73 ± 4.8[a]
Amplitude $\dot{V}O_2$ (L min^{-1})	0.74 ± 0.18	1.20 ± 0.40[a]
Amplitude MCA V_{mean} (cm s^{-1})	14.5 ± 8.0	15.5 ± 5.6
Amplitude eP_aCO_2 (mmHg)	3.2 ± 1.6	3.6 ± 1.6
$\tau\dot{V}O_2$ (s)	21.7 ± 6.6[b]	24.7 ± 8.4[b]
τMCA V_{mean} (s)	26.7 ± 9.2[b]	24.2 ± 9.2[b]
τeP_aCO_2 (s)	14.8 ± 7.6	14.0 ± 6.2

Values are means ± SD, $n = 8$, τ time constant; *WR* work rate
[a]Significance ($P < 0.05$) compared with the moderate intensity
[b]Significance ($P < 0.05$) compared with τeP_aCO_2

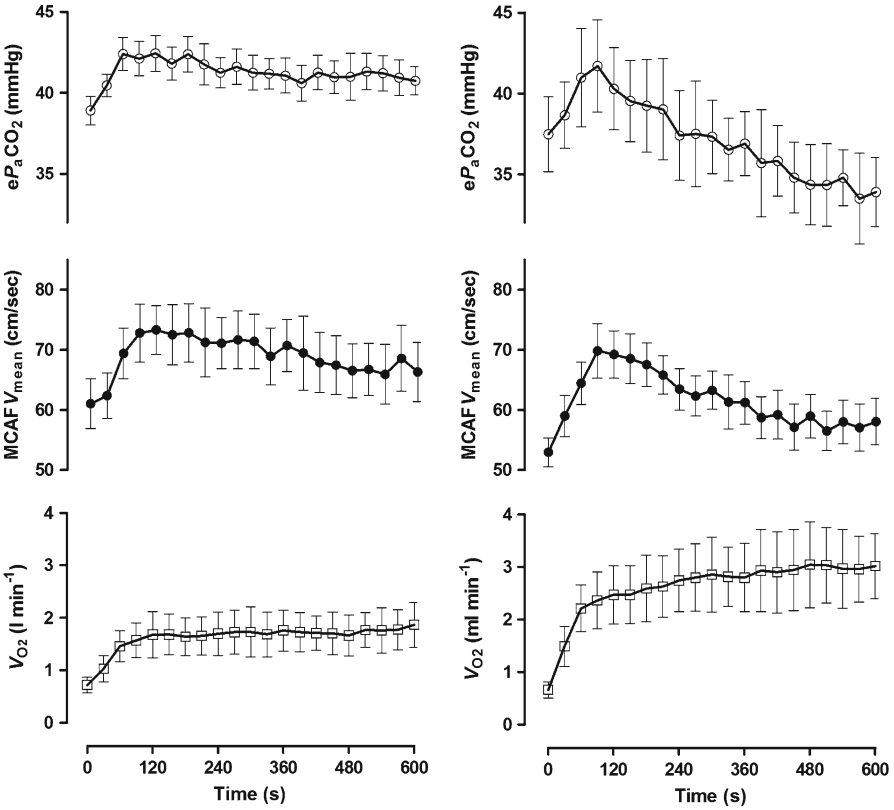

Fig. 4.1 Response profiles of the estimated arterial carbon dioxide tension (eP_aCO_2) and middle cerebral artery blood flow velocity (MCA V_{mean}) during moderate- (*left*) and heavy-intensity (*right*) constant work rate exercise

τVO_2 was significantly related with τMCA V_{mean} in moderate ($r^2 = 0.64$, $P = 0.02$) and heavy intensity ($r^2 = 0.81$, $P = 0.002$). There was no significant relationship between τeP_aCO_2 and τMCA V_{mean} in moderate ($r^2 = 0.01$) and heavy intensity ($r^2 = 0.0003$).

4 Discussion

The main and novel finding of the present study is demonstrating that response of MCA V_{mean} during the transition from rest to exercise mimicked that of VO_2 (Figs. 4.1 and 4.2) and that τVO_2 correlated with τMCA V_{mean} (Fig. 4.3) in both the moderate- and heavy-intensity exercise. As the phase II response of VO_2 kinetics is thought to closely represent the kinetics of muscle oxygen consumption [12], it is likely that the changes in utilization of oxygen and substrates within muscles would be reflected

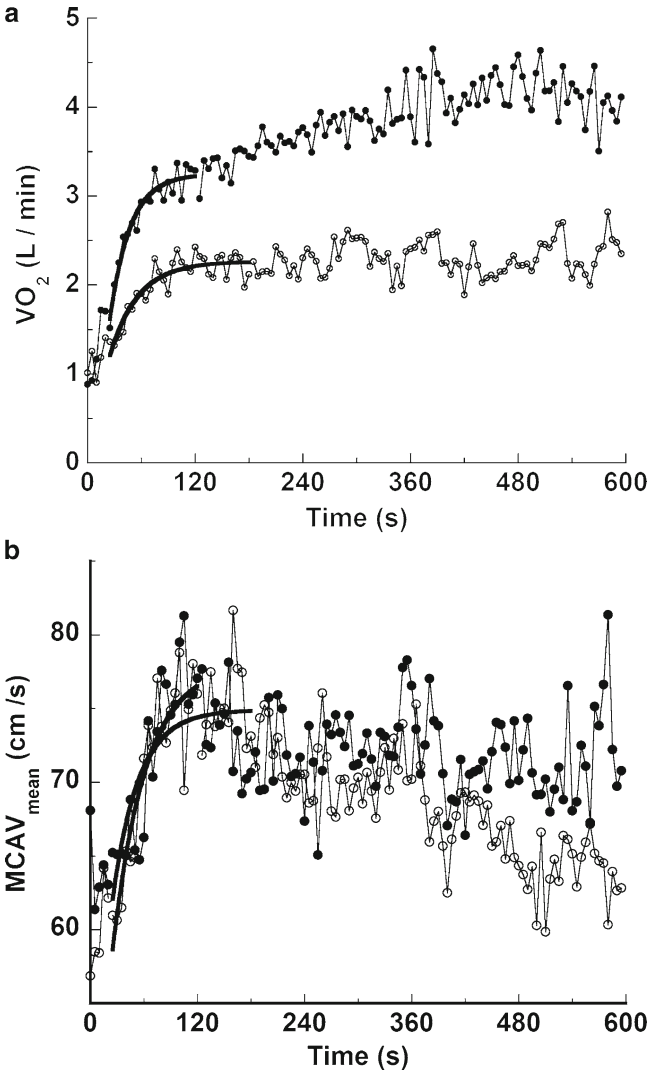

Fig. 4.2 Response of pulmonary oxygen uptake ($\dot{V}O_2$) (**a**) and middle cerebral artery blood flow velocity (MCA V_{mean}) (**b**) in a representative subject during the transient to moderate- (*open circle* and *gray line* of best fit) and heavy- (*filled circle* and *black line* of best fit) intensity exercise

in the corresponding area of brain and that the related neuronal activity would contribute to kinetics of MCA V_{mean}.

With respect to regulation of the circulation during exercise, multiple neural mechanisms such as central command [13], the exercise pressor reflex arising from skeletal muscles [14], and the carotid baroreflex [15] are likely to be involved. Considering that exercise starts with central command and afferent signals from contracting muscles generate the perception and integration of various sensory input

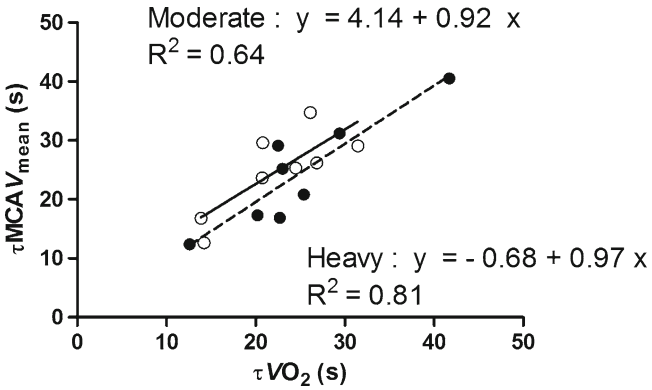

Fig. 4.3 Relationship between the time constant for pulmonary oxygen uptake (τVO_2) and middle cerebral artery blood flow velocity (τMCA V_{mean}) in moderate (*open circle*) and heavy (*filled circle*) intensity exercise. Regression lines for moderate (*solid line*) and heavy (*dashed line*) intensity are shown

in brain, we speculate that increase in both CO and muscle metabolism, which is the main cause of the response of VO_2 during exercise, would have an association with the neural activation in the brain. Although P_aCO_2 has a major role for controlling CBF, our data indicated that it was the response of VO_2 rather than eP_aCO_2 that related to changes in MCA V_{mean} at the on-transit phase of cycling exercise (Fig. 4.1 and Table 4.1). It seems that CO, as the contributing factor for VO_2 kinetics at the onset of exercise [3, 4], would be related to CBF. With regards to changes in CO and MCA V_{mean} during cycling exercise, Gonzalez-Alonso et al. [5] demonstrated the concomitant changes of the two parameters in the moderate intensity and the disturbed relationship during maximal intensity. However, the on-transient kinetics of CO and MCA V_{mean} were not investigated previously.

The goodness of fit for the kinetics of MCA V_{mean} is relatively low compared with that of VO_2 but a finding that τVO_2 had tendency to correlate with τMCA V_{mean} (Fig. 4.3) would support the possibility of application of the VO_2 kinetic model for MCA V_{mean}. Further investigation for sampling and smoothing the data of MCA V_{mean} might improve the quality of the kinetic analysis.

5 Conclusions

Responses of VO_2, MCA V_{mean}, and e$PaCO_2$ during moderate- and heavy-intensity constant work rate cycling exercise were investigated. The present study implies that the kinetics of MCA V_{mean} mimicked that of VO_2 at the onset of constant work rate cycling exercise.

Acknowledgments We acknowledge the technical support provided by Dr. Muneyuki Sakata (Positron Medical Center, Tokyo Metropolitan Institute of Gerontology) and the subjects for their participation.

References

1. Hellstrom G, Fischer-Colbrie W, Wahlgren NG et al (1996) Carotid artery blood flow and middle cerebral artery blood flow velocity during physical exercise. J Appl Physiol 81:413–418
2. Ide K, Secher NH (2000) Cerebral blood flow and metabolism during exercise. Prog Neurobiol 61:397–414
3. Whipp BJ, Ward SA, Lamara N et al (1982) Parameters of ventilator and gas exchange dynamics during exercise. J Appl Physiol 52:1506–1513
4. Whipp BJ, Ward SA (1990) Physiological determinants of pulmonary gas exchange kinetics during exercise. Med Sci Sports Exerc 22:62–71
5. Gonzalez-Alonso J, Dalsgaard MK, Osada T et al (2004) Brain and central haemodynamics and oxygenation during maximal exercise in humans. J Physiol 557:331–342
6. Beaver WL, Wasserman K, Whipp BJ (1986) A new method for detecting anaerobic threshold by gas exchange. J Appl Physiol 60:2020–2027
7. Jones NL, Robertson DG, Kane JW (1979) Difference between end-tidal and arterial PCO2 in exercise. J Appl Physiol 47:954–960
8. Aaslid RT, Markwalder M, Nornes H (1982) Noninvasive transcranial Doppler ultrasound recording of flow velocity in basal cerebral arteries. J Neurosurg 57:769–774
9. Valzueza JM, Schreiber SJ, Roehl JE et al (2008) Neurosonology and neuroimaging of stroke. Thieme, New York
10. Koga S, Shiojiri T, Shibasaki M et al (1996) Kinetics of oxygen uptake and cardiac output at onset of arm exercise. Respir Physiol 103:195–202
11. Whipp BJ (1994) The slow component of O_2 uptake kinetics during heavy exercise. Med Sci Sports Exerc 26:1319–1326
12. Rossiter HB, Ward SA, Doyle VL et al (1999) Inferences from pulmonary O_2 uptake with respect to intramuscular [phosphocreatine] kinetics during moderate exercise in human. J Physiol 518:921–931
13. Goodwin GM, McCloskey DI, Mitchell JH (1972) Cardiovascular and respiratory response to changes in central command during isometric exercise at constant muscle tension. J Physiol 226:173–190
14. Kaufman MP, Waldrop TG, Rybicki KJ et al (1984) Effect of static and rhythmic twitch to contractions on the discharge of group III and IV muscle afferents. Cardiovasc Res 18:663–668
15. Rowell LB, O'Leary DS (1990) Reflex control of the circulation during exercise: chemoreflex and mechanoreflexes. J Appl Physiol 69:407–418

Chapter 5
Colored Light and Brain and Muscle Oxygenation

J. Weinzirl, M. Wolf, M. Nelle, P. Heusser, and U. Wolf

1 Introduction

Light of different colors (CL) is applied for various medical conditions to improve the physical, emotional, or mental state of patients. Examples are the use of blue light in the treatment of the neonatal jaundice [1], a phenomenon due to the immature liver function of newborns, the application of red [2] and UV light in dermatology (physical level), and the use of bright white light to treat seasonal affective disorders [3] (emotional or mental level). It is known that blue light is strongly absorbed by the skin, suppresses melatonin production, and is generally associated with coldness. In contrast, red light penetrates tissue relatively deeply and is associated with warmth. However, little is known about the effects of CL on hemodynamics and tissue oxygenation.

We therefore investigated potential effects of blue and red light, being the two main colors used in medical treatments, on blood volume and tissue oxygenation in the brain and skeletal leg muscle using near-infrared spectrophotometry (NIRS).

J. Weinzirl • U. Wolf (✉)
Institute of Complementary Medicine KIKOM, University of Bern, Inselspital, Imhoof Pavillon, 3010 Bern, Switzerland
e-mail: ursula.wolf@kikom.unibe.ch

M. Wolf
Division of Neonatology, University Hospital Zurich, Zurich, Switzerland

M. Nelle
Division of Neonatology, University Hospital Bern, Bern, Switzerland

P. Heusser
Center for Integrative Medicine, University of Witten-Herdecke, Witten, Germany

M. Wolf et al. (eds.), *Oxygen Transport to Tissue XXXIII*, Advances in Experimental Medicine and Biology 737, DOI 10.1007/978-1-4614-1566-4_5,

2 Materials and Methods

Ten healthy volunteers (5 male, 5 female; mean age 27, range 23–44 years) were measured during blue and red light exposure. Light was generated using thermal white light sources (60 W, OSRAM Inc., Germany) and color filters (Lee Inc., Germany). During exposure phases the CL was projected onto a white wall. The subjects were seated in a comfortable chair facing the wall. Subjects were asked to keep their eyes open throughout the entire measurement. Otherwise the room was completely dark and instruments were shielded in order to avoid ambient light.

All subjects were measured twice on different days, exposed to blue or red light in a randomized crossover protocol. The protocol consisted of 8-min baseline (darkness), 10-min CL (blue or red) exposure, followed by 16-min recovery (darkness). Blood volume, i.e., total hemoglobin concentration ([tHb] in μM) and tissue oxygen saturation (StO_2 in %) were measured with a Hamamatsu NIRO 300 instrument. One sensor was attached to the forehead and the other to the lateral calf muscle. By using a paired *t* test, the last 5 min of the baseline were compared to the first and last 5 min of the CL exposure, and to three periods of 5 min of the recovery. Blue and red exposures were compared by a linear mixed effects (LME) model (R statistical software).

3 Results

In the leg, tHb concentration increased significantly during and after exposure by up to (mean ± SEM) 1.08 ± 0.19 μM ($p = 0.0002$) for blue and 1.52 ± 0.33 μM ($p = 0.0013$) for red light (Fig. 5.1). Although StO_2 did not change significantly compared to baseline, StO_2 was significantly higher under blue than under red light conditions (Table 5.1).

In the brain, StO_2 increased significantly during blue exposure by 0.51 ± 0.21% ($p = 0.0367$), with a maximum shortly after exposure 0.98 ± 0.40% ($p = 0.0324$) while tHb concentration did not change significantly (Fig. 5.2). During red exposure StO_2 changed a little but not significantly. The increase in StO_2 during exposure to blue light was significantly different from red light (Table 5.1).

4 Discussion and Conclusion

In the leg, the [tHb] increased continuously in the course of time and independently of the color, which most probably indicates venous pooling of the blood in the calf muscle during the measurement. StO_2 remained relatively constant, but was significantly different between blue and red light exposure (Table 5.1). This may indicate a decreased oxygen consumption due to exposure to blue light.

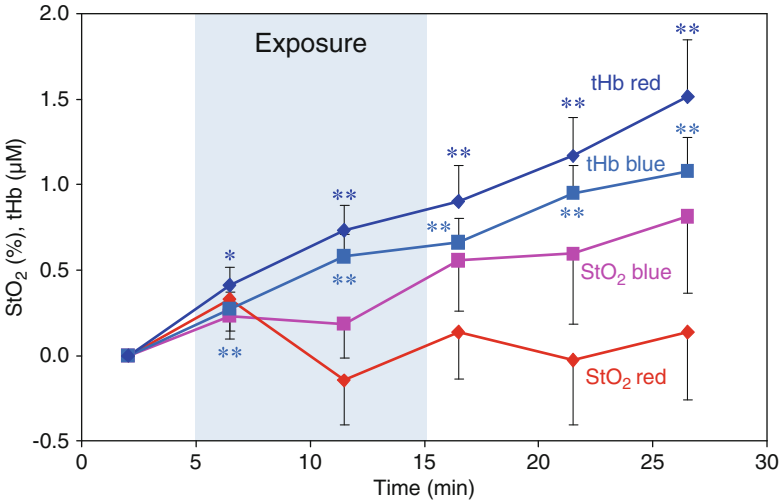

Fig. 5.1 Changes in muscle blood volume (tHb) and tissue oxygenation (StO_2) during exposure to *blue* and *red* light. tHb increases continuously, while StO_2 remains more of less constant. *Single asterisk* indicates a significant ($p<0.05$) difference between the period before exposure (0–5 min) compared to another period. *Double asterisks* indicates high significance ($p<0.001$). The *shaded area* indicates the exposure period to colored light

Table 5.1 Results of a linear mixed-effects statistical analysis to compare changes during and after exposure to blue light to changes during and after exposure to red light

Parameter	Location	*p*-Value blue vs. red
StO_2	Brain	**0.001**
	Muscle	**0.006**
tHb	Brain	0.609
	Muscle	0.102

In the brain, the [tHb] remained relatively constant, which may indicate that blood volume and blood flow did not change due to exposure to light of different colors. However, the simultaneous significant increase in StO_2 during exposure to blue light indicates that oxygen consumption in the brain decreased. This is particularly interesting because blue light is known to induce alertness, an effect that might be expected to be related to increased oxygen consumption. Clearly, blue and red light have different effects on hemodynamics and tissue oxygenation.

The underlying reasons for the observed phenomena are not yet clear. Aspects that need to be considered in future research are the distribution of cones and rods in the retina, the sensitivity of the eye to different colors, and exposure to colored light in addition to red and blue.

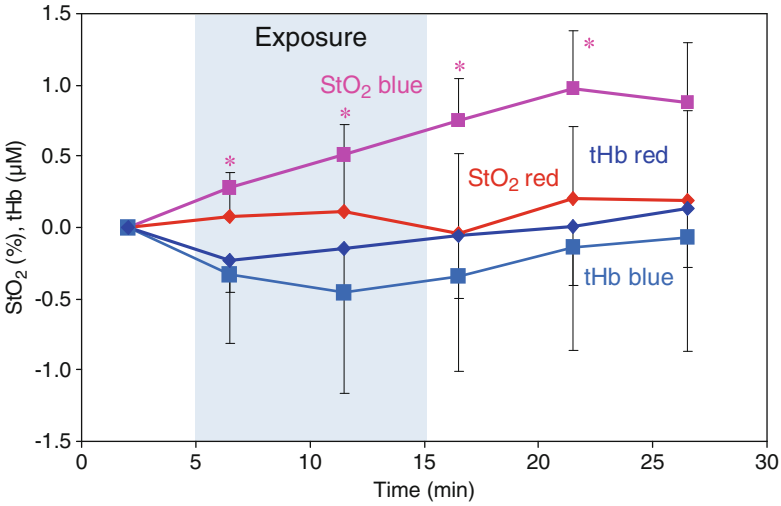

Fig. 5.2 Changes in brain blood volume (tHb) and tissue oxygenation (StO_2) during exposure to *blue* and *red* light. tHb remains constant, while StO_2 increases significantly during and after exposure to *blue* light. *Asterisk* indicates a significant ($p<0.05$) difference between the period before exposure (0–5 min) compared to another period. The *shaded area* indicates the exposure period to colored light

Acknowledgment The authors thank Massimo Merlini (statistician, ETH Zurich) for his valuable comments and great support.

References

1. Maisels MJ, McDonagh AF (2008) Phototherapy for neonatal jaundice. N Engl J Med 358(9):920–928
2. Zane C, Capezzera R, Pedretti A et al (2008) Non-invasive diagnostic evaluation of phototherapeutic effects of red light phototherapy of acne vulgaris. Photodermatol Photoimmunol Photomed 24(5):244–248
3. Even C, Schröder CM, Friedman S et al (2008) Efficacy of light therapy in nonseasonal depression: a systematic review. J Affect Disord 108(1–2):11–23

Chapter 6
Assessment of the Myogenic and Metabolic Mechanism Influence in Cerebral Autoregulation Using Near-Infrared Spectroscopy

Alexander Caicedo, Gunnar Naulaers, Martin Wolf, Petra Lemmers, Frank Van Bel, Lieveke Ameye, and Sabine Van Huffel

1 Introduction

Cerebral autoregulation is a complex process that refers to the maintenance of a constant cerebral blood flow (CBF) over a broad range of arterial blood pressures. This process avoids damage in the brain due to hemorrhagic brain injury and ischemia. Several mechanisms are involved in this process. So far, evidence of the myogenic, metabolic, and neurogenic ones has been described in the literature [1]. Cerebral autoregulation can be assessed by analyzing the relation between mean arterial blood pressure (MABP) and CBF, which can be measured continuously. The similarity in the dynamics of both signals has been quantified so far by means of correlation (partial) coherence [2–4], among other methods. However, the role of other variables in cerebral autoregulation, such as partial pressure of carbon dioxide (pCO_2) and partial pressure of oxygen (pO_2), has not been well explored in clinical studies.

In this chapter, we examine how well the myogenic and the metabolic mechanisms involved in cerebral autoregulation can be assessed by mean of transfer

A. Caicedo (✉) • L. Ameye • S. Van Huffel
Department of Electrical Engineering (ESAT-SCD), Katholieke Universiteit Leuven, Kasteelpark Arenberg 10 bus 2446, Leuven, Heverlee 3001, Belgium
e-mail: Alexander.CaicedoDorado@esat.kuleuven.be

G. Naulaers
Neonatal Intensive Care Unit, University Hospital Gasthuisberg, Katholieke Universiteit Leuven, Leuven, Belgium

M. Wolf
Division of Neonatology, Department of Obstetrics and Gynecology, University Hospital Zurich, Zurich, Switzerland

P. Lemmers • F. Van Bel
Department of Neonatology, University Medical Center, Wilhelmina Children's Hospital, Utrecht, The Netherlands

M. Wolf et al. (eds.), *Oxygen Transport to Tissue XXXIII*, Advances in Experimental Medicine and Biology 737, DOI 10.1007/978-1-4614-1566-4_6,

function analysis and near-infrared spectroscopy (NIRS) signals. Moreover, we study how these derived measures are related to the long- and short-term clinical outcome in premature infants.

2 Data

The study was performed in 42 infants from the University Hospital Zurich (Switzerland), with a gestational age of 28.1 ± 2.27 weeks and a birth weight of $1{,}155 \pm 467$ g. In all infants, the pCO_2 was measured by a transcutaneous monitor, peripheral oxygen saturation (SaO_2) was measured continuously by pulse oximetry, and MABP by an indwelling arterial catheter. With NIRS, the cerebral intravascular oxygenation (HbD) was continuously and noninvasively recorded using the Critikon Cerebral RedOx Monitor from Johnson & Johnson Medical. MABP, SaO_2, and NIRS signals were simultaneously measured during the first 3 days of life and downsampled at 0.333 Hz.

3 Methods

Signal Analysis. Artifacts shorter than 30 s were removed and corrected by interpolation using robust least squares support vector machines for function estimation [5]. Artifacts longer than 30 s were truncated. Remaining artifacts, if any, were removed manually. Hence, a single continuous measurement was replaced by a set of continuous artifact-free segments. Moreover, only the segments with variations of SaO_2 lower than 5% were included in the analysis. The resulting signals were filtered with a mean average filter and then downsampled to 0.333 Hz in order to obtain a common sampling frequency and minimize the loss of information.

Mathematical Tools. Assessment of the myogenic mechanism in cerebral autoregulation was done via analysis of the MABP/HbD transfer function; the metabolic mechanism was assessed by analysis of the pCO_2/HbD transfer function. After preprocessing, the signals were divided into segments of 20 min with the maximum overlap (step size: one sample). For each segment, the transfer function gain and phase coefficients were calculated. The transfer function was estimated by means of the following equation

$$H(f) = \frac{G_{\mathrm{io}}(f)}{G_{\mathrm{ii}}(f)}$$

where $G_{\mathrm{io}}(f)$ represents the input–output cross-power spectrum and $G_{\mathrm{ii}}(f)$ represents the input auto-power spectrum. The Welch method was used for the calculation

of the respective cross-power and auto-power spectral densities. This method involves a further segmentation of the signals into 10-min epochs with an overlap of 7.5 min. The average of the coefficients in the frequency ranges 0.003–0.02 Hz (very low frequency range: VLF), 0.02–0.05 Hz (low frequency range: LF), and 0.05–0.1 Hz (high frequency range: HF) were calculated [3] for further analysis. Moreover, in order to study the influence of different frequencies in autoregulation assessment, the values of the gain and the phase in all frequencies were also analyzed.

With respect to clinical outcomes, infants were classified as abnormal for short term or long term according to their clinical scores. For short-term outcomes, infants were classified as abnormal whenever bleedings, periventricular leukomalacia (PVL), intra-ventricular hemorrhage (IVH), or death occurred; otherwise they were classified as normal. For long-term clinical outcomes classification, the Bayley scores (Mental and Physicomotor Development Index: MDI and PDI, respectively) were used. Infants were classified as normal if MDI and PDI > 85, otherwise they were classified as abnormal. In addition, in order to study the relation between birth weight (BW) and autoregulation state, the scores of infants with very low birth weight (BW < 1,200 g)[1] were group-wise compared to those with a BW > 1,200 g.

Statistical Analysis. To assess whether the concordance scores were predictive for outcome (normal or abnormal) the nonparametric Kruskal–Wallis test was applied, due to the lack of normality in the data distributions. The statistical analysis was performed using the statistics toolbox from MATLAB. All reported p-values were two-tailed and a nominal p-value < 0.05 was considered as statistically significant.

4 Results

Table 6.1 presents the median, minimum, and maximum values of the gain and phase scores, calculated in the VLF, LF, and HF frequency ranges for the normal and abnormal population according to the short- and long-term classification criteria. In the short-term outcome analysis, there were 23 infants classified as normal and 19 infants classified as abnormal, while in the long-term analysis 8 infants were classified as normal and 34 infants as abnormal. Statistically significant differences between the groups were found only in the gain score for the HF range, with a median value of 0.43 and 0.20 for the normal and abnormal classes (p-value 0.02). All other scores did not differ significantly between the normal and abnormal subgroups.

Figure 6.1 shows the high- and low-pass filter characteristic behavior for the gain median values. However, for the myogenic mechanism (MABP-HbD) it seems that

[1] Clinically, low birth weight is defined for babies with BW < 1,500 g; however, due to the small population with BW > 1,500 g in this dataset, this criterion was modified to BW < 1,200 g.

Therefore, better statistics can be computed.

Table 6.1 Comparison between normal and abnormal population scores for short- and long-term outcomes using the gain and the phase scores

Outcome	Frequency range	Scores	Normal median (min:max)	Abnormal median (min:max)	*p*-Value
Short-term (23 normal, 19 abnormal infants)	VLF	Gain			
		MABP-HbD	0.79 (0.37:2.04)	0.55 (0.34:2.43)	0.07
		pCO_2-HbD	15.30 (7.03:66.52)	14.61 (6.21:28.05)	0.55
		Phase			
		MABP-HbD	−0.15 (−1.08:0.45)	−0.06 (−0.68:0.77)	0.71
		pCO_2-HbD	0.01 (−0.40:0.30)	−0.06 (−0.54:0.32)	0.45
	LF	Gain			
		MABP-HbD	0.48 (0.19:4.45)	0.39 (0.15:5.23)	0.07
		pCO_2-HbD	17.03 (9.00:43.13)	13.72 (4.94:41.43)	0.24
		Phase			
		MABP-HbD	−0.08 (−1.0:0.32)	−0.07 (−0.58:0.67)	0.71
		pCO_2-HbD	0.02 (−0.20:0.28)	−0.02 (−0.23:0.20)	0.31
	HF	Gain			
		MABP-HbD	0.43 (0.11:10.02)	0.20 (0.09:14.74)	**0.02**
		pCO_2-HbD	9.28 (3.02:42.48)	6.72 (2.08:45.12)	0.14
		Phase			
		MABP-HbD	0.005 (−0.42:1.39)	−0.005(−0.27:0.26)	0.81
		pCO_2-HbD	−0.01(−0.15:0.14)	−0.01(−0.17:0.16)	0.79

Long-term (8 normal, 34 abnormal infants)	VLF	Gain			
		MABP-HbD	0.80 (0.43:1.78)	0.66 (0.34:2.43)	0.22
		pCO_2-HbD	14.57 (8.75:66.52)	15.44 (6.21:56.54)	0.79
		Phase			
		MABP-HbD	−0.21 (−1.08:0.29)	−0.09 (−0.76:0.77)	0.40
		pCO_2-HbD	−0.01 (−0.54:0.23)	−0.03 (−0.43:0.32)	0.70
	LF	Gain			
		MABP-HbD	0.45 (0.32:1.63)	0.39 (0.15:5.23)	0.35
		pCO_2-HbD	16.65 (11.78:23.23)	14.02 (4.94:43.13)	0.50
		Phase			
		MABP-HbD	−0.07 (−0.67:0.32)	−0.18 (−1.00:0.67)	0.77
		pCO_2-HbD	−0.03 (−0.23:0.20)	0.014 (−0.20:0.28)	0.46
	HF	Gain			
		MABP-HbD	0.45 (0.21:4.00)	0.23 (0.09:14.74)	0.23
		pCO_2-HbD	9.62 (6.35:12.08)	7.95 (2.08:45.12)	0.54
		Phase			
		MABP-HbD	0.17 (−0.42:1.39)	−0.03 (−0.32:0.26)	0.09
		pCO_2-HbD	−0.04 (−0.09:0.14)	−0.013 (−0.17:0.16)	0.92

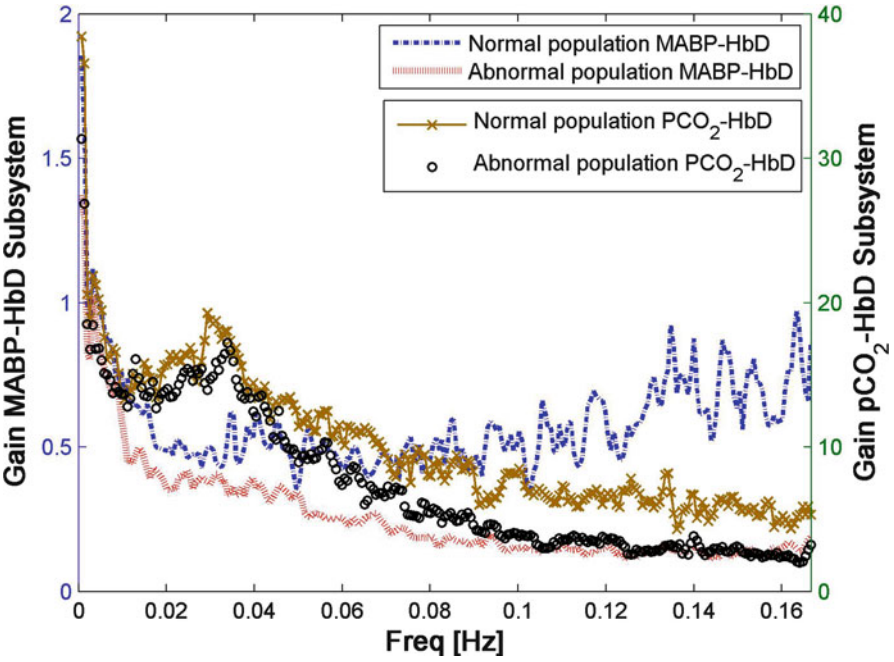

Fig. 6.1 Median values of the gain frequency response for the MABP/HbD and the pCO_2/HbD subsystems

the high-pass filter behavior is only present in the normal population. The metabolic (pCO_2-HbD) subsystem presents a low-pass filter behavior in both classes. The area under the curves was compared for the normal and the abnormal population. The areas for the median gain values for the myogenic mechanism were 0.096 and 0.043 μmol Hz/mmHg L for the normal and abnormal population, respectively; for the metabolic mechanism, the areas were 1.67 and 1.23 μmol Hz/mmHg L. Those areas were statistically different between normal and abnormal populations with *p*-values 0.022 and 0.042 for the myogenic and metabolic mechanism, respectively.

Figure 6.2 presents the *p*-values from the Kruskal–Wallis test performed for the gain values of the metabolic subsystem (pCO_2-HbD) in frequency domain for the BW analysis. In this analysis, 15 infants were classified as abnormal with BW < 1,200 g and 27 infants classified as normal with BW > 1,200 g. The differences between the median values in the normal and abnormal subgroups are statistically more significant in the VLF frequencies. As frequency increases, the gain scores in both populations are similar.

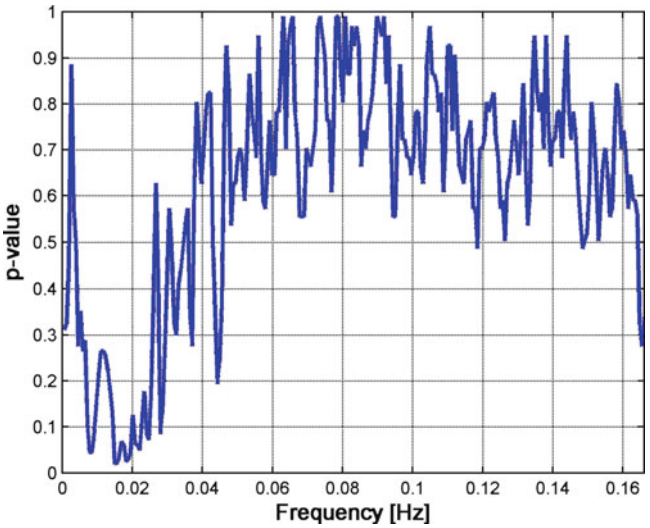

Fig. 6.2 *p*-Values from the Kruskal–Wallis test performed for each gain value (pCO_2-HbD) in frequency domain

5 Discussion

Cerebral autoregulation is a property of the brain and is regulated by three different mechanisms, namely: a myogenic, metabolic, and neurogenic one. On the one hand, the myogenic mechanism is in charge of minimizing the impact of the variations in MABP in the CBF. This mechanism is hypothesized to behave as a high-pass filter [1] where the slow oscillations in MABP are damped but the fast oscillations are reflected in the CBF. This hypothesis appears to be correct according to the results shown in Fig. 6.1. However, this high-pass characteristic was only found outside the normal frequency ranges where autoregulation is normally explored and is absent in the abnormal population. If only the VLF, LF, and HF ranges are analyzed the system behavior reflects a low-pass filter characteristic. This can be due to the disturbances included for the pCO_2 in the MABP and CBF in the VLF. The coupled dynamics between MABP and pCO_2 have not been studied in this chapter; therefore, further investigation is needed to prove this claim.

On the other hand, the metabolic mechanism is hypothesized to behave as a low-pass filter [1]. In this system, the slow variations in pCO_2 are reflected in the CBF while the fast variations are neglected. This is consistent with the results shown in Fig. 6.1. This behavior can be attributed to the time constant involved in the metabolic mechanism to adjust the muscular tone around the vascular wall. Thus, fast changes in pCO_2 are of too short duration to produce big changes in CBF.

We use the gain and phase values in the myogenic and the metabolic subsystems present in cerebral autoregulation to classify between normal and abnormal infants

based on different criteria. Only infants with abnormal short-term outcomes presented statistically different gain scores for the myogenic mechanism. All the other gain and phase scores given in Table 6.1 did not present statistically significant differences between the normal and abnormal population. Moreover, the scores were higher in the normal population compared to the abnormal population, contrary to what was expected. Indeed, according to the literature, higher gain values are expected in the abnormal population as this population should present a stronger link in dynamics compared to the normal infants. Nevertheless, important trends could be observed. As given in Table 6.1, all median values of the gain score were higher in the normal than the abnormal population. Moreover, Fig. 6.1 shows that the difference in median values for the normal and abnormal population becomes more pronounced as frequency increases. The results presented in this chapter point out the importance of the frequency range selected for cerebral autoregulation assessment. Moreover, the frequency response shown in Fig. 6.1 suggests that the metabolic mechanism can be acting as a modulator of the myogenic mechanism in the VLF. This hypothesis should be proven in a more extensive study where more babies, and with more critical outcomes, are included.

Acknowledgments Research supported by GOA AMBioRICS, GOA-MANET, CoE EF/05/006 (OPTEC), IUAP P6/04 (DYSCO).

References

1. Peng T, Rowley A, Ainslie PN et al (2008) Multivariate system identification for cerebral autoregulation. Ann Biomed Eng 36(2):308–320
2. Tsuji M, Saul J, du Plessis A et al (2000) Cerebral intravascular oxygenation correlates with mean arterial pressure in critically ill premature infants. Pediatr Rev 106(4):625–632
3. Wong F, Leung T, Austin T et al (2008) Impaired autoregulation in preterm infants identified by using spatially resolved spectroscopy. Pediatrics 121:604–611
4. De Smet D, Jacobs J, Ameye L, Vanderhaegen J, Naulaers G et al. (2008) The partial coherence method for assessment of impaired cerebral autoregulation using near-infrared spectroscopy: potential and limitations. In: Proceedings ISOTT 2008, August 3–7, Sapporo, Japan
5. Caicedo A, Van Huffel S (2010) Weighted LS-SVM for function estimation applied to artifact removal in biosignal processing. In: Proceedings of the 32nd annual international conference of the IEEE Engineering in Medicine and Biology Society (EMBC 2010), Buenos Aires, Argentina, August 31–September 4, 2010, paper 1578

Chapter 7
Frontal Cortex Activation During Electrical Muscle Stimulation as Revealed by Functional Near-Infrared Spectroscopy

Makii Muthalib, Marco Ferrari, Valentina Quaresima, and Kazunori Nosaka

1 Introduction

Electrical muscle stimulation (EMS) is a widely applied technique in clinical medicine and sports training to generate muscle contractions by activating peripheral motor axons [7]. Although less well studied, EMS can also activate peripheral sensory axons that send proprioceptive and pain signals from the muscle to the sensory, motor, and association cortices, thereby increasing cortical excitability and activation [1, 2, 6]. For example, Blickenstorfer et al. [1] used fMRI to measure cortical and subcortical activation responses during EMS of the wrist extensors/flexors, and showed an activation pattern comprising the contralateral primary motor and somatosensory cortex, and premotor cortex; the ipsilateral cerebellum; bilateral secondary somatosensory cortex, the supplementary motor area, and anterior cingulate cortex. Moreover, Smith et al. [6] showed a relationship between changes in sensorimotor cortical activation using fMRI and increased current intensity during EMS of the knee extensors, which the authors presumed was related to pain processing.

It has been reported that the role of frontal cortex (FC) regions in pain processing is linked to more cognitive and emotional responses [4]. However, the effect of increasing EMS current intensity to the maximum tolerated pain threshold, which is

M. Muthalib, Ph.D. (✉)
School of Exercise and Health Sciences, Edith Cowan University, Joondalup, WA, Australia

Movement Neuroscience Program, Institute of Health and Biomedical Innovation, Queensland University of Technology, Kelvin Grove, Brisbane, QLD 4059, Australia
e-mail: m.muthalib@qut.edu.au; makii.muthalib@gmail.com

M. Ferrari • V. Quaresima
Department of Health Sciences, University of L'Aquila, L'Aquila, Italy

K. Nosaka
School of Exercise and Health Sciences, Edith Cowan University, Joondalup, WA, Australia

M. Wolf et al. (eds.), *Oxygen Transport to Tissue XXXIII*, Advances in Experimental Medicine and Biology 737, DOI 10.1007/978-1-4614-1566-4_7,

a common practice in EMS strength training [7], on FC activation has not been clarified. Previous fMRI [3] and functional near-infrared spectroscopy (fNIRS) [5] studies have reported a proportional relationship between FC activation and contraction intensity during voluntary (VOL) exercise, indicating that FC activation is positively correlated to voluntary efforts, as a high level of effort is required to exert greater muscle force. Compared with fMRI, fNIRS is characterized by a very high experimental flexibility, for example, fNIRS is (1) silent and more tolerant to subtle movement artifacts, (2) can measure oxygenated-hemoglobin (ΔO_2Hb) and deoxygenated-Hb (ΔHHb) thereby providing a more complete evaluation of the cortical hemodynamic response, (3) allows long-time continuous measurements and repeated measurements within short intervals, and (4) has a higher temporal resolution. The aim of this study was to investigate FC oxygenation responses to EMS-evoked contractions at increasing current intensity, and to compare these changes to VOL contractions, performed at two different intensities (30 and 100% maximum voluntary isometric contraction, MVC), using fNIRS.

2 Methods

Nine healthy men participated in this study, and their mean (±SD) age, height, and body mass were 30.0 ± 7.3 years, 175.9 ± 5.0 cm, 80.8 ± 10.0 kg, respectively. All subjects had no known health problems (e.g., metabolic or neuromuscular disorders) or any upper extremity muscle or joint injuries. The study conformed to the recommendations of the local Human Research Ethics Committee in accordance with the Declaration of Helsinki.

All subjects participated in two sessions separated by 24 h (1) EMS session performed with one arm and (2) VOL session with the other arm. The use of the dominant and nondominant arm was counterbalanced among subjects and sessions.

Subjects were seated on a preacher arm curl bench, securing the shoulder angle at 45° flexion with a supinated forearm position and an elbow joint angle of 90°. The elbow joint was aligned with the axis of rotation of an isokinetic dynamometer (Cybex6000, Lumex Inc., Ronkonkoma) with HUMAC2004 software (Computer Sports Medicine, Inc., Massachusetts). Torque signals were collected onto a data acquisition system (PowerLab16, ADInstruments, Bella Vista, Australia) at a sampling rate of 200 Hz, and real-time visual feedback of torque signals were displayed on the computer monitor.

A portable stimulator (Compex2, Medicompex SA, Ecublens, Switzerland) was used to deliver biphasic symmetric rectangular pulses with frequency of 30 Hz and pulse duration of 200 μs. Two self-adhesive surface electrodes of 25 cm^2 (5 × 5 cm) were placed along the mid-belly of the biceps brachii and brachioradialis muscles. A dispersive electrode of 50 cm^2 (5 × 10 cm) was placed on the elbow crease.

Subjects initially performed two 3-s MVCs with a 45 s rest between contractions, and the peak torque was used as the preexercise MVC torque. Both EMS and

VOL sessions consisted of repeated (1-s contraction and 1-s relaxation) isometric contractions of the elbow flexors. Thirty contractions were performed at 30% MVC during the first 60 s in both VOL and EMS sessions. Then 30 contractions, performed at the maximal intensity (100% MVC and at the maximal tolerable current amplitude for VOL and EMS session, respectively) were completed in the next 60 s. Additional 15 maximal contractions (30-s duration) were performed until MVC was decreased by ~30%. Torque integral during the exercise was determined as the area under the torque traces every 15 s.

This study used a NIRO-200 oximeter (Hamamatsu Photonics K.K., Hamamatsu, Japan). The probe unit has two silicon photodiodes as photodetectors on one side and three laser-emitting diodes (775, 810, and 850 nm) on the other side separated from each other by a distance of 4 cm. One probe unit was firmly attached over the skin of the forehead (in a region corresponding to either Fp1 or Fp2) contralateral to the exercising arm with a double-sided adhesive tape. The probe unit, in turn, was covered with a black band. The NIRO-200 provides estimates of absolute concentration changes (from an arbitrary baseline of zero) in oxygenated-hemoglobin (ΔO_2Hb) and deoxygenated-Hb (ΔHHb) at a sampling rate of 6 Hz. The quantification of Hb concentration changes, expressed in $\Delta\mu M$, was obtained by including an age-dependent constant differential pathlength factor ($5.13 + 0.07 \times age^{0.81}$). NIRS variables were presented as the average value of every 15 s and the areas under the curve (AUC) were computed using the ΔO_2Hb curves over the time associated with the exercise during the first 60 s (30% MVC) and second 60 s (maximum intensity).

Changes in ΔO_2Hb and ΔHHb over time (baseline: pre, during 30% MVC: 15, 30, 45, 60 s, during maximum intensity: 75, 90, 105, 120 s, and during recovery: 15 and 30 s post) were compared between the EMS and VOL sessions by a two-way repeated measures ANOVA. When a significant main or time effect, or interaction (session × time) effect was found, a Fisher's LSD post hoc test was performed. A Student's *t* test was used to compare between the EMS and VOL sessions for torque integral and ΔO_2Hb AUC during 30% MVC and the respective maximum intensity. Pearson's correlation analysis was used to determine the relationship between EMS current amplitude and ΔO_2Hb changes. Significance was set at $P \leq 0.05$. Data are presented as mean ± SEM.

3 Results

In the EMS session, the current amplitude during the first 30 contractions was increased from 49.4 ± 3.7 to 54.2 ± 4.1 mA to maintain the 30% MVC target, and the current amplitude during the subsequent contractions was continually increased, such that current amplitude was maintained at the maximum tolerated pain threshold (56.0 ± 4.3 to 68.7 ± 5.0 mA). The maximum current amplitudes were tolerated by all the subjects; however, the range of current amplitudes that could be tolerated varied amongst subjects.

Table 7.1 Changes in frontal cortex oxygenated Hb (O_2Hb) and deoxygenated Hb (HHb) during the 30% MVC and maximal intensity contractions for the electrical muscle stimulation (EMS) and voluntary (VOL) sessions

			30% MVC				Maximum intensity				Recovery	
		Pre	15 (s)	30 (s)	45 (s)	60 (s)	75 (s)	90 (s)	105 (s)	120 (s)	15 (s)	30 (s)
ΔO_2Hb (μM)	EMS	0.0	1.8[a,b]	4.0[a,b]	3.7[a,b]	3.9[a,b]	4.9[b]	6.3[b]	6.8[b]	7.1[b]	3.8	2.4
			(0.3)	(0.9)	(1.5)	(1.3)	(1.2)	(1.0)	(1.1)	(1.3)	(0.7)	(0.5)
	VOL	0.0	0.0	0.2	0.6	0.8	6.2[b]	9.7[b]	10.7[b]	10.0[b]	2.6	0.7
			(0.3)	(0.3)	(0.4)	(0.4)	(1.3)	(1.9)	(2.2)	(2.2)	(1.5)	(0.8)
ΔHHb (μM)	EMS	0.0	−0.1	−0.3	−0.1	−0.2	−0.6	−0.4	−0.2	−0.2	0.0	0.4
			(0.1)	(0.2)	(0.2)	(0.2)	(0.3)	(0.3)	(0.2)	(0.2)	(0.3)	(0.3)
	VOL	0.0	−0.2[b]	−0.4[b]	−0.5[b]	−0.6[b]	−0.5	0.4	0.8	0.8	0.8	1.1
			(0.1)	(0.1)	(0.2)	(0.1)	(0.3)	(0.4)	(0.5)	(0.5)	(0.5)	(0.5)

$n=9$; SEM values in parenthesis
[a]EMS significantly different from VOL
[b]Significantly different from baseline (Pre)

The torque produced during the first 30 contractions was close to 30% MVC for both protocols, and no significant difference in the torque integral existed between EMS (670.3 ± 35.2 Nm s) and VOL (565.1 ± 49.3 Nm s). When the contractions were performed at the respective maximum intensity, torque integral was greater ($P<0.001$) for VOL (1,431.6 ± 109.8 Nm s) than EMS (639.3 ± 24.7 Nm s).

Table 7.1 shows the FC oxygenation changes during the EMS and VOL sessions. In the EMS session, ΔO_2Hb increased ($P<0.05$) and thereafter progressively increased ($P<0.05$) with raising current amplitude (i.e., maximum tolerated pain threshold) during the 30% MVC contractions, and the two variables were correlated ($r=0.68$, $P<0.001$). In the VOL session, ΔO_2Hb did not change from baseline levels during 30% MVC; however, ΔO_2Hb progressively increased ($P<0.05$) during the 100% MVC contractions. ΔO_2Hb was greater ($P<0.05$) during the maximum intensity than 30% MVC contractions for both EMS and VOL sessions. ΔO_2Hb AUC was greater ($P<0.05$) for EMS (203.6 ± 58.4 μM s) than VOL (24.7 ± 20.7 μM s) at 30% MVC, whilst no difference in ΔO_2Hb AUC was evident between EMS (377.9 ± 62.1 μM s) and VOL (549.9 ± 107.7 μM s) at the respective maximum intensity (Table 7.1). ΔO_2Hb progressively returned to the baseline during the recovery period after both EMS and VOL.

For the VOL session, ΔHHb decreased ($P<0.05$) from baseline during 30% MVC and was at baseline levels during the 100% MVC contractions, whilst ΔHHb did not change from baseline levels in the EMS session (Table 7.1).

4 Discussion

For the VOL session, the results of the present study confirm the previous neuroimaging studies [3, 5] suggesting that the FC plays a role in modulating the strength of the exercising muscles and ensuring a correct execution of the motor task.

For the EMS session, due to the painful character of the electrical stimulation, increased activation within the FC areas, such as the prefrontal cortex [4] and anterior cingulate cortex [1, 6], may be related to subjective sensations of the discomfort. Therefore, in the EMS session, the FC may play a role in integrating sensorimotor information and evaluating an emotional response to pain.

In conclusion, this study demonstrated intensity-related increases in FC activation during EMS of the elbow flexors using fNIRS.

Acknowledgments We would like to thank Dr. Marc Jubeau, Dr. Nicola Maffiuletti, and Prof. Guillaume Millet for their assistance in the research.

References

1. Blickenstorfer A, Kleiser R, Keller T et al (2009) Cortical and subcortical correlates of functional electrical stimulation of wrist extensor and flexor muscles revealed by fMRI. Hum Brain Mapp 30:963–975
2. Han BS, Jang SH, Chang Y et al (2003) Functional magnetic resonance image finding of cortical activation by neuromuscular electrical stimulation on wrist extensor muscles. Am J Phys Med Rehabil 82:17–20
3. Liu JZ, Shan ZY, Zhang LD et al (2003) Human brain activation during sustained and intermittent submaximal fatigue muscle contractions: an FMRI study. J Neurophysiol 90:300–312
4. Lorenz J, Minoshima S, Casey KL (2003) Keeping pain out of mind: the role of the dorsolateral prefrontal cortex in pain modulation. Brain 126:1079–1091
5. Mottola L, Crisostomi S, Ferrari M et al (2006) Relationship between handgrip sustained submaximal exercise and prefrontal cortex oxygenation. Adv Exp Med Biol 578:305–309
6. Smith GV, Alon G, Roys SR et al (2003) Functional MRI determination of a dose-response relationship to lower extremity neuromuscular electrical stimulation in healthy subjects. Exp Brain Res 150:33–39
7. Vanderthommen M, Duchateau J (2007) Electrical stimulation as a modality to improve performance of the neuromuscular system. Exerc Sport Sci Rev 35:180–185

Chapter 8
Cerebral Oxygen Saturation Measurements in Red Cell Transfusion

Zareen Bashir, Sarah Haynes, Peter Sandbach, Robin Calderwood, Charles McCollum, and Maureen Thorniley

1 Introduction

Major vascular surgery is associated with moderate to major blood loss and allogeneic red cell transfusion maybe given to compensate for the loss. However, the risks associated with red blood cell transfusion have potentially long-term consequences for patients and are costly for health services [1]. The current clinical reasons on which the decision to transfuse is made are multifactorial. Clinical parameters indicating blood transfusion include haemoglobin concentration (Hb) and vital signs or volume of blood loss, but these are poor measures of tissue oxygenation [2]. In critically ill patients with cardiovascular disease, a haemoglobin concentration of 90 g/L has been suggested as a trigger or threshold for blood transfusion [3]. During blood loss haemoglobin concentration falls with an initial increase in cardiac output to maintain systemic oxygen delivery. However, if the haemoglobin concentration continues to fall, the increase in cardiac output (CO) can no longer maintain oxygen delivery, and hence demand will exceed delivery [4]. The balance between oxygen delivery and consumption can be described by oxygen extraction which is determined by VO_2/DO_2 where VO_2 is oxygen consumption and DO_2 is oxygen delivery

Z. Bashir • S. Haynes • P. Sandbach • R. Calderwood • C. McCollum
The University of Manchester, Manchester Academic Science Centre, University Hospital of South Manchester NHS Foundation Trust, Wythenshawe, Manchester, UK

M. Thorniley (✉)
The University of Manchester, Manchester Academic Science Centre, University Hospital of South Manchester NHS Foundation Trust, Wythenshawe, Manchester, UK

Holcroft Lane, Culcheth, Warrington, Cheshire, WA3 5AN, UK
e-mail: maureen.s.thorniley@gmail.com

M. Wolf et al. (eds.), *Oxygen Transport to Tissue XXXIII*, Advances in Experimental Medicine and Biology 737, DOI 10.1007/978-1-4614-1566-4_8,

and $DO_2 = CO \times CaO_2$ ($CaO_2 = CO \times [Hb] \times 1.39 \times SaO_2$) and $VO_2 = CO(CaO_2 - CvO_2)$ [5, 6]. Thus:

$$OER = \frac{CaO_2 - CvO_2}{CaO_2},$$

where CaO_2 = arterial oxygen content and CvO_2 = venous oxygen content.

If the cardiac output cannot be increased the oxygen extraction ratio (OER) will increase to maintain tissue oxygenation. Systemic OER can be a sensitive indication of changes in oxygen consumption/delivery and it has been reported by Orlov et al. [7] that it can be used as a more appropriate transfusion trigger [7]. Ideally, blood ought to be given when oxygen delivery becomes insufficient to meet the tissue's needs [4].

This research was part of a research programme designed to develop a transfusion trigger based on tissue oxygenation. In previous research, we demonstrated that following blood transfusion in patients undergoing aortic or spinal surgery, significant increases in cerebral and peripheral haemoglobin oxygen saturation were observed in response to transfusion [8]. In this study we used changes in OER as an appropriate indicator of the need for transfusion. We then examined the relationship between NIRS and other physiological measurements to determine whether any of these parameters could be used reliably as a non-invasive surrogate for OER in isolation or combination. Note, this is not a test of the accuracy of whether to transfuse – it is a test of the *decision to* transfuse and to guide the progression of transfusion.

2 Methods

This study was approved by the Local Research Ethics Committee. All patients gave written informed consent to participate.

Regional haemoglobin oxygen saturation from the cerebral cortex (CsO_2) was measured in 25 patients and from the forearm (PsO_2) in 21 of these patients, undergoing autologous (cell salvage) red cell transfusion during elective abdominal aortic aneurysm (AAA) repair. Measurements were made using the 2-pad INVOS 4100 oximeter (Somanetics, Michigan, USA). Light at two wavelengths (730 and 810 nm) is emitted and measured using two detectors, 3 and 4 cm from and in line from the light source. The 3 cm data were subtracted from the 4 cm data, cancelling the effect of pathlength.

Further monitoring included haemoglobin concentration (Hb in g/L) which was measured using Hemocue (HemoCue Limited, Dronfield, UK), oxygen partial pressure (pO_2 in kPa), lactate concentration (Lac in mmol/L) and OER (in %) from central venous blood samples analysed using a Stat Profile pHOx Plus L blood gas analyser (Nova medical, Massachusetts, USA). Systolic (Sys in mmHg), diastolic (Dia in mmHg) and mean arterial pressure (MAP in mmHg) were measured using

an indwelling radial artery catheter. Arterial oxygen saturation (SaO_2 in %) was measured via pulse oximetry, and end-tidal carbon dioxide ($EtCO_2$ in mmHg) was measured by capnograph.

The results were retrospectively split two groups: patients showing a decrease in OER post-transfusion (group 1, $n=15$), and patients showing an increase/no change in OER post-transfusion (group 2, $n=10$). Statistical analysis (SPSS 16.0) was by independent t test with $p<0.05$ considered significant. Results are presented as mean ± SD. Relationships for volume of red blood cells transfused, CsO_2 and $MvSO_2$ were determined using Pearson's correlation for normally distributed data.

3 Results

Patients' mean (SD) blood volume, estimated from published height and weight nomograms [9] was 5,032 (676) mL. There was no significant difference between estimated blood volume of group 1 5,007 ± 662 compared to 5,067 ± 733 group 2 mL. The mean (SD) salvaged red cell volume transfused was 763 (489) mL.

Hb increased by 19.1 ± 10.4 g/L in group 1 and this was significantly higher compared to the increase of 8.7 ± 11.1 g/L in group 2 ($p=0.025$, Fig. 8.1). The change in

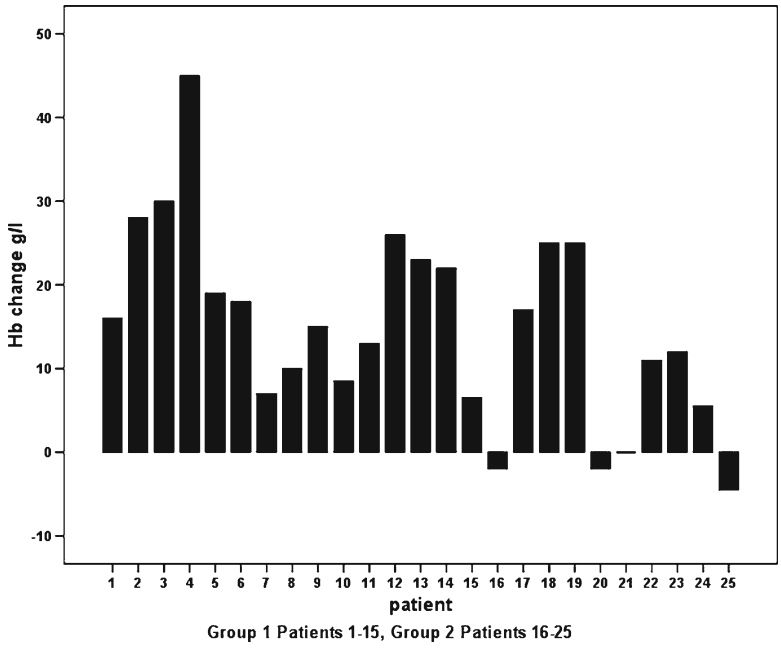

Fig. 8.1 Individual changes in haemoglobin concentration following red cell transfusion for patients with a decrease in OER [group 1] and patients with an increase/no change in OER [group 2]

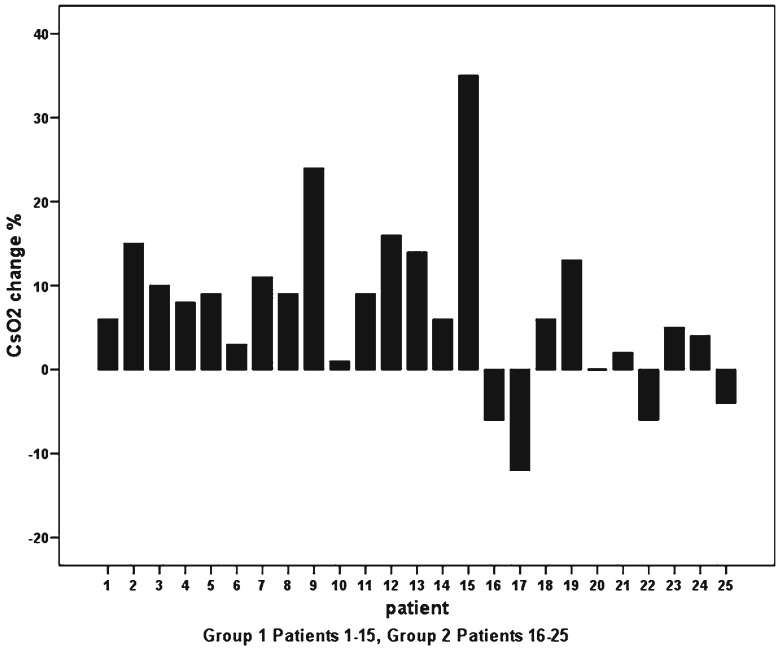

Fig. 8.2 Individual changes in cerebral haemoglobin oxygen saturation following red cell transfusion for patients with a decrease in OER [group 1] and patients with an increase/no change in OER [group 2]

CsO_2 in group 1 was also significantly greater: 11.7 ± 8.6% compared to an increase of 0.2 ± 7.3% in group 2 ($p = 0.002$, Fig. 8.2). This was accompanied by a significant increase in pO_2 in group 1 by 1.5 ± 2.0 kPa ($p = 0.013$) compared to a non-significant change to 0.5 ± 1.9 kPa in group 2. This resulted in a significant increase in $MvSO_2$ by 8.9 ± 10.5% in group 1 ($p = 0.001$) compared to 1.2 ± 2.7% in group 2 (Fig. 8.3). Red cell transfusion resulted in no significant change in PsO_2 in either group: +5.33 ± 6.88 % (Grp1) and −0.23 ± 5.32% (Grp2).

There was no significant difference in the volume of red cell transfusion between groups (864 ± 514 mL in group 1 versus 611 ± 429 mL in group 2). In group 1, the volume of red cells transfused correlated with haemoglobin concentration (PC = 0.60, $p = 0.029$) but not in group 2. There were no significant changes in SaO_2, Sys, Dias or MAP in either group (Table 8.1).

4 Conclusions

Cerebral oxygen saturation increased significantly in response to autologous red cell transfusion with an associated increase in haemoglobin concentration and mixed venous oxygen saturation indicating higher saturation with a concomitant

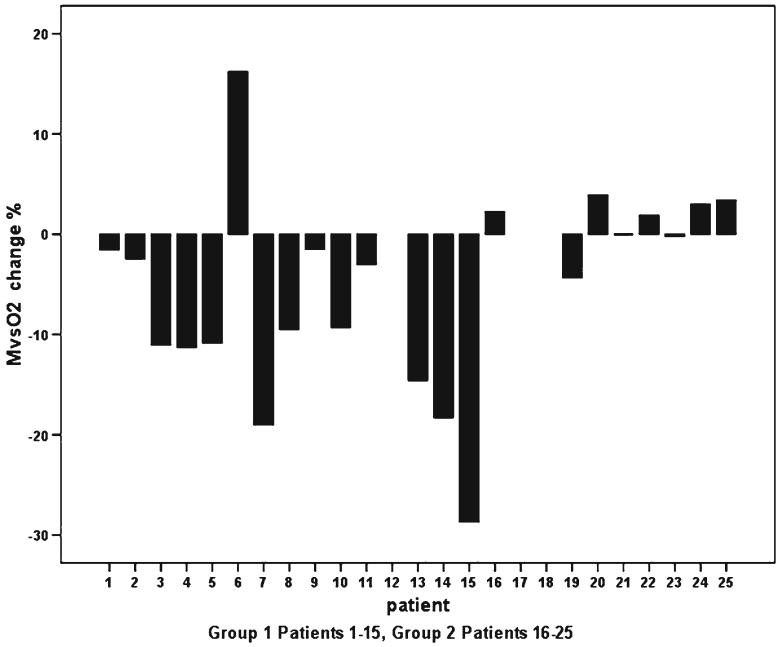

Fig. 8.3 Individual changes in mixed venous oxygen saturation following red cell transfusion for patients with a decrease in OER [group 1] and patients with an increase/no change in OER [group 2]

Table 8.1 Non-significant changes in systolic, diastolic and mean arterial pressure, arterial oxygen saturation, lactate concentration and end-tidal carbon dioxide following red cell transfusion

	Before transfusion	Mean change
Sys (mmHg)	104 ± 26	−12 ± 37
Dias (mmHg)	55 ± 13	−4 ± 15
MAP (mmHg)	75 ± 18	−2 ± 25
SaO_2 (%)	98 ± 1	0 ± 1
Lac (mmol/L)	2.9 ± 1.5	−0.1 ± 1.2
$EtCO_2$ (mmHg)	34 ± 4	−5 ± 6

fall in oxygen extraction in group 1 patients. In group 2 patients where oxygen extraction increased or did not change, no significant change was observed in haemoglobin concentration, cerebral oxygenation and mixed venous oxygen saturation. There were no significant changes in arterial oxygen saturation, or acid base parameters, including lactate concentration and end-tidal carbon dioxide, which may account for the rise in cerebral oxygenation in group 1 patients.

There are an increasing number of studies emerging indicating that OERs are a good guide to blood transfusions in pre-term infants [10, 11]. In cardiac surgery, O'Farrell et al. demonstrated that OER may be a more appropriate transfusion trigger

than low Hb, and speculated that 40% of transfusions would have been avoided if OER had been used as a transfusion trigger [12]. Similar studies in cardiac surgery have also reported that the use of OER as a transfusion trigger could lead to a reduction in blood transfusions [7, 13]. Cerebral oxygen consumption is dependent upon several factors including oxygen delivery, which in turn is dependent upon cardiac output, Hb concentration and pO_2. It can be hypothesised that in patients where oxygen extraction fell upon transfusion, associated with an increase in cerebral saturation this is due to effect of increased Hb resulting in an increase in DO_2. In the patients where there was no change in OER and CSo_2 upon transfusion, it could be inferred that the effect of the red cell transfusion had no effect on delivery and was unnecessary. In this group of patients, CsO_2 is a more useful indicator of tissue oxygenation than PsO_2. In the future, in our major vascular surgery patients, NIRS measurements maybe useful in determining non-invasive oxygen extraction.

In the group of patients where OER decreased post-transfusion, cerebral oxygenation improved with an associated increase in Hb concentration. The current study suggests that changes in CsO_2 maybe useful in assessing the efficacy of transfusion with the ultimate goal in deciding when to transfuse red blood cells, thereby possibly reducing unnecessary transfusions.

References

1. Reeves BC, Murphy GJ (2008) Increased mortality, morbidity, and cost associated with red blood cell transfusion after cardiac surgery. Curr Opin Cardiol 23:607–612
2. American College of Anesthesiologists Task Force on Blood Component Therapy (1996) Practice guidelines for blood component therapy. Anesthesiology 84:732
3. Herbert PC, Yetisir E, Martin C (2001) Is a low transfusion threshold safe in critically ill patients with cardiovascular disease? Crit Care Med 29:227–234
4. Madjdpour C, Spahn DR, Weiskopf RB (2006) Anemia and perioperative red blood cell transfusion: a matter of tolerance. Crit Care Med 34:S102–S108
5. Leach RM, Treacher DF (2002) The pulmonary physician in critical care 2: oxygen delivery and consumption in the critically ill. Thorax 57:170–177
6. McLellan SA, Walsh TS (2004) Oxygen delivery and haemoglobin. Crit Care Pain 4:123–126
7. Orlov D, O'Farrell R, McCluskey SA et al (2009) The clinical utility of an index of global oxygenation for guiding red blood cell transfusion in cardiac surgery. Transfusion 49:682–688
8. Torella F, Haynes SL, McCollum CN (2003) Cerebral and peripheral oxygen saturation during red cell transfusion. J Surg Res 110:217–221
9. Nadler SB, Hidalgo JU, Bloch T (1962) Prediction of blood volume in normal human adults. Surgery 51:224–232
10. Wardle SP, Weindling AM (2001) Peripheral fractional oxygen extraction and other measures of tissue oxygenation to guide blood transfusions in preterm infants. Semin Perinatol 25:60–64
11. Wardle SP, Garr R, Yoxall CW, Weindling AM (2002) A pilot randomised controlled trial of peripheral fractional oxygen extraction to guide blood transfusions in preterm infants. Arch Dis Child Fetal Neonatal Ed 86:F22–F27
12. O'Farrell R, Ghannam M, McCluskey M et al (2006) Oxygen extraction ratio (OER) and blood transfusion in cardiac surgery. Can J Anaesth 53:26342
13. Sehgal LR, Zebala LP, Takagi I et al (2001) Evaluation of oxygen extraction ratio as a physiologic transfusion trigger in coronary artery bypass graft surgery patients. Transfusion 41:591–595

Chapter 9
Influence of Stress Preconditioning on Hippocampal Neuronal Cell Death and Neurogenesis in Rat Cerebral Ischemia

Takashi Eriguchi, Nobuo Kutsuna, Yuko Kondo, Jie Shi, Yoshihiro Murata, Hideki Oshima, Kaoru Sakatani, and Yoichi Katayama

1 Introduction

Numerous studies have demonstrated that the subgranular zone (SGZ) in dentate gyrus of the hippocampus is vulnerable in cerebral ischemia [1]. Selective and delayed neuronal cell death after global ischemia occurs in rat SGZ [2], and the delayed neuronal cell death is increased by stress after ischemia [3]. It was also reported that neurogenesis proceeds constantly in the subventricular zone (SVZ) and SGZ [4]. Neurogenesis in SVZ and SGZ is deeply involved in memory, learning, and mood disorders [5]. Neurogenesis in rat SGZ is enhanced by learning and neuronal damage, such as seizure and ischemic insult, and reduced by stress after ischemia [6].

In the present study, we evaluated the influence of stress prior to cerebral ischemia on neuronal cell death in rats.

2 Methods

All experiments were performed following an institutionally approved protocol in accordance with the guidelines of the Nihon University Laboratory Animal Research Committee.

T. Eriguchi (✉) • N. Kutsuna • Y. Kondo • J. Shi • Y. Murata • H. Oshima • Y. Katayama
Division of Neurosurgery, Department of Neurological Surgery, Nihon University School of Medicine, 30-1 Oyaguchi-Kamimachi, Itabashi-ku, Tokyo 173-8610, Japan
e-mail: eriguchi.takashi@nihon-u.ac.jp

K. Sakatani
Division of Neurosurgery, Department of Neurological Surgery, Nihon University School of Medicine, 30-1 Oyaguchi-Kamimachi, Itabashi-ku, Tokyo 173-8610, Japan

Division of Optical Brain Engineering, Department of Neurological Surgery, Nihon University School of Medicine, Tokyo, Japan

M. Wolf et al. (eds.), *Oxygen Transport to Tissue XXXIII*, Advances in Experimental Medicine and Biology 737, DOI 10.1007/978-1-4614-1566-4_9,

Twenty-four Sprague–Dawley male rats (250–300 g) were anesthetized with isoflurane (1–1.2%) in 30% oxygen/70% nitrous oxide. Temperature was maintained at 37°C with a heating pad. Femoral arteries were cannulated to monitor pressure, pH, and blood gases. Rats were assigned into the following groups: controls housed in normal cages ($n=6$); ischemia ($n=6$); stress ($n=6$); ischemia following stress ($n=6$).

Global ischemia was induced by means of bilateral carotid arterial occlusion for 10 min [7].

A forced swimming test was used to impose stress. Briefly, rats were obliged to swim from 2 days before induction of ischemia [8].

Rats were euthanized at 7 days after ischemia. The brain was perfused with saline and 4% paraformaldehyde, then 50 μm coronal sections were cut. Fluoro-Jade B staining and BrdU staining were used to evaluate hippocampal neuronal cell death and neurogenesis, respectively. Fluoro-Jade B-positive cells were counted in 1 mm length of a horizontal section of hippocampal CA1 area. BrdU-positive cells were counted in 1 mm^2 of hippocampal dentate gyrus. Fluoro-Jade B-positive and BrdU-positive cells were evaluated in a double-blind manner.

Data are expressed as mean ± SD. The significance of differences in positive cell counts was assessed by means of ANOVA followed by Tukey–Kramer tests. Differences with $p<0.05$ were considered significant.

3 Results

Hippocampal neuronal cell death in the ischemia group, the stress group, and the ischemia following stress group was significantly increased compared with that in the control group (Fig. 9.1).

The ischemia following stress group showed a much greater increase of hippocampal neuronal cell death than the other groups.

As for neurogenesis, BrdU-positive cells in the ischemia group were significantly increased compared with the control and stress groups ($p<0.05$) (Fig. 9.2). In the ischemia following stress group, BrdU-positive cells were significantly decreased compared with the ischemia group ($p<0.05$). BrdU-positive cells in the stress group were decreased compared with the control. However, there was no significant difference in neurogenesis between the stress group and the control.

4 Discussion

Exposure to a stress condition after global cerebral ischemia leads to exacerbation of neuronal cell death in rat SGZ. However, little is known about whether stress prior to cerebral ischemia influences neuronal cell death and neurogenesis.

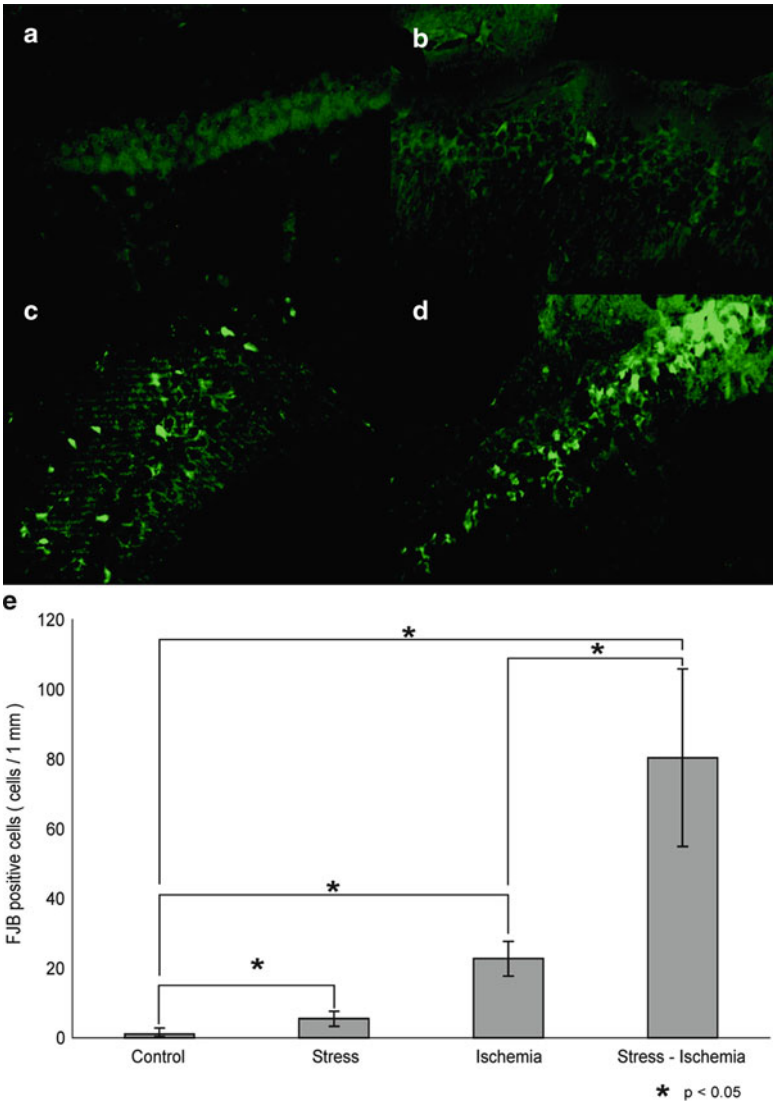

Fig. 9.1 Evaluation of neuronal cell death by Fluoro-Jade B staining. Hippocampal neuronal cell death in the ischemia group was significantly increased compared with that in the control group (**a**, **c**). The stress group also showed a significant increase of cell death compared with the control (**a**, **b**). The ischemia following stress group showed a much greater increase of hippocampal neuronal cell death than the other groups (**d**). The results of statistical analysis of cell counts of Fluoro-Jade B stained cells are summarized (**e**)

In the present study, exposure to a stress condition prior to cerebral ischemia resulted in an increase of neuronal cell death in SGZ. Previous studies have shown exacerbation of neuronal cell death in SGZ due to cardiac pulmonary arrest,

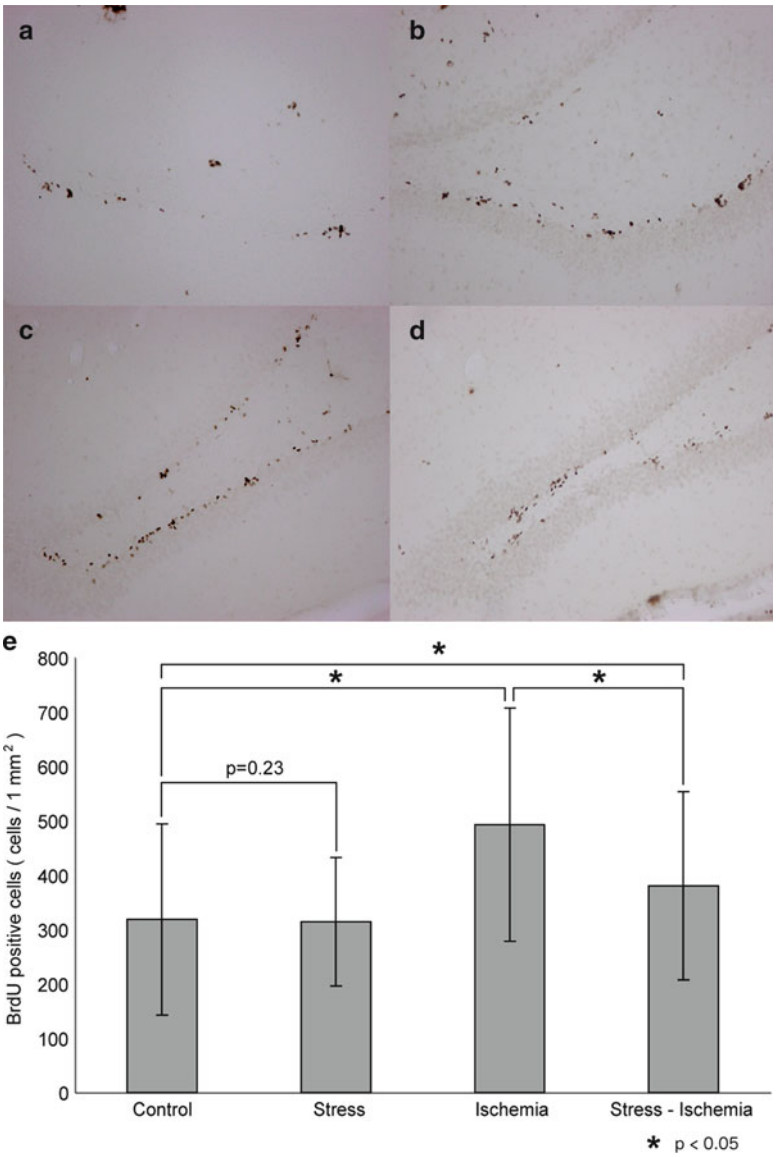

Fig. 9.2 Evaluation of neurogenesis by BrdU staining. BrdU-positive cells in the ischemia group were significantly increased compared with the control and stress groups. In the ischemia following stress group, BrdU-positive cells were significantly decreased compared with the ischemia group. There was no difference in neurogenesis between the control and stress groups. The results of statistical analysis of cell counts of BrdU-stained cells are summarized (**e**)

hypoglycemia, and so on [9]. Those stresses induce an increment of glucocorticoid, which exhibits neurotoxicity [10], and so may increase neuronal cell death after ischemia [11]. Glucocorticoid also decreases neurotropic factors, such as brain-derived

neurotrophic factor (BDNF) and vascular endothelial growth factor (VEGF), and therefore may inhibit neurogenesis as well as increasing neuronal cell death [12].

In conclusion, our results suggest that a stress environment before cerebral ischemia may increase neuronal cell death and impair neurogenesis. Thus, relief of stress may decrease damage and promote recovery following cerebral ischemia. These findings may also have implications for preventive medicine.

References

1. Kinno T (1982) Delayed neuronal death in the gerbil hippocampus following ischemia. Brain Res 239:57–69
2. Petito CK, Pulsinelli WA (1984) Delayed neuronal recovery and neuronal death in rat hippocampus following severe cerebral ischemia: possible relationship to abnormalities in neuronal processes. J Cereb Blood Flow Metab 4(2):194–205
3. Watanabe Y, Gould E, McEwen BS et al (1992) Stress induces atrophy of apical dendrites of hippocampal CA3 pyramidal neurons. Brain Res 588:341–345
4. Goldman SA, Nottebohm F (1983) Neuronal production, migration, and differentiation in a vocal control nucleus of the adult female canary brain. Proc Natl Acad Sci USA 80(8):2390–2394
5. Brown ES, Rush AJ, McEwen BS (1999) Hippocampal remodeling and damage by corticosteroids: implications for mood disorders. Neuropsychopharmacology 21(4):474–484
6. Parent JM (2003) Injury-induced neurogenesis in the adult mammalian brain. Neuroscientist 9:261–272
7. Smith ML, Auer RN, Siesjo BK (1984) The density and distribution of ischemic brain injury in the rat following 2–10 min forebrain ischemia. Acta Neuropathol (Berl) 64:319–332
8. Cryan JF, Valentino RJ, Lucki I (2005) Assessing substrates underlying the behavioral effects of antidepressants using the modified rat forced swimming test. Neurosci Biobehav Rev 29(4–5):547–569
9. Sapolsky R (1996) Stress, glucocorticoids, and damage to the nervous system: the current state of confusion. Stress 1(1):1–19
10. Sapolsky R (1985) A mechanism for glucocorticoid toxicity in the hippocampus: increased neuronal vulnerabilityto metabolic insults. J Neurosci 5:1227
11. Wang SH, Zhang ZJ, Guo YJ et al (2008) Hippocampal neurogenesis and behavioural studies on adult ischemic rat response to chronic mild stress. Behav Brain Res 189:9–16
12. Smith MA, Makino S, Kvetnansky R et al (1995) Stress and glucocorticoids affect the expression of brain-derived neurotrophic factor and neurotrophin-3 mRNA in the hip- pocampus. J Neurosci 15:1768–1777

Chapter 10
Differential Effects of Delta and Epsilon Protein Kinase C in Modulation of Postischemic Cerebral Blood Flow

Hung Wen Lin, David Della-Morte, John W. Thompson, Victoria L. Gresia, Srinivasan V. Narayanan, R. Anthony DeFazio, Ami P. Raval, Isabel Saul, Kunjan R. Dave, Kahlilia C. Morris, Min-Liang Si, and Miguel A. Perez-Pinzon

1 Introduction

Cerebral ischemia is defined by little or no blood flow in cerebral circulation characterized by low oxygen, glucose, and accumulation of metabolic products [1]. Upon reperfusion, hyperemia (increased blood flow) and subsequent hypoperfusion (decreased blood flow) of cerebral blood vessels [1] leads to enhanced superoxide generation [2]. The hyperemia phase leads to ischemia-induced cell death to different areas of the brain [2] as well as decreased blood flow (hypoperfusion) [3] resulting in yet another possible ischemic/hypoxic condition.

Protein kinase C (PKC) isozyme, namely δPKC, plays an important role in mediating cerebral reperfusion injury after ischemia [4]. Previously, we demonstrated that δPKC played a key role in CA1 rat hippocampal histopathology following asphyxial cardiac arrest (ACA) [5]. δPKC also modulates micro-cerebrovascular function in acute ischemia by mediating vascular tone, suggesting that δPKC may be involved in microvascular dynamics in the brain [6], which is functionally important and not well characterized due to previous technological limitations. Thus, the neuroprotection afforded by the specific δPKC inhibitor in our previous study after ACA [5] may also be due to CBF modulation.

εPKC is another novel PKC isozyme that has also been implicated in CBF dysfunction and neuronal viability during ischemia. Activation of εPKC during

H.W. Lin • D. Della-Morte • J.W. Thompson • V.L. Gresia • S.V. Narayanan • R.A. DeFazio • A.P. Raval • I. Saul • K.R. Dave • K.C. Morris • M.A. Perez-Pinzon, Ph.D. (✉)
Department of Neurology, Cerebral Vascular Disease Research Center,
D4-5 University of Miami, Miller School of Medicine, Miami, FL 33136, USA
e-mail: Mperez18@med.miami.edu

M.-L. Si
Department of Pharmacology, Southern Illinois University School of Medicine,
Springfield, IL 62794, USA

M. Wolf et al. (eds.), *Oxygen Transport to Tissue XXXIII*, Advances in Experimental Medicine and Biology 737, DOI 10.1007/978-1-4614-1566-4_10,

ischemia is thought to be beneficial, providing neuroprotection [7] and appropriate modulation of CBF after ischemia. The neuroprotective properties of εPKC in preconditioning have led to the testing of agonists of εPKC [ψε receptors for activated C kinase (RACK)] as possible therapy in cerebral ischemia. We present the detrimental effects (CBF derangement and neuronal damage) of δPKC activation in the brain after global cerebral ischemia [8], while activation of εPKC can reverse these pathologies caused by ischemia [9].

2 Methods

2.1 Chemicals

δPKC inhibitor (δV1-1), εPKC agonist (ψεRACK) [εPKC activator, amino acids 85-92 (HDAPIGYD)], and tat carrier peptide (control) were dissolved in sterile saline (0.9%) (KAI Pharmaceuticals Inc., San Francisco, CA, USA). A final volume of 700 μl (Tat peptide or δV1-1) was injected intravenously (IV) 30 min before induction of two-vessel occlusion with hypotension (2-VO) or ACA. Fluorescein isothiocyanate (FITC)-dextran (MW, 2,000,000) (0.2 mg/ml) was injected IV every 30 min to visualize blood flow and microvessels.

2.2 Animal Model

All experimental procedures were approved by the laboratory animal care and use committee (University of Miami, Miller School of Medicine). Adult male Sprague-Dawley rats (250–350 g) were fasted overnight before surgery. Rats were anesthetized with 4% isoflurane and a 30:70 mixture of oxygen and nitrous oxide followed by endotracheal intubation. Isoflurane was lowered to 1.5–2% for endovascular access. The femoral vein and artery were cannulated using a single-lumen (PE-50) catheter for blood pressure monitoring, blood gas analysis, and intravenous (IV) injection of pharmacological agents.

2.3 Two-Vessel Occlusion with Hypotension

After cannulation, hypotension was induced by withdrawing blood from the femoral artery reducing systemic blood pressure to 45–50 mmHg during ischemia. Next, cerebral ischemia was induced by tightening the carotid ligatures bilaterally for 10 min. To allow postischemic reperfusion, the carotid ligatures were removed, and shed blood re-injected into the artery restoring mean arterial blood pressure to baseline levels (~130–140 mmHg) [10].

2.4 Asphyxial Cardiac Arrest

To induce ACA, apnea was induced by disconnecting the ventilator from the endotracheal tube. Six minutes after asphyxia, resuscitation was initiated by administering a bolus injection of epinephrine (0.005 mg/kg, IV) and sodium bicarbonate (1 meq/kg, IV) followed by mechanical ventilation. Arterial blood gases were then measured. After ACA, the animal was placed directly on the 2-photon microscopy (2-PM) stage with the stereotaxic device in place for cortical microvessel imaging [8].

2.5 Two-Photon Microscopy

A thin circular area of the skull (~2 mm in diameter, 1 mm from bregma) was made via micro-drill until the skull was half the thickness. The rat was placed on a custom stereotaxic device on the microscope stage of the 2-PM (Lasersharp2000, BioRad). Fluorescent images were captured at 910 nm with the introduction of FITC-dextran (0.2 mg/kg), IV. Linescans for red blood cell (RBC) velocities and blood vessel diameter measurements were analyzed with Image J analysis software [8].

2.6 Laser-Doppler Flowmetry

A 2 mm^2 burr hole was made over the left frontoparietal cortex approximately 5.0 mm posterior and 3.5 mm lateral to bregma. A fiber-optic probe (1 mm) was placed measuring cerebral blood perfusion on a 1 mm^3 tissue region [8].

2.7 Histopathology

Seven days after ACA insults, rats were anesthetized and perfused from the ascending aorta with physiologic saline (1 min), following a mixture of 40% formaldehyde, glacial acetic acid, and methanol (FAM) for 19 min and immersed in FAM at 4°C (24 h). Rat brains were removed from the skull and coronal sections (10 μm thickness) from the brains were paraffin embedded and stained with hematoxylin and eosin. CA1 hippocampal sections were visualized at 40× magnification. Ischemic neurons were counted at 18 fields/section along the medial to lateral extent of the CA1 region of the hippocampus 3.8 mm posterior to the bregma. In the same series of animals, brain sections spanning the subfornical organ (SFO) were analyzed to assess cortical (layers II–IV) neuronal damage 7 days after ACA. This region was determined to be −1.4 to −0.8 mm with respect to bregma, similar to the location where 2-PM imaging of cortical microvessels was analyzed [8].

3 Results and Discussion

Representative images of cortical microvasculature are shown in Fig. 10.1a, b. Linescans of RBC traversing the microvasculature were measured (Fig. 10.1c). Black shadows traveling from left to right indicate RBC flow across the scanned vessel. A less negative slope (rise/run) represents RBC (baseline) traveling at a faster rate whereas a more negative slope represents RBC traveling at a slower rate.

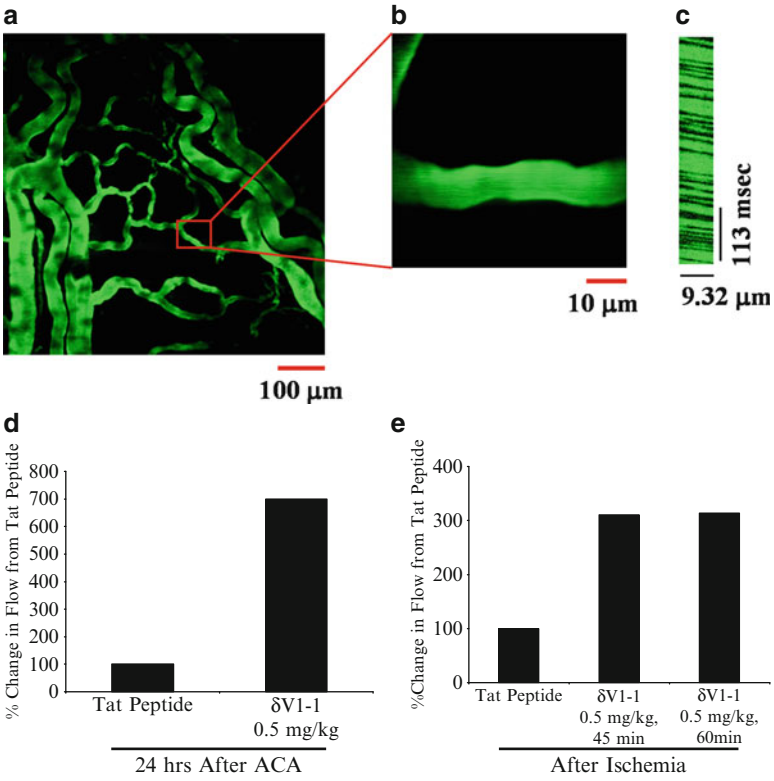

Fig. 10.1 In vivo imaging of cerebral blood vessels using 2-photon microscopy (2-PM). Rats were injected with fluorescein isothiocyanate (FITC)-dextran (0.2 mg/kg) shown in *green* (**a**, **b**). Images were captured at 20× (**a**) and 200× (**b**) of a particular cortical blood vessel. Blood flow measurements using linescans from single vessels (linescans at 512 Hz) were used to determine red blood cell (RBC) flow (**c**). RBC flow values were calculated based on the slope of the shadows (measured using NIH Image J) produced by RBCs when traversed through the blood vessel. Pretreatment with δV1-1-induced attenuation of hypoperfusion 24 h after ACA. Rats pretreated (30 min) with δV1-1 after 24 h of ACA significantly enhanced CBF by 700% as compared to tat peptide (vehicle) (**d**). In a separate set of experiments, δV1-1 was administered directly after 6 min of ACA and CBF changes were monitored. CBF was enhanced 45 and 60 min after ACA by 311 and 314%, respectively, as compared to tat peptide (**e**). For more details, please see Lin et al. [8]

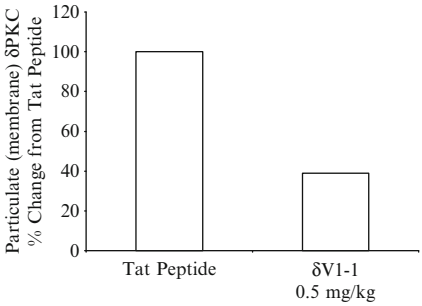

Fig. 10.2 δV1-1 inhibits δPKC translocation in cortical lysates. Pretreatment with δV1-1 in the rat inhibited δPKC translocation after 6 min of ACA with a 61% reduction in protein as compared to tat peptide (vehicle) detected by Western blot analysis. For more details, please see Lin et al. [8]

Rats pretreated with δV1-1 for 30 min significantly attenuated hyperemia (<75% change in flow at 5 and 15 min) and hypoperfusion (<75% change in flow at 45 and 60 min) after 2-VO [8]. In the presence of δV1-1, postischemic hyperemia and hypoperfusion suggest cortical microvessel vasoconstriction (<20% change in blood vessel diameter 5 and 10 min with δV1-1 treated animals) followed by vasodilation (>10% change in blood vessel diameter 45 and 60 min with δV1-1 treated animals) after 2-VO [8]. Moreover, δV1-1 pretreatment significantly attenuated hyperemia 5 min after 2-VO [52% ± 28% increase in flow measured by laser-Doppler flowmetry (LDF)] [8]. Vasoactive factors that influence vasoconstriction/vasodilation during reperfusion have been highly debated over the years. Nonetheless, a recent development in cerebral vascular physiology describes a novel and highly potent vasodilator (palmitic acid methyl ester) that may be involved in PKC regulation during cerebral ischemia [11].

We also measured CBF changes with the 2-PM technique 24 h after ACA in the presence or absence of δV1-1. Rats pretreated with δV1-1 enhanced CBF 24 h after ACA (700% increase in flow as compared to tat peptide) (Fig. 10.1d). Since δV1-1 pretreatment may be protecting the brain parenchyma against the deleterious effects of the ischemic insult, in a separate set of experiments, δV1-1 was administered directly after ACA and CBF changes were monitored via 2-PM. CBF was enhanced in the presence of δV1-1 postarrest (311 and 314% increase in CBF 45 and 60 min after ACA, respectively, as compared to tat peptide) (Fig. 10.1e). These results suggest that posttreatment with δV1-1 attenuated ACA-induced hypoperfusion. Additionally, our results also showed that pretreatment with δV1-1 in the rat inhibited δPKC translocation after ACA with a 61% reduction as compared to tat peptide (vehicle) treatment (Fig. 10.2). These results further confirm that δV1-1 inhibits translocation of δPKC to the cellular membrane in the brain, rendering δPKC inactive. These findings can also be extended from CBF dynamics to neuronal cell viability by influence via δPKC levels. Our findings suggest that δPKC promotes neuronal cell death following 6 min of ACA. Sham-operated experimental group (1,023 ± 11 normal neurons in CA1 region of the hippocampus) was used as control. Rats pretreated with δV1-1 afforded neuroprotection (813 ± 62 normal neurons) in the CA1 region of the rat hippocampus 7 days after 6 min of ACA, as compared to tat

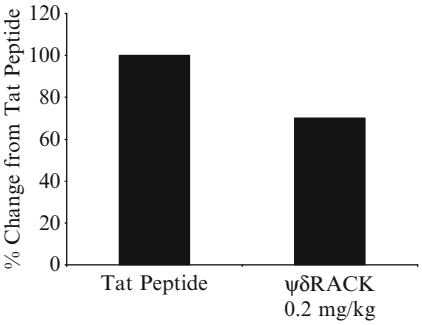

Fig. 10.3 Rats pretreated with ψεRACK reduced cerebral reperfusion after 2-VO. A bolus IV injection of ψεRACK 30 min before ischemia reduced postischemic hyperemia by 30% as compared to tat peptide 25 min after 2-VO detected via laser-Doppler flowmetry. For more details, please see Della-Morte et al. [9]

peptide-treated animals (639 ± 20 normal neurons) and control (527 ± 19 normal neurons). Similar results were found in the cortex since cortical CBF was measured throughout this study. Rats pretreated with δV1-1 (3,187 ± 458.0 dead neurons) afforded neuroprotection suggesting a decrease in the number of dead cortical neurons as compared to no drug (8,400 ± 1,621 dead neurons) and tat peptide (6,863 ± 645.5 dead neurons) experimental groups. These results suggest that δPKC is intimately involved in neuronal cell viability in the hippocampus as well as in cortex [8].

It has already been demonstrated that εPKC activation in certain pathological situations can prove beneficial in the heart and brain [7,12,13]. The role of εPKC during ischemia is thought to be beneficial during and after injury but this has not been well defined. Our histological assessment of the CA1 of the rat hippocampus 7 days after 2-VO suggests that upon pretreatment of ψεRACK, the number of normal neurons (712 ± 109) increased as compared to vehicle (429 ± 90) or tat peptide (429 ± 90) treated groups by 38 and 25%, respectively. These results suggest that pretreatment with ψεRACK (712 ± 109) afforded neuroprotection due to the fact that the number of normal neurons in sham-operated rats was 1,034 ± 58 [9].

Similar to δPKC, we suspect that the neuroprotective effect of εPKC is directly related to CBF after 2-VO. Therefore, we measured regional CBF with LDF 30 min before induction of ischemia and up to 1 h following reperfusion. There was a 30% reduction in regional CBF in ψεRACK-treated groups during the first 25 min of reperfusion after ischemia as compared to tat peptide groups (Fig. 10.3) [9]. These results suggest that εPKC activation may be important in regulating hyperemia after ischemia. The differential actions of δ and εPKCs can be further emphasized by the fact that inhibition of δPKC can attenuate hyperemia after 2-VO [8].

Our data suggest that δ and εPKCs are involved in mediating hyperemia and during reperfusion after global cerebral ischemia. Currently, only δPKC is thought to mediate both states of hyperemia and hypoperfusion during cerebral ischemia. In addition, δV1-1 can modulate postischemic blood flow/vessel dynamics that may

be beneficial in the treatment of cerebral ischemia. Using in vivo models of cerebral ischemia, we have demonstrated that δPKC is activated following cardiac arrest. When activation of δPKC is attenuated with a peptide inhibitor or enhanced with εPKC agonist, the brain is protected from ischemic damage [8,9] through possible revival and/or stabilization of cerebral circulation. The therapeutic potential by inhibiting δPKC and/or activating εPKC may prove beneficial in the treatment of cerebral ischemia.

Acknowledgments This work was supported by National Institutes of Health grants NS45676-01, NS054147-01, NS34773, T32-NS007459-10, and American Heart Association-Philips grant 10POST4340011. Tat peptide, δV1-1, and ψεRACK were purchased from KAI Pharmaceuticals Inc., San Francisco, CA, USA.

References

1. Hossmann KA (1997) Reperfusion of the brain after global ischemia: hemodynamic disturbances. Shock 8:95–101
2. Zhao H, Sapolsky RM, Steinberg GK (2006) Interrupting reperfusion as a stroke therapy: ischemic postconditioning reduces infarct size after focal ischemia in rats. J Cereb Blood Flow Metab 26:1114–1121
3. Caplan LR, Wong KS, Gao S, Hennerici MG (2006) Is hypoperfusion an important cause of strokes? If so, how? Cerebrovasc Dis 21:145–153
4. Bright R, Raval AP, Dembner JM et al (2004) Protein kinase C delta mediates cerebral reperfusion injury in vivo. J Neurosci 24:6880–6888
5. Raval AP, Dave KR, Prado R et al (2005) Protein kinase C delta cleavage initiates an aberrant signal transduction pathway after cardiac arrest and oxygen glucose deprivation. J Cereb Blood Flow Metab 25:730–741
6. Ramzy D, Rao V, Tumiati LC et al (2006) Elevated endothelin-1 levels impair nitric oxide homeostasis through a PKC-dependent pathway. Circulation 114:I319–I326
7. Bright R, Sun GH, Yenari MA et al (2008) epsilonPKC confers acute tolerance to cerebral ischemic reperfusion injury. Neurosci Lett 441:120–124
8. Lin HW, Defazio RA, Della-Morte DA et al (2010) Derangements of post-ischemic cerebral blood flow by protein kinase c delta. Neuroscience 171:566–576
9. Della-Morte D, Raval AP, Dave KR et al (2011) Post-Ischemic activation of protein kinase C epsilon protects the hippocampus from cerebral ischemic injury: possible alterations in cerebral blood flow. Neurosci Lett 487:158–162
10. Perez-Pinzon MA, Dave KR, Raval AP (2005) Role of reactive oxygen species and protein kinase C in ischemic tolerance in the brain. Antioxid Redox Signal 9–10:1150
11. Lin HW, Liu CZ, Cao D et al (2008) Endogenous methyl palmitate modulates nicotinic receptor-mediated transmission in the superior cervical ganglion. Proc Natl Acad Sci USA 105:19526–19531
12. Dave KR, Defazio RA, Raval AP et al (2009) Protein kinase C epsilon activation delays neuronal depolarization during cardiac arrest in the euthermic arctic ground squirrel. J Neurochem 110:1170–1179
13. Inagaki K, Begley R, Ikeno F et al (2005) Cardioprotection by epsilon-protein kinase C activation from ischemia: continuous delivery and antiarrhythmic effect of an epsilon-protein kinase C-activating peptide. Circulation 111:44–50

Chapter 11
Optical Topography to Measure Variations in Regional Cerebral Oxygenation in an Infant Supported on Veno-Arterial Extra-Corporeal Membrane Oxygenation

Maria D. Papademetriou, Ilias Tachtsidis, Murad Banaji, Martin J. Elliott, Aparna Hoskote, and Clare E. Elwell

1 Introduction

Extracorporeal membrane oxygenation (ECMO) is a life support system incorporating cardiopulmonary bypass in infants and children with intractable cardiorespiratory failure. Establishing ECMO involves cannulation of major vessels in the neck – right common carotid artery (RCCA) and internal jugular vein (IJV). Maintaining and weaning from ECMO requires manipulation of ECMO flows, which can affect cerebral blood flow and potentially lead to neurologic complications. Reports show that about 28–52% of ECMO survivors show abnormal neuroimaging related both to pre-ECMO events and to the ECMO procedure itself [1].

Near infrared spectroscopy (NIRS) has the advantage of monitoring cerebral oxygenation non-invasively and continuously by the bedside. NIRS was used on ECMO patients to study the effect of cannulation on cerebral oxygenation. Ligation of RCCA was associated with a decrease in HbO_2, an increase in HHb [2] and a decrease in tissue oxygen saturation (TOS) [3] while no changes were seen during IJV ligation. Also, an increase in HbO_2, a decrease in HHb and an increase in TOS was reported after ECMO was established compared to pre-cannulation values. In a previous study, we used spectral analysis on HbO_2 and identified vasomotion, respiratory, cardiac and ECMO circuit roller pump oscillations in cerebral and peripheral circulation during ECMO flow changes [4]. To date, conventional NIRS uses single

M.D. Papademetriou (✉) • I. Tachtsidis • M. Banaji • C.E. Elwell
Biomedical Optics Research Laboratory, Department of Medical Physics and Bioengineering, University College London, Malet Place Engineering Building, Gower Street, London, WC1E 6BT, UK
e-mail: mpapa@medphys.ucl.ac.uk

M.J. Elliott • A. Hoskote
Cardiothoracic Unit, Great Ormond Street Hospital for Children, London, WC1N 3JH, UK

M. Wolf et al. (eds.), *Oxygen Transport to Tissue XXXIII*, Advances in Experimental Medicine and Biology 737, DOI 10.1007/978-1-4614-1566-4_11,

or dual channel systems with the optodes usually placed on the forehead of the patients providing information related to perfusion of only a small area of the anterior cerebrum and therefore do not allow evaluation of the status of the cerebral circulation and oxygenation in the extended cerebral regions.

The aim of this study is to use optical topography (OT) to monitor multisite brain oxygenation responses during manipulations in the ECMO circuit flows.

2 Methods

In this pilot study, OT data were obtained from a 1-month-old veno-arterial (VA) ECMO patient undergoing changes in the ECMO circuit flows. Flow in the ECMO circuit was successively decreased by 10% from initial flow every 10–15 min, down to 70% of the initial flow and it was then gradually brought back to initial flow. During this procedure, ETG-100 OT system (Hitachi Medical Ltd.) was used to measure changes in HbO_2, HHb and HbT (HbO_2 + HHb) haemoglobin concentrations using the modified Beer–Lambert Law. A novel neonatal cap was designed and constructed to accommodate the optical fibres in a 3 × 3 array (inter-optode distance = 3 cm) utilising spring-loaded optical fibre holders. The probe array was positioned on the patient's head with the middle optode corresponding to C_z of the 10–20 EEG electrode placement system [5]. This optode configuration allows for optical data to be collected from 12 channels distributed symmetrically around C_z and covering an area of 6 cm × 6 cm. Optical data collected at a sampling frequency of 5 Hz were resampled at 1 Hz and low pass filtered at 0.05 Hz to remove physiological noise. For the conversion of the optical attenuation changes to chromophore concentration changes, a differential pathlength factor (DPF) of 4.99 was applied [6]. Multimodal data were collected synchronously with the optical data that included systemic parameters: arterial blood pressure (ABP), heart rate (HR), respiration rate (RR), end-tidal CO_2, temperature and arterial saturation (SpO_2); and ECMO circuit parameters: venous saturation (SvO_2), arterial saturation measured at the arterial cannula side (SaO_2), haematocrit and ECMO flow.

Changes in HbO_2, HHb and HbT between phase I [from baseline flow (100%) to minimum flow (70%)] and phase II [from 70% flow back to baseline flow] were calculated from the differences in mean values over a 60-s period just before changing the flow. The results were analysed using a paired t-test ($p < 0.05$).

3 Results

Figure 11.1 shows concentration changes in HbO_2 (red), HHb (blue) and HbT (black) collected from the 12 channels during changes in ECMO flows. The channel configuration is shown by the schematic at the top left of the figure. As annotated in the haemoglobin plots of channel 1, the vertical dotted lines represent the time at

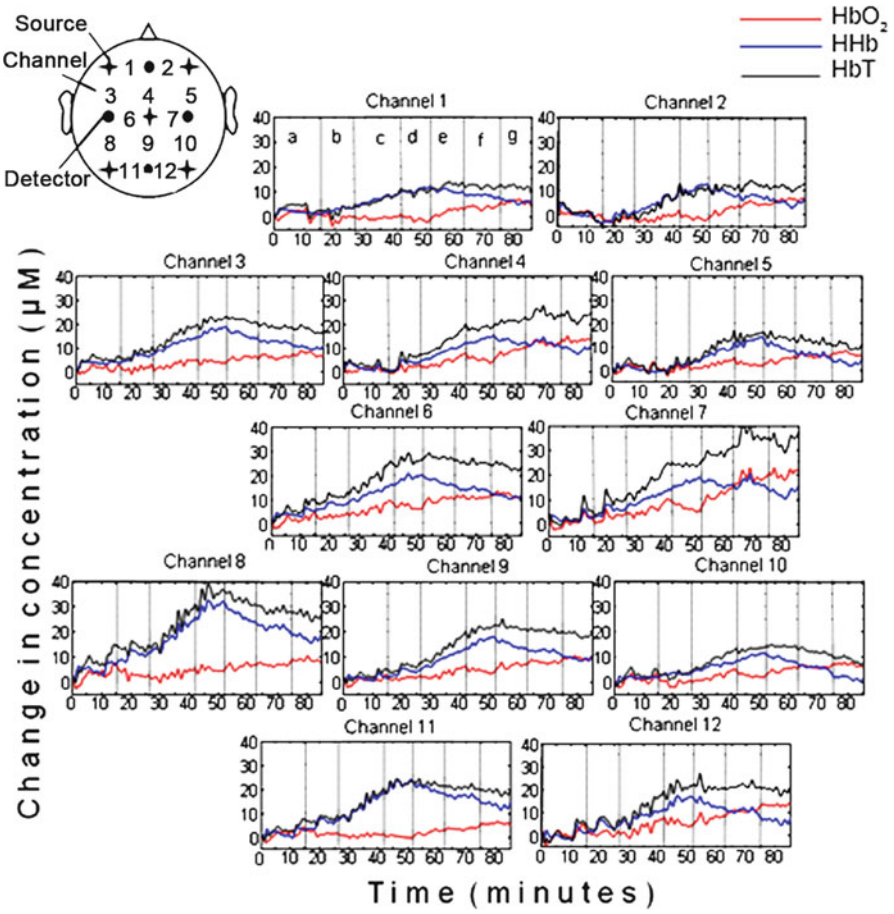

Fig. 11.1 HbO_2, HHb and HbT concentration changes from 12 channels during ECMO circuit flow changes. Each *vertical line* in the figures denotes where the ECMO circuit flow change occurred as annotated on channel 1 [a = baseline (100% flow), b = 90% flow, c = 80% flow, d = 70% flow, e = 80% flow, f = 90% flow, g = 100% flow]

which a change in flow was induced so that each section in the plots corresponds to a specific flow. Sequential reduction in ECMO flows resulted in considerable increase in HHb and HbT in all 12 channels, with moderate increases seen in HbO_2. Table 11.1 lists the responses in HHb, HbO_2 and HbT during phase I and phase II. The range in the change of HHb concentration during phase I was from 9.7 μM (channel 8) to 25.1 μM (channel 10). Regional variations in cerebral oxygenation can be seen, particularly interhemispheric differences, e.g., comparing channel 10 (right parietal lobe) with channel 8 (left parietal lobe).

The variation in HR, MAP, SpO_2 and SvO_2 during flow changes are shown in Fig. 11.2. Figure 11.3 shows the responses of these parameters during phase I and

Table 11.1 Mean changes in HHb, HbO_2 and HbT during phases I [between baseline flow (100%) and minimum flow (70%)] and II (between minimum flow and return to baseline)

	HHb (μM)		HbO_2 (μM)		HbT (μM)	
Channel	I	II	I	II	I	II
1	**11.2**	**−6.1**	**−2.9**	**7.0**	**8.3**	**1.0**
2	**15.9**	**−6.5**	**−1.2**	**8.2**	**14.7**	**1.7**
3	**15.2**	**−8.7**	**1.4**	**2.8**	**16.5**	**−5.9**
4	**14.8**	**−4.7**	**3.8**	**9.2**	**18.6**	**4.5**
5	**14.9**	**−10.8**	**−0.3**	**4.2**	**11.8**	**−6.6**
6	**15.0**	**−9.2**	**1.9**	**4.8**	**14.6**	**−4.5**
7	**16.2**	**−4.4**	**3.1**	**15.8**	**16.9**	**11.4**
8	**25.1**	**−14.7**	**−2.8**	**3.7**	**19.4**	**−11.1**
9	**16.1**	**−8.7**	**1.3**	**5.2**	**22.3**	**−3.5**
10	**9.7**	**−10.8**	**−0.6**	**4.3**	**17.4**	**−6.5**
11	**20.6**	**−10.7**	**−4.3**	**5.8**	**16.3**	**−5.0**
12	**15.7**	**−11.0**	**0.5**	**9.2**	**16.2**	**−1.8**

Note: Bold letters indicate that changes are statistically significant ($p < 0.05$)

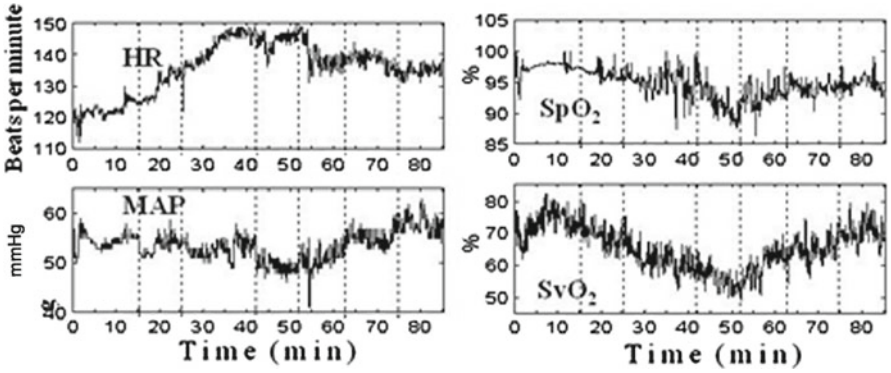

Fig 11.2 HR, MAP, SpO_2 and SvO_2 during ECMO circuit flow changes

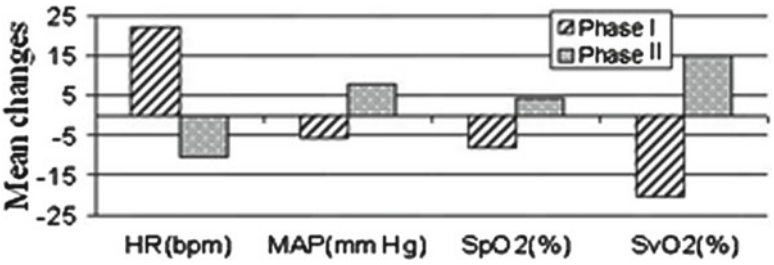

Fig 11.3 Mean changes in systemic and ECMO parameters during phases I and II

phase II. In this patient a decrease in ECMO flow is associated with a decrease in SvO_2 and SpO_2 and an increase in HR and MAP. The effect is reversed when the flow is gradually increased back to baseline. Similar to the haemoglobin concentration data, these systemic and ECMO circuit parameters do not return to their baseline values by the end of the monitoring period.

4 Discussion

This single patient study showed significant changes in systemic oxygenation parameters and cerebral haemoglobin concentration in response to changes in ECMO flows. Reduction in flows was associated with a decrease in SvO_2 and SpO_2 and a significant increase in HHb but in the absence of a decrease in HbO_2.

A decrease in ECMO flow is associated with a decrease in oxygen delivery especially in the early course of ECMO treatment when the heart and lungs have not fully recovered. If ECMO flow is inadequate, there is a reduction in SvO_2 and a subsequent decrease in SpO_2. Consequently, in an effort to increase cardiac output, there is a compensatory increase in HR. The decrease in SpO_2 and SvO_2 seen in this patient suggest that the lowering ECMO flows has a similar effect to a hypoxemic challenge and the absence of decrease in HbO_2 in relation to increase in HHb could be explained by arterial dilation as a compensatory response to decreased blood flow due to decreased ECMO flows [7].

The changes seen in the total haemoglobin during this challenge in this patient are relatively large compared to the suggested total cerebral blood volume in an infant of 2.2 mL/100 g (50 μM) [8]. Van Heijst et al. report changes in HbO_2 and HHb in the order of 1 μmol/100 g (10 μM) 60 min after ECMO induction and suggest no interhemispheric differences. EIjike et al. report no relationship between ECMO flow and tissue oxygen saturation but changes in the individual HbO_2 and HHb parameters were not reported.

We noted significant differences between channel 10 and 8 which are difficult to explain and could be related to alterations in cerebral blood flow related to ligation of the RCCA and IJV; however, we need further data to support this. In addition, regional variations in cerebral oxygenation could be related both to the procedure itself and to inhomogeneous differential pathlength factor [9]. The changes associated with ECMO flows did not return to baseline as the flow changes were reversed in the time period of the study. This might have been seen if we had extended the duration of the monitoring which we plan to do with further studies.

5 Conclusions

Multichannel optical topography can provide information on regional cerebral haemodynamics and oxygenation in ECMO patients. Simultaneous measurement of systemic and cerebral parameters can be used to characterise the response to changes

in ECMO flows. In the patient studied here, ECMO flows appear to present a significant haemodynamic challenge to cerebral circulation. ECMO flow changes may have the potential to inform on cerebral autoregulation but further studies are required to more fully explore the relationship between regional variations in cerebral oxygenation during different ECMO phases.

Acknowledgment This work is supported by Hitachi Medical Ltd.

References

1. Bulas D, Glass P (2005) Neonatal ECMO: neuroimaging and neurodevelopmental outcome. Semin Perinatol 29:58–65
2. Van Heijst A, Liem D, Hopman J, Van der Staak F, Sengers R (2004) Oxygenation and hemodynamics in the left and right cerebral hemispheres during induction of veno-arterial extracorporeal membrane oxygenation. J Pediatr 144:223–228
3. Ejike JC, Schenkeman KA, Seidel K, Ramamoothy C, Roberts JS (2006) Cerebral oxygenation in neonatal and pediatric patients during veno-arterial extracorporeal life support. Pediatr Crit Care Med 7:154–158
4. Papademetriou MD, Tachtsidis I, Leung TE, Elliott MJ, Hoskote A, Elwell CE (2010) Cerebral and peripheral tissue oxygenation in infants and children supported on ECMO for cardiorespiratory failure. Adv Exp Med Biol 662:447–453
5. Jasper H (1958) Report to the committee on methods and clinical examination in electroencephalography. Electroencephalogr Clin Neurophysiol 10:371–375
6. Duncan A, Meek JH, Clemence M, Elwell CE, Tyszczuk L, Cope M, Delpy DT (1995) Optical pathlength measurements on adults head, calf and forearm and the head of the newborn infant using phase resolved optical spectroscopy. Phys Med Biol 40:295–304
7. Hurn PD, Traystman RJ (2002) Changes in arterial gas tension. In: Edvinsson L, Krause DN (eds) Cerebral blood flow and metabolism. Lippincott Williams & Wilkins, Philadelphia, pp 384–394
8. Wyatt JS, Cope M, Delpy DT, Richardson CE, Edwards AD, Wray S, Reynolds EOR (1990) Quantitation of cerebral blood volume in human infants by near-infrared spectroscopy. J Appl Physiol 68:1086–1091
9. Katagiri A, Dan I, Tuzuki D, Okamoto M, Yokose N, Igarashi K, Hoshino T, Fujiwara T, Katayama Y, Yamaguchi Y, Sakatani K (2010) Mapping of the optical pathlength of human adult head at multi-wavelengths in near infrared spectroscopy. Adv Exp Med Biol 662:213

Chapter 12
Effects of the Autonomic Nervous System on Functional Neuroimaging: Analyses Based on the Vector Autoregressive Model

A. Seiyama, Y. Sasaki, A. Takatsuki, and J. Seki

1 Introduction

Currently used noninvasive neuroimaging techniques can be divided into the following three categories judging from the property of their measured parameters: magnetoencephalogram (MEG) and electroencephalogram (EEG), which can measure direct neural activity (the primary signal), positron emission tomography (PET), and magnetic resonance spectroscopy (MRS), which can measure metabolic activities (the secondary signal) such as rates of glucose and oxygen uptakes, and functional magnetic resonance imaging (fMRI) and fNIRS, which can measure hemodynamic responses (the tertiary signal) such as regional cerebral blood flow, blood volume and oxygen saturation of the blood, accompanied with neural activation. However, fMRI and fNIRS inevitably include responses from the respiratory and cardiovascular systems as physiological artifacts [1–3]. Therefore, it is required to elucidate whether and how signals obtained by fMRI and fNIRS suffer from such artifacts originating from the autonomic nervous system.

In the present study, we evaluated the effects of the autonomic nervous system on functional neuroimaging using fNIRS, based on the auto-regressive and moving average (ARMA) and vector autoregressive (VAR) models. Based on the above results, we discuss the effects of the autonomic nervous system on functional neuroimaging using fNIRS.

A. Seiyama (✉) • Y. Sasaki • A. Takatsuki
Division of Medical Devices for Diagnoses, Human Health Sciences, Graduate School of Medicine, Kyoto University, 53 Shogoin, Kawahara-cho, Sakyo-ku, Kyoto 606-8507, Japan
e-mail: aseiyama@hs.med.kyoto-u.ac.jp

J. Seki
Department of Biomedical Engineering, National Cerebral and Cardiovascular Center Research Institute, Osaka, Japan

M. Wolf et al. (eds.), *Oxygen Transport to Tissue XXXIII*, Advances in Experimental Medicine and Biology 737, DOI 10.1007/978-1-4614-1566-4_12,

2 Methods

2.1 Experimental Design

Four healthy male volunteers (age 23 ± 0.8 years), who were all right-handed, were subjected to both mental task (volunteers traced a picture shown on a PC monitor with an inverted mouse) and physiological task (their right fingers were immersed into the ice-cold water). A set of "resting (30 s) + task (60 s) + resting (30 s)" was repeated 3 times. Written informed consent was obtained after a complete description of the study was given to the subjects before the experiments.

2.2 fNIRS Measurements

Optical probes (2 × 6) of fNIRS (FOIRE-3000, Shimadzu, Japan) were attached on the prefrontal cortex, which gave a 16-channel measurement area [4], and the bottom-center channel 8 (ch. 8) was positioned at Fpz of International 10–20 system of EEG. A sensor probe of a pulse oximeter (Nihon Kohden, Japan) was attached on the left middle finger. Instantaneous values of pulse rate (PR) and respiratory rate (RR) were calculated from peak-to-peak intervals of pulse oximeter output and output of CO_2 monitor (Nihon Kohden, Japan) as shown in Fig. 12.1, respectively. All measurements were performed at 25-ms sampling intervals (40 Hz) simultaneously.

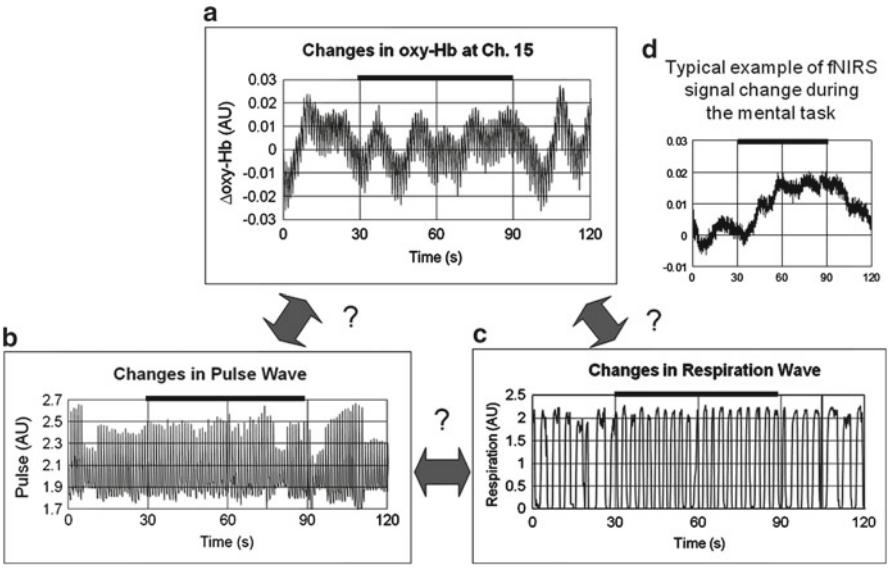

Fig. 12.1 Typical examples of temporal changes in fNIRS signal (**a**), pulse wave (**b**), and respiratory wave (**c**) during the physiological task. Inserted figure (**d**) shows a typical example of change in oxy-Hb during mental task. Only the first set of tasks is shown

2.3 *Data Analyses*

The left dorsolateral prefrontal cortex (DLPFC) (cf., ch. 15 in Ref. [4]) showed a focal and typical hemodynamic response during mental task. Mutual contributions among signal changes of oxy-Hb in the left DLPFC, PR, and RR were estimated using the vector auto-regressive (VAR) model [5]. Functional changes in the autonomic nervous system, the sympathetic (SN) and parasympathetic (PN) nerve systems during experiments were analyzed by applying the auto-regressive and moving average (ARMA) model to the data of PR [6]. Activity of the PN was defined as power ratio of [High Frequency (0.15–0.4 Hz)]/[Total Frequency (0–0.4 Hz)] (i.e., HF/TF), and that of the SN was defined as power ratio of [Low Frequency (0.035–0.15 Hz)]/[Total Frequency (0–0.4 Hz)] (i.e., LF/TF) [7].

3 Results

Figure 12.1 shows a typical example of temporal changes in fNIRS signal (oxy-Hb; A), pulse rate (PR; B), and respiratory rate (RR; C) during the physiological task. The stimulus-induced increase in oxy-Hb in the DLPFC was not observed during the physiological task, but was observed during the mental task (see inset Fig. 12.1d). Figure 12.2 shows a typical example of mutual contributions among oxy-Hb,

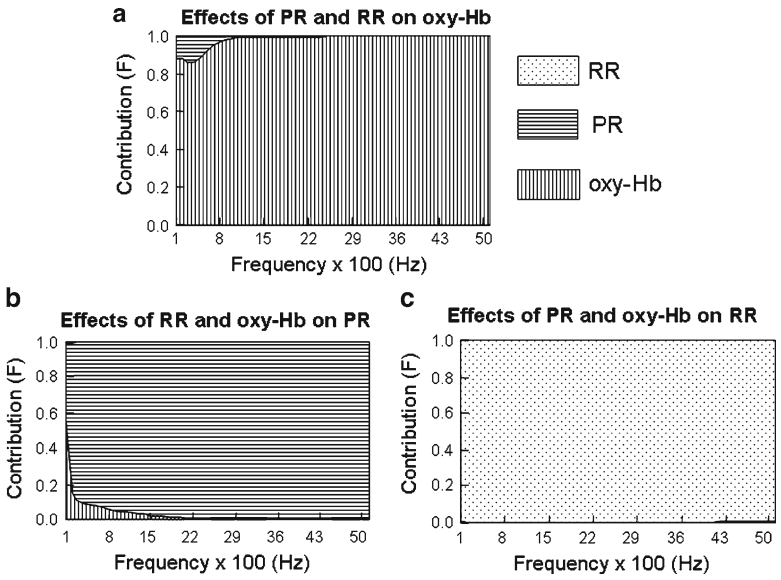

Fig. 12.2 Mutual contributions among parameters during the physiological task estimated using the vector AR model

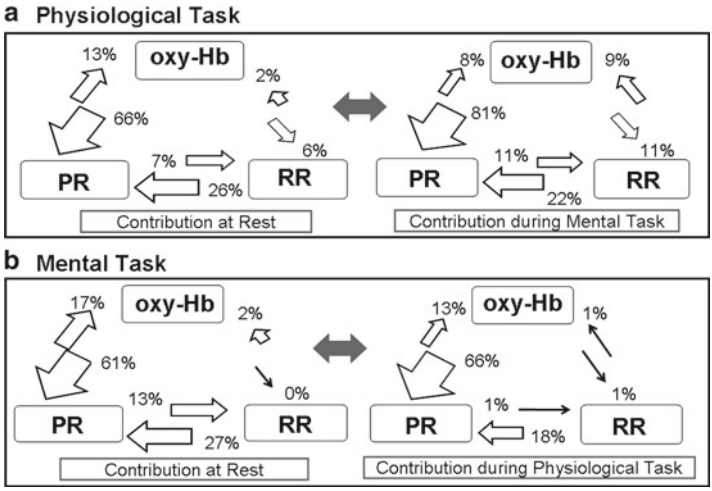

Fig. 12.3 Mutual contributions among the parameters during the task and rest periods

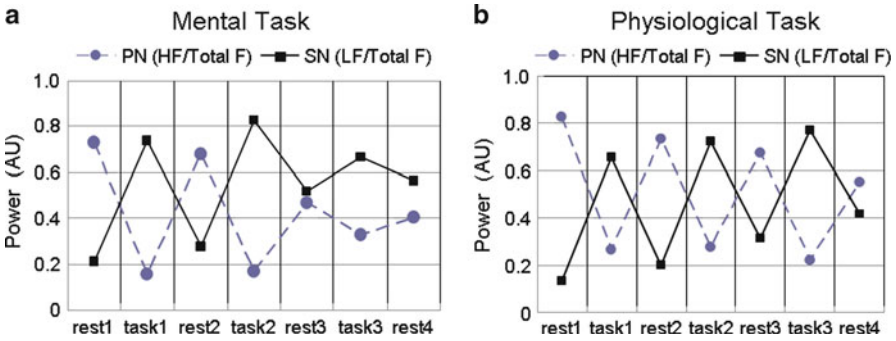

Fig. 12.4 Typical examples of the effect of task performance on the autonomic nerve systems. PN was defined as power ratio of HF(0.15–0.4 Hz)/TF(0–0.4 Hz). SN was defined as power ratio of LF(0.035–0.15 Hz)/TF(0–0.4 Hz). Fluctuation of the pulse rate was analyzed using the auto-regressive and moving average (ARMA) model

PR, and RR during physiological task, which were analyzed using the VAR model. Effects of PR and RR on changes in oxy-Hb were small and <17% even at around 0.03 Hz (Fig. 12.2a). Averaged values of mutual contributions among oxy-Hb, PR, and RR during mental and physiological tasks obtained from four subjects are shown in Fig. 12.3. Effects of PR and RR on changes in oxy-Hb were small and <20% (Fig. 12.3a, right). These effects were almost the same as those during resting conditions (Fig. 12.3a, left). Further, no distinct change was observed between the physiological and mental tasks (Fig. 12.3a vs. b). A typical example of effect of task performance on the autonomic nerve system is shown in Fig. 12.4.

Both mental (Fig. 12.4a) and physiological (Fig. 12.4b) tasks induced activation of the sympathetic nerve activity (SN) and suppression of parasympathetic nerve activity (PN). All subjects gave similar responses in the autonomic nerve system.

4 Discussion

Effects of the autonomic nerve system are major concern for neuroimaging techniques such as fNIRS, because fNIRS measures the stimulus-induced hemodynamic response in the brain. The effects can be expected from both the extra and intra cortex physiological alterations accompanied by systemic changes in the heart and respiratory rates. The former includes increase or decrease in the skin blood flow, and the latter includes alterations of cerebral hemodynamics and metabolic change. Both these alterations work as physiological artifacts for the functional neuroimaging. Present results indicate both physiological and mental tasks activate the sympathetic nerve system and suppress the parasympathetic nerve system (Fig. 12.4). Further, effect of the sympathetic nerve system (LF components around 0.03 Hz) is larger than that of the parasympathetic nerve system (HF components around 0.3 Hz) on fNIRS signals (cf., Fig. 12.2a). However, effects of the autonomic nerve system on fNIRS signals were small and <20% during performance of both physiological and mental tasks, and these effects were almost the same as those during resting conditions (Fig. 12.3). Using information transfer analysis, Katura et al. reported recently that during resting condition effects of the heart rate and arterial blood pressure on the cerebral hemodynamics were about 20% [8]. Our results obtained by the VAR model gave similar results (Fig. 12.3a, left and b, left). These results suggest that during functional neuroimaging using fNIRS (and possibly fMRI) effects of the autonomic nervous system on fNIRS signals are not negligible, but <20% under both resting and task conditions.

5 Conclusion

(1) Effects of the autonomic nerve system on fNIRS signals are small and <20% during performance of both physiological and mental tasks, and these effects were almost the same as those during resting conditions. (2) Effect of the sympathetic nerve system (LF components around 0.03 Hz) is larger than that of the parasympathetic nerve system (HF components around 0.3 Hz) on fNIRS signals.

Acknowledgments This work was supported by Grants-in-Aid for CREST of Japan Society and Technology Agency (JST).

References

1. Zhang R, Zuckerman JH, Levine BD (2000) Spontaneous fluctuations in cerebral blood flow: insights from extended-duration recordings in humans. Am J Physiol Heart Circ Physiol 278:H1848–H1855
2. Kiviniemi V, Ruohonen J, Tervonen O (2005) Separation of physiological very low frequency fluctuation from aliasing by switched sampling interval fMRI scans. Magn Reson Imag 23:41–46
3. Kohno S, Miyai I, Seiyama A et al (2007) Removal of the skin blood flow artifact in functional near-infrared spectroscopic imaging data through independent component analysis. J Biomed Opt 12:062111
4. Hoshi Y, Huang J, Kohri S et al (2011) Recognition of human emotions from cerebral blood flow changes in the frontal region: a study with event-related near-infrared spectroscopy. J Neuroimag 21:e91–e101
5. Wada T (1994) Multivariate autoregressive modeling for analysis of biological systems with feedback. In: Proceeding of the first US/Japan conference on frontiers of statistical modeling 2: 293–317
6. National Instruments Signal Processing Toolset User Manual (2002) Chap. 6, Introduction to model-based frequency analysis, and Chap. 7, Model-based frequency analysis algorithms
7. Akselrod S, Gordon D, Ubel FA et al (1981) Power spectrum analysis of heart rate fluctuation: a quantitative probe of beat-to-beat cardiovascular control. Science 213:220–222
8. Katura T, Tanaka N, Obata A et al (2006) Quantitative evaluation of interrelations between spontaneous low-frequency oscillations in cerebral hemodynamics and systemic cardiovascular dynamics. NeuroImage 31:1592–1600

Chapter 13
Assessment of Potential Short-Term Effects of Intermittent UMTS Electromagnetic Fields on Blood Circulation in an Exploratory Study, Using Near-Infrared Imaging

Sonja Spichtig, Felix Scholkmann, Lydia Chin, Hugo Lehmann, and Martin Wolf

1 Introduction

We investigated potential short-term effects (occurring within 80 s) of intermittent Universal Mobile Telecommunications System electromagnetic fields (UMTS-EMF) on blood circulation in the human head using near-infrared imaging (NIRI). NIRI measures changes in oxy, deoxy, and total hemoglobin concentration ($\Delta[O_2Hb]$, Δ[HHb], and Δ[tHb]), which reflect changes in cerebral activity, perfusion, and/or oxygenation. Its insensitivity to EMF, the high temporal resolution, and the flexibility in choosing the exposure sequence makes NIRI an excellent tool to study immediate physiological effects of continuous and intermittent EMF.

The aim of this exploratory study was (1) to investigate several UMTS signal types and exposure positions in eight subjects for potential effects, and (2) to define a final protocol for a more extensive study.

S. Spichtig • L. Chin • M. Wolf (✉)
Biomedical Optics Research Laboratory, Division of Neonatology, Department of Obstetrics and Gynecology, University Hospital Zurich, Frauenklinikstrasse 10, 8091 Zurich, Switzerland

Institute for Biomedical Engineering, University and ETH Zurich, 8092 Zurich, Switzerland
e-mail: martin.wolf@usz.ch

F. Scholkmann
Biomedical Optics Research Laboratory, Division of Neonatology, Department of Obstetrics and Gynecology, University Hospital Zurich, Frauenklinikstrasse 10, 8091 Zurich, Switzerland
e-mail: martin.wolf@usz.ch

H. Lehmann
Swisscom (Switzerland) Ltd., Innovation Competence Centre, Environment & Electromagnetic Compatibility, 3050, Bern, Switzerland

M. Wolf et al. (eds.), *Oxygen Transport to Tissue XXXIII*, Advances in Experimental Medicine and Biology 737, DOI 10.1007/978-1-4614-1566-4_13,

2 Materials and Methods

2.1 Optical Setup

Hardware and software changes on the commercially available ISS Oxiplex® (ISS Inc., Champaign, Illinois, USA) quadrupled the number of detector and light source combinations available for a single optical sensor. The available 2 detectors and 8 source positions enable to collect in total 16 light bundles, also called light paths. Each light bundle comprised light at two wavelengths, namely 690 and 830 nm. The NIRI sensor was custom built in our lab and contains no active parts to be insensitive to UMTS-EMF. Ten-meter long optical fibers were used for the NIRI sensor to enable the placement of the NIRI instrument outside of the exposure chamber and therefore to minimize potential electrical interferences. For more details about the modifications on the ISS Oxiplex® refer to [1].

2.2 Exposure Setup

The measurements were carried out in an experimental room located in the basement of the University Hospital Zurich, where the electromagnetic background fields were determined to be very low (@1.9 GHz the background electrical field strength was 0.0002 V/m). The noticeable contributions to the background electrical field strength were a GSM downlink signal (@900 MHz: 0.005 V/m), a FM radio signal (@88 MHz: 0.0005 V/m), and the hospital pager (@451 MHz: 0.0003 V/m). Absorber walls were arranged around the subject's bench to minimize possible UMTS-EMF reflections of the exposure setup.

The electronics was programmed to produce four different UMTS signal types with a carrier frequency of 1.9 GHz (1) continuous wave (cw), (2) base station-like (bs, as in the TNO-study [2]), (3) W-CDMA uplink 1 communication channel (1up; similar to the signal proposed by Ndoumbe Mbonjo et al. [3], (4) W-CDMA uplink 6 communication channels (6up; as proposed by Ndoumbe Mbonjo et al. [3]). Two exposure positions were defined, one located close to the ear (Fig. 13.1: T3) and the other (Fig. 13.1: B-C3) midway between the motor cortex and position B where previously a change in the regional cerebral blood flow was reported for a Global System for Mobile Communications (GSM) signal [4, 5]. The center point of the optical sensor was positioned directly on these positions and a planar patch antenna (SPA 2000/80/8/0/V, Huber & Suhner, Switzerland) emitting the EMF at a distance of 4 cm.

The spatial peak specific absorption rate (SAR) over 10 g of the exposure setup was simulated with SEMCAD X (Version 13, Schmid and Partner Engineering, Zurich, Switzerland) using the Specific Anthropomorphic Mannequin (SAM) phantom defined in CENELEC 50361 [6]. The simulation results were verified with an experimental SAR measurement using the DASY5 Dosimetric Assessment System

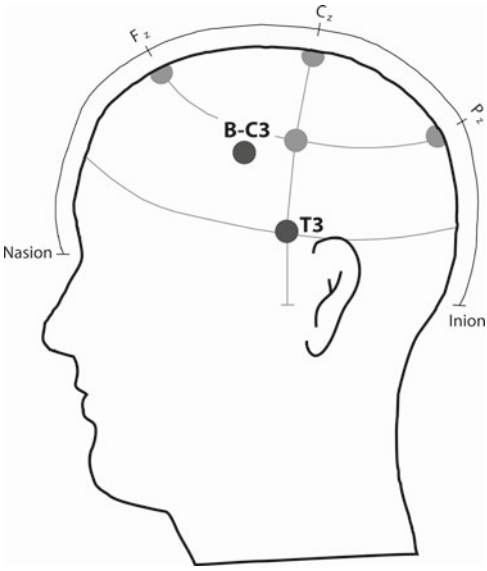

Fig. 13.1 Graphical representation of the exposure positions T3 and B-C3 in the international 10–20 EEG positioning system [11]

(Schmid and Partner Engineering, Zurich, Switzerland) at the IT'IS foundation in Zurich. The simulated and experimental data showed deviations smaller than ±5% and thus a high agreement. Maximum peak SAR (over 10 g) applied was 1.8 W/kg, which is below the ICNIRP guidelines. For more information about the exposure system and dosimetry see [7].

2.3 Subjects and Study Protocol

Eight right-handed male subjects (age: 28.6 ± 2.9 years) participated after giving written informed consent. They were asked to abstain from coffee, cigarettes, and mobile phone use within 2 h before a measurement. Each subject underwent eight measurements on different days experiencing all possible combinations of UMTS signal types and exposure positions in a single-blind paradigm.

A measurement consisted of 15 cycles, the exposure segments, 20 s of UMTS-EMF exposure alternated with 60-s recovery. Before and after the cycles a baseline was recorded for 3 min. In total, a measurement lasted 26 min.

2.4 Data Analysis

Data were band pass filtered (0.008–0.8 Hz) to remove high frequency noise and very low physiological contributions. $\Delta[O_2Hb]$ and $\Delta[HHb]$ were calculated using the modified Lambert–Beer law. The differential pathlength factors (DPF) for C3 given

in the literature [8] were linearly interpolated to $DPF_{690\ nm} = 8.21$ and $DPF_{830\ nm} = 7.3$ and used in the modified Lambert–Beer law.

To reduce present movement artifacts, the algorithm presented by [9] was applied to the concentration time series of $\Delta[O_2Hb]$ and Δ[HHb]. The sum of the MA reduced $\Delta[O_2Hb]$ and Δ[HHb] yielded Δ[tHb].

The last 10 s of UMTS-EMF exposure (ON) and recovery (OFF) were averaged. The difference between ON-OFF was modeled using a linear mixed-effects model with the factors *signal type* (levels: cw, bs, 1up and 6up), *exposure position* (levels: T3, B-C3), *light path* (defined as the different source-detector combinations; levels: light path 1 to light path 16), and *exposure segments* (levels: exposure segment 1 to exposure segment 15). The *subject* was defined as random factor.

3 Results

The histograms for the difference between ON and OFF are displayed in Fig. 13.2 for $\Delta[O_2Hb]$, Δ[HHb], and Δ[tHb] with all 15'360 observations. They show normally distributed concentration differences with a mean close to zero. No statistically significant differences between exposure and recovery were found for any condition and measurement parameter.

The *signal type* and *exposure position* with maximum and minimum differences (ON-OFF) in $\Delta[O_2Hb]$, Δ[HHb], and Δ[tHb] are summarized in Table 13.1.

4 Discussion and Conclusion

The largest differences in $\Delta[O_2Hb]$, Δ[HHb], and Δ[tHb] (Table 13.1) occurred for the majority of cases at the position T3 and the signal typ bs. Hence, this *signal type* and *exposure position* were selected for the protocol of a more extensive study.

To set the size of the obtained changes in perspective, we compared them to concentration changes elicited by functional activation of the brain, e.g., for a motor

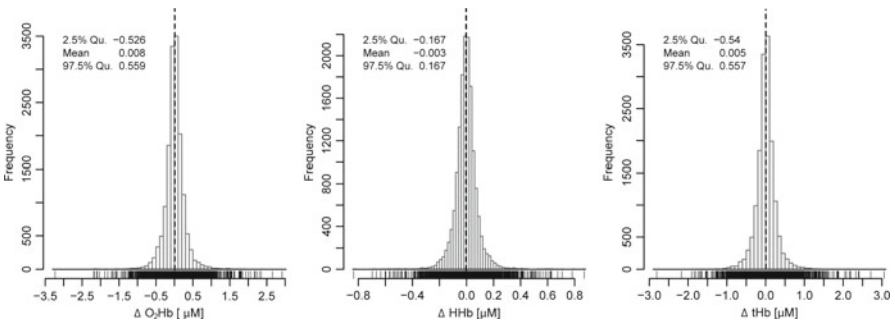

Fig. 13.2 Histograms of $\Delta[O_2Hb]$, Δ[HHb], and Δ[tHb] for all observations. Mean (*black dotted vertical line*), 2.5% and 97.5 quantiles are given for each distribution

Table 13.1 Maximum and minimum concentration changes in μM described by a linear mixed-effects model

Parameter	Position	Signal	Δ [μM]
Max(Δ[O_2Hb])	C3	1up	0.1357
Min(Δ[O_2Hb])	T3	bs	–0.1818
Max(Δ[HHb])	C3	cw	0.0418
Min(Δ[HHb])	T3	cw	–0.0380
Max(Δ[tHb])	T3	bs	0.1421
Min(Δ[tHb])	T3	bs	–0.1752

cortex activation their size is approximately 0.8 μM for Δ[O_2Hb], 0.15 μM for Δ[HHb], and 0.65 μM for tHb. These values are reference values based on the literature including the results of functional measurements on adults in several studies [10]. The changes presented in Table 13.1 were 4–6 times smaller.

In previous studies [4, 5] significant changes in cerebral blood flow (CBF) were detected using PET. Subjects were exposed for 30 min to a 0.9 GHz handset-like signal mimicking a GSM mobile phone with 1.0 W/kg SAR in 16 subjects (for comparison in our study: totally 5 min exposure, 1.9 GHz UMTS-signal, intermittent, 1.8 W/kg, 8 subjects). Changes in CBF were measured 10–30 min after exposure, while we analyzed short-term changes during exposure. Significantly increased CBF was found close to the C3 position and <2 cm deep [4, 5], where we measured as well. Any of the discrepant factors may be responsible for not finding significant changes in contrast to the PET studies [4, 5].

There could be different reasons why no significances were detected: firstly, the effect could be very small as the detected maximum and minimum differences indicate and the number of subjects was too low to detect the effect with statistical measures. Thus, the power of the study was not sufficient to detect such small effects. And secondly, it could be that there is no effect of UMTS-EMF on the blood circulation at this measurement positions or anywhere.

To further investigate this, a more extensive study with enhanced power (twice the number of subjects) and the exposure parameters mentioned above will be carried out.

Acknowledgments The authors gratefully acknowledge the support of the Swiss National Foundation (National Research Programme NRP 57). We thank Massimo Merlini (Statistician, ETH Zurich) for his valuable comments and great support.

References

1. Spichtig S (2010) Multi-distance and multi-frequency frequency-domain near-infrared spectroscopy: characterization and application. PhD thesis No 19006, Swiss Federal Institute of Technology Zurich
2. Zwamborn APM, Vossen SHJA, Van Leersum BJAM et al (2003) Effects of global communication system radio-frequency fields on well being and cognitive functions of human subjects

with and without subjective complaints. TNO Physics and Electronics Laboratory, FEL-03-C148
3. Ndoumbe Mbonjo H, Streckert J, Bitz A et al (2004) Generic UMTS test signal for RF bioelectromagnetic studies. Bioelectromagnetics 25:415–425
4. Huber R, Treyer V, Borbély AA et al (2002) Electromagnetic fields, such as those from mobile phones, alter regional cerebral blood flow and sleep and waking EEG. J Sleep Res 11(4):289–295
5. Huber R, Treyer V, Schuderer J et al (2005) Exposure to pulse-modulated radio frequency electromagnetic fields affects regional cerebral blood flow. Eur J Neurosci 21:1000–1006
6. CENELEC (2001) Basic standard for the measurement of specific absorption rate related to human exposure to electromagnetic fields from mobile phones (300 MHz–3 GHz). Technical report, EN5036.1
7. Lehmann H, Pollara L, Spichtig S, Kühn S, Wolf M. Head exposure system for a human provocation study to assess the possible influence of UMTS-like electromagnetic fields on cerebral blood circulation using near-infrared imaging. Bioelectromagnetics. 2011 Aug 12. doi: 10.1002/bem.20688. [Epub ahead of print]
8. Zhao H, Tanikawa Y, Gao F et al (2002) Maps of optical differential pathlength factor of human adult forehead, somatosensory motor and occipital regions at multi-wavelengths in NIR. Phys Med Biol 47:2075–2093
9. Scholkmann F, Spichtig S, Mühlemann T et al (2010) How to detect and reduce movement artifacts in near-infrared imaging using moving standard deviation and spline interpolation. Physiol Meas 31:649–662
10. Wolf M, Haensse D, Morren G et al (2006) Do GSM 900 MHz signals affect cerebral blood circulation? A near-infrared spectrophotometry study. Opt Express 14(13):6128–41
11. Jasper HH (1958) Report of the committee on methods of clinical examination in electroencephalography. Electroenceph Clin Neurophysiol 10:370–375

Chapter 14
Optical Diagnosis of Mental Stress: Review

Kaoru Sakatani

1 Introduction

In recent years, the incidence of stress-induced psychological and somatic diseases has been increasing rapidly. Although activation of the stress system improves homeostasis, persistent activation of this system under everyday stress may lead to stress-induced diseases. It is, therefore, important to clarify the neurophysiological mechanism of stress response and to develop a simple, noninvasive method for assessment of stress response and for evaluation of the efficacy of relaxation methods for prevention of stress-induced diseases. We have used near-infrared spectroscopy (NIRS) for investigation of neurophysiological mechanisms of mental stress and relaxation methods [1–4]. We found that the prefrontal cortex (PFC) plays an important role in stress response and NIRS is useful for the diagnosis of mental stress. The present chapter reviews recent NIRS studies on stress and relaxation, including neuroimaging studies.

2 Role of the Prefrontal Cortex in Stress Response

The main components of the stress response system are the hypothalamic-pituitary-adrenal (HPA) system and the autonomic nervous system (ANS), within which the sympathetic medullary system plays a dominant role [5]. The PFC plays an important role in mediating behavioral and somatic responses to stress via projections to the

K. Sakatani, M.D., Ph.D. (✉)
Division of Optical Brain Engineering, Department of Neurological Surgery,
Nihon University School of Medicine, 30-1, Oyaguchi Kami-cho, Itabashi-ku
173-8610, Tokyo, Japan
e-mail: sakatani@med.nihon-u.ac.jp

M. Wolf et al. (eds.), *Oxygen Transport to Tissue XXXIII*, Advances in Experimental Medicine and Biology 737, DOI 10.1007/978-1-4614-1566-4_14,

centers of the HPA system and ANS in the medial hypothalamus [6]. Interestingly, a number of studies have demonstrated that the right PFC dominates the regulation of the HPA axis and ANS during mental stress. Electroencephalographic studies have shown that a greater right frontal activation is associated with increased heart rate during unpleasant emotional stimuli [7]. Sullivan and Gratton observed that lesions to the right or bilateral PFC, but not the left PFC, decrease prestress corticosterone levels and the stress-induced corticosterone response in rats [8]. In addition, a recent functional MRI study revealed that right dominance of PFC activity during mental stress tasks is correlated with changes in salivary cortisol level and heart rate [9]. These findings suggest that subjects with right dominant PFC activity during mental stress may be more sensitive to mental stress, and may be more prone to exhibit various stress-induced somatic disorders, including skin disorders.

3 Roles of PFC in Stress Response Evaluated by NIRS

NIRS is a noninvasive optical technique that can measure changes in the concentrations of oxyhemoglobin (oxy-Hb) and deoxyhemoglobin (deoxy-Hb) in cortical vessels [10]. Changes in oxy-Hb concentration during tasks reflect neuronal activity, as they correlate with evoked changes in regional cerebral blood flow (rCBF) [11–13]. Neuronal activation decreases deoxy-Hb, which causes an increase of the blood oxygen level-dependent (BOLD) signal in functional magnetic resonance imaging (f-MRI) [14]. NIRS thus provides more information about the evoked cerebral blood oxygenation changes than does the BOLD image, although the spatial resolution of NIRS is poor due to light scattering within the tissues. Unlike f-MRI, NIRS does not require head constraint, and therefore NIRS measurements may be less stressful for subjects.

We studied normal young right-handed females ($n = 30$, mean age of 21.4 ± 1.4 years). We employed a mental arithmetic task as a psychological stressor. The subjects were asked to consecutively subtract a two-digit number from a four-digit number (e.g., 1,022 − 13) as quickly as possible for 60 s. We measured cerebral blood oxygenation in the bilateral PFC with a NIRS monitor which uses spatially resolved reflectance spectroscopy (NIRO-300, Hamamatsu Photonics K.K., Hamamatsu, Japan). The center between the emitter and detector was identical to the Fp2 position of the international electroencephalographic 10–20 system used previously. MRI confirmed that the emitter–detector was placed over the PFC and the medial PFC.

We evaluated the asymmetry of PFC activity during the task by calculating the laterality index (LI) (i.e., [(right − left)/(right + left)]) of oxy-Hb changes. Positive values of LI indicate right-dominant PFC activity while negative values indicate left-dominant PFC activity. Then, we evaluated the relation between LI and heart rate changes during the task, as well as skin condition (i.e., level of sebum secretion, population of *Propionibacterium acnes*). Skin condition was evaluated because acne vulgaris is known to develop under mental stress. Activation of the HPA

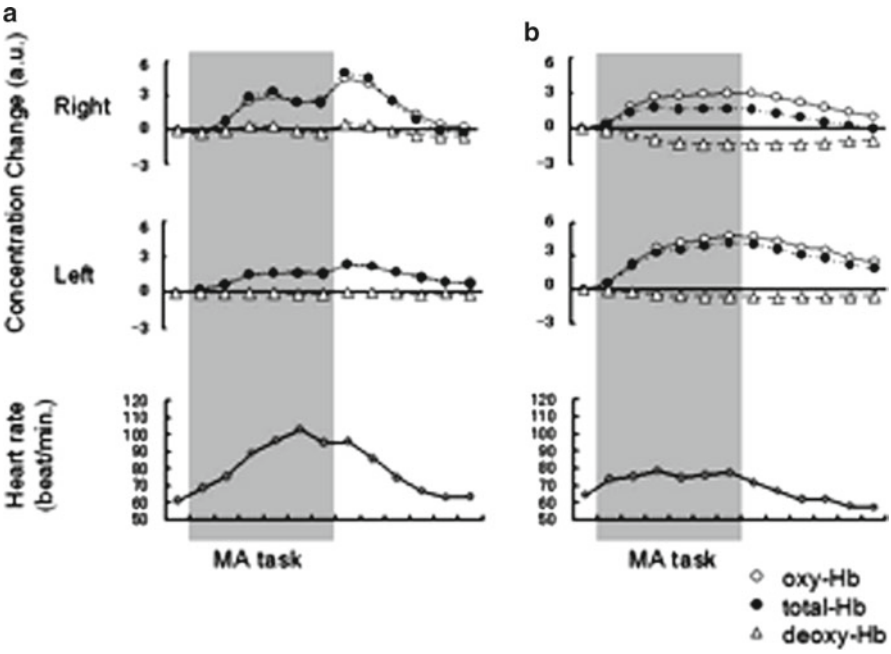

Fig. 14.1 Typical examples of changes in NIRS parameters and heart rate (HR) during mental arithmetic task in subjects with high HR increases (**a**) and low HR increases (**b**). The ordinate of NIRS parameters indicates the concentration changes of Oxy-Hb, Deoxy-Hb, and Total-Hb in arbitrary units. The ordinate of HR indicates number of beats per min. The *gray* area denotes the task period (60 s)

axis during mental stress induces secretion of corticotropin-releasing hormone and adrenal steroid hormones, which cause sebaceous hyperplasia and aggravate acne.

NIRS demonstrated that oxy-Hb increased in the bilateral PFC during the task, in association with a decrease of deoxy-Hb (Fig. 14.1). The task significantly increased heart rate ($p=0.0000049$). We found that right PFC dominant increase in oxy-Hb during the task was associated with a large heart rate increase during the task (Fig. 14.1a), while left PFC dominant increase in oxy-Hb was associated with a small heart rate increase (Fig. 14.1b). The LI of oxy-Hb change was positively correlated with heart rate change ($r=+0.52$, $p=0.020$) (Fig. 14.2a). In addition, there was a positive correlation between the LI of oxy-Hb change and sebum level ($r=+041$, $p=0.0093$) (Fig. 14.2b) and *Propionibacterium acnes* population in the facial skin before the task ($r=+0.41$, $p=0.0087$) (Fig. 14.2c).

These results indicate that subjects with a greater increase in heart rate and higher sebum level and *Propionibacterium acnes* population in the facial skin showed right dominant PFC activity during the mental stress task, and suggest that such subjects are more sensitive to mental stress associated with hyperactivity of the stress response system, including the HPA axis and ANS system.

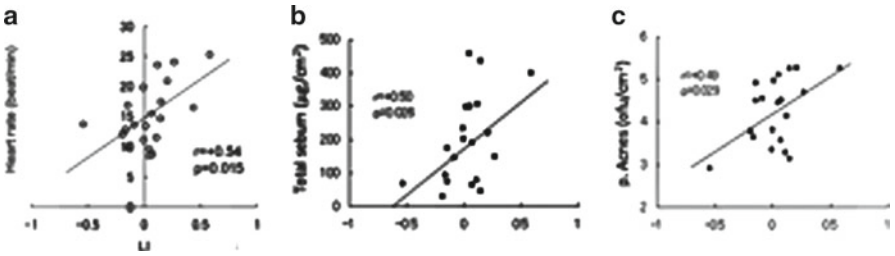

Fig. 14.2 (**a**) Relationship between the laterality index (LI) of oxy-Hb changes and heart rate (HR) changes during a mental arithmetic task. There was a significant positive correlation between LI and HR ($r = +0.54$, $p < 0.015$). (**b** and **c**) The correlation between the LI of oxy-Hb changes during the task and the facial skin content of sebum (**b**) and the *P. acnes* population (**c**) before the task. Significant positive correlations were observed for the amount of sebaceous secretion ($r = +050$, $p = 0.026$) and the *P. acnes* population ($r = +0.49$, $p = 0.029$)

4 Effects of Relaxation on PFC Activity and Stress Response

We evaluated the effects of fragrance on the subjects who exhibited right PFC dominant activity during the stress task and a high level of sebum secretion ($n = 12$) [3]. Fragrances have long been known to influence stress-induced psychosomatic disorders [15, 16]. We used a fragrance which was blended by a perfumer for this experiment. All subjects were asked to use the fragrance spray at least three times during the day and then to put the room fragrance at their bedside every night for 4 weeks. We compared the prestress level of sebum secretion before and after fragrance administration. In addition, we measured the PFC activity during the mental arithmetic task before and after fragrance administration, and compared the LI of oxy-Hb change (Fig. 14.3).

Administration of fragrance for 4 weeks significantly reduced the level of sebum ($p = 0.02$) in the fragrance group ($n = 6$). In addition, the LI-oxyHb decreased significantly from 0.11 ± 0.07 to -0.10 ± 0.18 ($p = 0.01$), indicating that the dominant side of the stress-induced PFC activity changed from the right to left side. In contrast, neither LI-oxyHb nor the level of sebum secretion changed significantly in the control group ($n = 6$). These results suggest that administration of fragrance reduced the level of sebum secretion by modulating the stress-induced PFC activity. That is, fragrance altered the dominant side of the stress-induced PFC activity from the right to the left side, and reduced the hyperactivity of the HPA system, which caused hypersecretion of sebum. The physiological mechanism of the effect of fragrance is not clear; however, one possibility is neuronal conditioning of PFC activity by olfactory stimulation, since the olfactory system connects to the PFC via the hypothalamus and limbic system. Indeed, the NIRS results demonstrated that olfactory stimulation causes an increase of oxy-Hb in the bilateral PFC. Therefore, repeated olfactory stimulation with fragrance could change the stress-induced PFC activity via the olfactory system.

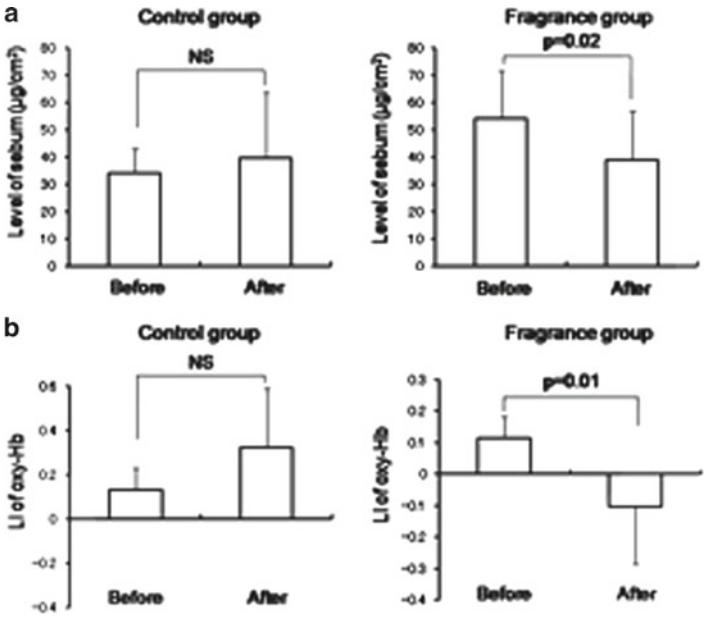

Fig. 14.3 Effects of fragrance administration on the prestress level of sebum secretion in the facial skin (**a**) and the laterality of PFC activity during a mental arithmetic task (**b**). The ordinates in (**a**) and (**b**) indicate the level of sebum secretion (μg/cm^2) and the laterality index (LI) of oxy-Hb changes, respectively. The error bars indicate standard deviation. Fragrance administration significantly decreased the level of sebum secretion ($p = 0.02$) and the LI of oxy-Hb ($p = 0.01$)

5 Usefulness of Time-Resolved Spectroscopy for Stress Study

Conventional NIRS which employs continuous light does not allow measurement of Hb concentration at rest. In contrast, time-resolved spectroscopy, which employs picosecond pulses of light, can quantitatively evaluate Hb concentration at rest [17]. TRS has been employed for functional studies on normal adults [18–20] and for evaluation of the cerebral circulation in patients with cerebrovascular diseases [21, 22] and newborn infants [23].

Tsunetsugu et al. employed TRS to evaluate the effect of "forest therapy" on the PFC activity at rest [24]; forest therapy (i.e., forest-air bathing and walking) is popular in Japan. They compared the Hb concentration in the PFC at rest in a city environment and in a forest environment. The total Hb in the PFC in the forest environment was significantly smaller than that in the city environment. In addition, the salivary cortisol level in the forest environment was significantly smaller than that in the city environment. These results suggest that the city environment caused hyperactivity in the PFC, which was normalized by the forest environment.

6 Limitations of NIRS Measurements

Finally, potential limitations of NIRS should be discussed. NIRS measures the blood oxygenation changes within the illuminated area, which includes both intracranial and extracranial tissues. NIRS parameter changes may therefore be caused by changes in the blood flow of the scalp; however, we observed minimal changes in the skin blood flow during the task in a preliminary experiment. We therefore believe that the NIRS parameter changes predominantly reflect the blood oxygenation changes in the activated cortices. In addition, NIRS does not allow the measurement of cerebral blood oxygenation changes in the whole brain, including deep brain structures. Although the PFC plays an important role in stress responses, further studies are necessary to evaluate the precise activation areas within the brain that are related to the effect of fragrance and mental stress.

References

1. Tanida M, Sakatani K, Takano R, Tagai K (2004) Relation between asymmetry of prefrontal cortex activities and the autonomic nervous system during a mental arithmetic task: near infrared spectroscopy study. Neurosci Lett 369:69–74
2. Tanida M, Katsuyama M, Sakatani K (2007) Relation between mental stress-induced prefrontal cortex activity and skin conditions: a near infrared spectroscopy study. Brain Res 1184:210–216
3. Tanida M, Katsuyama M, Sakatani K (2008) Effects of fragrance administration on stress-induced prefrontal cortex activity and sebum secretion in the facial skin. Neurosci Lett 432:157–161
4. Sakatani K, Tanida M, Katsuyama M (2010) Effects of aging on activity of the prefrontal cortex and autonomic nervous system during mental stress task. Adv Exp Med Biol 662:473–478
5. Tsigos C, Chrousos GP (2002) Hypothalamic-pituitary-adrenal axis, neuroendocrine factors and stress. J Psychosom Res 53:865–871
6. Buijs RM, van Eden CG (2000) The integration of stress by the hypothalamus, amygdale and prefrontal cortex: balance between the autonomic nervous system and the neuroendocrine system. Prog Brain Res 126:117–132
7. Waldstein SR, Kop WJ, Schmidt LA et al (2000) Frontal electrocortical and cardiovascular reactivity during happiness and anger. Biol Psychol 55:3–23
8. Sullivan RM, Gratton A (1999) Lateralized effects of medial prefrontal cortex lesions on neuroendcrine and autonomic stress responses in rats. J Neurosci 19:2834–2840
9. Wang J, Rao H, Wetmore GS et al (2005) Perfusion functional MRI reveals cerebral blood flow pattern under psychological stress. Proc Natl Acad Sci U S A 102:17804–17809
10. Jöbsis FF (1977) Noninvasive, infrared monitoring of cerebral and myocardial oxygen sufficiency and circulatory parameters. Science 198:1264–1267
11. Sakatani K, Xie Y, Lichty W et al (1998) Language-activated cerebral blood oxygenation and hemodynamic changes of the left prefrontal cortex in poststroke aphasic patients: a near infrared spectroscopy study. Stroke 29:1299–1304
12. Sakatani K, Katayama Y, Yamamoto T et al (1999) Cerebral blood oxygenation changes of the frontal lobe induced by direct electrical stimulation of thalamus and globus pallidus. A near infrared spectroscopy study. J Neurol Neurosurg Psychiatr 67:769–773

13. Sakatani K, Lichty W, Xie Y et al (1999) Effects of aging on language-activated cerebral blood oxygenation changes of the left prefrontal cortex: near infrared spectroscopy study. J Stroke Cerebrovasc Dis 8:398–403
14. Fujiwara N, Sakatani K, Katayama Y et al (2004) Evoked cerebral blood oxygenation changes in false-negative activations in BOLD contrast functional MRI of patients with brain tumors. Neuroimage 21:1464–1471
15. Hosoi J, Tanida M, Tsuchiya T (2003) Regulation of plasma substance P and skin mast cells by odorants. J Cutan Med Surg 7:287–291
16. Atsumi T, Tonosaki K (2007) Smelling lavender and rosemary increases free radical scavenging activity and decreases cortisol level in saliva. Psychiatry Res 150:89–96
17. Patterson MS, Chance B, Wilson C (1989) Time resolved reflectance and transmittance for the non-invasive measurement of tissue optical properties. Appl Opt 28:2331–2336
18. Hoshi Y (2003) Functional near-infrared optical imaging: utility and limitations in human brain mapping. Psychophysiology 40:511–520
19. Quaresima V, Ferrari M, Torricelli A et al (2005) Bilateral prefrontal cortex oxygenation responses to a verbal fluency task: a multichannel time-resolved near-infrared topography study. J Biomed Opt 10:11012
20. Sakatani K, Yamashita D, Yamanaka T et al (2006) Changes of cerebral blood oxygenation and optical pathlength during activation and deactivation in the prefrontal cortex measured by time-resolved near infrared spectroscopy. Life Sci 78:2734–2741
21. Liebert A, Wabnitz H, Steinbrink J et al (2005) Bed-side assessment of cerebral perfusion in stroke patients based on optical monitoring of a dye bolus by time-resolved diffuse reflectance. Neuroimage 24:426–435
22. Yokose N, Sakatani K, Murata Y et al (2010) Bedside assessment of cerebral vasospasms after subarachnoid hemorrhage by near infrared time-resolved spectroscopy. Adv Exp Med Biol 662:505–511
23. Ijichi S, Kusaka T, Isobe K et al (2005) Developmental changes of optical properties in neonates determined by near-infrared time-resolved spectroscopy. Pediatr Res 58:568–573
24. Tsunetsugu Y, Miyazaki Y (2005) Measurement of absolute hemoglobin concentrations of prefrontal region by near-infrared time-resolved spectroscopy: examples of experiments and prospects. J Physiol Anthropol Appl Human Sci 24:469–472
25. Shibata H, Fujiwara R, Iwamoto M et al (1991) Immunological and behavioral effects of fragrance in mice. Int J Neurosci 57:151–159

Chapter 15
Neuroprotective Properties of Ketone Bodies

Kui Xu, Joseph C. LaManna, and Michelle A. Puchowicz

1 Introduction

The brain, unlike other organs, is normally completely dependent on glucose as a primary energy substrate, but is capable of using ketones (C_4 ketone bodies) as occurs with fasting, prolonged starvation or chronic feeding of a high-fat low-carbohydrate diet (ketogenic diet). Various studies have shown with acute or chronic conditions that ketosis is protective against seizures, focal stroke and recovery after cardiac arrest, and other neuropathologic conditions. Recently, we have shown that in diet-induced ketotic aged rats cognitive performance was improved. The specific mechanism(s) that link ketosis and neuroprotection remains exploratory.

Based on our experiences, the neuroprotective effects of ketones act through various regulatory pathways, most of which are related to glucose metabolism. We have recently reported that ketosis was neuroprotective in focal ischemia which may be through succinate-mediated increased accumulation of hypoxic-inducible factor-1 alpha (HIF-1α) [1]. Our working hypothesis is that ketone bodies are effective agents against pathology associated with oxidative stress and/or altered glucose metabolism by supplying carbon to the citric acid cycle (CAC) as acetyl-CoA,

K. Xu
Department of Neurology, School of Medicine, Case Western Reserve University, Cleveland, OH 44106, USA

J.C. LaManna
Department of Physiology and Biophysics, School of Medicine, Case Western Reserve University, Cleveland, OH 44106, USA

M.A. Puchowicz, Ph.D. (✉)
Department of Nutrition, School of Medicine, Mouse Metabolic Phenotyping Center, Case Western Reserve University, 10900 Euclid Avenue, BRB 927, Cleveland, OH 44106-4954, USA
e-mail: map10@case.edu

M. Wolf et al. (eds.), *Oxygen Transport to Tissue XXXIII*, Advances in Experimental Medicine and Biology 737, DOI 10.1007/978-1-4614-1566-4_15,

bypassing glycolysis. Additionally, carbon flux through the CAC is balanced by equal carbon entry to that of carbons exiting, a process known as anaplerosis and cataplerosis, respectively. Unlike C_4 ketone bodies, propionate and related precursors, such as odd-chain C_5 ketones (β-keto and *R*-β-hydroxypentanoate), have anaplerotic properties [2–4]. These compounds have been described to rescue or improve catabolic state in heart following ischemia [4, 5] and energy balance in liver, for reviews [3, 6, 7], but little is known about their application in brain. Thus, we propose that anaplerotic compounds are beneficial to recovery of brain following transient global or focal brain ischemia. We present data from two in vivo models of transient brain ischemia, cardiac arrest and resuscitation and focal stroke (via MCAO) where ketosis either induced by ketogenic diet (C_4 ketosis) or infusion of propionate ester results in improved outcome following an ischemic insult.

2 Methods

2.1 Diet-Induced Ketosis, Rat Model of Cardiac Arrest and Resuscitation and Hypoxic Ventilatory Response

Male Wistar rats (2 months old) were fed a ketogenic diet (KG-diet, Fat: 89.5%, Protein: 10%, Carbohydrate: 0.1%, Research Diets, NJ) for 3 weeks to induce chronic ketosis [1] prior to cardiac arrest and resuscitation. Matched controls were fed a standard rodent diet (STD-diet, Teklad, USA). Rats underwent cardiac arrest and were allowed to survive for 4 days following resuscitation. Briefly, cardiac arrest was induced in the conscious rat by intra-atrial injection of KCL (0.5 M; 0.12 ml/100 g bodyweight); resuscitation (ventilation, chest compressions, and saline infusion) was initiated 7 min after arrest; the total ischemic time was about 12 min [8]. Overall survival rate was determined on day 4 of recovery. HVR, the ratio of minute volumes (10% oxygen vs. normoxic baseline), was measured using plethysmography before cardiac arrest and daily following resuscitation [8].

2.2 Postreperfusion Treatment Following Transient Focal Cerebral Ischemia

In another group, rats (2 months old) were maintained on a STD-diet and underwent intravenous treatment with odd-chain keto-acid ester, *N*,*S*-dipropionyl cysteine ethyl ester (DPNCE; 450 μmol/kg/min × 30 min), following reversible middle cerebral artery occlusion (MCAO). MCAO was induced using a monofilament model, occluded for 2 h. Infarct volumes were determined following a 72 h reperfusion period relative to contralateral hemisphere [1].

2.3 Statistics

Data are expressed as mean ± SD. Statistical analyzes were performed using SPSS V13.0 for windows. The comparison between any two groups was analyzed with a *t*-test. Significance was considered at the level of $p < 0.05$.

3 Results

3.1 Diet-Induced Ketosis and Recovery Following Cardiac Arrest and Resuscitation

The overall survival rates and HVR were determined in ketotic rats (KG-diet group) and the STD-diet group following cardiac arrest and resuscitation. The number of deaths was decreased in the KG-diet group compared to the STD-diet group over the 4-day period (see table insert). As seen in Fig. 15.1, at day 4 of recovery, the overall survival rate was improved in the KG-diet group (86%, 6/7) compared to the STD-diet group (55%, 10/11). HVR was used to assess brain stem function with respect to respiration regulation. HVR in the KG-diet group (3.0 ± 0.5, mean ± SD, $n = 3$) was similar to the STD-diet group (2.9 ± 0.2, $n = 9$) before cardiac arrest (Fig. 15.1). During 1–4 days of resuscitation, HVR was significantly decreased (30–36%) compared to the prearrest value in the STD-diet group, and the lower

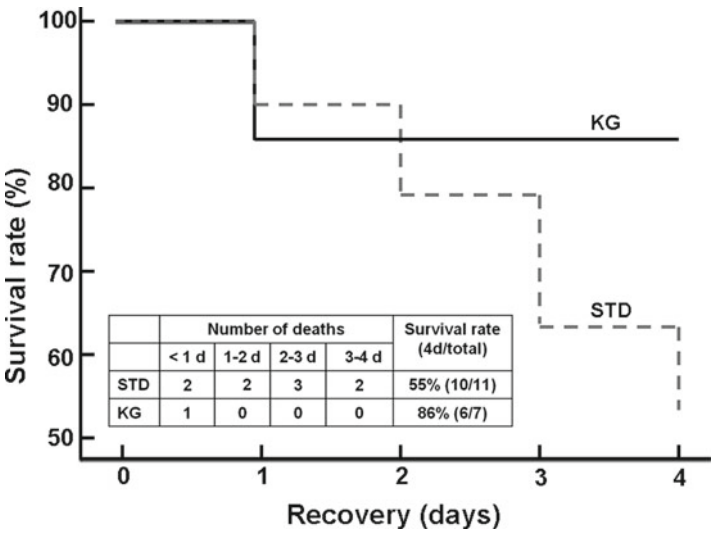

	Number of deaths				Survival rate (4d/total)
	< 1 d	1-2 d	2-3 d	3-4 d	
STD	2	2	3	2	55% (10/11)
KG	1	0	0	0	86% (6/7)

Fig. 15.1 Overall survival 4 days following cardiac arrest and resuscitation. *STD* Standard-diet group, *KG* ketogenic diet group. The table inset shows the number of deaths over the 4-day recovery phase and the survival rates at day 4

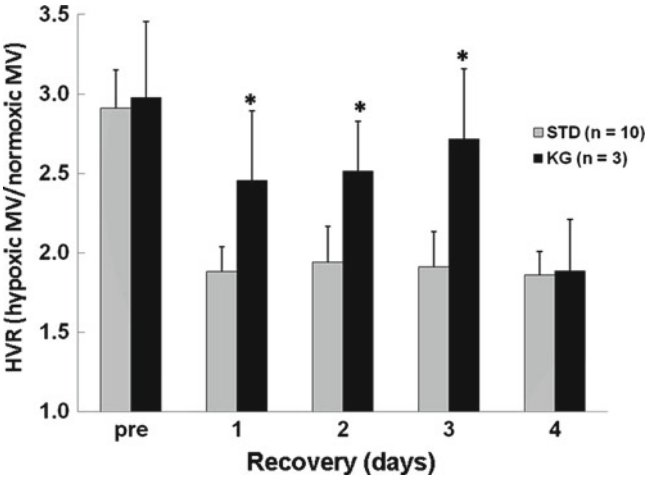

Fig. 15.2 HVR before (pre) and 1–4 days following cardiac arrest and resuscitation. HVR = hypoxic minute volume (MV)/normoxic baseline MV. MV = tidal volume × frequency. *STD* Standard-diet group, *KG* ketogenic diet group. Data are mean ± SD, *asterisk* indicates significance ($p < 0.05$, *t*-test) KG vs. STD at the same time point

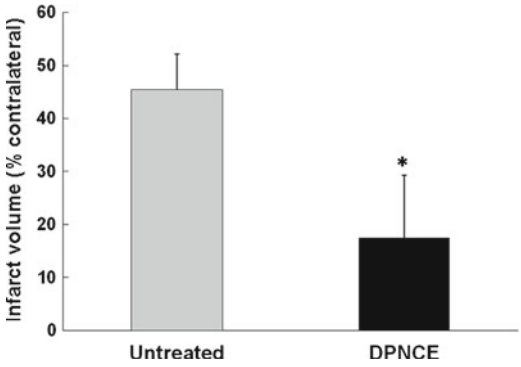

Fig. 15.3 Infarct volume (% contralateral hemisphere) following reversible middle cerebral artery occlusion (MCAO; 2 h occlusion followed by 72 h reperfusion). Data are mean ± SD, DPNCE treatment group ($n = 7$) had significantly lower ($p < 0.05$, *t*-test) infarct volume compared to the untreated group ($n = 6$)

HVR was associated with poorer recovery. However, HVR was improved in the KG-diet group at 1–3 days of recovery (Fig. 15.2).

3.2 MCAO and DPNCE Treatment

DPNCE was used as a postischemia reperfusion treatment following reversible MCAO. Similar to what we have previously reported in diet-induced ketotic rats undergoing reversible MCAO (1), DPNCE treatment resulted in decreased infarct volume compared to sham by 61% (17.5 ± 11.8; $n = 7$ vs. 45.4 ± 6.7; $n = 6$, % contralateral hemisphere, respectively) (Fig. 15.3).

4 Discussion

We have recently reported that ketosis was neuroprotective in focal ischemia and improved cognitive performance in aged rats. In this study we continued to investigate the potential of C_4 ketosis as a strategy for improving outcome following an ischemic insult, as well as investigate a novel anaplerotic substrate DPNCE. Anaplerotic substrates are known to sustain the balance between anaplerosis vs. cataplerosis, thus stabilizing energy transfer and homeostasis during conditions when the balance between these two processes is altered. Pyruvate when metabolized to oxaloacid/malate (via pyruvate carboxylase and/or malic enzyme) and glutamate/glutamine to alpha-ketoglutarate (via glutamate dehydrogenase and/or transaminases) are considered anaplerotic substrates. Additionally, although not well described in brain, so is the odd-chain fatty acid propionate and its precursors. We investigated propionate ester (administered as DPNCE) as this compound enters the CAC as succinyl-CoA. DPNCE can be administered as an enteral sodium free neutral compound which has shown promise as a posttreatment agent in pig heart [4, 7]. In this study, the rationale for using an anaplerotic treatment strategy was to improve outcome following an ischemic event, such as with heart, and that brain can metabolize anaplerotic substrates. We hypothesized that diet-induced ketosis improves brainstem function, as exemplified by the hypoxic ventilatory response, and survival following cardiac arrest and resuscitation and treatment with an anaplerotic and antioxidative compound, DPNCE, is neuroprotective following stroke (via MCAO). The data from this study, where ketosis was induced either by ketogenic diet (C_4 ketosis) or infusion of DPNCE (propionate ester), resulted in improved outcome following an ischemic insult. HVR was shown to increase in diet-induced ketotic rats in the early recovery period following cardiac arrest and resuscitation, which was associated with improved overall survival rate. This work also showed that an anaplerotic compound, such as DPNCE, is a promising potential pharmacological agent poststroke. These findings support the concept that the mechanistic link between neuroprotection by C_4-ketosis and propionate, an odd-chain anaplerotic compound, is most likely through the maintenance of energy transfer at the level of the CAC either via acetyl-CoA or succinyl-CoA, respectively, which may confer protection through HIF-1α stabilization [1, 8].

Acknowledgments This study was supported by NIH grants: NS 062048, HL 092933 and MMPC U24 DK76169. The authors thank Dr. T. Kasumov , Lerner Institute, Cleveland Clinic Foundation, and Dr. H. Brunengraber, Case Western Reserve University, Department of Nutrition, for their generous contribution towards supplying the DPNCE compound and the Mouse Metabolic Phenotyping Center (MMPC) for analytical services.

References

1. Puchowicz MA, Zechel J, Valerio J, Emancipator D, Xu K, Pundik S, LaManna JC, Lust WD (2008) Neuroprotection in diet induced ketotic rat brain following focal ischemia. J Cereb Blood Flow Metab 28(12):1907–1916
2. Deng S, Zhang GF, Kasumov T, Roe CR, Brunengraber H (2009) Interrelations between C_4 ketogenesis, C_5 ketogenesis, and anaplerosis in the perfused rat liver. J Biol Chem 284(41):27799–27807
3. Brunengraber H, Roe CR (2006) Anaplerotic molecules: current and future. J Inherit Metab Dis 29(2–3):327–331
4. Kasumov T, Sharma N, Huang H, Kombu RS, Cendrowski A, Stanley WC, Brunengraber H (2009) Dipropionylcysteine ethyl ester compensates for loss of citric acid cycle intermediates during post ischemia reperfusion in the pig heart. Cardiovasc Drugs Ther 23(6):459–469
5. Martini WZ, Stanley WC, Huang H, Rosiers CD, Hoppel CL, Brunengraber H (2003) Quantitative assessment of anaplerosis from propionate in pig heart in vivo. Am J Physiol Endocrinol Metab 284(2):E351–E356
6. Roe CR, Mochel F (2006) Anaplerotic diet therapy in inherited metabolic disease: therapeutic potential. J Inherit Metab Dis 29(2–3):332–340
7. Kasumov T, Sharma N, Huang H, Kombu RS, Cendrowski A, Stanley WC, Brunengraber H (2009) Dipropionylcysteine ethyl ester compensates for loss of citric acid cycle intermediates during post ischemia reperfusion in the pig heart. Cardiovasc Drugs Ther 23(6):459–469
8. Xu K, LaManna JC (2009) The loss of hypoxic ventilatory responses following resuscitation after cardiac arrest in rats is associated with failure of long-term survival. Brain Res 3(1258): 59–64

Chapter 16
The Confounding Effect of Systemic Physiology on the Hemodynamic Response in Newborns

B.B. Zimmermann, N. Roche-Labarbe, A. Surova, D.A. Boas, M. Wolf, P.E. Grant, and M.A. Franceschini

1 Introduction

During neural activity, increases in glucose and oxygen consumption and release of vasoactive neurotransmitters cause a local increase in cerebral blood flow (CBF) [1] and cerebral blood volume (CBV). Increases in oxygen consumption are significantly lower than increases in CBF and as a result we see a net increase in the amount of oxygen in the blood and tissue [2]. Typical measures of neural activity in adults with near-infrared spectroscopy (NIRS) show a local increase in oxy-hemoglobin concentration (HbO) and a decrease in deoxy-hemoglobin concentration (HbR), which corresponds to a local increase in BOLD signal measured with fMRI. In many neonatal functional studies inversions of these hemoglobin signals have been reported, across visual [3, 4], olfactory [5], sensory-motor [6] and auditory [7] cortices. In general, the inversion starts at a few weeks of age.

B.B. Zimmermann (✉)
Athinoula A. Martinos Center for Biomedical Imaging, Harvard Medical School, Massachusetts General Hospital, 13th Street, Building 149, Charlestown, MA 02129, USA
e-mail: bzim@mgh.harvard.edu

Biomedical Optics Research Laboratory, Clinic for Neonatology, University Hospital Zürich, Zürich, Switzerland

N. Roche-Labarbe • A. Surova • D.A. Boas • M.A. Franceschini
Athinoula A. Martinos Center for Biomedical Imaging, Harvard Medical School, Massachusetts General Hospital, 13th Street, Building 149, Charlestown, MA 02129, USA

M. Wolf
Biomedical Optics Research Laboratory, Clinic for Neonatology, University Hospital Zürich, Zürich, Switzerland

P.E. Grant
Newborn Medicine and Radiology, Children's Hospital of Boston, Boston, MA, USA

M. Wolf et al. (eds.), *Oxygen Transport to Tissue XXXIII*, Advances in Experimental Medicine and Biology 737, DOI 10.1007/978-1-4614-1566-4_16,

The reason for such an inversion in the functional hemodynamic signals is not yet understood. We hypothesize that changes in hematocrit during the transition from fetal to adult hemoglobin and the consequent period of low hematocrit cause such an inversion. To test this hypothesis, we performed a longitudinal auditory functional study in premature infants.

2 Materials and Methods

We recruited six premature neonates from either the neonatal intensive care unit (NICU) or the Well Baby Nursery at the Massachusetts General Hospital (MGH) [26–33.4 weeks, mean 30 weeks gestational age (GA)]. All of the neonates had APGAR scores between 6 and 9 after 5 min. We conducted a total of 18 recording sessions, with an average of three sessions per infant (range: 2–5). The age of the infants at the time of each session ranged from 1 to 11 weeks of age, with a mean of 5.5 weeks [30–38 weeks, mean 35 weeks corrected gestational age (CGA)]. Our Institutional Review Board approved the study and parents provided informed consent.

All measurements were done at the infant's bedside. The protocol consisted of two parts: a measure of evoked hemodynamic changes in response to auditory stimuli (functional measurements) with a continuous-wave (CW-NIRS) system, and a measure of baseline hemoglobin concentration and oxygenation during rest (baseline measurements) with a frequency-domain system (FD-NIRS).

2.1 Functional Measurements

Auditory stimuli consisting of computer-generated repetitive syllables (e.g., "ma, ma, ma," or "bi, bi, bi") read by a female computer voice (AT&T Labs, Inc., Florham Park, NJ) were presented in periods of 6 s followed by 6- to 16-s periods of silence (event-related presentation). Depending on cooperativeness of the baby, a session consisted of four runs of 250 s and 15 stimulation periods each. A sound-level meter allowed us to adjust the volume of the sound to a level of 60–65 dB.

For the functional measurements, we used a commercial continuous-wave NIRS imaging system (CW4, TechEn Inc.) with 18 laser sources and 16 avalanche photo diode (APD) detectors [8]. Light from the sources is conducted to the functional probe and from there to the detectors by means of fiber-optic bundles. Each source fiber combines the light of a 690- and an 830-nm laser. For these measurements, we used three source and six detector positions. The custom-made probe was made of black latex-free rubber and cushioning foam, and sources and detectors were arranged in two rows with a minimum source–detector distance of approximately 2.5 cm. The functional probe was positioned over the left auditory cortex and fixed in position with sterile, self-adhesive elastic gauze. Data were acquired continuously during the functional runs and down-sampled to 10 Hz.

2.2 Baseline Measurements

The baseline hemoglobin measurements were performed a few minutes after the functional measurements, with a customized near-infrared frequency-domain oximeter (ISS Inc., Champaign, IL, USA), as in [9, 10]. The system includes 16 laser sources emitting at eight wavelengths with two redundant pairs (659, 2×685, 755, 778, 798 and 2×825 nm) and two photomultiplier tube (PMT) detectors. The sources are modulated at 110 MHz, and the detectors at 110.005 MHz, to achieve heterodyne detection. Separation of the sources is achieved by rapid (10 ms) multiplexing. Two groups of eight lasers (~1 mW power each) are combined into two source fiber bundles, and each detector is coupled to a fiber bundle. The fiber bundles are arranged in a row on a black rubber probe with source–detector distances of 1, 1.5, 2, and 2.5 cm. Multiple distances are necessary to quantify tissue optical properties and to derive hemoglobin concentration and saturation with this system. The probe was hand-held above the left-temporal position for 8 s and the measure was repeated 3–5 times as in [9].

2.3 Data Analysis

CW-NIRS data were analyzed with a new version of Homer (Homer 2) which, instead of working with a graphical user interface [11], is fully script-based and allows for comfortable batch processing of all measurements with the same parameters for an unbiased analysis. First the data are converted from light intensity to changes in optical density (□OD). Segments of data showing rapid changes in optical density larger than a preset threshold of 1.5% are discarded as motion artifacts. Remaining evident motion artifacts are manually removed. If the motion artifacts occur during a stimulus period, that stimulus is removed from the average. Channels with low SNR or with Fourier spectra that do not show an arterial pulsation peak are removed. The 10 Hz ΔOD data are then band-pass-filtered between 0.02 and 0.5 Hz to remove slow drift and arterial and respiratory oscillations. To remove 0.1 Hz Mayer oscillations and remaining noise common to all channels, we performed principal component analysis (PCA) and removed principal components that described up to 75% of temporal covariance. Finally, the optical densities are converted to oxy and deoxy-hemoglobin concentration (HbO, HbR) changes using the modified Beer–Lambert law and all stimulation sequences in a subject are block-averaged. To quantify the amplitude of HbO and HbR changes, we calculated the difference between the mean concentration of the last second of stimulation and the last second before stimulation. For every subject, the channel with the largest HbO absolute change is selected and reported and further analyzed.

Frequency domain multi-distance and multi-wavelength data are used to quantify baseline hemoglobin concentration and tissue oxygenation. To achieve standardized analysis of the FD-NIRS data, an automated routine developed in [10] was used. This script includes data quality assessment and rejection based on previously established statistical criteria. In particular, measurements were discarded if $R^2 < 0.9$

for the fit of the raw optical data (amplitude and phase) to the light transportation model, if $p > 0.05$ for the fit of the absorption coefficients with the hemoglobin spectra, and for a linear fit of the reduced scattering coefficient versus wavelength.

3 Results

3.1 Baseline Measurements

In agreement with previous results [9, 10], we found that, at ~4–6 weeks of age, total hemoglobin concentration (HbT) and HbO have a minimum corresponding to the minimum of hematocrit due to conversion of fetal to adult hemoglobin (see Fig. 16.1a, c). In contrast, HbR concentrations during the first 6 weeks of life remain constant (see Fig. 16.1b) probably because of two counterbalancing factors: decrease of hemoglobin in the blood because of faster depletion of fetal hemoglobin than formation of adult hemoglobin and increase of oxygen extraction fraction with adult

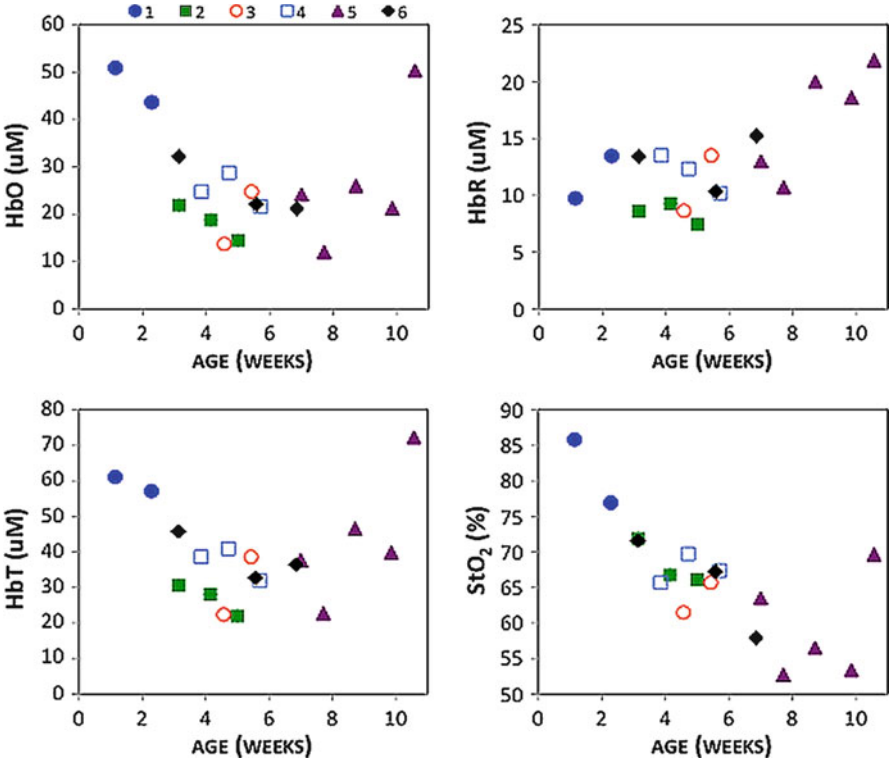

Fig. 16.1 (**a**) Scatter plot of baseline oxy-hemoglobin (HbO) versus age, (**b**) deoxy-hemoglobin versus age, (**c**) total hemoglobin versus age, and (**d**) tissue oxygen saturation versus age. Different babies are indicated by different symbols

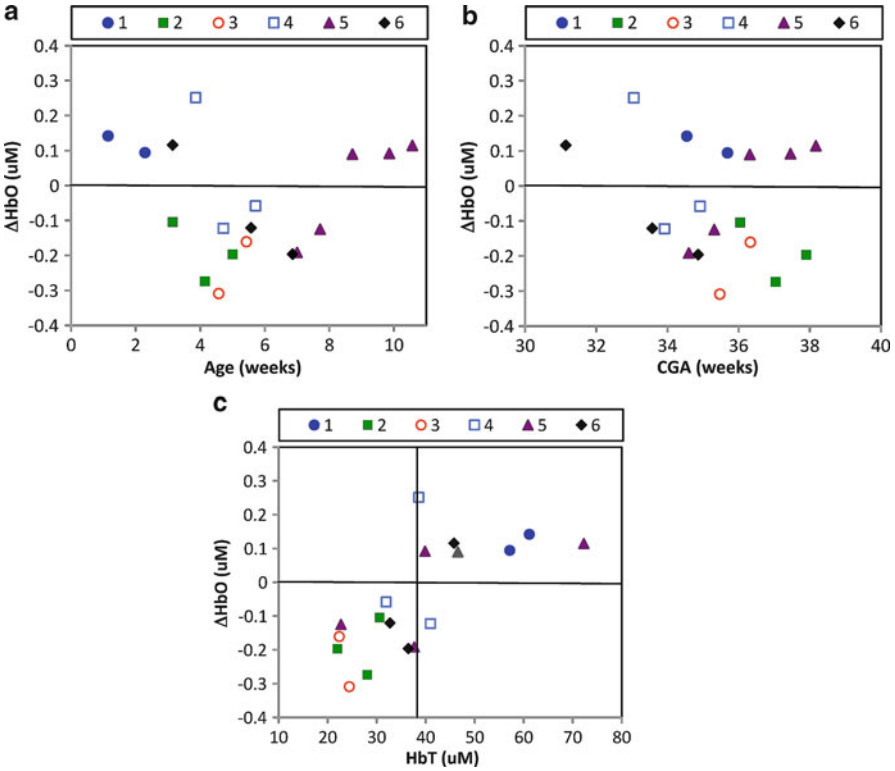

Fig. 16.2 (**a**) Scatter plot of functional oxy-hemoglobin changes (ΔHbO) versus baseline total hemoglobin concentration (HbT), (**b**) ΔHbO versus age, and (**c**) ΔHbO versus corrected gestational age. Different babies are indicated by different symbols. A line through the zero *y*-axis is shown in all graphs. Also in (**a**) a *dashed line* at 38 μM *x*-axis divides the data in two groups: negative and positive ΔHbO changes

relative to fetal hemoglobin. After this initial period HbR increases as HbO and HbT. Consequently, tissue oxygenation (StO_2) decreases during the first 6 weeks of life and then becomes constant (see Fig. 16.1d). As in our previous studies, we did not observe any correlation between any hemoglobin parameter and corrected gestational age.

3.2 Functional Measurements

We observed the expected increase in ΔHbO with stimulation in only 7 out of 18 cases. The remaining 11 measurements showed a decrease in ΔHbO with stimulation. In all but one case ΔHbT followed ΔHbO and in all but four cases ΔHbR was inversely proportional to ΔHbO. The inverted hemoglobin responses are not correlated with age or corrected gestational age (see Fig. 16.2b, c), but all occur

between ages 3 and 8 weeks, when hematocrit and hemoglobin are low. Though for most of these babies we did not have a direct measure of hematocrit on the day of the measurement, we do have the measure of baseline cerebral hemoglobin and we can correlate it with the functional hemoglobin changes. If we divide the ΔHbO responses into two groups, positive and negative, we found a strong correlation between the sign of the functional changes and the baseline total hemoglobin concentration (p-value =0.002 for HbT (two-sample, two-tailed, unequal variance T-test), p-value = 0.01 for HbO and HbR). The R^2 of the scatter plot of ΔHbO versus baseline HbT is 0.5. More importantly we found that, for baseline HbT lower than 38 μM all ΔHbO were negative, while for baseline HbT larger than 38 μM, all but one ΔHbO were positive (see Fig. 16.2a). Results were similar when considering baseline HbO or HbR. Results for ΔHbT were consistent with the results for ΔHbO, while results for ΔHbR were less statistically significant (p-value = 0.026 between ΔHbR and baseline HbR, larger than 0.05 for the HbO and HbT) probably due to the smaller changes in ΔHbR with respect to ΔHbO, and to consequent larger relative noise.

4 Conclusions

Our results show that the inversion in the functional hemodynamic responses in infants correlates with the total hemoglobin concentration. We used auditory stimuli which is known to cause neuronal activity in premature babies 30 weeks GA and older. While neural activity increases with age because of an increase in synaptogenesis and increasing synaptic density, an inversion of the hemodynamic responses is difficult to explain solely based on neural activity differences in the period 3–8 weeks of age. Our results suggest that while neural activity and metabolic demand increase with age, the available hemoglobin supply during the low hematocrit period is not sufficient to overcome oxygen demand during functional activation. We are developing a mathematical model to describe these results.

Acknowledgments The authors thank all the families for their participation and the nurses, physicians, and staff in the Neonatal ICU, Special Care Nursery, Pediatric Neurology, and maternity units at the Massachusetts General Hospital. This work is supported by NIH grant R01 HD42908.

References

1. Fox PT, Raichlie ME, Mitun MA et al (1988) Nonoxidative glucose consumption during focal physiologic neural activity. Science 241(4864):462–464
2. Malonek D, Grinvald A (1996) Interactions between electrical activity and cortical microcirculation revealed by imaging spectroscopy: implications for functional brain mapping. Science 272(5261):551–554

3. Meek JH, Firbank M, Elwell CE et al (1998) Regional hemodynamic responses to visual stimulation in awake infants. Pediatr Res 43(6):840–843
4. Kusaka T, Okubo K, Nagano K et al (2003) Activation of the visual cortex in newborn infants under natural sleep using multichannel near-infrared spectroscopy. Adv Exp Med Biol 510:255–259
5. Bartocci M, Winberg J, Ruggiero C et al (2000) Activation of olfactory cortex in newborn infants after odor stimulation: a functional near-infrared spectroscopy study. Pediatr Res 48(1):18–23
6. Hintz SR, Benaron DA, Siegel AM et al (2001) Bedside functional imaging of the premature infant brain during passive motor activation. J Perinat Med 29(4):335–343
7. Zaramella P, Freato F, Amigoni A et al (2001) Brain auditory activation measured by near-infrared spectroscopy (NIRS) in neonates. Pediatr Res 49(2):213–219
8. Franceschini MA, Fantini S, Thompson JH et al (2003) Hemodynamic evoked response of the sensorimotor cortex measured noninvasively with near-infrared optical imaging. Psychophysiology 40(4):548–560
9. Franceschini MA, Thaker S, Themelis G et al (2007) Assessment of infant brain development with frequency-domain near-infrared spectroscopy. Pediatr Res 61(5 Pt 1):546–551
10. Roche-Labarbe N, Carp SA, Surova A et al (2010) Noninvasive optical measures of CBV, StO(2), CBF index, and rCMRO(2) in human premature neonates' brains in the first six weeks of life. Hum Brain Mapp 31(3):341–352
11. Huppert TJ, Diamond SG, Franceschini MA et al (2009) HomER: a review of time-series analysis methods for near-infrared spectroscopy of the brain. Appl Opt 48(10):D280–D298

Chapter 17
How to Conduct Studies with Neonates Combining Near-Infrared Imaging and Electroencephalography

M. Biallas, I. Trajkovic, F. Scholkmann, C. Hagmann, and M. Wolf

1 Introduction

In newborn infants, hemodynamic responses (HR) to visual stimulation can be detected by fNIRI. However, available literature is not conclusive with regard to fNIRI sensitivity, or whether [O_2Hb] as part of the HR raises or declines after visual stimulus onset [1]. To be able to determine fNIRI sensitivity, electroencephalography (EEG) is utilized as a reference in this experiment. The visual evoked potential (VEP) provides not only an indication of the existence of a response to a visual stimulation, it is also beneficial when neurovascular coupling is examined and it can be used as reference in further analyzes of the fast neuronal signal. The aims of this study were (1) to develop, test and optimize a fNIRI-EEG-set-up; (2) to achieve high fNIRI sensitivity; and (3) to characterize [O_2Hb]'s changes (Δ[O_2Hb]) during stimulation.

2 Methods

After assembling and testing the equipment first measurements were conducted. Responses to the visual stimulation in fNIRI and EEG occurred rarely. Therefore, the protocol of the experiment had to be revaluated. Throughout more than 30

M. Biallas (✉) • I. Trajkovic • M. Wolf
Biomedical Optics Research Laboratory, Division of Neonatology, Department of Obstetrics and Gynecology, University Hospital Zurich, Frauenklinikstrasse 10, 8091 Zurich, Switzerland
e-mail: martin.biallas@gmx.ch

Institute for Biomedical Engineering, ETH Zürich (Swiss Federal Institute of Technology), 8092 Zurich, Switzerland

F. Scholkmann • C. Hagmann
Biomedical Optics Research Laboratory, Division of Neonatology, Department of Obstetrics and Gynecology, University Hospital Zurich, Frauenklinikstrasse 10, 8091 Zurich, Switzerland

M. Wolf et al. (eds.), *Oxygen Transport to Tissue XXXIII*, Advances in Experimental Medicine and Biology 737, DOI 10.1007/978-1-4614-1566-4_17,

measurements, different parameters of the protocol were varied, for example positioning and attachment of sensors, the effect of electrode-skin impedance, bedding of the subject, frequency of stimulation and intensity of stimulation. In each individual measurement only one parameter was varied to allow grading the impact on potential responses. No parameter, except intensity of the visual stimulation device, led to a measureable increase in sensitivity. All further descriptions reflect the latest, most successful protocol in regard to sensitivity.

2.1 Subjects and Protocol

Fifteen healthy, term neonates (mean gestational age 39.9 weeks [standard deviation (SD) 0.92 weeks], mean postnatal age 2.7 days (SD 0.94 days)) were stimulated visually during sleep. The HR of the primary visual cortex is registered by an fNIRI-sensor, whereas the VEP is recorded by EEG.

The protocol of stimulation has a maximum duration of 20 min containing periods of stimulation and rest periods. While the duration of rest periods are different (12–32 s), the stimulation periods are constantly 20 s long. Flash frequency is 0.5 Hz and duration is 10 ms. The flash device is held 15 cm in front of the subjects eyes. After10 min of recording, a preliminary data analysis was performed in order to decide whether to position the fNIRI-sensor differently or to proceed with the recording. If the fNIRI-sensor needed to be readjusted, then only data which were acquired after sensor adjustment were included in the final analysis.

Recordings were performed when room light was turned off and without day light. Throughout preparing and recording, a conversation takes place between the conductors and the mother to establish a relaxed ambiance which supported continuous sleep of the infant.

Preparation of subject: Minimal handling of the newborn infant was done to avoid wakening the infant. Measurements were scheduled to take place shortly after feeding, the newborn infants were held comfortably by their mother sitting in an armchair. Cushions were provided to support the mother holding her infant.

After explaining the experiment to the mother, the first step was to clean the skin of the electrode placement with pre-warmed NaCl solution. Then abrasive electrode gel was applied gently with cotton swaps. Finally, the self-adhesive foil-electrode was applied on top of the gel. This procedure was repeated for all electrodes. The positions of the electrodes refer to the 10/20 system [2]. C_Z, F_Z, O_Z, and F_3 were used. C_Z acted as reference electrode and F_Z as ground electrode. The O_Z electrode was cut to fit beneath the fNIRI-sensor without obscuring any light sources or detectors. Relatively high electrode-skin impedances, in the range of up to 40 kΩ, were accepted.

The NIRI-sensor was attached in its center at O_Z. It covered an area of 1.8 cm below and above O_Z, and 1.2 cm in directions O_1 and O_2. The fNIRI-sensor was attached to the head with elastic bandages. Several shorter straps of these bandages were used to ensure the flexible fNIRI-sensor adapts to the form of the infant's head and has good contact to it. When all bandages were placed they covered the head

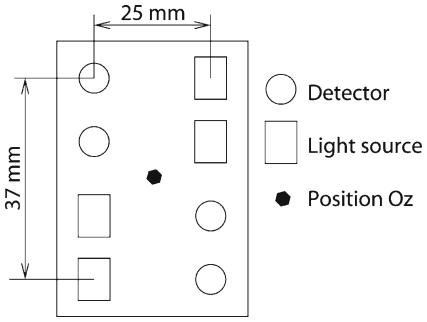

Fig. 17.1 fNIRI-sensor. Interoptode distances and alignment of light sources and detectors

in a cap-like order. This improved the electrode attachment to the skin. If after the experiment electrodes stuck firmly to the hair, almond oil was used to moisten the electrodes and hence facilitate detachment.

2.2 Instrumentation and Material

The continuous-wave NIRI-device "Multi-Channel-Photometer II" (MCP-II), an in-house development, was employed. Its configuration, used for the measurements described here, features the registration of 11 different light paths at three wavelengths with a sampling frequency of 100 Hz by time multiplexing. A more detailed description of the MCP-II has been published previously in ref. [3]. The light-sensor connected to the MCP-II is flexible, biocompatible, and easy to disinfect. It covers an area of 3.75 cm × 2.5 cm. The shortest interoptode distance is 1.25 cm, and the longest one is 3.75 cm. The sensor consists of four light sources, each composed of three LEDs (750, 800, and 875 nm) and four silicon-based detector diodes. The arrangement of the sources and detectors is shown in Fig. 17.1.

The device controlling the visual stimulation is designed as an extension to the MCP-II. It is configurable through software and provides several outputs which can be switched with a maximum frequency of 100 Hz. Here, only the LED-driver output (IC UDN2981A, 15 V_{cc}) was used to switch red LED arrays. The array of the high-luminance device contains eight high-intensity LEDs (dominate wavelength $\lambda = 660$ nm, 600 cd/m^2 at stimulation device). Duration of a flash for visual stimulation is set to 10 ms. The stimulation device is connected to the MCP-II and the EEG device. Each time a flash occurs an event marker is sent to both devices. To derive the partial EEG, the commercially available NicoletOne from VIASYS Healthcare Inc® is utilized. Its Tornado V44 amplifier records data with 2 kHz sampling frequency. The cutoff frequency of the high-pass filter is 0.01 Hz. Connected to the amplifier are Ambu® Blue Sensor NF electrodes. Those are single patient use, Ag/AgCl, solid gel, self-adhesive, and ECG foil electrodes. Major advantages are their thinness and the possibility to trim them to a size which enables location beneath the light-sensor.

2.3 Data Analysis

All algorithms used for analyzes were implemented in Matlab®. The NIRI device MCP-II provides raw values reflecting the change of light intensity per wavelength and light path over time. An algorithm converts the raw values into $\Delta[O_2Hb]$ and changes in deoxy-hemoglobin concentration (Δ[HHb]) based on the modified Beer–Lambert law [4] using extinction coefficients as given in [5] and the following DPFs extrapolated from data given in [6]: 4.714 at 750 nm, 4.249 at 800 nm, 3.5515 at 875 nm. The unfiltered $\Delta[O_2Hb]$ and Δ[HHb] traces undergo artifact reduction by the MARA approach [7]. Afterwards the artifact-reduced data are high- and low-pass filtered (high-pass: substraction of moving average filter, span 40 s; low-pass: least squares smoothing filter, 1 s frame size, first order). To determine whether an HR is present in the data of a subject, its 11 $\Delta[O_2Hb]$ channels are examined independently with a nonparametric test (Wilcoxon) for significant changes ($p<0.05$) during stimulus onset. Therefore, the data of the time interval from −6 s to stimulus onset and the interval from 8 to 14 s after the onset are paired for all stimulation periods and used for the statistical test. Raw data of the EEG device are processed for each channel independently. Data are low-pass filtered (100 Hz cutoff frequency, fifth-order FIR filter). Due to acceptance of high electrode-skin impedances and the nonshielded electromagnetic environment of measurement, 50 Hz pick-up can be considerable; notch filtering the data is unavoidable. Therefore, and to reduce electrical coupling of the fNIRI-sensor, data are notch-filtered at 50 and 100 Hz. Amplitudes exceeding a threshold of 200 μV are excluded from further processing. In the final step, time-triggered block-averages (TTBA) of stimulation events and TTBA of sham events during rest periods are displayed with their standard error mean. Since the existence of VEPs is simple to find, a computerized analysis of the TTBAs has not yet been implemented. Two persons screened the TTBA traces of channel O_Z independently for transients occurring before 500 ms after stimulus onset and exceeding in amplitude all other data within the given time window. Furthermore, the amplitude of the transient must exceed the amplitudes of the TTBA resulting from the sham stimulation events in the same time window. When these prerequisites were met, and a trace is defined by both persons as a VEP, the measurement is regarded as containing a response in EEG data.

3 Results

Examples of responses in EEG and fNIRI are shown in Figs. 17.2 and 17.3, respectively. In 73.3% of the subjects, VEPs could be detected. In contrast, significant HRs occurred in 46.7%. No HRs were detected without a corresponding VEP. When EEG data are taken as reference for whether stimulation was successful, the sensitivity of fNIRI increases to 63.6%. Seventy-five percent of the HRs are based on a rise of $\Delta[O_2Hb]$ after stimulation onset, while 25% are on a decrease.

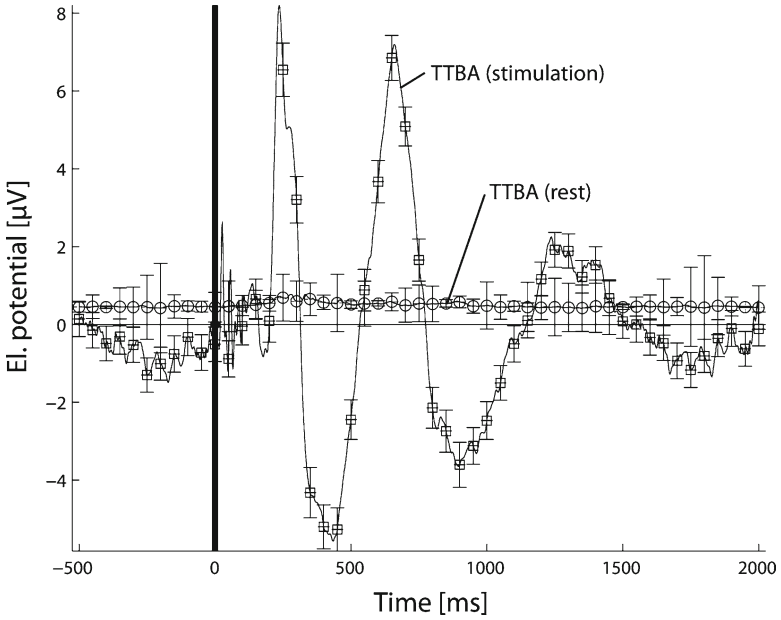

Fig. 17.2 TTBA (272 single events) of EEG's channel O_z. Error bars indicate standard error mean. Stimulus onset is at time 0 s. A clear difference between stimulation and rest periods is noticeable

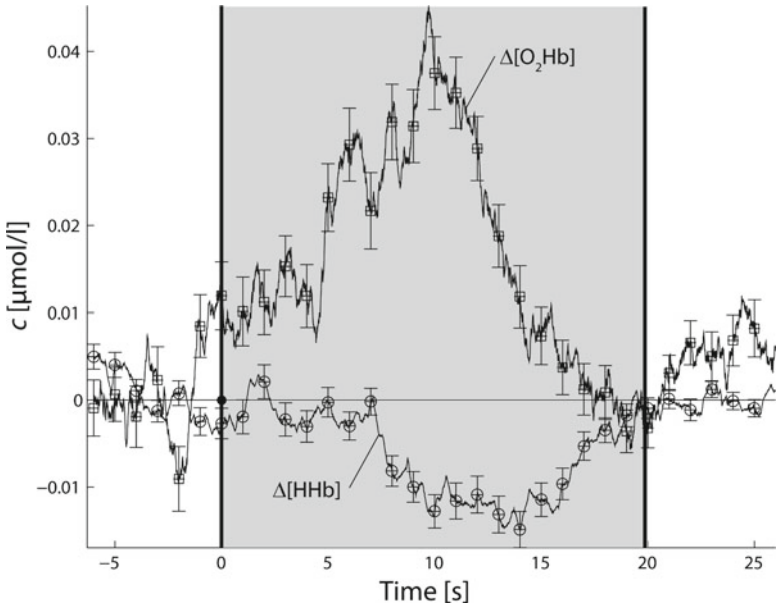

Fig. 17.3 HR of a single NIRI channel after TTBA over 30 stimulation periods. Error bars indicate standard error mean. *Gray* shaded area marks interval of stimulation

4 Discussion

As shown in this fNIRI study, the gain by the simultaneous EEG is worthwhile the effort. VEPs could be seen only in 73.3% of subjects; hence it must be considered that not each attempt of stimulation succeeds, and this raises the question of EEG sensitivity for VEP detection. The EEG sensitivity could be improved by better electrode-skin impedances. However, these high impedances were accepted in order not to wake up the infant by preparing more thoroughly the infant's skin. Consequence of high impedances was increased pick-up of electromagnetical interference, especially in nonshielded environments like the rooms the measurements were performed. Major contribution to the noise was the mains with their characteristic 50 Hz noise. Although the mains interference was attenuated by employing a notch filter during analysis, it could not be excluded completely that a VEP in the noise remained undetected and lead to a false-negative result of the analysis. By analyzing the EEG data by TTBA of the amplitudes during rest periods, the EEG analysis was more stringent than if only latency and amplitude of stimulation periods were determined. This, and most likely less luminance of the stimulation device, could contribute to our EEG sensitivity being smaller than 100% as reported by others [8].

The relatively low sensitivity of fNIRI, 46.7%, is based on all infants, but it increases to 63.6% when only the infants are considered which responded to the stimulation by VEP. The latter sensitivity seems reasonable, yet much higher numbers are reported in literature, as for example 100% by Hoshi et al. [9]. In contrast to their study, our procedure of stimulation differed widely from theirs [9] by stimulation frequency, the length and distribution of rest periods.

Another interesting circumstance is that, under the assumption of 100% sensitivity and selectivity of EEG analysis, there was no false-positive occurrence in fNIRI data.

5 Conclusions

An fNIRI-EEG set-up was developed and optimized by conducting more than 30 measurements with subjects. That followed successful measurement of 15 subjects without changes of the protocol. It was found that fNIRI sensitivity improved with higher luminance (600 cd/m^2) of the stimulation's light; 63.6% sensitivity was achieved. $\Delta[O_2Hb]$ increased in 75% and decreased in 25% of significant HRs detected by fNIRI.

Acknowledgments The authors gratefully acknowledge the funding of the Swiss National Science Foundation

References

1. Wolf M, Greisen G (2009) Advances in near-infrared spectroscopy to study the brain of the preterm and term neonate. Clin Perinatol 36:807–834
2. Jaspers HH (1958) Report of the committee on methods of clinical examination in electroencephalography. Electroen Clin Neuro 10:370–375
3. Haensse D, Szabo P, Brown D et al (2005) A new multichannel near infrared spectrophotometry system for functional studies of the brain in adults and neonates. Opt Express 13:4525–4538
4. Kocsis L, Herman P, Eke A (2006) The modified beer-lambert law revisited. Phys Med Biol 51:N91
5. http://www.medphys.ucl.ac.uk/research/borl/research/NIR_topics/spectra/spectra.htm
6. Cooper CE, Elwell CE, Meek JH et al (1996) The noninvasive measurement of absolute cerebral deoxyhemoglobin concentration and mean optical path length in the neonatal brain by second derivative near infrared spectroscopy. Pediatr Res 39:32–38
7. Scholkmann F, Spichtig S, Mühlemann T et al (2010) How to detect and reduce movement artifacts in near-infrared imaging using moving standard deviation and spline interpolation. Physiol Meas 31:649–662
8. Benavente I, Tamargo P, Tajada N et al (2005) Flash visually evoked potentials in the newborn and their maturation during the first six months of life. Doc Opthalmol 110:255–263
9. Hoshi Y, Kohri S, Matsumoto Y et al (2000) Hemodynamic responses to photic stimulation in neonates. Pediatr Neurol 23:323–237

Chapter 18
Use of a Hybrid Optical Spectrometer for the Measurement of Changes in Oxidized Cytochrome *c* Oxidase Concentration and Tissue Scattering During Functional Activation

Arnab Ghosh, Ilias Tachtsidis, Christina Kolyva, Chris E. Cooper, Martin Smith, and Clare E. Elwell

1 Introduction

Near-infrared spectroscopy (NIRS) is finding increasing utility in the investigation of functional activation, but in most cases its use is limited to the measurement of oxyhaemoglobin (HbO_2) and deoxyhaemoglobin (HHb) concentration. However, since the advent of NIRS, there has been great interest in the measurement of oxidized cytochrome *c* oxidase [oxCCO]. CCO is the terminal electron acceptor in the mitochondrial electron transport chain and change in its redox state has been suggested as a potential marker of cellular energy status. The NIRS measurement of [oxCCO] in the adult human brain, however, has posed a number of technical challenges [1], including concerns about the effect on the signal from possible changes in optical scattering. Nevertheless, a number of studies have reported the measurement of [oxCCO] within a number of contexts including during manipulation of cerebral oxygen delivery [2, 3] and in functional activation [4].

A. Ghosh
Neurosurgical Critical Care Unit, National Hospital for Neurology and Neurosurgery, University College London Hospitals, London, UK

I. Tachtsidis • C. Kolyva • C.E. Elwell (✉)
Biomedical Optics Research Laboratory, Department of Medical Physics and Bioengineering, University College London, Malet Place Engineering Building, London WC1E 6BT, UK
e-mail: celwell@medphys.ucl.ac.uk

C.E. Cooper
Department of Biological Sciences, University of Essex, Colchester, UK

M. Smith
Neurosurgical Critical Care Unit, National Hospital for Neurology and Neurosurgery, University College London Hospitals, London, UK

Biomedical Optics Research Laboratory, Department of Medical Physics and Bioengineering, University College London, Malet Place Engineering Building, London WC1E 6BT, UK

M. Wolf et al. (eds.), *Oxygen Transport to Tissue XXXIII*, Advances in Experimental Medicine and Biology 737, DOI 10.1007/978-1-4614-1566-4_18,

Anagram-solving has been shown by NIRS to evoke a bilateral frontal hemodynamic response consistent with functional activation, although these changes are associated with potentially confounding changes in systemic physiology [5, 6]. Whilst prior studies have shown an increase in [oxCCO] in response to visual activation [4], theoretical models suggest that either an increase or decrease in [oxCCO] could potentially occur [7].

The aims of this study are to use a hybrid optical spectrometer (pHOS) comprising a novel combination of broadband and frequency domain NIR systems [8] to investigate (1) the direction and magnitude of [oxCCO] change; (2) the change in optical scattering in the presence of a hemodynamic response consistent with functional activation of the frontal cortex during anagram-solving; and (3) the effects of the use of a novel algorithm utilizing DPF measured in real-time to scale chromophore concentration changes.

2 Methods

Eleven subjects (seven male, four female; age range 21–34 years) were studied. This study was approved by the UCL Ethics Committee and informed written consent was obtained from each subject. Optodes from the pHOS were affixed over the FP1 point bilaterally prior to the initiation of the anagram protocol, which was identical to that previously reported by our group [5, 6]. The protocol consisted of a 2-min baseline recording, followed by the presentation of six alternating 60-s blocks of four- and seven-letter anagrams, each with a single correct solution (e.g. DISEASE = SEASIDE), which the subjects were asked to solve. This was followed by a further 2-min baseline recording.

The pHOS has been described in detail elsewhere [8]. Briefly, it comprises two identical broadband spectrometers and a two-channel frequency domain spectrometer capable of absolute measurements of optical absorption and scattering at 690, 750, 790 and 850 nm. [HHb], [HbO_2], and [oxCCO] were calculated using the UCLn algorithm [9] by fitting to the changes in NIR attenuation from 740 to 860 nm using a 35 mm source–detector separation. The quantification of measured chromophore concentration changes was performed (1) using a constant DPF derived from measured optical absorption and scattering during the baseline period of recording and (2) using a variable DPF updated in real-time (using the DPF derived from optical absorption and scattering measured at 790 nm from the frequency domain component of the pHOS and applying additional correction factors for the wavelength dependence of pathlength). Other measurements included continuous blood pressure and heart rate (Portapres®, Finapres Medical Systems) and laser Doppler monitoring of frontal scalp blood flow (FloLab, Moor Instruments).

Two channels were recorded per subject. The resulting NIRS-derived data were post-processed by resampling to a sample period of 3 s, application of a linear detrending function and a fifth-order Butterworth filter with a 0.08 Hz cut-off (MatLab, Mathworks, USA).

Individual channels were tested for the presence of a hemodynamic response consistent with functional activation, i.e. an increase in $\Delta[HbO_2]$ and no increase in Δ[HHb] between baseline and activation windows. The baseline window was defined as the 60 s immediately prior to the onset of the anagram exercise; 60 s activation windows were then defined separately for $\Delta[HbO_2]$ and Δ[HHb] for each channel independently. This was achieved through the use of an automated algorithm scanning the $\Delta[HbO_2]$ signal following the beginning of the anagram exercise to identify the 60-s window of maximal increase and then scanning for the Δ[HHb] window, starting 57 s before and finishing 57 s after the $\Delta[HbO_2]$ activation window, to identify the maximal change in Δ[HHb]. The mean changes in $\Delta[HbO_2]$ and Δ[HHb] between baseline and activation windows were then compared using an unpaired *t*-test; channels that thus met the hemodynamic criteria detailed above – i.e., $p<0.05$ for $\Delta[HbO_2]>0$ and $p>0.05$ for $\Delta[HHb]>0$ – were retained for further analysis.

The Δ[oxCCO] change was identified using an algorithm that identified the 60 s window of maximal change in a fashion analogous to that used for Δ[HHb]. Using this time period for each channel, averages were calculated for optical scattering and systemic variables. Significance was then inferred using an unpaired *t*-test comparing baseline and activation windows, with a significance threshold of $p \leq 0.05$.

3 Results

A hemodynamic response consistent with functional activation was seen in 9 out of 11 subjects (13/22 channels); mean chromophore concentration changes for these channels are shown in Fig. 18.1 and Table 18.1. In this group of channels there was no significant change in [oxCCO], although every individual subject did show a statistically significant change in [oxCCO] between baseline and activation. Table 18.2 shows the magnitude of [oxCCO] change in two groups defined post-hoc by its direction. There was no significant change in optical scattering or mean arterial blood pressure (MAP) between baseline and activation, although there was a significant increase in both heart rate and laser Doppler (LD) flux.

Bland–Altman comparison between fixed DPF- and variable DPF-based algorithms revealed a high level of agreement in the chromophore concentrations derived using the two methods, as shown in Table 18.3.

4 Discussion

We have used a novel hybrid NIRS system to simultaneously measure hemodynamic, metabolic, and optical scattering changes during functional activation of the frontal cortex. Using a data analysis methodology designed to investigate [oxCCO] changes in the presence of a hemodynamic response consistent with functional

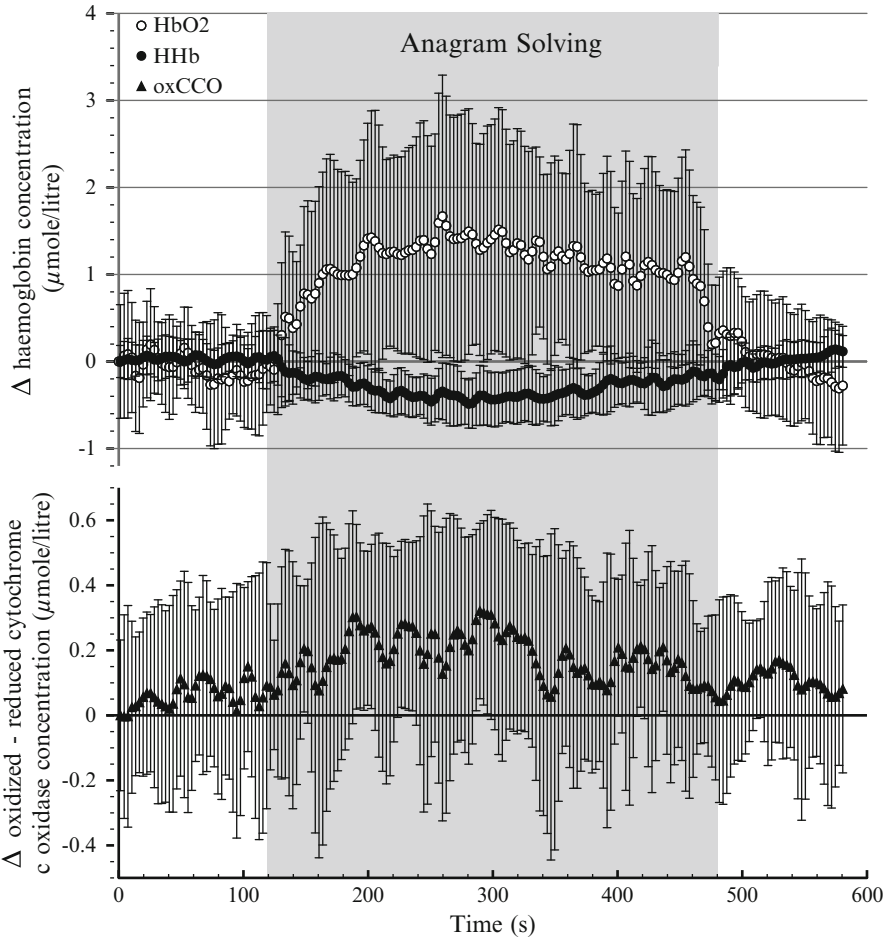

Fig. 18.1 Grouped data showing chromophore concentration (mean ± SD) using fixed DPF algorithm

Table 18.1 Changes in chromophore concentration, optical scattering and physiological parameters between baseline and activation windows

	Baseline (mean ± SD)	Activation (mean ± SD)	*p**
$\Delta[HbO_2]$ (μmol l^{-1})	0 ± 0.501	1.728 ± 1.292	0.001
Δ[HHb] (μmol l^{-1})	0 ± 0.178	−0.394 ± 0.268	0.00001
Δ[oxCCO] (μmol l^{-1})	0 ± 0.281	0.142 ± 0.383	0.3369
μs 690 nm (cm^{-1})	10.7 ± 2.31	11.1 ± 3.26	0.42
μs 750 nm (cm^{-1})	9.45 ± 2.46	9.81 ± 2.87	0.49
μs 790 nm (cm^{-1})	9.43 ± 1.76	9.54 ± 1.82	0.15
μs 850 nm (cm^{-1})	8.53 ± 1.91	8.28 ± 2.78	0.51
MAP (mmHg)	72.6 ± 35.5	73.5 ± 36.3	0.42
HR (bpm)	81.9 ± 38.2	88.5 ± 41.3	0.0042
ΔLD flux (% age change)	0 ± 20.9	41.94 ± 26.5	0.002

*Paired Students' *t*-test

Table 18.2 Changes in [oxCCO] divided by direction of change during functional activation

	No. of subjects	No. of channels	Baseline [oxCCO] (μmol l^{-1}; mean ± SD)	Activation [oxCCO] (μmol l^{-1}; mean ± SD)
Increase in [oxCCO]	7	8	0 ± 0.279	0.485 ± 0.317
Decrease in [oxCCO]	4	5	0 ± 0.136	–0.406 ± 0.145

Table 18.3 Bland–Altman analysis showing agreement between chromophore concentrations derived using constant DPF and variable DPF algorithms

Chromophore	Mean difference (95% limit of agreement)	
ΔHbO_2	0.0007551	(–0.0719–0.0734) μmol l^{-1}
ΔHHb	–0.0005352	(–0.0238–0.0227) μmol l^{-1}
ΔoxCCO	0.0009688	(–0.0252–0.0272) μmol l^{-1}

activation, we have demonstrated no significant change in the group data in either [oxCCO] or optical scattering, although significant changes in [oxCCO] were seen in each individual channel. Furthermore, we have demonstrated a high level of agreement between the conventional UCLn algorithm for broadband spectroscopy using a fixed DPF and a novel algorithm incorporating real-time measurements DPF derived from real-time measurements of optical scattering, in accordance with previous findings using the pHOS during a Valsalva maneuvre [10]. In agreement with previous studies [6], we have shown significant increases in heart rate and scalp blood flow during activation, but conflictingly not in MAP; this may be a consequence of our treatment of multiple channels from the same individual as independent variables.

Functional activation may cause an increase or decrease in [oxCCO] depending on the particular hemodynamic and metabolic circumstances present during activation [7]. However, mathematical modeling of brain metabolism suggests that an increase is the most likely outcome [11] and such an increase in [oxCCO] has been shown during passive visual stimulation [4]. Whilst our group data (as shown in Fig. 18.1) are suggestive of an increase in [oxCCO], it is of importance to note that there was a great deal of heterogeneity in our observed [oxCCO] response, with all subjects showing a statistically significant change – that is, increase or decrease – in [oxCCO] between baseline and activation windows, with changes in both directions occurring in the presence of similar hemodynamic changes. There are many potential explanations for this heterogeneity some of which maybe related to the optical measurement of [oxCCO], variations in underlying functional anatomy and differences in individuals' metabolic responses to the activation task. Further analysis is underway to investigate the possible confounds in the optical measurement of [oxCCO] during functional activation, for example, the choice of source–detector separation, which may affect depth sensitivity. In addition to the development of further algorithms utilizing the data from the pHOS we are also using a mathematical model of cerebral physiology [11] to aid the interpretation of the observed responses

in each individual. This may improve our understanding of the confounds involved in the optical measurement of the metabolic consequences of functional activation.

Acknowledgements This work was undertaken at University College London Hospitals and partially funded by the Department of Health's National Institute for Health Research Centres funding scheme. This research was supported by MRC program grant G0701458 and EPSRC grant EP/D0609821/1. IT is supported by Wellcome Trust grant 088429/Z/09/Z.

References

1. Cooper CE, Cope M, Quaresima V et al (1997) Measurement of cytochrome oxidase redox state by near infrared spectroscopy. Adv Exp Med Biol 413:63–73
2. Tisdall MM, Tachtsidis I, Leung TS et al (2007) Near-infrared spectroscopic quantification of changes in the concentration of oxidized cytochrome c oxidase in the healthy human brain during hypoxemia. J Biomed Opt 12:24002
3. Tachtsidis I, Tisdall MM, Leung TS et al (2009) Relationship between brain tissue haemodynamics, oxygenation and metabolism in the healthy human adult brain during hyperoxia and hypercapnea. Adv Exp Med Biol 645:315–320
4. Heekeren HR, Kohl M, Obrig H et al (1999) Noninvasive assessment of changes in cytochrome-c oxidase oxidation in human subjects during visual stimulation. J Cereb Blood Flow Metab 19:592–603
5. Tachtsidis I, Leung T, Devoto L et al (2008) Measurement of frontal lobe functional activation and related systemic effects: a near-infrared spectroscopy investigation. Adv Exp Med Biol 614:397–403
6. Tachtsidis I, Leung TS, Tisdall MM et al (2008) Investigation of frontal cortex, motor cortex and systemic haemodynamic changes during anagram solving. Adv Exp Med Biol 614: 21–28
7. Banaji M (2006) A generic model of electron transport in mitochondria. J Theor Biol 243: 501–516
8. Tachtsidis I, Leung TS, Elwell CE et al. (2010) Multi-Wavelength, Depth Resolved, Scattering and Pathlength Corrected in vivo Near-Infrared Spectroscopy of Brain Tissue. Optical Society of America Biomedical Optics (BIOMED) BTuB, Miami, Florida, 11 April 2010
9. Matcher SJ, Elwell CE, Cooper CE et al (1995) Performance comparison of several published tissue near-infrared spectroscopy algorithms. Anal Biochem 227:54–68
10. Gao L, Elwell C, Kohl-Bareis M et al (2010) Effects of assuming constant optical scattering on haemoglobin concentration measurements using NIRS during a Valsalva Manoeuvre. Adv Exp Med Biol 915:15–20
11. Banaji M, Mallet A, Elwell C et al (2008) A model of brain circulation and metabolism: NIRS signal changes during physiological challenges. PLoS Comput Biol 4:e1000212

Part II
Tumor Oxygenation

Chapter 19
Isolated Hypoxic Liver Perfusion with Melfalan in Humans and Its Anesthesiologic Aspects

J.B. van den Bosch, C. Verhoef, F.L. Teng-van de Zande, J. Bakker, W. Erdmann, and R. Tenbrinck

1 Introduction

Colorectal carcinoma has a poor prognosis, especially if hepatic metastases are already present. Occurrence in the Netherlands is approximately 8000–9000 persons per year [1]. The natural course of multiple liver metastases has a median survival of only 3–6 months, with a survival of 1–2 years with solitary metachronous hepatic metastases. Resection is still the optimal treatment but, due to tumor location near the great vessels or spread in multiple liver segments, it is only possible in about 20% of the patients [2]. Control of hepatic metastases implies improved overall survival and justifies aggressive palliative treatment modalities.

IHHP is aimed at gaining control of tumor progression. Its goal is to provide maximum palliative comfort for the patient and extend the duration and quality of life. IHHP means complete isolation of the hepatic vasculature and enables simultaneous

J.B. van den Bosch (✉)
Department of Anesthesiology, Erasmus Medical Center Rotterdam, 's Gravendijkwal 230, 3015 Rotterdam, The Netherlands

Department of Intensive Care Medicine, Erasmus Medical Center Rotterdam, 's Gravendijkwal 230, 3015 Rotterdam, The Netherlands
e-mail: j.b.vandenbosch@erasmusmc.nl

C. Verhoef
Department of Surgical Oncology, Erasmus Medical Center Rotterdam, 's Gravendijkwal 230, 3015 Rotterdam, The Netherlands

F.L. Teng-van de Zande • W. Erdmann • R. Tenbrinck
Department of Anesthesiology, Erasmus Medical Center Rotterdam, 's Gravendijkwal 230, 3015 Rotterdam, The Netherlands

J. Bakker
Department of Intensive Care Medicine, Erasmus Medical Center Rotterdam, 's Gravendijkwal 230, 3015 Rotterdam, The Netherlands

M. Wolf et al. (eds.), *Oxygen Transport to Tissue XXXIII*, Advances in Experimental Medicine and Biology 737, DOI 10.1007/978-1-4614-1566-4_19,

administration of high-dose chemotherapy (melfalan) by perfusion [3]. During IHHP, there is full clamping of the caval vein and aorta just beneath the diaphragm (C1). After completion of the perfusion and subsequent release of both clamps, abdominal reperfusion (AR) follows. We examined hemodynamic and metabolic changes during the IHHP procedure in 22 patients with metastases in the liver during the period 2002–2009. This is the first description from the anesthesiologic viewpoint during this technically complicated procedure.

2 Materials and Methods

A radical resection of the primary tumor was performed in all patients before entering the study protocol. Hepatic tumor size should be less than 50% of the total liver volume to prevent massive necrosis in case of a response. All patients were evaluated by computed tomography (CT) scan of the thorax and abdomen before operation. All patients had a Karnofsky performance score of at least 90, liver enzymes (ALT, AST, and AF) not higher than 5× the normal values, and bilirubin not higher than 2× the normal values.

Exclusion criteria included age less than 18 or above 75 years, signs of portal hypertension, significant central nervous system disease, significant cardiovascular, pulmonary, or renal disease, uncontrolled infection(s), presence of organ grafts and chemotherapy or radiotherapy within 4 weeks before IHHP. Angiography was routinely performed to exclude aberrant hepatic arteries or to visualize other anatomic anomalies. Patients with severe arteriosclerosis of the aortic, iliac, or femoral vessels were also excluded.

All IHHPs were performed at the Erasmus University Medical Center, Daniel den Hoed Cancer Center. The study protocol was approved by the Medical Ethical Committee of the Erasmus Medical Center, and written informed consent was obtained from all patients.

A dosage of 1 mg/kg melfalan (Alkeran; Wellcome Ltd., London, UK) was used in all patients and infused through a sideline into the perfusion circuit. The perfusate was circulated by a constant flow. Stable perfusion was monitored by pressure measurement and the perfusate level in the bubble trap. Methylene blue was injected into the arterial catheter to check homogeneous distribution over both lobes of the liver. Perfusion of melfalan took place over a 20-min period. After 20 min, a washout procedure was performed by using 1 l of Hemaccel to collect the venous effluent. Total liver ischemia time never exceeded 60 min. The isolation was terminated by release of the vascular clamps, tension-guided, and closing of the (de)-canulated vessels. During IHHP, potential drug leakage was monitored by using a radioactive tracer. A small calibration dose of human serum albumin, radiolabeled with iodine-131, was injected into the systemic circulation before the perfusion, and a tenfold higher dose of the same isotope was injected into the IHHP circuit. Continuous monitoring was performed with a precordial scintillation probe.

All anesthetic procedures were conducted by anesthesiologists familiar with the procedures at our hospital and in conformance with the standard of the American Society of Anesthesiologists.

A Foley catheter was inserted and fluid warmers and air blankets were used. In addition to recording routine monitor measurements, mean arterial pressure (MAP), heart rate (HR), central venous pressure (CVP), temperature, and acid–base profile were measured. We established baseline values at the steady-state (SS) phase, after induction of general anesthesia, and during the preparation phase of surgery: i.e. after clamping of the aortic artery and caval vein (C1), during hepatic perfusion and after completion of hemofiltration (P), after abdominal reperfusion (AR), and upon arrival at the postanesthesia care unit (PACU). Oxygen consumption (VO_2) was measured in three patients only using the PhysioFlex anesthesia machine. Anesthesiologists were allowed to select anesthetics judged most appropriate after evaluation of the preoperative data. All patients underwent IHHP under general anesthesia with or without epidural analgesia. For induction we used propofol, sufentanyl and cisatracurium or rocuronium. Anesthesia was maintained with volatile anesthetics or a propofol TCI-perfusor, sufentanyl. A bispectral index system (BIS) [4] monitor (Aspect Medical Systems, de Meern, the Netherlands) was attached to the patient to establish anesthetic depth, with a target between 35 and 47. Ventilation was pressure-controlled with a target end tidal CO_2 between 4.5 and 5.5 kPa, controlled by taking arterial blood samples. For the first eight patients, in anticipation of inferior caval vene occlusion, on average, 2000–3000 ml of crystalloids were administered prior to clamping. No epidural analgesia was given in this group. For the following 14 patients the fluid regimen was changed to a more restricted one with minimum fluids, and all patients received a thoracic epidural. At abdominal reperfusion, mannitol (Baxter B.V., Utrecht, the Netherlands) 0.25 g/kg was given intravenously. After completion of IHHP, the endotracheal tube was removed in the operation room as soon as possible.

3 Results

Of the 22 patients [13 male and 9 female; with a mean age of 63 years (range 41–70 years), height 175 cm and weight 74 kg], 16 patients had irresectable colorectal liver metastases, four had ocular melanoma hepatic metastases, and one had a sarcoma, and one an unknown primary tumor.

The mean total ischemia time (C1 until AR) was 54.5 min; average blood loss was 826 ml, obviously less in the patients after revision of the anesthetic technique to restrictive fluid regimen. The MAP at C1 versus SS increased 10.6%; after AR 1.8%. The HR increased at C1 7.8% and after AR 27.6%. Compared to SS, VO_2 dropped 30% after C1 and increased 40% after AR (Fig. 19.1). All patients were observed for one night at the PACU. Changes in hemodynamics or core temperature, during C1, AR or at the PACU, were treated by infusion of crystalloid solutions or by administering vasoactive drugs (fenylefrine and dobutamine). These drugs were

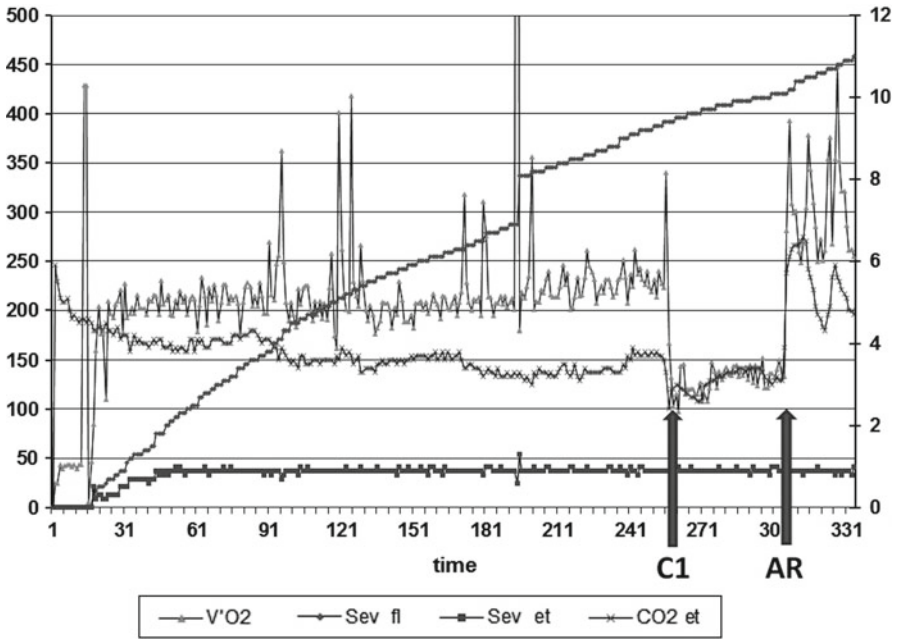

Fig. 19.1 Changes over time of the clamping and release phase. *C1* clamping of aortic artery and caval vene, *AR* abdominal reperfusion, $V'O_2$ oxygen consumption (ml/min), *Sev fl* sevoflurane consumption (ml), *Sev et* sevoflurane end tidal concentration (vol%), CO_2 *et* CO_2 end tidal concentration (vol%)

titrated to keep MAP above 60 mmHg. There were no perioperative deaths during this entire study. In 10% of the procedures, patients complained of postoperative nausea and/or vomiting and required treatment with more than one antiemetic. Patients were discharged (median) 9 days after the procedure and resumed their normal daily activities within 2–3 weeks.

There were no anesthesia-related complications except for one patient who had significant nasal bleeding after nasal placement of a temperature probe. No cardiac, gastrointestinal, spinal cord, or nephrologic complications were noted in these procedures. The increase in serum creatinine the first day postoperatively was (median) 24%, but all patients normalized to preoperation levels in the subsequent days. Of all patients, 75% had a stable to reduced tumor size after IHHP with a median time to progression of 9 months.

4 Discussion

IHHP seems to meet the criteria for palliative treatment despites its complex technique and possible major perioperative metabolic and hemodynamic changes. The full clamping and hypoxic period – lasting average of 54 min – of the abdominal

compartment is well tolerated in this population. Only a small temporarily increase in serum creatinine is observed, in all patients there is full recovery of kidney function to preoperative conditions. Hofland et al. [5] described serious hemodynamic changes occurring during simultaneous occlusion of the thoracic aorta and inferior vena cava. Although we do not have a total explanation for these differences, our study differs from that of Hofland by the use of full clamping instead of occlusion by balloon catheters. Leakage of blood to the hypoxic area and subsequent increase of free radicals and increased hemodynamic instability may occur. In the present study, release of the clamps is slow and tension-guided, which is easier performed by means of clamp release than by (blind) deflation of a balloon catheter. Communication between an experienced team of anesthesiologist and surgeon is vital. Unfortunately, no *trans*-esophageal echocardiography was available to study cardiac abnormalities during the C1, P or AR phase. The choice between propofol and isoflurane seems to have a minimal influence on the right ventricle ejection fraction during orthotopic liver transplantation (OLT), which followed similar trends irrespective of the anesthetic technique [6, 7]. Positive end-expiratory pressure in mechanical ventilation of up to 15 cm H_2O does not impair liver outflow or systemic hemodynamics in OLT [8]. These results can be considered to be equal to our population and relate to our findings. With the clamping of the aorta in the thoracolumbar region, the artery of Adamkiewicz, which may be located between levels T9 and L2 and supplying the ventral part of the lower spinal cord, could be jeopardized resulting in potential spinal cord injury. Since we found no cardiac, nephrologic, gastrointestinal or spinal cord injury, some protection mechanism must be active. A beneficial effect of volatile anesthetics might be involved, as described by Tritapepe et al. [9] in cardiac precondition with sevoflurane. Ischemic preconditioning (IPC), defined as a brief period of liver ischemia followed by reperfusion, has demonstrated protection against a prolonged ischemia/reperfusion injury and improved the capacity of regeneration. IPC plays an essential role in hepatectomy before and after harvest of living donor liver and implantation of liver graft [10]. The use of thoracic epidural analgesia reduces opiate use, mortality, and pulmonary complications. In animal models and in a retrospective study, a positive trend was noted toward better outcome in tumor surgery when a thoracic epidural analgesia was used [11].

In future, we have to find other surgical applications of this relatively safe technique as is proved in this study that might help to prevent procedural perioperative damage.

5 Conclusions

This treatment for irresectable liver metastases can be safely performed by an experienced team of surgeon and anesthesiologist. Despite the severe physiologic changes the IHHP procedure fulfills the criteria for palliative treatment very well, so more research is needed to explore new applications of simultaneous clamping.

References

1. Siesling S, van Dijck JA et al (2003) Trends in incidence of and mortality from cancer in the Netherlands in the period 1989–1998. Working group of the Netherlands cancer registry. Eur J Cancer 39(17):2521–2530
2. Penna C, Nordlinger B (2002) Surgery of liver metastases from colorectal cancer new promises. Br Med Bull 64:127–140
3. Verhoef C, De Wilt et al (2008) Isolated hypoxic hepatic perfusion with retrograde outflow in patients with irresectable liver metastases; a new simplified technique in isolated hepatic perfusion. Ann Surg Oncol 15(5):1367–1374
4. Aniset L, Knitschke R, Frietsch T (2010) Narkosetiefenmessung in der anästhesie. Anasthesiol Intensivmed Notfallmed Schmerzther 45:230–237
5. Hofland J, Tenbrinck R et al (2002) Cardiovascular effects of simultaneous occlusion of the inferior vena cava and aorta in patients treated with hypoxic abdominal perfusion for chemotherapy. Br J Anaesth 88(2):193–198
6. Gouvêa G, Diaz R et al (2010) Right ventricular ejection fraction during orthotopic liver transplantation: Does anesthetic technique make a difference? J Crit Care 25(4):657.e1–657.e6
7. Zheng SS et al (2002) Functional changes of the heart and lung in perioperative period of orthotopic liver transplantation. Hepatobiliary Pancreat Dis Int 1:335–339
8. Saner FH et al (2010) How far can we go with positive end-expiratory pressure (PEEP) in liver transplant patients? J Clin Anesth 22:104–109
9. Tritapepe L, Landoni G, Guarracino F et al (2007) Cardiac protection by volatile anaesthetics: a multicentre randomized controlled study in patients undergoing coronary artery bypass grafting with cardiopulmonary bypass. Eur J Anaesthesiol 24:323–331
10. Yan S et al (2010) Outcomes and mechanisms of ischemic preconditioning in liver transplantation. Hepatobiliary Pancreat Dis Int 9:346–354
11. Gottschalk A (2010) Perioperative organprotektion – regionalanästhesie: Die rolle der thorakalen epiduralanästhesie. Anasthesiol Intensivmed Notfallmed Schmerzther 45:264–269

Chapter 20
Blood Flow and Oxygenation Status of Gastrointestinal Tumors

Peter Vaupel and Debra K. Kelleher

1 Introduction

Tumor hypoxia is a major driving force for malignant progression since it can promote local invasion of cancer cells and metastatic spread to distant sites [1–7]. Tumor hypoxia also plays a key role in the development of acquired treatment resistance since it is capable of directly and/or indirectly conferring resistance to therapy [8, 9]. As a result, hypoxia has been shown to act as an independent, adverse prognostic factor [10–14]. Due to this seminal role of tumor hypoxia, knowledge concerning the oxygenation status of malignant tumors in terms of O_2 tension distributions and detection of hypoxia are indispensable in the clinical setting. For this reason, the respective oxygenation status for gastrointestinal (GI) malignancies have been compiled in this review, together with blood flow values (where available), which are major determinants of the oxygen status. Pretherapeutic data of the following tumor entities will be presented: Cancers of the stomach, gallbladder, common bile duct, pancreas, colon, rectum, and primary and metastatic liver tumors.

P. Vaupel (✉)
Tumor Pathophysiology Division, Department of Radiooncology and Radiotherapy, University Medical Center, Langenbeckstrasse 1, 55131, Mainz, Germany

Department of Radiotherapy and Radiooncology, Klinikum rechts der Isar, Technische Universität München, Ismaninger Strasse 22, 81675, München, Germany
e-mail: vaupel@uni-mainz.de

D.K. Kelleher
Institute of Functional and Clinical Anatomy, University Medical Center, Johannes-Joachim-Becher-Weg 13, 55128, Mainz, Germany

M. Wolf et al. (eds.), *Oxygen Transport to Tissue XXXIII*, Advances in Experimental Medicine and Biology 737, DOI 10.1007/978-1-4614-1566-4_20,

2 Blood Flow and Oxygenation Status of Gastrointestinal Cancers

The incidence of GI tract cancers in Central Europe in 2006 was 25% in men and 24% in women (leading GI tract cancer: colorectal, approx. 16%). Due to the relatively high incidence of gastrointestinal cancers, knowledge of their oxygenation status is of great importance. For this reason, data on tumor blood flow and the oxygenation status which have been collected over the past 25 years will be presented.

2.1 Blood Flow in Gastrointestinal Tumors

Current knowledge of blood flow values of GI tumors is summarized in Table 20.1. There is clear evidence that cancers of the pancreas, liver, colon and rectum have, on average, a lower blood flow rate (in ml/ml/min or ml/g/min, depending on the method of measurement used) than their normal tissue of origin (see Table 20.2).

Table 20.1 Blood flow of gastrointestinal tumors

Tissue	Method	Blood flow (ml/ml/min)[a]	References
Benign pancreatic tumors	$H_2{}^{15}O$-PET	0.59 ± 0.27	[15]
Malignant pancreatic tumors		0.46 ± 0.18 (0.13–0.81)[b]	
Primary liver cancers	Data review	0.03–0.25	[2]
Metastatic liver tumors		0.06–0.90	
Colon cancer	Venous outflow	0.43 ± 0.05 (0.14 – 0.81)[b]	[16]
	Venous outflow	0.57 ± 0.26	[17]
	Data review	0.018–0.20	[2]
Primary rectal cancer	MRI	Therapy-responders 0.075 ± 0.015 (0.051–0.10)[b]	[18]
		Non-responders 0.107 ± 0.027 (0.068–0.10)[b]	
Primary and recurrent rectal cancers	Temperature–time curves	0.09	[19]
		0.07	
Primary and recurrent rectal cancers	$H_2{}^{15}O$-PET	0.36 ± 0.19	[20]
		0.37 ± 0.18	[21]

[a]Or ml/g/min, depending on the method used
[b]Range of blood flow values given in parentheses

Table 20.2 Blood flow of normal tissue of the gastrointestinal tract

Tissue	Method	Blood flow (ml/ml/min)	Reference
Pancreas	$H_2{}^{15}O$-PET	1.14 ± 0.48	[15]
Liver	Data review	1.00–1.10	[2]
Colon	Data review	Approx. 0.5	[2]
Rectum	Data review	0.4–0.5	[2]

In *pancreatic tumors*, blood flow is significantly lower than in the normal pancreas (normal tissue versus benign tumors: $p = 0.012$, and normal tissue versus pancreatic cancers: $p < 0.01$). In general, perfusion in *primary and metastatic liver tumors* is lower than in normal liver tissue.

Using a venous outflow technique, blood flow through *colon cancers* was found to be substantially higher than in reports published later [2, 16, 17]. Data reported using the outflow technique are similar to those described for normal colon mucosa [2]. This may hint to a technical bias, indicating possible venous blood collection from both normal colon and from cancer tissues.

Blood flow values for *rectal cancers* in absolute terms may also be biased by technological problems depending on the method used. Data published by the same group clearly show that tumor perfusion assessment using temperature–time curves during regional hyperthermia treatment and $H_2{}^{15}O$-PET can differ by a factor of approx. 5 at the same location within a given tumor [19–21]. Unexpectedly, blood flow values in therapy-responders were approx. 40% lower than in non-responders. Higher perfusion levels in the non-responding group were explained by substantial arterio-venous shunt flow or increased angiogenic activity in aggressive tumor cell clusters [18].

2.2 Pretherapeutic Oxygenation Status of Gastrointestinal Cancers

The first systematic studies on the pretherapeutic oxygenation status of gastrointestinal cancers have been published by Wendling et al. in 1984 [22]. Using a cryospectrophotometric ex vivo microtechnique allowing for the measurement of oxyhemoglobin (HbO_2) saturation of individual red blood cells in tumor micro-vessels, we could show that the mean HbO_2 values observed in rectal cancers were distinctly lower than those found in the normal mucosa at the site of tumor growth. There was considerable intra- and inter-tumor heterogeneity with steep local gradients in the oxygenation. The medians of the HbO_2 frequency distributions of the normal rectal mucosa and of cancers of stage Dukes B decreased from around 80 sat.% to 46 sat.%, indicating substantial hypoxia in the cancer specimens investigated [22].

In a case report, Endrich [23] studied the oxygenation status of superficial tissue layers of a gastric cancer using O_2 surface polarography. Using this direct technique, there was again a tremendous shift of the mean pO_2 values from approx. 50 mmHg in duodenal and antral mucosa to 20 mmHg in superficial cancer layers.

Clinical investigations carried out over the last 15 years using the Eppendorf histography system [24] have clearly shown that the prevalence of hypoxic tissue areas is a characteristic property of locally advanced solid tumors of the gastrointestinal tract (see Table 20.3). In all studies, poor and heterogeneous oxygenation was found in primary and metastatic lesions compared to the respective normal tissue (see Table 20.4).

In recurrent and metastatic rectal cancers, the oxygenation status seems to be even poorer than in the primary lesions [26–28]. The lowest pO_2 values were found in pancreatic cancers and in cancers of the biliary system [30], although the number of tumors investigated so far does not allow a detailed analysis in the latter tumor entities.

Table 20.3 Pretherapeutic oxygenation status of gastrointestinal cancers

Tumor type	*n*	Median pO_2 (mmHg)	HF 2.5 (%)	HF 5 (%)	HF 10 (%)	References
Gastric cancer (superficial)	1	≈20	n.a.	≈7	≈23	[23]
Primary rectal cancers	14	32	n.a.	10	n.a.	[25, 26]
	15	19				[27]
Recurrent rectal cancers	5	8	7	35	55	[28]
Liver metastases of rectal cancer	5	8	7	35	55	[25, 26]
	4	6	n.a.	45	75	
Pancreatic cancers	7	2	59	n.a.	n.a.	[29]
	1	2	n.a.	98	98	[30]
Gall bladder cancer	1	4	n.a.	95	100	[30]
Bile duct cancer	1	8	n.a.	n.a.	72	[30]

n number of patients, *n.a.* data not available
HF 2.5 = fraction of measured pO_2 values ≤ 2.5 mmHg, HF 5 = fraction of measured pO_2 values ≤ 5 mmHg, HF 10 = fraction of measured pO_2 values ≤ 10 mmHg

Table 20.4 Oxygenation status of normal tissues of the gastrointestinal tract (for abbreviations see Table 20.3)

Tissue	*n*	Median pO_2 (mmHg)	HF 2.5 (%)	HF 5 (%)	HF 10 (%)	Reference
Antral and duodenal mucosa	1	≈50	0	0	0	[23]
Rectal mucosa	15	52				[25]
Liver	14	30		5		[26]
Pancreas	7	57	2	n.a.	n.a.	[30]

3 Conclusions

Blood flow values measured in gastrointestinal tumors do not deviate from those of other tumor entities. Perfusion data at the same location in rectal cancers can differ by a factor of 5 depending on the method used. Thus flow values in absolute terms may be biased by technological problems.

Hypoxia is a characteristic of locally advanced tumors of the GI tract. In general, the extent, severity and heterogeneity of hypoxia in GI cancers do not deviate from that of other tumor entities [2]. Cancers of the pancreato-biliary system may be the most hypoxic tumors investigated so far. Hypoxia may contribute to malignant progression and acquired treatment resistance in gastrointestinal tract malignancies, especially in the latter tumor entities.

Acknowledgments This work has been supported by a grant from the Deutsche Krebshilfe (106758).

References

1. Vaupel P, Harrison L (2004) Tumor hypoxia: causative factors, compensatory mechanisms, and cellular response. Oncologist 9:4–9
2. Vaupel P (2009) Pathophysiology of tumors. In: Molls M, Vaupel P, Nieder C et al (eds) The impact of tumor biology on cancer treatment and multidisciplinary strategies. Springer, Berlin, pp 51–92
3. Vaupel P (2004) Tumor microenvironmental physiology and its implications for radiation oncology. Semin Radiat Oncol 14:198–206
4. Vaupel P (2004) The role of hypoxia-induced factors in tumor progression. Oncologist 9:10–17
5. Vaupel P, Mayer A (2007) Hypoxia in cancer: significance and impact on clinical outcome. Cancer Metastasis Rev 26:225–239
6. Vaupel P, Mayer A, Hoeckel M (2004) Tumor hypoxia and malignant progression. Methods Enzymol 381:335–354
7. Hoeckel M, Vaupel P (2001) Tumor hypoxia: definitions and current clinical, biologic, and molecular aspects. J Natl Cancer Inst 93:266–276
8. Vaupel P (2009) Physiological mechanisms of treatment resistance. In: Molls M, Vaupel P, Nieder C et al (eds) The impact of tumor biology on cancer treatment and multidisciplinary strategies. Springer, Berlin, pp 273–290
9. Vaupel P (2008) Hypoxia and aggressive tumor phenotype: implications for therapy and prognosis. Oncologist 13(Suppl 3):21–36
10. Hoeckel M, Knoop C, Schlenger K et al (1993) Intra-tumoral pO_2 predicts survival in advanced cancer of the uterine cervix. Radiother Oncol 26:45–50
11. Hoeckel M, Schlenger K, Aral B et al (1996) Association between tumor hypoxia and malignant progression in advanced cancer of the uterine cervix. Cancer Res 56:4509–4515
12. Brizel DM, Scully SP, Harrelson JM et al (1996) Tumor oxygenation predicts for the likelihood of distant metastases in human soft tissue sarcoma. Cancer Res 56:941–943
13. Fyles A, Milosevic M, Wong R et al (1998) Oxygenation predicts radiation response and survival in patients with cervix cancer. Radiother Oncol 48:149–156
14. Nordsmark M, Overgaard M, Overgaard J (1996) Pretreatment oxygenation predicts radiation response in advanced squamous cell carcinoma of the head and neck. Radiother Oncol 41:31–39
15. Komar G, Kauhanen S, Liukko K et al (2009) Decreased blood flow with increased metabolic activity: a novel sign of pancreatic tumor aggressiveness. Clin Cancer Res 15:5511–5517
16. Holm E, Hagmueller E, Staedt U et al (1995) Substrate balances across colonic carcinomas in humans. Cancer Res 55:1373–1378
17. Hagmueller E, Kollmar HB, Guenther H-J et al (1995) Protein metabolism in human colon carcinomas: in vivo investigations using a modified tracer technique with L-[1-^{13}C]leucine. Cancer Res 55:1160–1167
18. DeVries AF, Kremser C, Hein PA et al (2003) Tumor microcirculation and diffusion predict therapy outcome for primary rectal carcinoma. Int J Radiat Oncol Biol Phys 56:958–965
19. Rau B, Wust P, Tilly W (2000) Preoperative radiochemotherapy in locally advanced or recurrent rectal cancer: regional radiofrequency hyperthermia correlates with clinical parameters. Int J Radiat Oncol Biol Phys 48:381–391
20. Luedemann L, Sreenivasa G, Amthauer H et al (2009) Use of $H_2{}^{15}O$-PET for investigating perfusion changes in pelvic tumors due to regional hyperthermia. Int J Hyperthermia 25:299–308
21. Cho C-H, Sreenivasa G, Plotkin M et al (2010) Tumour perfusion assessment during regional hyperthermia treatment: comparison of temperature probe measurement with $H_2{}^{15}O$-PET perfusion. Int J Hyperthermia 26:404–411
22. Wendling P, Manz R, Thews G et al (1984) Heterogeneous oxygenation of rectal carcinomas in humans: a critical parameter for preoperative irradiation. Adv Exp Med Biol 180:293–300

23. Endrich B (1988) Hyperthermie und mikrozirkulation. Contr Oncol 31:1–138
24. Vaupel P, Hoeckel M, Mayer A (2007) Detection and characterization of tumor hypoxia using pO_2 histography. Antioxid Redox Signal 9:1221–1235
25. Kallinowski F, Buhr HJ (1995) Can oxygenation status of rectal carcinomas be improved by hyperoxia? In: Vaupel P, Kelleher DK, Guenderoth M (eds) Tumor oxygenation. Fischer, New York, pp 291–296
26. Kallinowski F, Buhr HJ (1995) Tissue oxygenation of primary, metastatic and xenografted rectal cancers. In: Vaupel P, Kelleher DK, Guenderoth M (eds) Tumor oxygenation. Fischer, New York, pp 205–209
27. Mattern J, Kallinowski F, Herfarth C et al (1996) Association of resistance-related protein expression with poor vascularization and low levels of oxygen in human rectal cancer. Int J Cancer 67:20–23
28. Feldmann HJ, Molls M, Auberger T et al (1995) Oxygenation and perfusion status of recurrent human tumors. In: Vaupel P, Kelleher DK, Guenderoth M (eds) Tumor oxygenation. Fischer, New York, pp 319–326
29. Koong AC, Mehta VK, Le QT et al (2000) Pancreatic tumors show high levels of hypoxia. Int J Radiat Oncol Biol Phys 48:919–922
30. Graffman S, Bjoerk P, Ederoth P et al (2001) Polarographic pO_2 measurements of intra-abdominal adenocarcinoma in connection with intraoperative radiotherapy before and after change of oxygen concentration of anaesthetic gases. Acta Oncol 40:105–107

Chapter 21
Delayed Effects of Radiation on Mitochondrial DNA in Radiation-Sensitive Organs

Steven B. Zhang, Mei Zhang, Yongbing Cao, Shanmin Yang, Amy P. Zhang, Liangjie Yin, Yeping Tian, Kuzhong Zhang, Yangsong Guo, Xiaohui Wang, Chun Chen, Jun Ma, Deping Han, Alexandra Litvinchuk, Steven Swarts, Sadasivan Vidyasagar, David Maguire, Lurong Zhang, and Paul Okunieff

Introduction

Ionizing radiation (IR) can lead to DNA damage by direct interaction with DNA or through the formation of hydroxyl (OH) radicals. Direct damage is expected to occur with similar frequency in both nuclear and mitochondrial cytoplasmic DNA. While DNA repair can be extremely efficient in the nucleus, double-stranded DNA repair in the cytoplasmic compartment is minimal. mtDNA must function normally throughout a cell's life and produce new mitochondria with operative reduction–oxidation reactions (redox).

In a previous study, we suggested that late-radiation damage in tissues, including muscular atrophy, neurocognitive changes, and fatigue, might be explained by progressive loss of mitochondrial function [1]. For example, exposure to IR can lead to fatigue – a characteristic of mitochondrial dysfunction. Even small changes in mitochondrial

S.B. Zhang • M. Zhang • S. Yang • A.P. Zhang • L. Yin • X. Wang • C. Chen • J. Ma • D. Han • A. Litvinchuk • S. Swarts • S. Vidyasagar • D. Maguire • L. Zhang • P. Okunieff (✉)
Department of Radiation Oncology, University of Florida College of Medicine, 2033 Mowry Road, Box 103633, Gainesville, FL, 32610, USA
e-mail: pokunieff@ufl.edu

Y. Cao • Y. Tian
Second Military Medical University, Shanghai, 200433, People's Republic of China

K. Zhang
Vascular Medicine Research, Brigham and Women's Hospital, Harvard Medical School, Room 270, Landsdowne Street, Cambridge, MA, 02139, USA

Y. Guo
Province Hospital of Fujian,
Fuzhou, 350001, People's Republic of China

M. Wolf et al. (eds.), *Oxygen Transport to Tissue XXXIII*, Advances in Experimental Medicine and Biology 737, DOI 10.1007/978-1-4614-1566-4_21,

function can cause neurological compromise [2] consistent with radiation toxicity, which progresses with time and often requires many years to become symptomatic. The mechanisms underlying mitochondrial dysfunction are complex, including mtDNA mutation and depletion [3]. In the acute stage, IR increases mitochondrial copy number in murine brains, spleens, small bowels, and bone marrow [4, 5]. This reactive response to preserve mtDNA may or may not protect tissues from long-term damage.

To determine if mtDNA might decrease at later times consistent with delayed radiation toxicity, we studied the effects of IR on the mtDNA copy number in two strains of mice, Balb/c and C57BL/6, known to have very different tolerances to acute hematopoietic syndrome (Balb/c is more sensitive) and late fibrosis (C57BL/6 is more sensitive).

Materials and Methods

Male Balb/c and C57BL/6 mice, 7–8 weeks old, were purchased from the National Cancer Institute's Mouse Repository (Frederick, MD), housed five per cage on a 12-h light/dark cycle in a micro-isolator room, and fed a standard diet. Five days after arriving, the mice were immobilized in plastic boxes and shaved (control) or administered either a single dose of total body irradiation (TBI) or a sub-TBI exposure (TBI with shielding of the left hind-leg) using a 137-caesium gamma source at a dose rate of 1.75 Gy/min.

Six months after treatment, the mice were weighed and sacrificed for brain, small bowel, liver, skeletal/muscle, and bone marrow tissue collection. The collected tissues were frozen immediately at −70°C until use. We extracted total genomic DNA (nuclear and mtDNA) from these tissues by standard proteolytic digestion, followed by phenol/chloroform/isoamyl alcohol purification. The extracted DNA was diluted in TE buffer (pH 8.0) and measured in an ultraviolet (UV) spectrometer using 260 and 280 nm absorbance for quantifying and qualifying the DNA.

The polymerase chain reaction (PCR) primer sets were developed in our laboratory [5]. We amplified the murine nuclear *18S ribosomal ribonucleic acid* (*rRNA*) gene and the mtDNA *12S rRNA* gene. The real-time quantitative PCR was carried out using the SYBR Green PCR Master Mix (Applied Bioscience by Life Technologies, Carlsbad, CA) and the Bio-Rad iQ5 program (Hercules, CA). The PCR reaction was subjected to an initial denaturation at 50°C for 5 min and 95°C for 10 min, followed by 40-amplification cycles of denaturation at 95°C for 15 s, annealing at 59°C for 25 s, and extension at 72°C for 50 s. We recorded the threshold cycle value (C_t).

Each DNA sample was run in duplicate or triplicate by PCR assay. The recorded C_t was used as a basis for quantification of relative nDNA and mtDNA copy number. A Student's *t*-test was used to determine a statistically significant difference between the groups. A value of $p < 0.05$ was regarded as statistically significant.

Results

Mice were weighed 6 months after IR (Fig. 21.1). Neither TBI nor sub-TBI produced long-lasting changes in body weight compared to control 0-Gy animals. Balb/c mice had higher body weights (21.6–22.3 g) than C57BL/6 mice (20.2–20.9 g).

Brain, skeletal/muscle, small bowel, liver, and bone marrow tissues from Balb/c and C57BL/6 mice were collected 6 months after a sham-IR procedure. The total DNA was extracted from each sample and subjected to real-time PCR. The various organs had different ratios of mtDNA to nDNA (Fig. 21.2). The highest ratio of mtDNA to nDNA, irrespective of murine strain, was seen in skeletal/muscle tissues, followed by the brain, liver, small bowel, and bone marrow. The ratio of mtDNA to nDNA in all C57BL/6 tissues was similar to or higher than that in Balb/c tissues; however, a significant difference was found only in the liver.

After mice were exposed to 5-Gy TBI or 9-Gy sub-TBI, skeletal/muscle, brain, small bowel, liver, and bone marrow tissues were harvested. The DNA was extracted from these tissues and subjected to real-time PCR. Results from irradiation groups were normalized to the non-irradiation control results of each strain. Increased mtDNA copy number after irradiation was dose- and strain-dependent (Fig. 21.3a–e). In C57BL/6 mice, an increased mtDNA copy number was found only in the brain after 5-Gy TBI (Fig. 21.3a). The effect on copy number was minor for this strain. There was a significant decrease in mtDNA in skeletal/muscle tissues at both 5-Gy TBI and 9-Gy sub-TBI for Balb/c mice, but there was no effect in C57BL/6 mice (Fig. 21.3b). In Balb/c mice, there was an apparent dose response in the liver (Fig. 21.3d). A 31% increase in mtDNA copy number was also found in the bone marrow of Balb/c mice 6 months after 9-Gy sub-TBI (Fig. 21.3e). Here, the repopulating marrow arose from the untreated marrow in the spared femur.

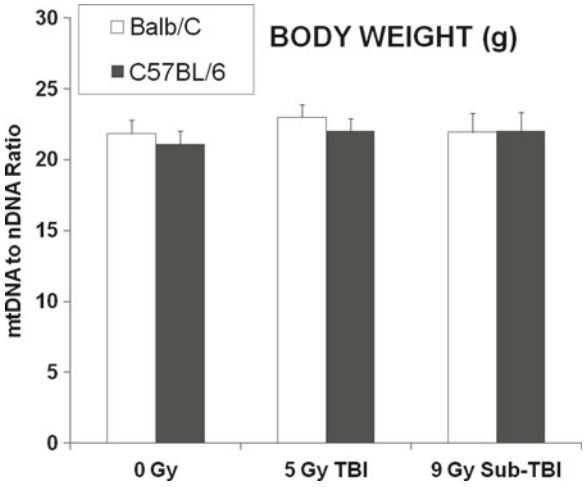

Fig. 21.1 Mice body weight changes 6 months after irradiation. Each group consisted of five mice. Values are mean ±2 SD

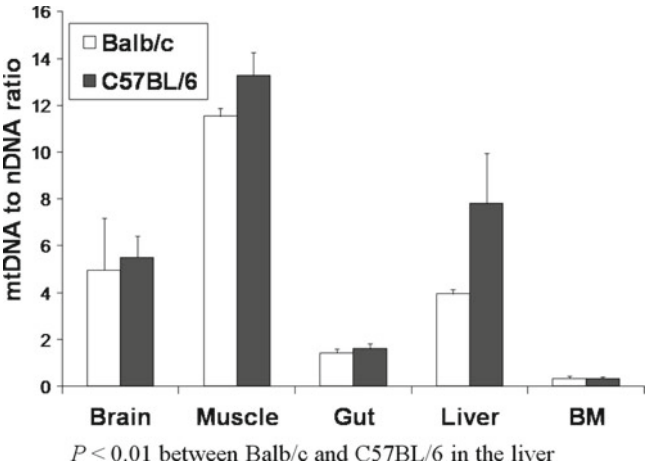

Fig. 21.2 The natural ratio of mtDNA to nDNA is strain- and tissue-dependent. In groups of five, mice were sham-irradiated and tissues were harvested 6 months later. Values are mean ±2 SD

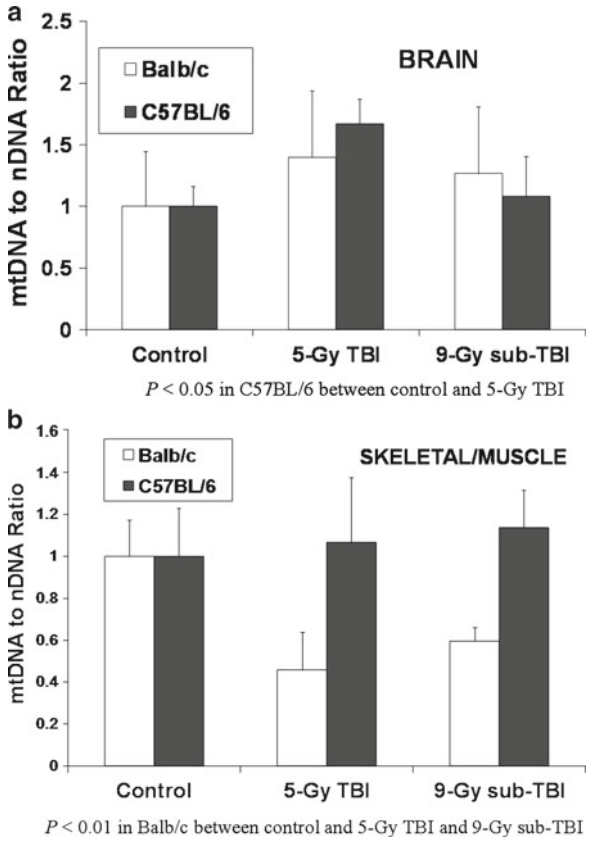

Fig. 21.3 Dose- and strain-dependent changes in mitochondrial copy number. In groups of five, mice were exposed to 5-Gy TBI or 9-Gy sub-TBI. Six months later (**a**) brain; (**b**) skeletal/muscle; (**c**) small bowel; (**d**) liver; and (**e**) bone marrow tissues were harvested. Results from irradiation groups were normalized to the non-irradiation control results of each strain. Values are mean ±2 SD

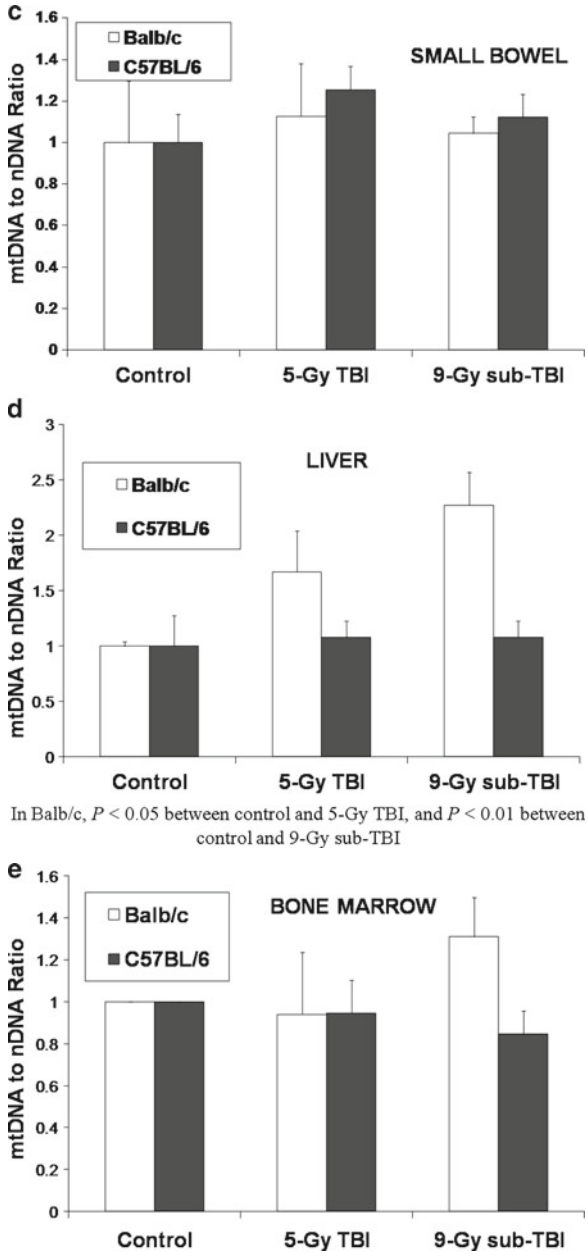

Fig. 21.3 (continued)

Discussion

We previously hypothesized that severely reduced DNA repair in the cytoplasm would cause enough damage in mtDNA so as to prevent proper proliferation and function of mitochondria during the years following radiation exposure and that these changes might explain late side effects, including myocardial and neurological dysfunction. In humans, these organs show delayed damage 4–8 years after exposure [6]. The delay in damage has sometimes been attributed to slow proliferation; however, there is little evidence that proliferation occurs in these organs in adults.

In previous studies, proliferation of mtDNA was seen shortly after radiation, and we continued to see increased mtDNA copy numbers in some organs up to 3 months after irradiation [7]. The increased DNA copy number was associated with increased polymerase gamma and decreased transcription factor-A [7], which is consistent with the cellular need to replicate mtDNA but not to make surplus mitochondria.

The Balb/c strain has poor DNA repair, which is associated with a higher rate of breast cancers as they naturally age, and increased mutagenesis in vivo and in vitro [8, 9]. This effect may be due to a functional polymorphism of the *protein kinase, DNA-activated, catalytic polypeptide* (*PRKDC*) gene. Our intent in this study was to determine if the aberrant repair in this strain resulted in more severe mtDNA changes.

We found that mice treated at the maximum-tolerated TBI or sub-TBI dose had no chronic change in body weight, indicating that the dose of radiation may not have been sufficient to produce late radiation toxicity to stromal tissues in the 6-month time period. Consistent with this interpretation, there was little difference in mtDNA/nDNA ratios between strains. We speculate that the higher mtDNA content in the liver of C57BL/6 mice was a consequence of that organ's adaptation to the high oxidative stress. The rise in mtDNA/nDNA ratios seen in Balb/c livers 6 months after radiation likely relates to a similar phenomenon, but this issue deserves future study. In contrast, muscle, a nonregenerative organ, in Balb/c exhibited a decrease in mtDNA consistent with our hypothesis.

These studies are preliminary, and longer follow-up may be needed to fully evaluate the effects of radiation on mtDNA replication and function. Higher doses of radiation, such as might be delivered to a local region (i.e., one hind-leg or brain hemisphere), may prove a better model than whole body to measure the effects on mtDNA. Additionally, the functional status of the mitochondria and their role in maintaining a normal oxidative state in the cell must be further examined. For example, irradiated tissues have chronically abnormal oxidative states after radiation exposure [10]. To remedy this problem, late radiation effects have been attenuated or delayed using chronic antioxidant therapy [11]. Among the successful antioxidant treatments are gene therapy with superoxide dismutase, a mitochondrial antioxidant [11]. The roles of mitochondrial function and the impact of mtDNA damage in late organ dysfunction remain unexplained.

Further studies are warranted as the mechanisms of late radiation effects are still unknown and as there are no mitigative or therapeutic approaches available.

References

1. Okunieff P, Swarts S, Keng P et al (2008) Antioxidants reduce consequences of radiation exposure. Adv Exp Med Biol 614:165–178
2. Bergsneider M, Hovda DA, McArthur DL et al (2001) Metabolic recovery following human traumatic brain injury based on FDG-PET: time course and relationship to neurological disability. J Head Trauma Rehabil 16(2):135–148
3. Weissman L, Souza-Pinto NC, Stevnsner T et al (2007) DNA repair, mitochondria, and neurodegeneration. Neuroscience 145:1318–1329
4. Malakhova L, Bezlepkin VG, Antipova V et al (2005) The increase in mitochondrial DNA copy number in the tissues of gamma-irradiated mice. Cell Mol Biol Lett 10(4):721–732
5. Zhang H, Zhang SB, Sun W et al (2009) B1 Sequence-based real-time quantitative PCR: a sensitive method for direct measurement of mouse plasma DNA levels after gamma irradiation. Int J Radiat Oncol Biol Phys 74(5):1592–1599
6. Paulino AC, Simon JH, Zhen W et al (2000) Long-term effects in children treated with radiotherapy for head and neck rhabdomyosarcoma. Int J Radiat Oncol Biol Phys 48(5):1489–1495
7. Zhang H, Maguire D, Swarts S et al (2009) Replication of murine mitochondrial DNA following irradiation. Adv Exp Med Biol 645:43–48
8. Yu Y, Okayasu R, Weil MM et al (2001) Elevated breast cancer risk in irradiated BALB/c mice associates with unique functional polymorphism of the *PRKDC* (DNA-dependent protein kinase catalytic subunit) gene. Cancer Res 61:1820–1824
9. Ponnaiya B, Cornforth MN, Ullrich RL (1997) Radiation-induced chromosomal instability in BALB/c and C57BL/6 mice: the difference is as clear as black and white. Radiat Res 147:121–125
10. Wang Y, Liu L, Pazhanisamy SK et al (2010) Total body irradiation causes residual bone marrow injury by induction of persistent oxidative stress in murine hematopoietic stem cells. Free Radic Biol Med 48(2):348–356
11. Epperly MW, Dixon T, Wang H et al (2008) Modulation of radiation-induced life shortening by systemic intravenous MnSOD-plasmid liposome gene therapy. Radiat Res 170(4):437–443

Chapter 22
Radiation-Induced Elevation of Plasma DNA in Mice is Associated with Genomic Background

Lei Zhang, Mei Zhang, Bingrong Zhang, Yongbing Cao, Shanmin Yang, Liangjie Yin, Yeping Tian, Kunzhong Zhang, Lulu Zhang, Steven Swarts, Paul Okunieff, and Lurong Zhang

1 Introduction

Ionizing radiation (IR) damages DNA directly by creating single- and double-strand breaks, and indirectly through the generation of destructive free radicals that break DNA or covalent bonds that modify the DNA. Because radiation exposure is ubiquitous in the natural environment, animal and plant species have developed multiple mechanisms to overcome this damage. Different species, therefore, tolerate radiation differently. Even within murine strains, the tolerance to radiation can vary. For example, some mice tolerate high-dose bone marrow exposure but are prone to fibrosis after localized radiation. We have shown that C57BL/6 mice are in this category; whereas, the C3H/HeN, NIH Swiss, and BALB/c strains are less tolerant of whole-body radiation exposure and less prone to soft-tissue fibrosis after localized radiation. Due to a deficiency in their ability to repair DNA, BALB/c mice are

L. Zhang
West China Hospital of Sichuan University, Chengdu, Sichuan 610041, P.R. China

Department of Radiation Oncology, University of Florida, 2033 Mowry Road, Box 103633, Gainesville, FL 32610, USA

M. Zhang • B. Zhang • S. Yang • L. Yin • S. Swarts • P. Okunieff, M.D. (✉) • L. Zhang
Department of Radiation Oncology, University of Florida, 2033 Mowry Road, Box 103633, Gainesville, FL 32610, USA
e-mail: pokunieff@ufl.edu

Y. Cao • Y. Tian
Second Military Medical University, Shanghai 200433, P.R. China

K. Zhang
Vascular Medicine Research, Brigham and Women's Hospital, Harvard Medical School, Room 270, Landsdowne Street, Cambridge, MA 02139, USA

L. Zhang
DiaCarta LLC, Foster City, CA 94404, USA

M. Wolf et al. (eds.), *Oxygen Transport to Tissue XXXIII*, Advances in Experimental Medicine and Biology 737, DOI 10.1007/978-1-4614-1566-4_22,

the most radiation sensitive of the four strains studied. The mechanisms behind this variability in radiation sensitivity have yet to be determined.

Recently, we developed an assay that utilizes branch-DNA technology to quantitatively measure the levels of plasma DNA that are released into the blood stream after irradiation. Using this assay, we measured the amount of DNA in circulation after irradiation in an attempt to better understand differential inter-strain sensitivity to radiation.

2 Materials and Methods

Four strains of mice (BALB/c, NIH Swiss, C3H/HeN, and C57BL/6) were selected based on their different intrinsic radiation sensitivities as demonstrated by varying $LD_{50/30}$ (the dose that causes death in half of exposed mice within 30 days). All mice, which were purchased through the National Cancer Institute (NCI), were male, 8 weeks old, approximately 20–23 g, and acclimated for at least 5 days prior to experimentation.

The mice (six to eight per group) were loaded into a Plexiglas total body irradiation (TBI)-animal restraint with five mice per box; the restraint was within the radiation field of the TBI collimator. Mice were irradiated with a caesium-137 (137Cs) γ-ray source at 1.84 Gy/min dose rate. Exposure times were determined by the Gy prescribed (0–13 Gy, depending on the strain). The control mice were placed in the same restraint and TBI collimator but received 0 Gy.

Nine hours after irradiation, the blood from each mouse was collected in an ethylenediaminetetraacetic acid (EDTA) tube, and the plasma was frozen at −80°C until the assay was performed. Plasma DNA was measured with the QuantiDNAassay kit (DiaCarta LLC, Foster City, CA) according to the manufacturer's instructions. Unless otherwise noted, all reagents and other required materials were QuantiGene-related (Panomics, Santa Clara, CA). Twentyfold diluted murine plasma with nuclease-free water was fully denatured at 100°C for 10 min and then immediately placed in cold water until samples were loaded into a 96-well assay plate. A working probe solution was prepared in diluted lysis buffer with proteinase K at a final concentration of 16.7 μg/ml together with 0.1% blocking reagent (cat# 1096176, Roche Applied Science, Indianapolis, IN), capture extender at 250 pM, and label extender at 1,000 pM. Five microliters of prepared murine plasma spiked with different concentrations (0, 3.12, 6.25, 12.5, 25, 50, 100, and 200 ng/ml) of murine genomic DNA was added into a capture-plate well containing 95 μl of working probe solution; the plate was sealed with a foil seal. After an overnight hybridization at 55°C, the plate was washed three times with washing buffer (0.1× standard citrate saline containing 0.3 g/l of lithium lauryl sulfate) after which all traces of buffer were removed.

For signal amplification and detection of bound B1-DNA, the standard QuantiGene protocol (QuantiGene 2.0 reagent system, user manual) was followed. Sequential hybridizations were conducted at 55°C for 1 h in 100 μl of 1:1,000 diluted bDNA pre-amplifier, then at 55°C for 1 h in 100 μl of 1:1,000 diluted bDNA amplifier, and finally at 50°C for 1 h in 100 μl of 1:1,000 dilution of alkaline-phosphatase-labeled probe.

All bDNA probes were diluted in probe dilutant. Wells were washed with washing buffer after each hybridization. After the final wash, 100 μl of the alkaline phosphatase luminescence substrate was added to each well, and the plate was left at room temperature for 10 min. Developed luminescence signals were read as relative light units (RLU) on a Perkin Elmer Victor 3V (PerkinElmer, Inc., Waltham, MA), using a 0.2-s integration time. The plasma DNA level was calculated from the standard curve that was analyzed simultaneously in the same plate with the plasma samples.

A Kruskal–Wallis H-test was used to determine the significant differences between the treatment groups. A P value of <0.05 was regarded as statistically significant. All statistical analyses were done by SPPS v17 Statistical Package. Box-and-whisker plots showed the median, 25th, and 75th percentiles and the range of plasma DNA levels.

3 Results

Among the strains chosen, the BALB/c is the most sensitive to TBI as demonstrated by its low $LD_{50/30}$ of 5.8 ± 0.3 Gy. We exposed the BALB/c cohort (eight per group) to 0, 3, 4, 5, 6, 7, and 10-Gy doses, and then collected plasma after the mice were sacrificed 9 h later. The plasma DNA increased with the dose from 0 to 6 Gy ($P<0.001$). A plateau was reached at ≈6 Gy (Fig. 22.1). The peakDNA level was approximately 4,000 ng/ml.

The NIH Swiss is an outbred strain with a more heterogeneous genetic background than the three inbred strains we studied. This strain had an intermediate

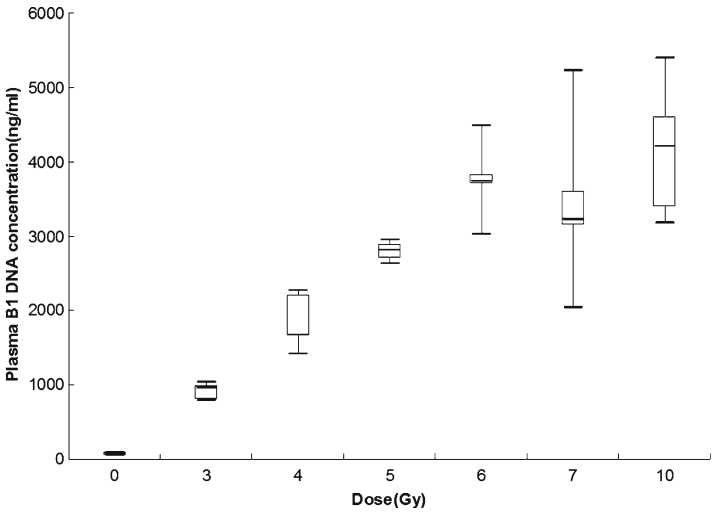

Fig. 22.1 Plasma DNA in irradiated BALB/c mice. BALB/c mice were subjected to 0, 3, 4, 5, 6, 7, and 10-Gy TBI. There was a significant difference between groups ($P<0.001$, Kruskal–Wallis H-test agnostic)

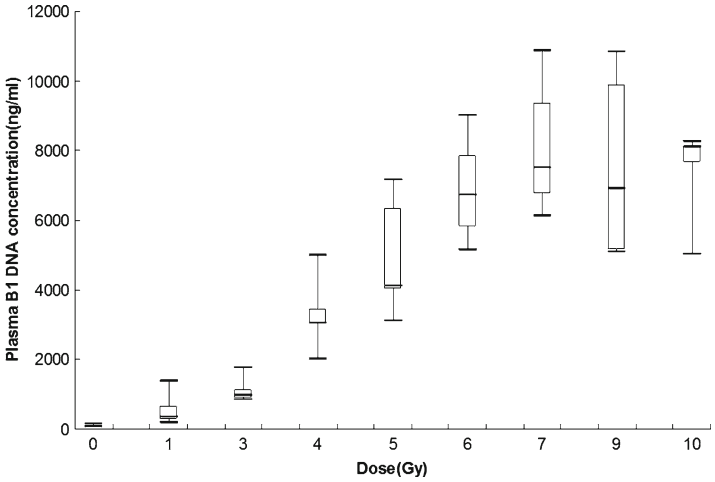

Fig. 22.2 Plasma DNA in irradiated NIH Swiss mice. NIH Swiss mice were subjected to 0, 1, 3, 4, 5, 6, 7, 9, and 10-Gy TBI. There was a significant difference between groups ($P<0.001$, Kruskal–Wallis H-test)

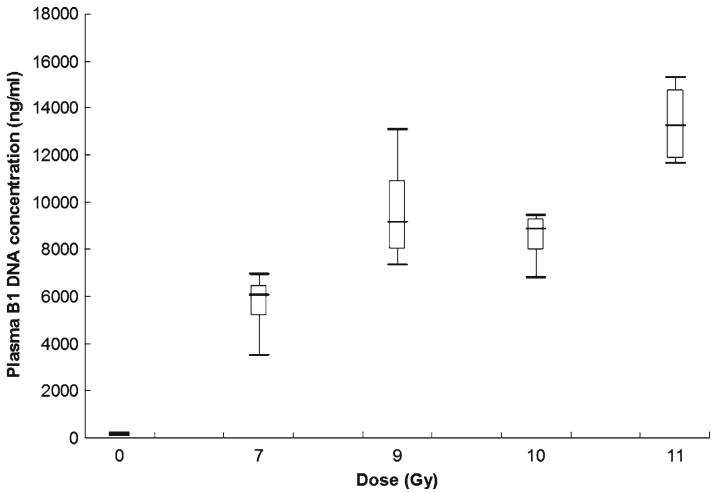

Fig. 22.3 Plasma DNA in irradiated C3H/HeN Mice. C3H/HeN mice were subjected to 7, 9, 10, and 11-Gy TBI. There was a significant difference between groups ($P=0.001$, Kruskal–Wallis H-test)

$LD_{50/30}$ of 7.3 ± 0.2 Gy. NIH Swiss mice were subjected to 0, 1, 3, 4, 5, 6, 7, 9, and 10-Gy TBI and exhibited increases in plasma DNA from 0 to 7 Gy and a plateau at 7 Gy (Fig. 22.2). The peakDNA level was approximately 7,000 ng/ml.

The C3H/HeN, like the NIH Swiss, has a moderate tolerance of TBI with an $LD_{50/30}$ of 7.4 ± 0.3 Gy. C3H/HeN mice were subjected to doses of 7, 9, 10, and 11 Gy with a plateau at 9 Gy (Fig. 22.3). The peakDNA for this strain was approximately 9,000 ng/ml, almost double that of more TBI-sensitive BALB/c mice.

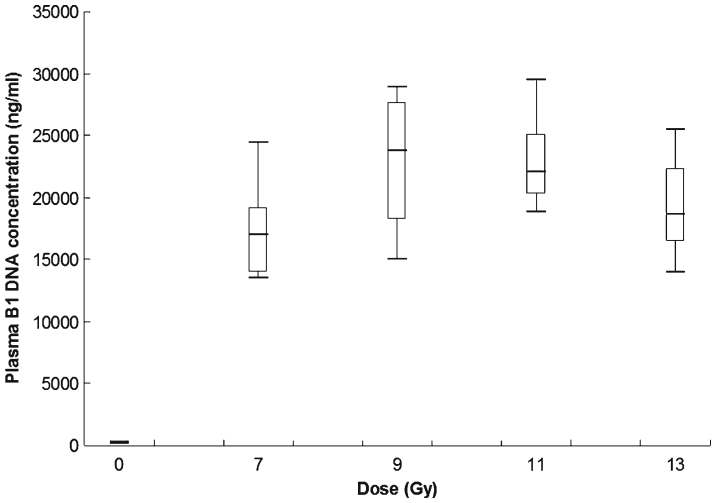

Fig. 22.4 Plasma DNA in irradiated C57BL/6 mice. C57BL/6 mice were subjected to 7, 9, 11, and 13-Gy TBI. There was a significant difference between groups ($P = 0.002$, Kruskal–Wallis H-test)

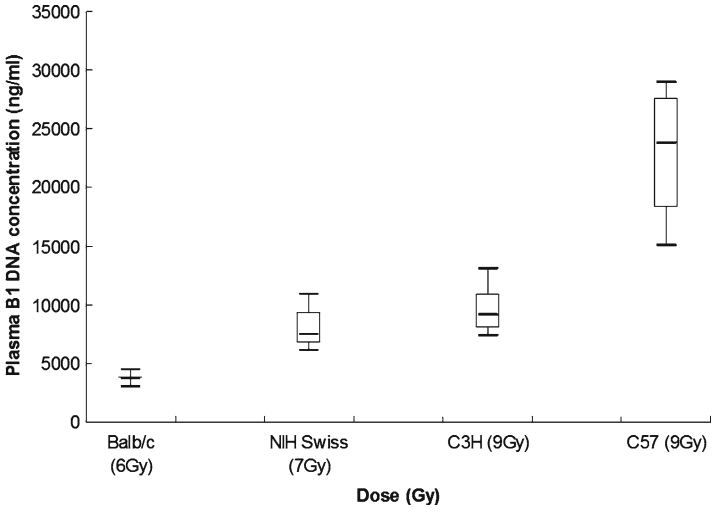

Fig. 22.5 PeakDNA in different murine strains. The IR dose that caused the plasma DNA level to reach a plateau was compared in the four strains of mice. The levels were 6, 7, 9, and 9-Gy for Balb/c, NIH Swiss, C3H/HeN, and C57BL/6, respectively. There was a significant difference between groups ($P = 0.002$, Kruskal–Wallis H-test)

The C57BL/6 was the most resistant strain with an $LD_{50/30}$ of 8.5 ± 0.3 Gy. The peakDNA exceeded 15,000 ng/ml (Fig. 22.4).

These various strains of mice with different genomic backgrounds exhibited correspondingly different susceptibilities to TBI. Figure 22.5 compares the doses that

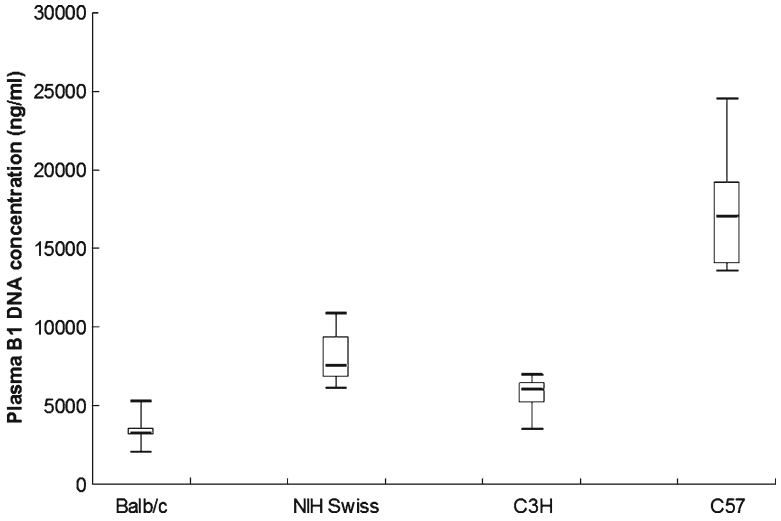

Fig. 22.6 DNA released amongst different strains of mice 9 h after 7-Gy TBI. Four strains of mice were subjected to 7-Gy TBI. The plasma DNA level was measured 9 h later. There was a significant difference between groups ($P < 0.003$, Kruskal–Wallis H-test)

induced the various plateaus of plasma DNA (peakGy). The peakDNA levels are shown in Fig. 22.6. PeakGy and peakDNA increased together. The peakGy of BALB/c, NIH Swiss, C3H/HeN, and C57BL/6 was 6, 7, 9, and 9 Gy, respectively. The peakDNA level followed the same order: C57BL/6 > C3H/HeN ~ NIH Swiss > BALB/c.

4 Discussion

After IR, some genomic DNA damage is not repaired, and these cells undergo reproductive failure or apoptosis. The latter can lead to a rapid release of DNA into circulation, and the circulating DNA can serve as a biodosimeter. Our ability to understand the release of DNA directly impacts our insight into the potential utility of this method for biodosimetry. To our knowledge there has been no comparison of plasma DNA levels between different murine strains after TBI. Using four strains of mice, this study demonstrated the following: (1) The plasma DNA level was different in the four strains even when they were given the same TBI dose; (2) Plasma DNA reached a plateau at doses correlating with each strain's $LD_{50/30}$.

The underlying mechanism by which the plasma DNA level measured after TBI varies for different murine strains is largely unknown. Since plasma DNA in a living body represents the DNA entering the blood stream from all damaged cells and removed by the retinoendothelial system, enzymes, or the kidney, the level of plasma DNA is representative of dynamic biological response to TBI. A high level of plasma DNA might be due to the following: (1) More total cells are damaged by radiation.

This possibility is excluded because the four tested strains had a similar age (8 weeks old) and body weight (roughly 20–23 g). (2) The clearance rate is lower. This is possible but unlikely, since we have previously shown a time course in different strains that is similar [1]. (3) There are larger compartments of cells prone to apoptosis, such as lymphocytes, to produce the circulating DNA. Although this hypothesis is logical, we do not yet have the necessary research data to support it.

We do not know if the phenomenon observed in the four murine strains is applicable to humans. C57BL/6 and BALB/c are purely inbred mice with extremely different gene expression and regulation, which lead to correspondingly different responses to radiation. For example, BALB/c is deficient in DNA repair, while C57BL/6 is prone to fibrosis. Since humans are more outbred, the variety of responses to IR among different races might be much smaller than that between C57BL/6 and BALB/c. The value of human plasma DNA level as a universal biodosimeter should be explored. The methods used in this study can be extended to other applications, such as the detection of tumor DNA or apoptosis after different physical, biological, and chemical assaults. They also have promising applications for radiation biodosimetry.

Acknowledgments The authors gratefully acknowledge the funding of this work in part by a grant (U19-AI067733) from the National Institute of Allergy and Infectious Diseases (NIAID) and a STTR from DARPA (W31P4Q08C0417).

Reference

1. Zhang L, Zhang M, Yang S et al (2010) A new biodosimetric method: branched DNA-based quantitative detection of B1 DNA in mouse plasma. Br J Radiol 83:694–701

Chapter 23
Could Multiple Myeloma VEGF Modify the Systemic Microcirculation?

S. Cicco, P. Ditonno, A. Reale, S. Savino, A. Castrovilli, I. Catacchio, R. Ria, and A. Vacca

1 Introduction

We studied multiple myeloma (MM), an incurable disease associated with an increased number of plasma cells (PCs) in the bone marrow. This neoplastic condition is the end stage of another disease: monoclonal gammopathy of undetermined significance (MGUS). In 2009, the scientific community definitively accepted the idea that MM was the end stage of a previous MGUS of many years standing. Both these diseases have increased levels of serum γ-globulin, with a monoclonal spike (M-protein). Progression from MGUS to MM is approximately 1% per year [1, 2].

We wished to investigate the modification of microcirculation and hemorheology in MM and MGUS. In fact, we already know that MM stimulates neoangiogenesis by producing cytokines. One of the most important molecules of this family is vascular endothelial growth factor (VEGF) [3, 4], and we wondered if the VEGF could interfere with vessels and red blood cells (RBCs).

2 Materials and Methods

To investigate blood flow we used a Periflux 5010/5020 laser Doppler (Periflux combined system, Perimed, Sweden), with the probe on the skin of the volar face of the left wrist, while the Combi-sensor measured transcutaneous tissue oxygen

S. Cicco (✉)
DIMO, Policlinico di Bari, Università Aldo Moro, Bari, Italy

Piazza San Giovanni Bosco, 6, Andria (BT) 70031, Italy
e-mail: sebacicco@yahoo.it

P. Ditonno • A. Reale • S. Savino • A. Castrovilli • I. Catacchio • R. Ria • A. Vacca
DIMO, Policlinico di Bari, Università Aldo Moro, Bari, Italy

M. Wolf et al. (eds.), *Oxygen Transport to Tissue XXXIII*, Advances in Experimental Medicine and Biology 737, DOI 10.1007/978-1-4614-1566-4_23,

Table 23.1 Periflux test time steps (in s)

In grey REC	60	30	30	5	15	150	30	210	90
600	60	30	30	5	15	60	120		
Calibr.	Basal (T_0)		Hand motion (T_1)		After motion (T_2)		Skin temp. 44°C (T_3)		After heat (T_4)

partial pressure ($TcpO_2$) in the same area. After a 10-min stabilization period with the probes in place, basal values (T_0) were recorded for 60 s. $TcpO_2$ and $TcpCO_2$ values and flow were also evaluated during 30 s of hand motion (T_1) and for 15 s after it (T_2). These parameters were also evaluated during warming of the skin with the Periflux 5010/5020 probe. We recorded values for the last 30 of 120 s while skin temperature was 44°C (T_3) and after heat stress for 90 s (T_4) with 210 s between T_3 and T_4 (Table 23.1).

Red blood cell (RBC) aggregation index (AI and *t½*) and elongation index (EI) were assessed with LORCA (Mechatronics, NL). To evaluate RBC deformability as elongation index (EI_{30Pa}) at 30 Pa shear stress, we diluted a 125 μl EDTA blood sample in 3 ml PVP and then recorded the values. We also evaluated RBC aggregability as half time (*t½* in s) needed to form clots in the LORCA cup, on a pure blood sample with EDTA.

Serum VEGF levels were evaluated using the enzyme-linked immunosorbent assay (ELISA) from Quantikine human VEGF, R&D Systems, Minneapolis, MN, using the manufacturer's proposed protocol, which is reported to produce inter-sample and intra-sample variability coefficients for the VEGF serum levels of 6.2–8.8% and 2–9% respectively. For each patient we collected serum at diagnosis and then stored them at −80°C. We compared the values for each studied group and values obtained from 63 healthy subjects (40 males and 23 females, mean age 61 years). It is known that platelet release of VEGF can occur during coagulation. To eliminate this problem VEGF serum levels detected were corrected to the values recorded in 30 "random" patients (we found a significant correlation: Pearson $r=0.51$; $p<0.0001$). These values were also correlated to the platelet values (VEGF serum $r=0.52$; VEGF plasma $r=0.44$; $p<0.0001$).

All statistical analyses were done using the analysis of variance (ANOVA) method considering significant only values with $p<0.05$.

3 Results

Since September 2008 we have evaluated 17 patients with MM (nine males and eight females; mean age 62 years), eight with active MM (aMM, six males and two females; mean age 62 years), nine patients in objective/complete response (rMM, three males and six females; mean age 70 years), and seven patients with MGUS (three males and four females; mean age 57 years).

Table 23.2 Studied groups

	MM	aMM	rMM		MGUS	
Number	17	8	9		7	
Age (years)	62	62	70		57	
Gender	9 M/8 F	6 M/2 F	3 M/6 F		3 M/4 F	
ImiDs/non ImiDs	12/5	3/5	9/0			
Hb (g/dl)		11.0 ± 2.2	11.7 ± 1.5	NS	12.7 ± 1.5	NS
M-component (g/dl)		2.32 ± 1.86	0.47 ± 0.35	NS	0.72 ± 0.55	NS
VEGF (pg/dl)		310.8 ± 136.1	183.0 ± 48.3	**	175.6 ± 46.8	**

Correlations were done between rMM vs. aMM and MGUS vs. aMM. **$p < 0.001$

Table 23.3 LORCA results

	MM attivo	MM non attivo		MGUS	
EI_{30Pa}	0.61 ± 0.02	0.61 ± 0.01	NS	0.62 ± 0.01	NS
t½ (s)	1.78 ± 0.52	2.07 ± 1.27	$p < 0.05$	2.15 ± 1.18	$p < 0.05$
AI (%)	67.78 ± 12.50	66.26 ± 10.40	$p < 0.05$	64.08 ± 12.77	$p < 0.05$

Correlations were done between rMM vs. aMM and MGUS vs. aMM

Haemoglobin (Hb) values were not significantly decreased in the aMM group compared to rMM (aMM 11.0 ± 2.2 g/dl vs. rMM 11.7 ± 1.5 g/dl) or MGUS (aMM 11.0 ± 2.2 g/dl vs. MGUS 12.7 ± 1.5 g/dl). M-protein values were not significantly different comparing the three groups (aMM 2.32 ± 1.86 g/dl vs. rMM 0.47 ± 0.35 g/dl, $p > 0.05$; aMM 2.32 ± 1.86 g/dl vs. MGUS 0.72 ± 0.55 g/dl). These results are presented in Table 23.2.

Aggregation time ($t½$) was significantly decreased in aMM vs. rMM (1.78 ± 0.52 s vs. 2.07 ± 1.27 s, $p < 0.05$) or vs. MGUS (1.78 ± 0.52 s vs. 2.15 ± 1.18 s, $p < 0.05$). There was also a significant increase in AI values in aMM patients vs. rMM (67.78 ± 12.50 vs. 66.26 ± 10.40, $p < 0.05$), and also vs. MGUS (67.78 ± 12.50 vs. 64.08 ± 12.77, $p < 0.05$). However, RBC deformability (EI_{30}) was not significantly different across the three studied groups (aMM vs. rMM: 0.61 ± 0.01 vs. 0.61 ± 0.02, NS; aMM vs. MGUS: 0.61 ± 0.01 vs. 0.62 ± 0.01, NS). These results are presented in Table 23.3.

In all groups there was a significant relationship between EI_{30} and VEGF ($p < 0.001$), but not between EI_{30} and Hb concentration or M-component. $t½$ was significantly related to VEGF ($p < 0.001$) but not to Hb concentration or M-component. Also AI was significantly related to the VEGF ($p < 0.001$) but not the Hb concentration and M-component in aMM; in rMM and MGUS groups AI values were however significantly related to VEGF ($p < 0.001$), Hb concentration ($p < 0.001$) and M-component ($p < 0.001$).

Laser Doppler flow values were significantly increased during muscular exercise ($t1$) compared to basal values ($t0$) in aMM group ($t0$ vs. $t1$: 16.45 ± 6.23 PU vs. 65.75 ± 21.87 PU, $p < 0.01$) but not during heat stress ($t0$ vs. $t3$: 16.45 ± 6.23 PU vs. 53.27 ± 30.59 PU, NS). Muscular exercise values were not significantly different from heat stress values ($t1$ vs. $t3$: 65.75 ± 21.87 PU vs. 53.27 ± 30.59 PU, NS). Post-stress values ($t2$ and $t4$) were not significantly different to basal ones ($t0$) – NS.

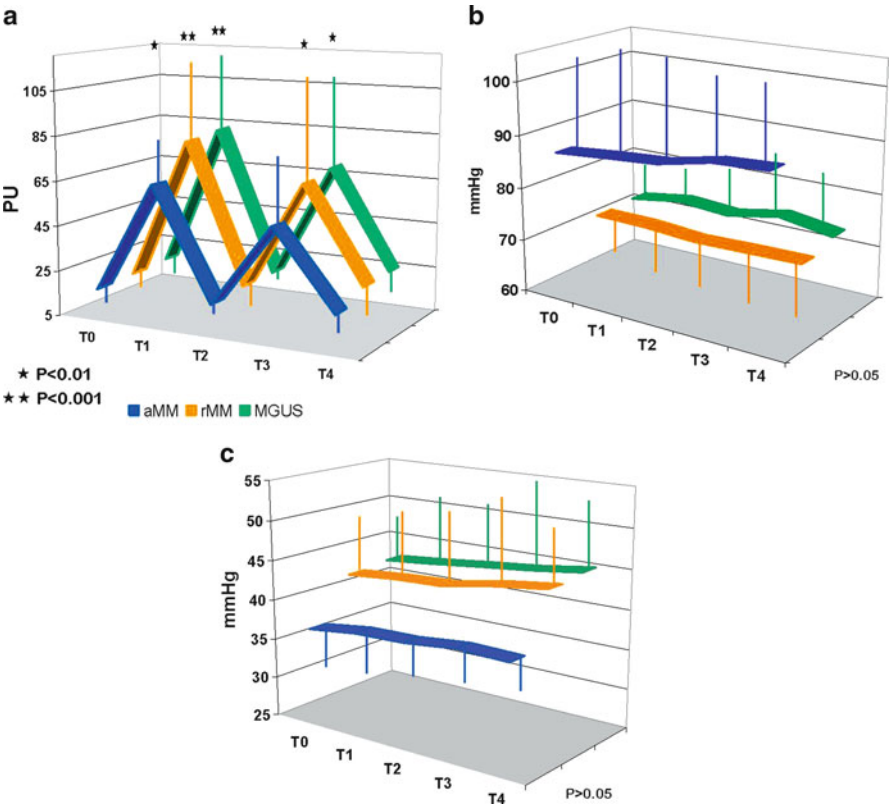

Fig. 23.1 (**a**) Laser Doppler values (PU values) recorded on the volar face of the left forearm; (**b**) $TcpO_2$ (mmHg) values and (**c**) $TcpCO_2$ (mmHg) values recorded using a transcutaneous oxymeter combi sensor, placed on the volar face of the left wrist. The correlation were done between basal values (T_0) and the blood flow values during muscular stress (T_1) and heat stress (T_4) respectively. There was done also the comparison for each time between each group

During stress in the rMM group flow values were significantly increased over basal measurements ($t0$ vs. $t1$: 17.45 ± 13.04 PU vs. 80.94 ± 40.51 PU, $p < 0.001$; $t0$ vs. $t3$: 17.45 ± 13.04 PU vs. 66.51 ± 47.47 PU, $p < 0.01$); this was also observed in the MGUS group ($t0$ vs. $t1$: 18.25 ± 12.46 PU vs. 82.59 ± 36.75 PU, $p < 0.001$; $t0$ vs. $t3$: 18.25 ± 12.46 PU vs. 69.26 ± 48.44 PU, $p < 0.01$). Post-stress values were not significantly different to basal ($t0$). No values in the aMM group were significantly different from other groups (Fig. 23.1a).

Basal values ($t0$) of VEGF in the aMM group were significantly higher than in the other two groups ($p < 0.001$ for both groups). There were no significant differences between $t0$ Hb concentrations or M-component values between groups.

Values were not significantly different ($p > 0.05$) comparing basal values ($t0$) of $TcpO_2$ and $TcpCO_2$ and were not significantly altered under stress ($t1$ and $t3$) either within or between groups (Fig. 23.1b, c).

$TcpO_2$ and $TcpCO_2$ ($t0$) values were differently related to VEGF, Hb and M-component values in the different groups. There was a significant correlation

between VEGF and both $TcpO_2$ and $TcpCO_2$ in all groups ($p<0.001$). There was no significant correlation between $TcpO_2$ values and Hb or M-component values in the aMM group, while significant correlations were seen in the rMM and MGUS groups ($p<0.001$). Also $TcpCO_2$ $t0$ values were significantly related to the M-component ($p<0.001$) in rMM and MGUS, but not in the aMM group ($p>0.05$). No significant correlations between the $TcpCO_2$ values and Hb values were observed in any group. VEGF values were significantly higher in the aMM group than in the rMM group (310.8 ± 136.1 pg/ml vs. 183.0 ± 48.27 pg/ml, $p<0.001$) or the MGUS group (310.8 ± 136.1 pg/ml vs. 175.6 ± 46.77 pg/ml, $p<0.001$).

4 Discussion

Our data show that the microcirculation is strictly linked to VEGF production. This cytokine is related to all parameters that we measured. Even if capillary blood flow and $TcpO_2$ are not greatly reduced, the correlation with VEGF suggests two hypotheses:

1. In MM, the microcirculation is not significantly modified.
2. Cytokines produced by PCs induce an increase in blood flow adequate for peripheral tissue requirements.

The first hypothesis is supported by the lack of correlation between the M-component, blood flow and $TcpO_2$ in aMM. On the other hand, the correlation between $TcpO_2$ and M-component in rMM and MGUS indicates the microcirculation is not completely independent in the MM disease. In fact, we found a significant correlation of VEGF with the parameters studied in all groups, leading to the conclusion that VEGF exerts an important effect on both the bone marrow circulation and the peripheral circulation.

MM also interferes with the RBC surface membrane. The increased aggregability we found indicates a change in the RBCs which is not only in the endothelium. It is possible that MM activates intracellular pathways that induce cell membrane modifications. Many authors think that the M-component is the base of the hyperviscosity syndrome [5]. Our data show that there is a correlation between RBC aggregability and VEGF values but there is no correlation with the M-component as suggested in the literature [5–8]. Maybe the M-component interferes with the plasma viscosity only if there is a big amount. The deformability is not modified by VEGF. This is important because this property of RBCs is necessary to access the capillary. This may explain why $TcpO_2$ level was adequate while the Hb value was not significantly lower. However, Hb is necessary for peripheral oxygenation and this would account for the correlation between $TcpO_2$ and Hb in rMM and MGUS whilst it is not present in aMM. The good $TcpO_2$ is possibly due to the good peripheral blood supply supplying nutrients to the peripheral cells even though Hb is decreased.

In the end, $TcpO_2$ values in aMM are similar to those in rMM and MGUS.

The blood flow is regulated by vessel diameter, as the result of the interaction of numerous patterns (metabolic, nervous, mechanical). The data show that in aMM there is an increase in blood flow in both stress tests, but there is no significant

difference between the values of these increases. However, in aMM we found a significant increase in muscular stress that is not found in heat stress. This test demonstrates nervous capacity to vary vessel diameter to increase the blood flow if there is an increase in skin temperature. This phenomenon may be due to nerve damage that is present in MM due to the disease itself or to the therapy (Bortezomib or Thalidomide) [9, 10].

From our results, we can speculate about possible microcirculatory modifications that are related to MM. Vacca et al. showed that MM alters microcirculation in peritumoural areas to increase the oxygen and glycogen supply (angiogenesis) [3, 4, 11, 12]. Analysis of the microcirculatory changes in the body close to the tumour and also peripherally could lead to a better understanding of how the tumour interferes with healthy tissue and how therapeutic measures may interfere with the patients' quality of life. However, further, larger-scale studies will be required for a full understanding of the events during neoplasia and to lead to the creation of "smart" drugs.

References

1. Landgren O, Kyle RA, Pfeiffer RM et al (2009) Monoclonal gammopathy of undetermined significance (MGUS) consistently precedes multiple myeloma: a prospective study. Blood 113:5412–5417
2. Weiss BM, Abadie J, Verma P et al (2009) A monoclonal gammopathy precedes multiple myeloma in most patients. Blood 113:5418–5422
3. Vacca A, Ribatti D, Roncali L, Ranieri G, Serio G, Silvestris F, Dammacco F (1994) Bone marrow angiogenesis and progression in multiple myeloma. Br J Haematol 87:503–508
4. Ria R, Roccaro AM, Merchionne F, Vacca A, Dammacco F, Ribatti D (2003) Vascular endothelial growth factor and its receptors in multiple myeloma. Leukemia 17:1961–1966
5. Baskurt O (2007) Mechanisms of blood rheology alterations. In: Baskurt O, Hardeman M, Rampling M, Meiselman H (eds) Handbook of hemorheology and hemodynamics. IOS Press, Amsterdam, pp 170–190
6. Tran-Soy-Tay R, Nash GB (2007) Mechanisms in hemorheology. In: Baskurt O, Hardeman M, Rampling M, Meiselman H (eds) Handbook of hemorheology and hemodynamics. IOS Press, Amsterdam, pp 137–152
7. Barosi G et al (2004) Management of multiple myeloma and related-disorders: guidelines from the Italian Society of Hematology (SIE), Italian Society of Experimental Hematology (SIES) and Italian Group for Bone Marrow Transplantation (GITMO). Haematologica 89:717–741
8. Eby CS (2007) Bleeding and thrombosis risks in plasma cell dyscrasias. Hematology 2007: 158–164
9. Steck AJ (1998) Neurological manifestations of malignant and non-malignant dysglobulinaemias. J Neurol 245:634–639
10. Dispenzieri A, Kyle RA (2005) Multiple myeloma: clinical features and indications for therapy. Best Pract Res Clin Haematol 18:553–568
11. Vacca A, Iurlaro M, Ribatti D, Minischetti M, Nico B, Ria R et al (1999) Bone marrow neovascularization, plasma cell angiogenic potential and matrix metalloproteinase-2 secretion parallel progression of human multiple myeloma. Blood 93:3064–3073
12. Vacca A, Ria R, Ribatti D, Semeraro F, Djonov V, Di Raimondo F et al (2003) A paracrine loop in the vascular endothelial growth factor pathway triggers tumor angiogenesis and growth in multiple myeloma. Haematologica 88:176–185

Chapter 24
Impact of Environmental Parameters on the Activity of the P-Glycoprotein

Philipp Trach, Nuse Afahaene, Martin Nowak, and Oliver Thews*

1 Introduction

Due to pronounced hypoxia in many tumors the cells force glycolytic metabolism leading to an acidic environment, low glucose and high lactate levels as well as ATP depletion [1]. In addition, intermittent blood flow in solid tumors [2] results in ischemia–reperfusion and by this force the formation of reactive oxygen species (ROS) [3]. These adverse parameters of the tumor microenvironment affect the efficacy of several nonsurgical treatment modalities such as radio- or chemotherapy.

Chemoresistance of tumors is (at least partially) caused by an overexpression of drug transporters which pump xenobiotics actively out of the cell. The most important member of these transporters is the P-glycoprotein (Pgp) responsible for the phenomenon of multidrug resistance [4]. In former studies, it has been shown that the functional activity of the Pgp depends on the extracellular pH [5, 6]. Under acidotic conditions (commonly found in solid growing tumors), the transport activity is more than doubled leading to a reduced chemosensitivity of the tumor. The increased transport rate is here the result of a functional activation and not caused by Pgp expression or protein translocation to the cell membrane [6].

The question arises whether other abnormal parameter of the tumor metabolic microenvironment also affect the Pgp activity and may also amplify the chemoresistance. For this reason, the aim of the present study was to analyze whether low

*This study forms part of the doctoral thesis of Philipp Trach.

P. Trach • N. Afahaene • M. Nowak
Institute of Physiology and Pathophysiology, University Medicine,
Duesbergweg 6, 55099 Mainz, Germany

O. Thews (✉)
Institute of Physiology and Pathophysiology, University Medicine,
Duesbergweg 6, 55099, Mainz, Germany
e-mail: oliver.thews@medizin.uni-halle.de

M. Wolf et al. (eds.), *Oxygen Transport to Tissue XXXIII*, Advances in Experimental Medicine and Biology 737, DOI 10.1007/978-1-4614-1566-4_24,

glucose or high lactate concentrations (as a result of tumor hypoxia) or reactive oxygen species (resulting from ischemia–reperfusion or ROS-generating treatment modalities) alter the functional Pgp transport rate in vitro.

2 Materials and Methods

2.1 Tumor Model and Cell Incubation

In all experiments, the subline AT1 of the R3327 Dunning prostate carcinoma was used. This cell line is known to functionally express the P-glycoprotein [5]. Cells were grown in RPMI 1640 medium supplemented with 10% fetal calf serum (FCS) at 37°C under a humidified 5% CO_2 atmosphere and passaged once per week. Twenty-four hours prior to the experiments, cells were transferred to RPMI medium without FCS supplementation. The medium was buffered with 20 mM HEPES adjusted to a pH of 7.4.

For the experiments cells were incubated for 3 h with medium without glucose (replaced by mannit to maintain osmolarity), 10 or 20 mM Na–lactate or 50 μM H_2O_2. In some experiments, the adverse concentrations were kept for up to 24 h.

2.2 Measurement of the Pgp Transport Activity

The Pgp activity was assessed by determining the efflux rate of a fluorescent substrate (daunorubicin [DNR]) in the presence or absence of a specific inhibitor (verapamil [VPL]) [7]. For this, cells were incubated with daunorubicin at a final concentration of 4 μM for 30 min at 37°C. In a second set of experiments, cells were incubated with a combination of DNR (4 μM) and VPL at a concentration of 10 μM. The intracellular daunorubicin concentration after incubation was assessed by measuring the daunorubicin-induced fluorescence by flow cytometry at an excitation wavelength of 488 nm and an emission wavelength of 575 nm. Since VPL inhibits the active efflux of daunorubicin, the intracellular concentration will be higher in the presence of verapamil. The DNR concentration ratio in the presence and absence of VPL ($FL_{DNR+VPL}/FL_{DNR}$) can therefore be used as an indirect measure of Pgp activity [7].

2.3 Measurement of the Pgp-Dependent Chemoresistance and Pgp Expression

The chemosensitivity of the cells was assessed either by counting the number of surviving cells after chemotherapy or by determining the caspase 3-activity as a measure of apoptosis. For cell survival, cells were incubated under different

environmental conditions followed by a second incubation with daunorubicin (4 μM) with or without verapamil (10 μM) also for 3 h. Thereafter, cells were kept under normal FCS-containing medium for 42 h and the number of cells was determined using a cell counter. For the apoptosis, assay cells were treated in the same manner. The caspase 3-activity was measured by adding the substrate DVED-AFC and determining the cleaved AFC with a fluorescence plate-reader. In the tumor model used, a linear correlation between the intracellular daunorubicin concentration and the apoptosis induction exists [6].

The cellular expression of Pgp was determined by Western blot analysis. After incubation for the respective time interval with H_2O_2-containing medium cells were lysated, the proteins were electrophoretically separated and blotted. For immunodetection of the Pgp the bands were stained using a Pgp-specific antibody (clone D11, Santa-Cruz) or (as a control) anti-β-actin antibody (clone I-19, Santa-Cruz). After reaction with the secondary antibody, bands were visualized and quantified with an imaging system.

3 Results

Since the P-glycoprotein is an ATP-dependent transporter, complete glucose deprivation was expected to reduce the activity of the pump. Medium without glucose led to a reduction of the cellular ATP level by 45% within 3 h from 4.1 ± 0.5 μmol/g protein to 2.3 ± 0.3 μmol/g (which corresponds roughly to an ATP concentration in a solid tumor of 1.01 ± 0.12 μmol/g tissue and 0.56 ± 0.06 μmol/g, respectively, values which are comparable to in vivo results) (Fig. 24.1a). Simultaneously, the

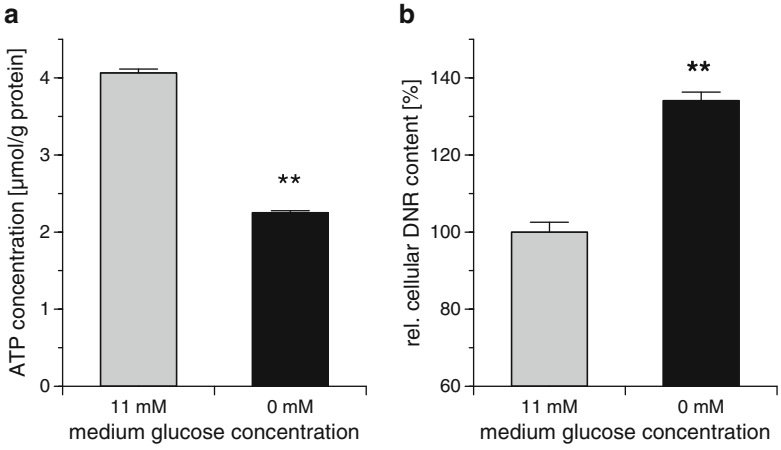

Fig. 24.1 (**a**) Cellular ATP content and (**b**) intracellular daunorubicin concentration in AT1 cells kept in medium with or without glucose for 3 h. Columns show mean ± SEM of at least 17 experiments. $^{**}p < 0.01$

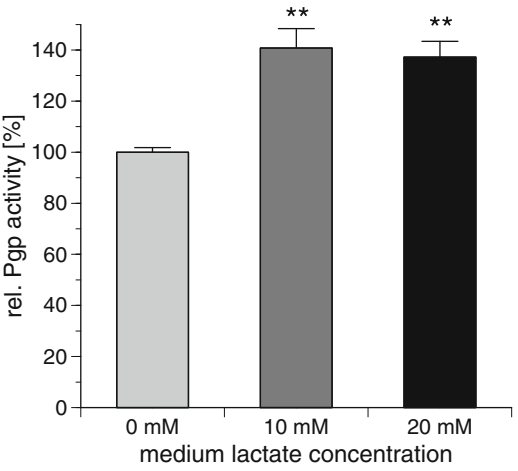

Fig. 24.2 Relative Pgp activity (measured by the daunorubicin efflux in the absence and presence of the Pgp inhibitor verapamil) normalized to cells kept under control conditions without any lactate. Columns show mean ± SEM of eight experiments. $^{**}p < 0.01$

intracellular concentration of a chemotherapeutic drug (daunorubicin) which is a substrate of the Pgp increased by 35% (Fig. 24.1b). From these results, it was postulated that low glucose levels reduce the ATP concentration and by this decreases the Pgp activity resulting in higher intracellular drug concentration. However, measuring the Pgp-dependent efflux rate showed no difference between the condition with glucose (rel. Pgp activity 100 ± 1%) and without glucose (96 ± 2%). As a consequence of the higher intracellular daunorubicin concentration in the absence of glucose, the cytotoxicity of the treatment was increased. The number of surviving tumor cells 42 h after chemotherapy was 55 ± 2% of the untreated control in the presence of glucose and 49 ± 1% without glucose ($p < 0.01$).

On the other hand, increased lactate levels of 10 or 20 mM increase the transport activity of the P-glycoprotein moderately by 40% which is a much smaller effect than with extracellular acidosis where the Pgp transport rate increased by 140% [5, 6]. The higher activity with lactate cannot be attributed to a change in pH since Na–lactate was added and the medium was buffered to pH 7.4.

Incubating the cells with H_2O_2 (50 μM) for 3 h lowered the Pgp transport rate down to 85 ± 6% of the control level. This reduction was not the consequence of a change in protein expression as indicated by the Western blot analysis which showed an unchanged protein level independent on the H_2O_2 incubation. The Pgp expression stayed on the control level for up to 24 h. The consequence of a reduced drug export by Pgp is an increase in cytotoxicity. In order to assess the impact of Pgp-mediated transport on the chemoresistance, the caspase 3-activity after daunorubicin treatment with or without the Pgp inhibitor verapamil (VPL) was measured. Since Pgp actively exports the drug out of the cell co-incubation with VPL increases the cytotoxicity. The ratio of caspase 3-activity with and without VPL acts as a measure of Pgp-mediated chemoresistance. Incubating cells with H_2O_2 for 3 h increased this ratio markedly (Figs. 24.2 and 24.3).

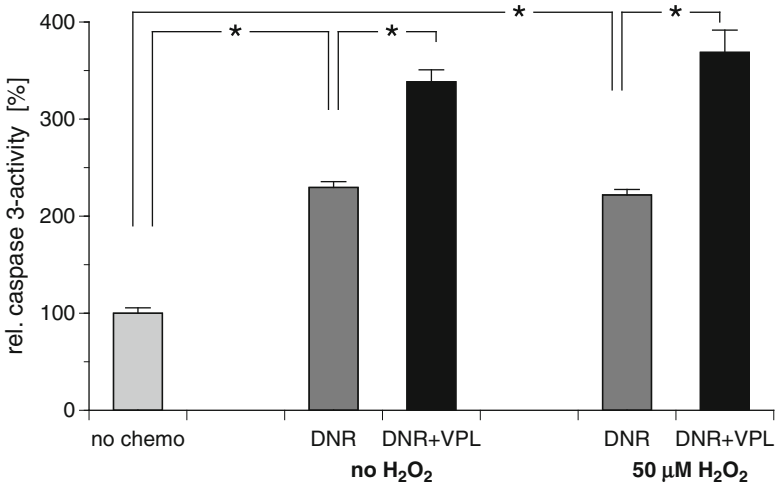

Fig. 24.3 Cytotoxicity of daunorubicin (DNR) measured by caspase 3-activity in AT1 cells supplemented with 50 µM H_2O_2 for 3 h. In order to quantify the Pgp-induced chemoresistance, cells were also incubated with the Pgp inhibitor verapamil (VPL). Columns show mean ± SEM of four experiments. *$p < 0.05$

4 Discussion

Multidrug resistance is a major problem in chemotherapeutic cancer treatment. Overexpression of the P-glycoprotein in several tumor entities leads to a reduced intracellular drug concentration followed by a decrease in cytotoxicity [4]. Besides constitutional differences in Pgp expression between individual tumors the expression and function can be modulated, e.g., by cytokines (IL-1β, IL-6). Recent studies demonstrated that the extracellular tumor pH affects the functional activity but not the expression. Acidosis with an pH of 6.5 led to more than a doubling of the transport rate [5, 6]. The origin of acidosis is multifactorial and can be caused by glycolysis (anaerobic or aerobic), other nonglycolytic metabolic changes or inflammation.

Since Pgp uses ATP as an energy source, ATP depletion has been proposed as a mechanism counteracting chemoresistance [8]. In the present study, complete absence of glucose in the medium resulted in a 50% reduction in the ATP level (Fig. 24.1a) which was not sufficient to reduce Pgp activity. Xu and coworkers found a marked increase in chemosensitivity only if the ATP level was reduced by more than 90% which cannot be achieved by glucose depletion. Obviously, the cell uses other energy sources (e.g., amino acids, fatty acids). Surprisingly, even the Pgp activity remained constant the intracellular daunorubicin content increased under these conditions (Fig. 24.1b). The cause of this finding remains unclear at the moment. However, the increased drug level increased the cytotoxicity. Ledoux and coworkers [9] described an increase in Pgp expression after glucose deprivation of more than 18 h. The experiments of the present study have also been carried out up

to 24 h (data not shown) but no increase in Pgp transport rate was observed. Ledoux et al. only measured the protein expression but not the Pgp function which could explain the contradictory results.

On the other hand, increasing the extracellular lactate concentration (but not decreasing the pH) to 10 or 20 mM (values which are commonly found in hypoxic tumors [10]) increased the Pgp transport rate marginally by up to 40%. This value is in the same range as Pgp changes found by severe hypoxia ($pO_2 < 0.5$ mmHg) [11]. However, the increase which is much smaller than that found with extracellular acidosis was not able to reduce the intracellular daunorubicin concentration or the cytotoxicity (data not shown). The mechanism by which lactate alone may improve Pgp-mediated drug efflux remains unclear.

The final parameter studied was the impact of reactive oxygen species (ROS) which can result either from ischemia–reperfusion within the tissue or by ROS-inducing treatments [12]. Previous studies showed that ROS induced by hyperthermia may increase Pgp expression (via a p38-mediated pathway) [12]. In the present study, external supply of H_2O_2 had practically no impact on the Pgp expression even over a period of 24 h (data not shown). The discrepancy in this finding might be the result from differences in either the mechanism of ROS induction (internal by hyperthermia vs. external H_2O_2) or by the amount of radicals induced. In contrast to the study of Wartenberg et al. [12], in the present study the functional transport rate was measured. The data reveal that H_2O_2 has an unspecific inhibitory effect resulting in a 15% decrease in transport rate. The reduced export of chemotherapeutics results in an increased chemosensitivity (Fig. 24.3). The higher rate of apoptosis induction could also be the result of a direct cell damage by ROS. However, previous experiments clearly show that at a dose of 50 μM H_2O_2 has practically no direct cell-killing effect (data not shown). This was the reason for choosing the dose. From these results, it might be obvious that ROS induction in tumors may be beneficial with respect to multidrug resistance.

In conclusion, the present study shows that the abnormal metabolic microenvironment in tumors affects the activity of drug transporters which might have an influence on the cytotoxicity of chemotherapy. Low glucose as well as ROS may slightly increase the intracellular drug concentration and by this increase chemosensitivity. However, the effects of these parameters are much less pronounced as compared with the impact of extracellular acidosis [5, 6].

Acknowledgments This study was supported by Deutsche Krebshilfe (grants 106774/109136).

References

1. Vaupel P, Kallinowski F, Okunieff P (1989) Blood flow, oxygen and nutrient supply, and metabolic microenvironment of human tumors: a review. Cancer Res 49:6449–6465
2. Bussink J, Kaanders JH, Rijken PF et al (1998) Multiparameter analysis of vasculature, perfusion and proliferation in human tumour xenografts. Br J Cancer 77:57–64

3. Brown NS, Bicknell R (2001) Hypoxia and oxidative stress in breast cancer. Oxidative stress: its effects on the growth, metastatic potential and response to therapy of breast cancer. Breast Cancer Res 3:323–327
4. Higgins CF (2001) ABC transporters: physiology, structure and mechanism - an overview. Res Microbiol 152:205–210
5. Thews O, Gassner B, Kelleher DK et al (2006) Impact of extracellular acidity on the activity of p-glycoprotein and the cytotoxicity of chemotherapeutic drugs. Neoplasia 8:143–152
6. Sauvant C, Nowak M, Wirth C et al (2008) Acidosis induces multi-drug resistance in rat prostate cancer cells (AT1) in vitro and in vivo by increasing the activity of the p-glycoprotein via activation of p38. Int J Cancer 123:2532–2542
7. Kunikane H, Zalupski MM, Ramachandran C et al (1997) Flow cytometric analysis of p-glycoprotein expression and drug efflux in human soft tissue and bone sarcomas. Cytometry 30: 197–203
8. Xu RH, Pelicano H, Zhou Y et al (2005) Inhibition of glycolysis in cancer cells: a novel strategy to overcome drug resistance associated with mitochondrial respiratory defect and hypoxia. Cancer Res 65:613–621
9. Ledoux S, Yang R, Friedlander G et al (2003) Glucose depletion enhances P-glycoprotein expression in hepatoma cells: role of endoplasmic reticulum stress response. Cancer Res 63: 7284–7290
10. Vaupel P, Schaefer C, Okunieff P (1994) Intracellular acidosis in murine fibrosarcomas coincides with ATP depletion, hypoxia, and high levels of lactate and total Pi. NMR Biomed 7:128–136
11. Thews O, Gassner B, Kelleher DK et al (2008) Activity of drug efflux transporters in tumor cells under hypoxic conditions. Adv Exp Med Biol 614:157–164
12. Wartenberg M, Gronczynska S, Bekhite MM et al (2005) Regulation of the multidrug resistance transporter P-glycoprotein in multicellular prostate tumor spheroids by hyperthermia and reactive oxygen species. Int J Cancer 113:229–240

Chapter 25
3-D High-Resolution Mapping of the Heterogeneity in Mitochondrial Redox State of Human Breast Tumor Xenografts

H.N. Xu, S. Nioka, B. Chance, and L.Z. Li

1 Introduction

The high variability in disease presentation and course is a hallmark of cancer [1], and intratumor heterogeneity or diversity has been associated with tumor progression/aggressiveness [2–4]. It is therefore of great interest to reveal the characteristics in tumor heterogeneity in various aspects including structure, function, and genetics. For example, tissue oxygenations measured under clinical settings were more heterogeneous in tumors than in normal tissue, and the intertumor variability of tissue oxygenation was more pronounced than intratumor heterogeneity; furthermore, variations of pO_2 measured by needle electrodes within breast tumors did not correlate with the measuring site (tumor center versus periphery) [5, 6].

Our previous work showed mitochondrial redox state and its heterogeneity in tumor tissue provide sensitive and potentially diagnosis-useful characteristics for differentiating among five human melanoma mouse xenografts and between two breast tumor mouse xenografts with different metastatic potentials [7, 8]. In those studies, the aggressive human cancer mouse xenografts have localized areas where higher Fp redox ratio, Fp/(Fp + NADH) exists (usually in their cores), resulting in a bi-modal distribution of Fp redox ratio in the histogram of a tumor section image. These results suggest that the redox state of the oxidized tumor core could be used to grade tumor aggressiveness of human melanoma and breast cancer. However, the tumors in those studies were only imaged for two to nine sections with various tissue depths less than ~4 mm.

H.N. Xu • L.Z. Li (✉)
Department of Radiology, School of Medicine, University of Pennsylvania,
423 Guardian Drive, Philadelphia, PA 19014, USA
e-mail: linli@mail.med.upenn.edu

S. Nioka • B. Chance
Department of Biochemistry and Biophysics, School of Medicine,
University of Pennsylvania, Philadelphia, PA, USA

M. Wolf et al. (eds.), *Oxygen Transport to Tissue XXXIII*, Advances in Experimental Medicine and Biology 737, DOI 10.1007/978-1-4614-1566-4_25,

To aid our full understanding of the tumor redox state, it would be very informative to quantitatively reveal how mitochondrial redox state varies in 3D within an entire tumor. In the present study, we report our preliminary results of mapping intratumor heterogeneity in mitochondrial redox state at a high spatial resolution (50 μm in-plane resolution with a section thickness down to 20 μm achievable) of the entire tumor for three human breast cancer lines having ascending order of aggressiveness: MCF-7 < MDA-MB-468 ≤ 231? (see Discussion section).

2 Methods

Three human breast cancer xenografts MCF-7, MDA-MB-468, and MDA-MB-231 were allowed to grow to 6–10 mm in diameter. The tumor-bearing mice under anesthesia were snap-frozen with liquid nitrogen to maintain the *in vivo* mitochondrial redox state for the *ex vivo* redox scanning. The preparation of samples for redox scanning were previously described [8, 9]. Briefly, the excised frozen tumors were embedded with chilled mounting buffer (ethanol–glycerol–water in 10:30:60). Frozen reference standards (one for NADH and one for Fp with known concentrations) were quickly mounted adjacent to the tissue.

The low-temperature redox scanner [10–12] was employed to obtain multi-slice fluorescence images NADH and Fp. The tumor samples ($N = 1$ for each tumor line) were scanned section by section with a total of 11–14 sections per tumor at different depths (d) with 400 μm spacing. The scanning matrix was 64 × 64 with a step size of 200 μm. The nominal concentrations of NADH and Fp in tissue were interpreted using reference standards and used to calculate the Fp redox ratio, Fp/(NADH + Fp), representing the mitochondrial redox state.

3 Results

The results (typical ones are shown in Fig. 25.1) revealed that both aggressive tumor tissues (MDA-MB-231 and MDA-MB-468) displayed distinct heterogeneity in the distributions of NADH, Fp and Fp redox ratio in each section, with a localized area (usually tumor core) exhibiting much higher Fp redox ratio than other regions (usually tumor rim); the indolent MCF-7 tumor displayed a relatively less heterogeneous distribution in Fp, NADH, and Fp redox ratio in each section, with lower Fp redox ratios on average than those oxidized regions of aggressive tumors.

Figure 25.2 depicts the depth-dependence of the three redox indices in the three tumors. Table 25.1 presents the mean values of the redox indices. The heterogeneities between tumor sections are shown.

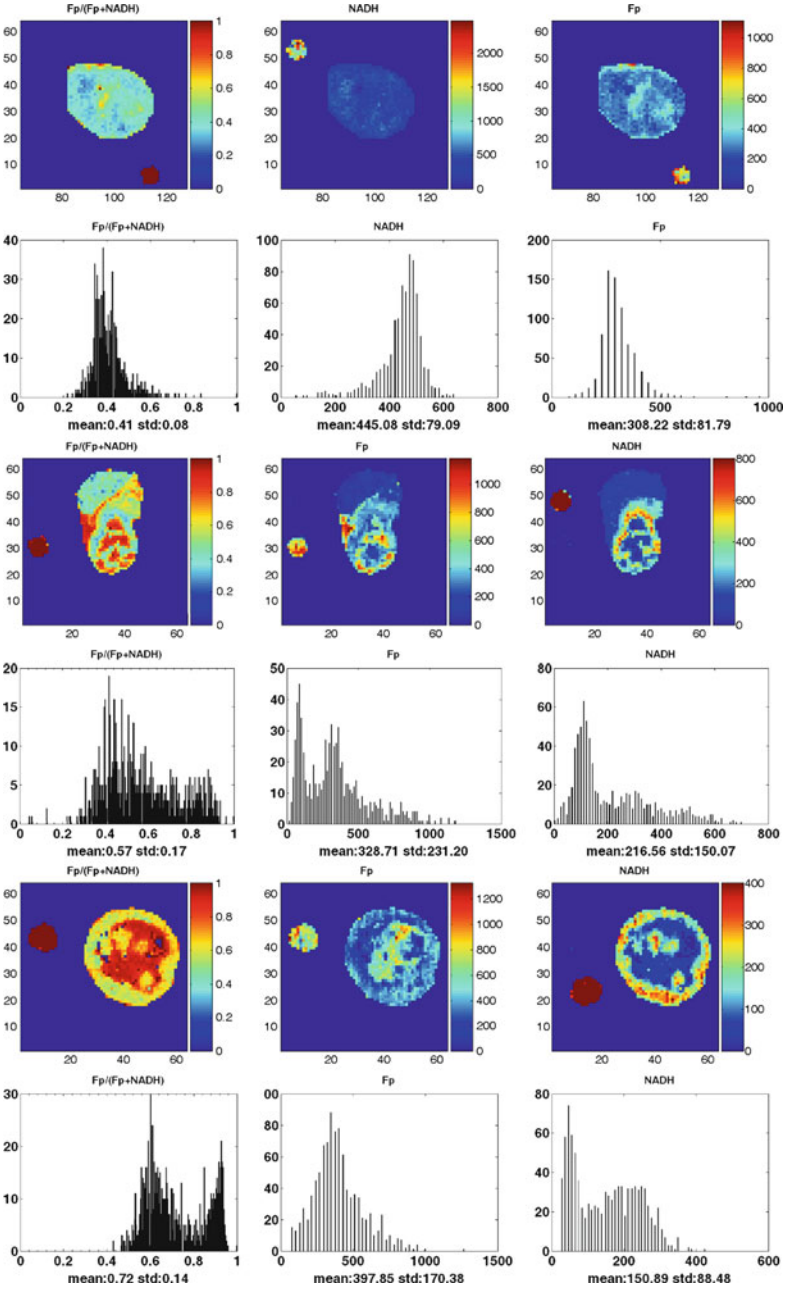

Fig. 25.1 Typical images of redox scanning of the mouse xenografts of MCF-7 (*top two rows*, $d = 1{,}400$ μm); MDA-MB-468 (*middle two rows*, $d = 1{,}400$ μm); MDA-MB-231 (*bottom two rows*, $d = 3{,}600$ μm) tumor lines. The Fp or NADH redox ratio ranges between 0 and 1; the Fp or NADH images are in the unit of μM in reference to the corresponding standards. The *x*-axes of the corresponding histograms represent the Fp redox ratio or concentration. The *y*-axes represent the number of pixels in the tumor sections having a specific value of Fp redox ratio or concentration. The small round spots outside the tumor sections are the images of Fp or NADH reference standards. The image matrix was 64×64 with a resolution of 200 μm

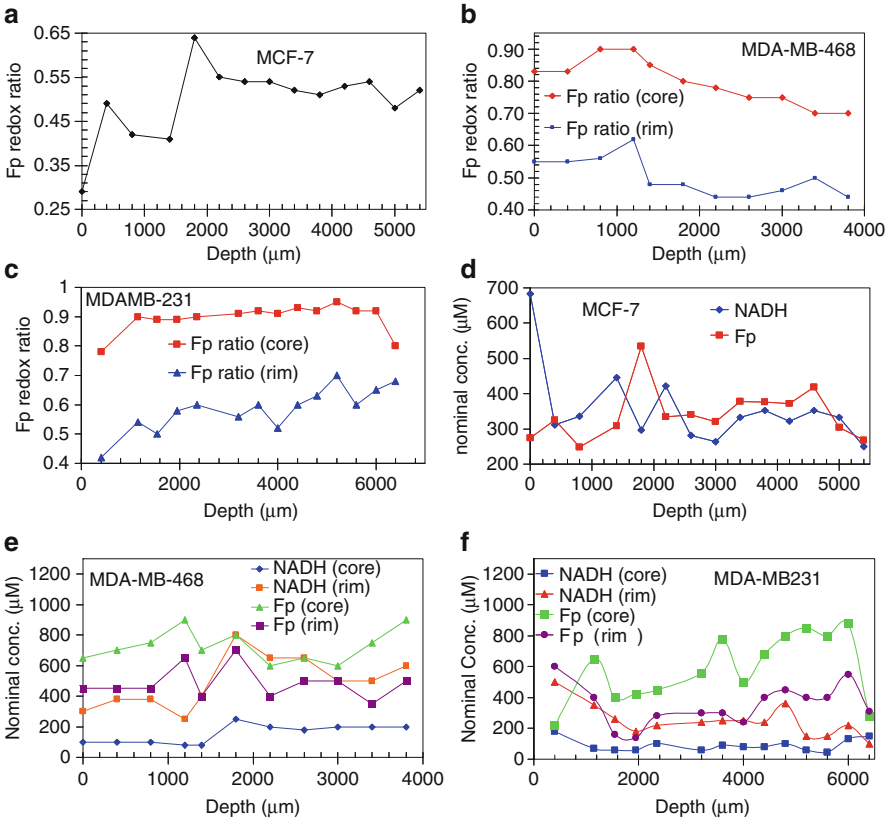

Fig. 25.2 Depth-dependent redox indices. The Fp redox ratios (**a-c**) and the Fp and NADH nominal concentrations in μM (**d-e**) at different depths of the three tumors: MCF-7, MDA-MB-468, and MDA-MB-231

Table 25.1 Mean values of the redox indices, where Fp and NADH are nominal concentrations in μM in reference of the respective solution standards

	Fp redox ratio (core)	Fp redox ratio (rim)	Fp (core)	Fp (rim)	NADH (core)	NADH (rim)
*MCF-7	0.53 ± 0.06	0.53 ± 0.06	359 ± 72	359 ± 72	332 ± 61	332 ± 61
MDA-MB-468	0.78 ± 0.07	0.50 ± 0.06	727 ± 106	486 ± 105	154 ± 62	492 ± 169
MDA-MB-231	0.91 ± 0.04	0.61 ± 0.05	636 ± 203	343 ± 112	87 ± 32	215 ± 69

*MCF-7 tumor had no core-rim difference therefore the overall averages were provided instead

4 Discussion

As revealed in our previous studies, mitochondrial redox state in tumor tissue was associated with melanoma and breast tumor metastatic potentials [7, 8]. Imaging intratumor heterogeneity in mitochondrial redox state in tumor tissue may provide

useful information for understanding tumor aggressiveness. This is the first study to reveal the 3D distribution of the mitochondrial redox state and Fp and NADH nominal concentration in an entire breast tumor xenograft. This study allows the comparison among the redox images of three breast cancer xenografts with ascending aggressiveness MCF-7 < MDA-MB-468 < MDA-MB-231 according to cancer literatures. Both MDA-MB-468 and MDA-MB-231 cells are triple-negative cells [13–15] and they belong to aggressive tumors. Although MDA-MB-468 cells are not as aggressive as MDA-MB-231 cells as determined by the Boyden Chamber method [16, 17], under chemotaxis condition the MDA-MB-468 cells become much invasive [17]. Thus the result in this study is consistent with what we obtained in our previous studies: aggressive tumors exhibit more oxidized redox state in some tumor regions.

5 Conclusions

In this paper, we reported the preliminary results on 3D high-resolution mapping of mitochondrial redox state of three breast tumor xenografts MCF-7, MDA-MB-468, and MDA-MB-231 having ascending aggressiveness. Heterogeneity in mitochondrial redox state in entire tumors was revealed for the first time. The work is in progress to study more breast tumor xenografts and identify imaging biomarkers that may benefit basic research, clinical diagnosis, and therapy of breast cancer.

Acknowledgments This work was supported by the Susan G. Komen Foundation Grant KG081069 (PI: L.Z. Li), the Center for Magnetic Resonance and Optical Imaging - a NIH supported research resource RR02305 (PI: R. Reddy), the SAIR grant 2U24-CA083105 (PI: J.D. Glickson and L.A. Chodosh).

References

1. Heppner GH, Miller FR (1998) The cellular basis of tumor progression. Int Rev Cytol 177:1–56
2. Heppner GH (1984) Tumor heterogeneity. Cancer Res 44:2259–2265
3. Allred DC, Wu Y, Mao S et al (2008) Ductal carcinoma in situ and the emergence of diversity during breast cancer evolution. Clin Cancer Res 14:370–378
4. Park SY, Lee HE, Li H et al (2010) Heterogeneity for stem cell-related markers according to tumor subtype and histologic stage in breast cancer. Clin Cancer Res 16:876–887
5. Vaupel P, Hockel M, Mayer A (2007) Detection and characterization of tumor hypoxia using pO_2 histography. Antioxid Redox Signal 9:1221–1235
6. Vaupel P, Schlenger K, Knoop C et al (1991) Oxygenation of human tumors: evaluation of tissue oxygen distribution in breast cancers by computerized O_2 tension measurements. Cancer Res 51:3316–3322
7. Li LZ, Zhou R, Xu HN et al (2009) Quantitative magnetic resonance and optical imaging biomarkers of melanoma metastatic potential. Proc Natl Acad Sci U S A 106:6608–6613

8. Xu HN, Nioka S, Glickson JD et al (2010) Quantitative mitochondrial redox imaging of breast cancer metastatic potential. J Biomed Opt 15:036010
9. Xu HN, Wu B, Nioka S et al (2009) Calibration of redox scanning for tissue samples. Proceedings of Biomedical Optics in San Jose, CA, Jan. 24, Ed. SPIE 7174:71742F
10. Chance B, Schoener B, Oshino R et al (1979) Oxidation-reduction ratio studies of mitochondria in freeze-trapped samples NADH and flavoprotein fluorescence signals. J Biol Chem 254:4764–4771
11. Gu Y, Qian Z, Chen J et al (2002) High-resolution three-dimensional scanning optical image system for intrinsic and extrinsic contrast agents in tissue. Rev Sci Instrum 73:172–178
12. Li LZ, Xu HN, Ranji M et al (2009) Mitochondrial redox imaging for cancer diagnostic and therapeutic studies. J Innov Opt Health Sci 2:325–341
13. Köster F, Engel J, Schally A et al (2009) Triple-negative breast cancers express receptors for growth hormone-releasing hormone (GHRH) and respond to GHRH antagonists with growth inhibition. Breast Cancer Res Treat 116:273
14. Bartholomeusz C, Gonzalez-Angulo AM, Kazansky A et al (2010) PEA-15 inhibits tumorigenesis in an MDA-MB-468 triple-negative breast cancer xenograft model through increased cytoplasmic localization of activated extracellular signal-regulated kinase. Clin Cancer Res 16:1802–1811
15. Anders C, Carey LA (2008) Understanding and treating triple-negative breast cancer. Oncology (Williston Park) 22:1233–1239, discussion 1239–40, 1243
16. Freund A, Chauveau C, Brouillet JP et al (2003) IL-8 expression and its possible relationship with estrogen-receptor-negative status of breast cancer cells. Oncogene 22:256–265
17. Thompson EW, Paik S, Brunner N et al (1992) Association of increased basement membrane invasiveness with absence of estrogen receptor and expression of vimentin in human breast cancer cell lines. J Cell Physiol 150:534–544

Chapter 26
High-Resolution Simultaneous Mapping of Mitochondrial Redox State and Glucose Uptake in Human Breast Tumor Xenografts

H.N. Xu, G. Zheng, S. Nioka, B. Chance, and L.Z. Li

1 Introduction

Cancer metabolism has been an active research area for developing biomarkers for cancer diagnosis and treatment response. Early studies have systematically investigated the glucose uptake and spatial distribution of glucose in breast cancer animal models using a enzymatic bioluminescent imaging assay [1]. Heterogeneity in glucose uptake was shown in tumor xenografts [1,2]. Our previous work [3, 4] revealed that the mitochondrial redox state of tumor tissue was a sensitive indicator of tumor aggressiveness and the more aggressive tumors have localized core regions with a more oxidized redox state. To understand the nature of the oxidized tumor core of the aggressive tumors, we performed both H&E and TUNEL assays. The H&E staining revealed that the cells in the tumor core appeared to be pinkish, indicative of necrosis. However, the TUNEL and DAPI staining for both melanoma [5] and breast tumor [4] indicated a low level of cell death. So what is the metabolic status of the cells in the tumor core?

To answer this question, one can measure tumor glucose metabolism simultaneously with the mitochondrial redox state. The mitochondrial redox state of tissue can be measured by using the low-temperature NADH/Fp fluorescence redox scanner [6, 7]. Both NADH and Fp including FAD are intrinsic fluorescent molecules in the electron transport chain. The Fp redox ratio represented by Fp/(NADH + Fp) is

H.N. Xu • L.Z. Li (✉)
Department of Radiology, School of Medicine, University of Pennsylvania, Philadelphia, PA, USA
e-mail: linli@mail.med.upenn.edu

G. Zheng
Department of Medical Biophysics, University of Toronto, Toronto, ON, Canada

S. Nioka • B. Chance
Johnson Research Foundation, Department of Biochemistry and Biophysics, School of Medicine, University of Pennsylvania, Philadelphia, PA, USA

M. Wolf et al. (eds.), *Oxygen Transport to Tissue XXXIII*, Advances in Experimental Medicine and Biology 737, DOI 10.1007/978-1-4614-1566-4_26,

a sensitive indicator of mitochondrial redox state [8], and was linked to tumor metastatic potential as described in our previous work [3, 4]. FDG-PET provides information on glucose uptake/metabolism in cells and has been widely used for cancer diagnosis and staging because the abnormally high glucose uptake/consumption is a well-established metabolic hallmark of cancer cells. However, FDG-PET cannot be used for such a purpose due to its relatively low spatial resolution (4–6 mm for humans and 1–2 mm for small animals). The typical size of a tumor core can be ~3 mm or less [3, 4].

Previously, Zheng and co-workers have utilized the high-resolution redox scanner (resolution down to 50 μm) in combination with a near-infrared fluorescence imaging agent Pyro-2DG to simultaneously image both the redox state and glucose uptake of tumors in animal models [9]. It was shown that Pyro-2DG was selectively accumulated in tumor cells via the glucose transporters. Their results showed that the glucose uptake correlated well with the reduced redox state in 9 L glioma [9] and c-MYC-induced mammary tumor on transgenic mouse [10]. It was also shown that Pyro-2DG did not affect the redox state of tumor tissue [9].

Based on these evaluations, we aimed to employ the same method to quantitatively image Pyro-2DG uptake simultaneously with the mitochondrial redox state in the breast cancer mouse xenografts. Knowing the metabolic status of the tumor xenografts may help to gain further insight into breast tumor aggressiveness and progression.

2 Methods

The animal protocol of this study was approved by the Institutional Animal Care and Use Committee of the University of Pennsylvania. MDA-MB-231 tumors were grown in athymic nude mice (NCr nu/nu from US National Cancer Institute) as previously described [4]. Pyro-2DG was administered to the mice through a tail vein at ~2.5 mg/kg after the mice were starved for 24 h followed by anesthetization. In approximately 2 h, the mice were snap-frozen using liquid nitrogen to maintain the in vivo mitochondrial redox state for the ex vivo redox scanning. The preparation of samples for the redox scan were performed as previously described [4, 11]. Frozen reference standards (one NADH (1318 μM), one Fp (719 μM), and one pyro-2DG (21 μM)) were placed adjacent to the tissue for redox scanning.

Two MDA-MB-231 tumors (>10 mm in diameter and with an apparent necrotic center, average tumor volume = 989 mm^3) were imaged under the following instrument setup. The Fp excitation and emission channel filters were 430 nm ± 25 nm and 525 nm ± 32 nm, respectively; the NADH ones were 360 nm ± 13 nm and 430 nm ± 25 nm, respectively; the pyro-2DG ones were 430 ± 28 nm and 670DF23 nm. Multi-slice fluorescence images of NADH, Fp, and pyro-2DG were obtained section by section with 400 μm spacing. The scanning matrix was 128 × 64 or 128 × 128 with a resolution of 200 μm.

Customized-matlab software was used to analyze the data and construct the images. The nominal concentrations of NADH, Fp, and pyro-2DG in tissue were interpreted using the reference standards. The nominal concentrations of NADH, Fp,

and Pyro-2DG were used to calculate the redox ratios, i.e., Fp/(NADH + Fp) and NADH/(NADH + Fp), and normalized Pyro-2DG, i.e., Pyro-2DG/(NADH + Fp). Normalization of Pyro-2DG signals with respect to NADH + Fp is to account for the cell or mitochondria density difference at different regions of tumors.

3 Results

Figure 26.1 shows the typical redox and Pyro-2DG images of the mouse xenografts of MDA-MB-231 tumor lines, where the NADH, Fp, and Pyro-2DG images are shown in their nominal concentrations. The aggressive MDA-MB-231 tumors clearly showed bimodal distribution of NADH and Fp redox ratios indicating a more oxidized tumor core [4].

The Pyro-2DG images also revealed heterogeneity in Pyro-2DG uptake. In the tumor rim, the pattern of Pyro-2DG uptake appears to correlate more with the NADH distribution. Interestingly, the oxidized tumor core (higher Fp redox ratio) also showed areas with significant Pyro-2DG uptake.

4 Discussion

Tumor heterogeneity has long been recognized and should be addressed in cancer diagnosis and treatment. From our preliminary imaging results the heterogeneity in glucose uptake and redox state was clearly seen at 200 μm spatial resolution, which demonstrates the advantage of using the redox scanner for tissue imaging. Much of the image details would have been lost had the resolution been on the order of 1 mm or above.

The normalized Pyro-2DG uptake (Pyro-2DG/(NADH + Fp)) image may better represent the cellular metabolic activity than Pyro-2DG uptake, because the cell density in the tumor core is significantly less than that in the rim, particularly for large tumors (diameter >10 mm) as shown by the H&E staining of MDA-MB-231 tumor xenografts.

The typical Pyro-2DG images showed higher glucose uptake in the tumor rim and pronounce uptake in some regions of the tumor core, indicating that the cells in these regions are metabolically active. This is quite interesting and could be rather surprising as cells in the tumor core are often considered necrotic due to limited blood perfusion that usually happens for aggressive tumors in mouse xenografts [3, 12–14]. This result might support the notion that some cells in the core of aggressive tumor might be viable and in the redox state of State 3, where cells had sufficient nutrient resulting in rapid oxidative metabolism, instead of State 2, where cells were nutrient-starved [15–17]. We need to image more tumor samples to confirm the observation.

We recognize that the animal models here hardly resemble/represent the human tumors in the clinic. However, the animal models provide a research basis for us to understand the tumor metabolism and its roles in tumor progression and develop novel imaging methods/markers that may be translatable into the clinic eventually.

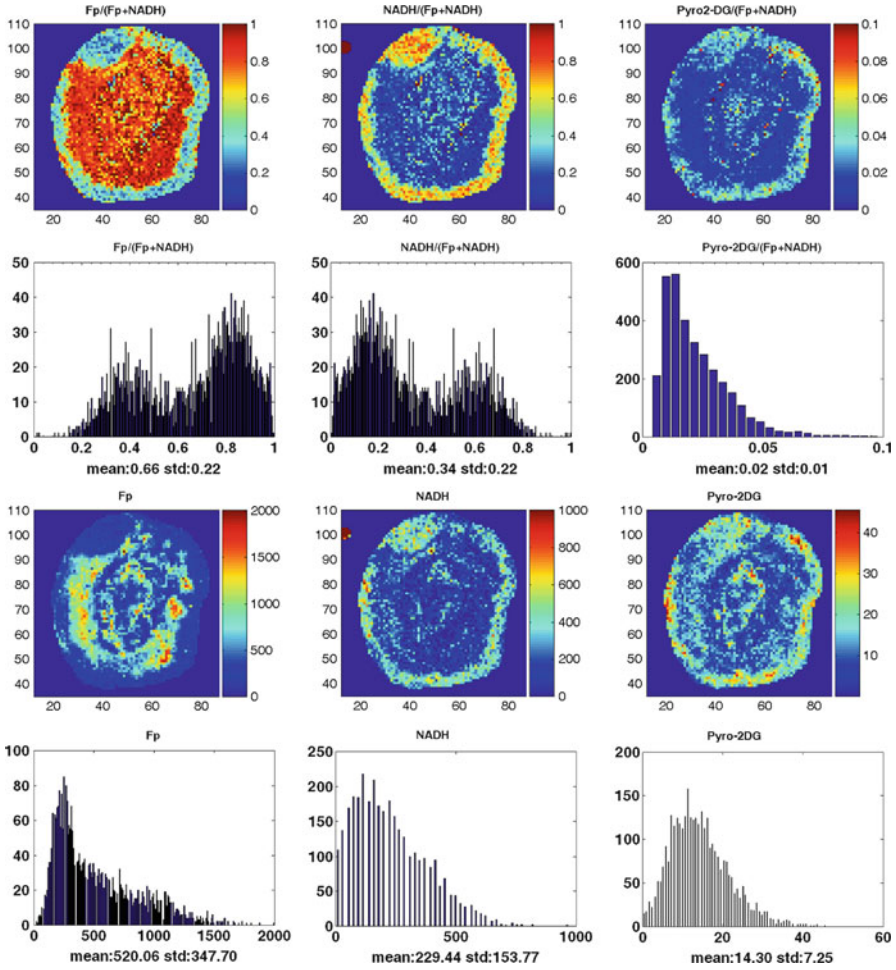

Fig. 26.1 Typical mitochondrial redox state and Pyro-2DG uptake images and their corresponding histograms of a representative MDA-MB-231 tumor (the tumor section had no scar). The Fp redox ratio, NADH redox ratio, and normalized Pyro-2DG range between 0 and 1; the Fp, NADH, and Pyro-2DG images are in the unit of μM in reference to the corresponding standards. The mean values and the corresponding standard deviations of these indices are also shown on the *x*-axes of the histograms. The *y*-axes represent the number of pixels in the tumor section having a specific value of the indices shown by the x-axes of the histograms

5 Conclusions

In this paper we reported our preliminary imaging findings of simultaneous mapping of mitochondrial redox state and glucose uptake in aggressive human breast tumor xenografts using the redox scanner. It was also observed that some areas in the oxidized core had significant Pyro-2DG uptake. Imaging the metabolic states of tumors

with high spatial resolution is significant for cancer diagnosis and treatment, such as developing imaging biomarkers for tumor stratification and treatment design.

Acknowledgments This work was supported by KG081069, NIH RR02305, and 2U24-CA083105. We thank Mr. Aron Roxin for synthesizing Pyro-2DG, Dr. Anatoliy Popov and Dr. Zhihong Zhang for Pyro-2DG solution preparation techniques.

References

1. Kallinowski F, Vaupel P, Runkel S et al (1988) Glucose uptake, lactate release, ketone body turnover, metabolic micromilieu, and pH distributions in human breast cancer xenografts in nude rats. Cancer Res 48:7264–7272
2. Dearling JLJ, Flynn AA, Sutcliffe-Goulden J et al (2004) Analysis of the regional uptake of radiolabeled deoxyglucose analogs in human tumor xenografts. J Nucl Med 45:101–107
3. Li LZ, Zhou R, Xu HN et al (2009) Quantitative magnetic resonance and optical imaging biomarkers of melanoma metastatic potential. Proc Natl Acad Sci U S A 106:6608–6613
4. Xu HN, Nioka S, Glickson JD et al (2010) Quantitative mitochondrial redox imaging of breast cancer metastatic potential. J Biomed Opt 15:036010
5. Xu HN, Zhou R, Nioka S et al (2009) Histological basis of MR/optical imaging of human melanoma mouse xenografts spanning a range of metastatic potentials. Adv Exp Med Biol 645:247–253
6. Quistorff B, Haselgrove JC, Chance B (1985) High spatial resolution readout of 3-D metabolic organ structure: an automated, low-temperature redox ratio-scanning instrument. Anal Biochem 148:389–400
7. Li LZ, Xu HN, Ranji M et al (2009) Mitochondrial redox imaging for cancer diagnostic and therapeutic studies. J Innov Opt Health Sci 2:325–341
8. Chance B, Schoener B, Oshino R et al (1979) Oxidation-reduction ratio studies of mitochondria in freeze-trapped samples NADH and flavoprotein fluorescence signals. J Biol Chem 254:4764–4771
9. Zhang M, Zhang Z, Blessington D et al (2003) Pyropheophorbide 2-deoxyglucosamide: a new photosensitizer targeting glucose transporters. Bioconjug Chem 14:709–714
10. Zhang Z, Liu Q, Luo Q et al (2003) 3D Imaging of the metabolic state of c-MYC-induced mammary tumor with the cryo-imager. Proceedings of in Ed. SPIE 4955:647–655
11. Xu HN, Wu B, Nioka S et al (2009) Quantitative redox scanning of tissue samples using a calibration procedure. J Innov Opt Health Sci 2:375–385
12. Bradley DP, Tessier JJ, Ashton SE et al (2007) Correlation of MRI biomarkers with tumor necrosis in Hras5 tumor xenograft in athymic rats. Neoplasia 9:382–391
13. Pedley RB, Hill SA, Boxer GM et al (2001) Eradication of colorectal xenografts by combined radioimmunotherapy and combretastatin a-4 3-O-phosphate. Cancer Res 61:4716–4722
14. Ranney D, Antich P, Dadey E et al (2005) Dermatan carriers for neovascular transport targeting, deep tumor penetration and improved therapy. J Control Release 109:222–235
15. Chance B, Williams GR (1955) Simple and rapid assay of oxidative phosphorylation. Nature 175:1120–1121
16. Chance B, Baltscheffsky H (1958) Respiratory enzymes in oxidative phosphorylation. VII. Binding of intramitochondrial reduced pyridine nucleotide. J Biol Chem 233:736–739
17. Chance B, Schoener B (1966) High and low energy states of cytochromes. J Biol Chem 241:4567–4573

Part III
Anemia and Hypoxia

Chapter 27
Regulation of Oxygen Delivery by the Reaction of Nitrite with RBCs Under Hypoxic Conditions

Joseph M. Rifkind, Maria T. Salgado, and Zeling Cao

1 Introduction

Nitric oxide (NO) as a vasodilator plays a major role in regulating blood flow and vascular tone [1]. The primary source for the synthesis of NO in the circulatory system involves endothelial nitric oxide synthase [2]. Since NO has a life time in plasma of <0.1 s [3], effective delivery of NO to the vasculature requires that NO is synthesized at the site where it is needed. This requirement limits the ability of endothelial nitric oxide synthase to supply the NO in the microcirculation where the reduced partial pressure of oxygen reduces the activity of nitric oxide synthase. To resolve this dilemma it has been proposed that red blood cells (RBCs) play a role in transporting NO to the vasculature. One of the several mechanisms proposed for RBC transport of NO involves the reduction of nitrite by deoxygenated hemoglobin back to NO [4, 5]. The feasibility of this mechanism, however, requires that the nitrite reduced back to NO is not quenched by hemoglobin (Hb). Although no satisfactory mechanism that explains how NO can escape from the RBCs without being quenched by Hb has been proposed, a number of studies indicate that the reaction of red cell Hb with nitrite does have a vascular effect. Deoxygenated hemoglobin binds to the cytoplasmic end of band 3 in the same region as glycolytic enzymes. Since the release of NO from Hb bound to the membrane can possibly diffuse out of the cell without reacting with Hb, a role for the known binding of Hb to the RBC membrane has been suggested by most investigators. However, the nanomolar range of RBC-NO found in vivo [4] would not be able to compete with the non-nitrite reacted Hb for the limited number of band 3 binding sites on the RBC membrane and a negligible fraction of the nitrite reacted Hb is expected to be on the membrane. This dilemma is in part resolved by recent studies [6], which indicate that nitrite

J.M. Rifkind (✉) • M.T. Salgado • Z. Cao
The Molecular Dynamics NIA/NIH, 251 Bayview Boulevard,
Baltimore, MD 21224, USA
e-mail: rifkindj@mail.nih.gov

M. Wolf et al. (eds.), *Oxygen Transport to Tissue XXXIII*, Advances in Experimental Medicine and Biology 737, DOI 10.1007/978-1-4614-1566-4_27,

reacted Hb has a much higher affinity for the red cell membrane than deoxyhemoglobin (deoxyHb). In this manuscript we review the data indicating an unusually high affinity of nitrite reacted Hb with the red cell membrane. We then propose two different pathways for nitrite induced vasodilation that result from nitrite reacted Hb interacting with the RBC membrane.

2 Methods

Male Wistar rats 250–350 g (3–4 month old) were housed and studied in accord with the NIH Guide for the Care and Use of Laboratory Animals, manual 3040-2 (1999) and approved by the Institutional Animal Care and Use Committee (protocol # 369-MDS-2010). RBCs were prepared by centrifuging the blood at 1,125 × *g* for 10 min at 4°C using an Allegra 21R centrifuge (Beckman Coulter, Fullerton, California). The plasma and buffy coat were removed by aspiration. Ghosts were prepared from RBCs hemolyzed by adding 5PBS8 (5 mM sodium phosphate, NaH_2PO_4, pH 8.0) in a 1:40 (RBC:buffer) volume ratio. White ghosts were prepared from these lysed cells by previously published procedures [7]. Hb was prepared from fresh RBCs as described earlier [5]. RBCs or Hb were deoxygenated in a Coy glove box (Coy Laboratory, Michigan), which uses a gas mixture of 5% hydrogen and 95% nitrogen together with a palladium catalyst to remove any residual oxygen. Cells or Hb were rocked for 2 h inside the glove box at 37°C for complete deoxygenation.

ATP levels were determined by the luciferin–luciferase luminescence technique using Invitrogen kits (Invitrogen, Carlsbad, California) with a reported sensitivity of 0.1 pmol. The assay for ATP was performed according to the manual provided with the kit. A suspension of RBCs (1% hct) in TBS (50 mM Tris–HCl, 150 mM NaCl, pH 7.4) was pre-equilibrated under anoxic conditions for 2 h at 37°C. Nitrite was then added to this suspension and rocked to initiate a reaction of nitrite with RBC Hb. The resultant 50 μM nitrite concentration corresponded to a 4:1 heme:nitrite molar ratio. The sample was equilibrated with nitrite for 30 min at 37°C and centrifuged at 2,200 × *g* for 3 min. The supernatants were analyzed for ATP by the luminescence method. The difference in ATP before nitrite incubation and 30 min after nitrite incubation measures the nitrite induced increase in the release of ATP.

Blood pressure was measured using CODA-6 pressure cuffs (Kent Scientific Co.), which were placed around the tail. Animals were given 10 min to stabilize followed by 5 min monitoring of the basal level of blood pressure. The change in blood pressure was then monitored for 15 min after 0.8 ml of nitrite reacted RBCs prepared under anoxia was injected into the femoral vein of the rat. The change in blood pressure was determined with and without the addition of apyrase (40 U/ml of 50% hct RBCs) to the RBCs before reacting with nitrite.

Analysis of NO was performed using a model 280 Nitric Oxide Analyzer (Sievers Instruments). The total heme associated NO was determined when the purge vessel contained 5.5 ml of 85% glacial acetic acid containing 100 mM sulfanilamide and 1.2 ml potassium ferricyanide (0.8 M). Prior to sample injection, the reagents in the

purge vessel are completely deoxygenated by flushing with argon. The concentration of heme-NO was determined by comparing the chemiluminescence signal obtained with data from a calibration curve generated by different concentrations of nitrite. For determinations of NO released from nitrite reacted Hb, 250 µl of the gas phase above the sample was injected into the purge vessel.

Deoxygenated Hb was reacted anaerobically with nitrite for 30–60 min. To determine the affinity of the nitrite reacted Hb for the membrane, 200 µl of white ghosts was added to a sample of nitrite reacted Hb. The reduction in heme-NO chemiluminescence when the sample was centrifuged indicates the amount of the nitrite reacted Hb bound to the membrane. With intact RBCs the binding of the basal RBC-NO to the membrane was determined by lysing the cells and comparing the total heme-NO chemiluminescence before and after centrifugation.

Origin 6.1 (Microcal Software, Northampton MA) was used for analysis of the data. Data are presented as means ± se. ANOVA and the paired Student's *t* test were used for comparing groups of samples with $P \leq 0.05$ considered statistically significant.

3 Results

3.1 Increased Membrane Affinity for NO Reacted Hemoglobin

RBCs contain 200–500 nM heme associated NO [4] and 20 mM total heme. Some of this NO is thought to be the result of the reaction of nitrite with Hb. Figure 27.1 shows that under anoxic conditions, a significant fraction of the total RBC heme-NO detected by chemiluminescence is associated with the membrane, as indicated by the reduced heme-NO detected in the supernatant when the sample was centrifuged.

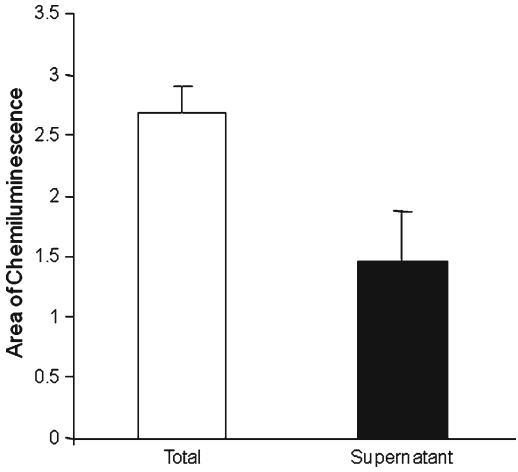

Fig. 27.1 Association of basal RBC heme-NO with the membrane. Heme-NO for lysed cells was determined by chemiluminescence before and after centrifugation

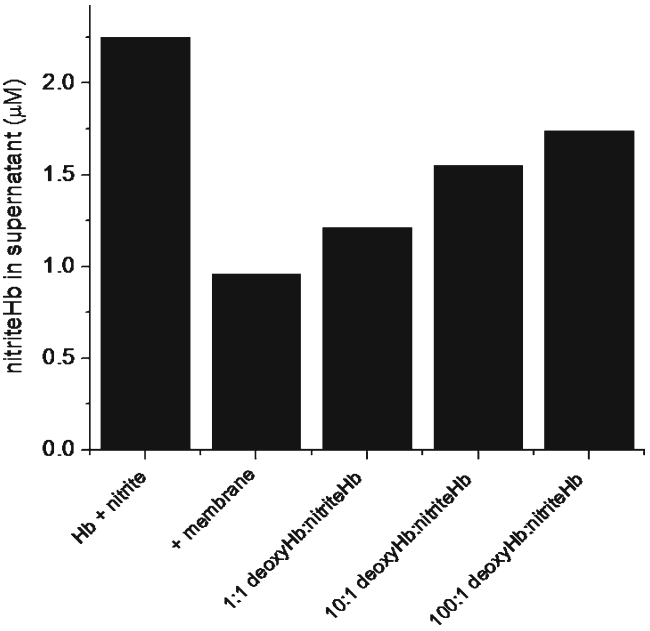

Fig. 27.2 Binding of nitrite reacted Hb to RBC ghosts. Hb was reacted with nitrite and the binding to ghosts in the presence of different concentrations of excess deoxyHb (1–100 fold) was determined by centrifugation

The high affinity of nitrite reacted Hb in the presence of a large excess of deoxyHb was investigated with RBC ghosts (Fig. 27.2). Hb reacted with a 1:10 nitrite:heme molar ratio was added to white membrane ghosts. The Hb in the supernatant after centrifugation was determined when different amounts of excess deoxyHb were added. Even with a 100-fold excess of deoxyHb, >20% of the nitrite reacted Hb was still bound to the membrane.

3.2 Nitrite and ATP Induced Vasodilation

The reaction of nitrite with deoxygenated RBCs results in an increase in ATP synthesis [6] and an increase in the hypoxic release of ATP (Fig. 27.3). This effect can be attributed to an increase in glycolysis due to the displacement of glycolytic enzymes from the RBC membrane by nitrite reacted Hb [8].

The affect of this ATP release on blood pressure was observed when nitrite reacted RBCs are injected into the femoral vein (Fig. 27.4). In the presence of apyrase (which degrades any ATP released), the decrease in blood pressure as a result of ATP release is eliminated.

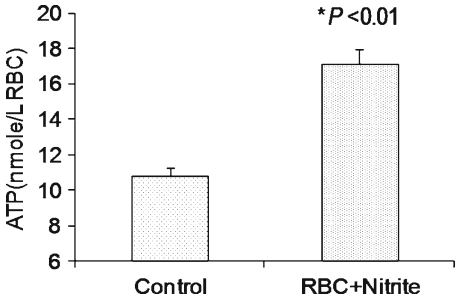

Fig. 27.3 Enhanced released of ATP from hypoxic RBCs by nitrite. ATP release after anoxic incubation was determined by luminescence before and after reacting with nitrite

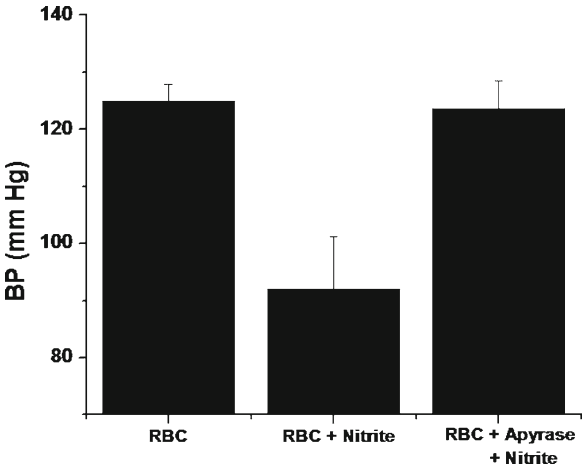

Fig. 27.4 Reduction in blood pressure by nitrite reacted RBCs. The decrease in blood pressure when 0.8 ml of nitrite reacted RBCs are injected into a rat is eliminated if apyrase is added to degrade the released ATP

3.3 Membrane Induced Release of NO from Hemoglobin

NO released during the reaction of nitrite with deoxyHb binds to the excess deoxyHb forming Hb(II)NO. The Hb(II)NO binds NO very tightly quenching NO bioactivity. However, most of the nitrite that reacts with an excess of deoxyHb is retained in intermediates. One of these intermediates is a delocalized species [9] with properties of Hb(III)NO and $Hb(II)NO^+$. This species retains potential NO bioactivity.

As shown in Fig. 27.5, a negligible amount of NO is released into the gas phase above the reaction mixture when nitrite reacts with Hb. However, in the presence of the RBC membrane a significant fraction of the nitrite/NO associated with the Hb is released into the gas phase. A similar fraction of NO is released into the gas phase when nitrite reacts with Hb that is already bound to the membrane.

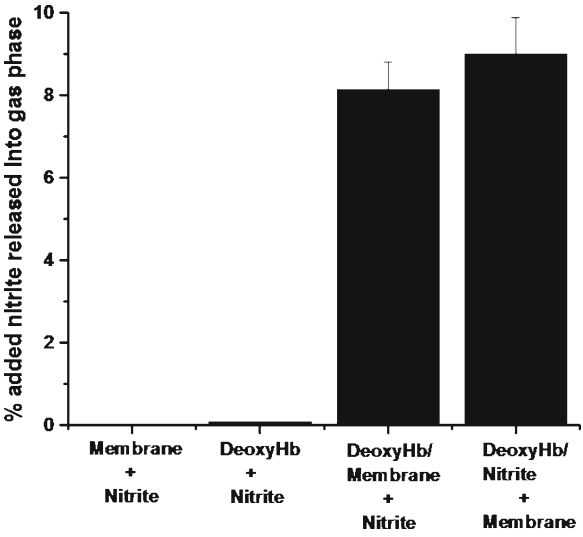

Fig. 27.5 A significant level of NO was detected by chemiluminescence in the gas phase above the sample when nitrite reacted Hb was added to the membrane or nitrite reacted with Hb bound to the membrane. NO was not released unless both Hb and membranes were present

4 Discussion

The dramatic increase in the binding of nitrite reacted Hb to the RBC membrane (Figs. 27.1 and 27.2) results in a pool of nitrite/NO that is removed from the large excess of cytoplasmic Hb that rapidly quenches any NO released.

Our studies indicate that the increased membrane affinity of nitrite reacted Hb can increase vasculature NO by two processes. (1) Glycolytic enzymes that bind in the same region of band 3 as Hb [10] are released from the membrane resulting in an increased rate of glycolysis. Increased glycolysis increases ATP production and the hypoxic release of ATP [8]. The released ATP interacts with purinergic receptors on the endothelium that activate eNOS [11]. This process bypasses the requirement to release NO from the RBC. (2) NO can, however, actually be released from the RBC into the vasculature (Fig. 27.5) as a result of membrane interactions that stimulate NO release from the nitrite reacted intermediates [9]. These studies provide important new insights into the contribution of RBCs to NO bioactivity.

NO released into the vasculature is known to cause dilatation of blood vessels. We have used blood pressure to monitor this dilatation, although a decrease in cardiac output can also contribute to the observed decrease in blood pressure. It should also be noted that the RBC induced NO dilatation cannot fully explain autoregulation whereby individual tissues maintain highly specific oxygen delivery to consumption ratios [12].

Acknowledgments This research was supported by the Intramural Research Program of the NIH, National Institute on Aging.

References

1. Ignore LJ, Cirino G, Casini A et al (1999) Nitric oxide as a signaling molecule in the vascular system: an overview. J Cardiovasc Pharmacol 34:879–886
2. Gautier C, Van FE, Mikula I et al (2006) Endothelial nitric oxide synthase reduces nitrite anions to NO under anoxia. Biochem Biophys Res Commun 341:816–821
3. Liu X, Miller MJ, Joshi MS et al (1998) Diffusion-limited reaction of free nitric oxide with erythrocytes. J Biol Chem 273:18709–18713
4. Nagababu E, Ramasamy S, Abernethy DR et al (2003) Active nitric oxide produced in the red cell under hypoxic conditions by deoxyhemoglobin-mediated nitrite reduction. J Biol Chem 278:46349–46356
5. Cosby K, Partovi KS, Crawford JH et al (2003) Nitrite reduction to nitric oxide by deoxyhemoglobin vasodilates the human circulation. Nat Med 9:1498–1505
6. Cao Z, Bell JB, Mohanty JG et al (2009) Nitrite enhances RBC hypoxic ATP synthesis and the release of ATP into the vasculature: a new mechanism for nitrite-induced vasodilation. Am J Physiol Heart Circ Physiol 297:H1494–H1503
7. Demehin AA, Abugo OO, Jayakumar R et al (2002) Binding of hemoglobin to red cell membranes with eosin-5-maleimide-labeled band 3: analysis of centrifugation and fluorescence data. Biochemistry 41:8630–8637
8. Tsai IH, Murthy SN, Steck TL (1982) Effect of red cell membrane binding on the catalytic activity of glyceraldehyde-3-phosphate dehydrogenase. J Biol Chem 257:1438–1442
9. Salgado MT, Nagababu E, Rifkind JM (2009) Quantification of intermediates formed during the reduction of nitrite by deoxyhemoglobin. J Biol Chem 284:12710–12718
10. Jagger JE, Bateman RM, Ellsworth ML et al (2001) Role of erythrocyte in regulating local O_2 delivery mediated by hemoglobin oxygenation. Am J Physiol Heart Circ Physiol 280: H2833–H2839
11. Boland B, Himpens B, Vincent MF et al (1992) ATP activates P2x-contracting and P2y-relaxing purinoceptors in the smooth muscle of mouse vas deferens. Br J Pharmacol 107: 1152–1158
12. Wolf CB (2007) Normal cardiac output, oxygen delivery and oxygen extraction. Adv Exp Med Biol 599:169–182

Chapter 28
Clinical Applications of Tissue Oxygen Saturation Measurements

David K. Harrison

1 Introduction

The application of the non-invasive techniques of visible light spectroscopy (VLS) and near infrared wavelength range spectroscopy (NIRS) for the measurement and monitoring of tissue oxygen saturation in the clinical setting has been proposed for many years. A large number of clinical research studies have been carried out to determine the efficacy and practicality of such monitoring, particularly, in the case of NIRS, in the brain. The results of many of these studies have been presented at ISOTT meetings. Similarly, a number of studies have been carried out to assess the clinical application of VLS in the diabetic foot and in skin ulcers, but these, too, have failed to produce sufficiently clear diagnostic reproducibility – mainly due to the confounding effects of inflammation [1]. Indeed it can still be claimed that VLS and NIRS are both "techniques looking for clinical applications."

In this paper, a number of studies are presented that have either already led to the routine application of tissue oxygen saturation measurement in clinical practice or show great promise for such application in the future.

2 Amputation Level Viability

In 1995 we proposed a new technique for predicting the outcome of below knee amputation (BKA) flaps in critical limb ischaemia [2]. This involved the spectrophotometric measurements of skin S_tO_2 using a Photal MCPD 1000 (Otsuka Electronics, Otsuka). In the initial study, the concept of the "degree of tissue hypoxia" (DTH)

D.K. Harrison (✉)
Institute of Cellular Medicine, Newcastle University,
Newcastle upon Tyne, NE1 7RU, UK
e-mail: d.k.harrison@ncl.ac.uk

M. Wolf et al. (eds.), *Oxygen Transport to Tissue XXXIII*, Advances in Experimental Medicine and Biology 737, DOI 10.1007/978-1-4614-1566-4_28,

was introduced. This was the percentage of S_tO_2 values along the leg (measured medially at 1 cm intervals from the level of the tibial tuberosity to the great toe) that were less than 10% SO_2. The mean S_tO_2 at two sites (10 cm distal from, and 3 cm medial and lateral to, the tibial tuberosity) along the line of the proposed BKA flap was also measured. If the DTH was less than 15%, or the mean site S_tO_2 greater than 30% healing was successful at the BKA level. The technique was adopted as a standard clinical technique at Ninewells Hospital, Dundee, UK, and later at the University Hospital of North Durham, Durham, UK, for assessing BKA viability in patients prior to amputation. An audit, reported in 2002 [3] showed a 94% healing rate at a BKA:AKA (above knee amputation) ratio of 9:2.

In 2005 we reported the introduction of the Whitland RM200 S_tO_2 monitor (Whitland Research, Whitland, UK) for amputation viability assessment [4]. A study to compare the values obtained using the new instrument and the MCPD 1000 was carried out, and the criteria for BKA viability changed such that the DTH was redefined as the percentage of S_tO_2 values along the leg less than a value of 15% S_tO_2, and the mean viable site S_tO_2 became 40%. An audit of 24 patients of the outcome of using the RM200 for amputation level viability assessments, carried out over a 3-year period, showed a 91% healing rate at a BKA:AKA ratio of 11:1 [5]. Of the two patients whose BKA flaps failed to heal, in one case the amputation was not carried out until 1 week after the assessment, and in the other not until 8 weeks after the assessment. A recommendation was therefore introduced that an amputation level viability assessment should ideally be carried out within 24 h prior to the amputation and, in any case, the results were only valid for 5 days.

3 Free Flap Monitoring

Free flaps, such as the transverse rectus abdominis myocutaneous (TRAM) flap, are frequently used in breast reconstruction following mastectomy. While the majority of flaps do well, the consequences of flap failure can be devastating. Early recognition of vascular problems post-operatively is vital if a failing flap is to be salvaged.

In 2006 we reported the results from 14 patients who had been monitored using VLS to detect early vascular compromise following free TRAM flap breast reconstruction [6]. Tissue oxygen saturation was compared with clinical observation and laser Doppler flowmetry (LD) (Moor Instruments DRT 4, Axminster, UK). Since then, a further eight patients, making a cohort of 22 (mean age 47 years), have been monitored on return from theatre for up to 70 h post-operatively (mean 57 h). In all patients laser Doppler flowmetry and tissue SO_2 were recorded. In 14 patients an additional parameter, the haemoglobin index (HbI, proportional to haemoglobin concentration) [7] was also measured.

Figure 28.1 shows the hourly averaged results from 19 patients who had an uneventful post-operative recovery. Figure 28.2 shows the recordings from a patient who developed venous congestion 2 h after returning to the ward. The flap could not be salvaged and had to be removed.

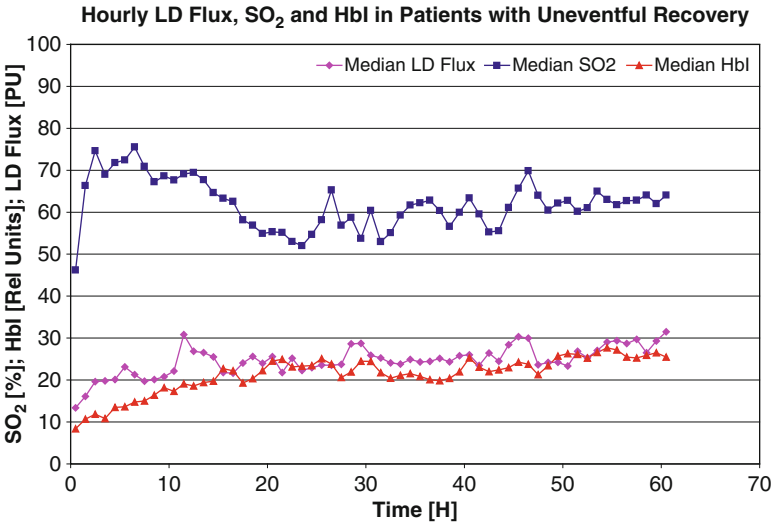

Fig. 28.1 Hourly average median values for LD flux (*filled diamond*), S_tO_2 (*filled square*) and HbI (*filled triangle*) for all 19 patients with an uneventful recovery

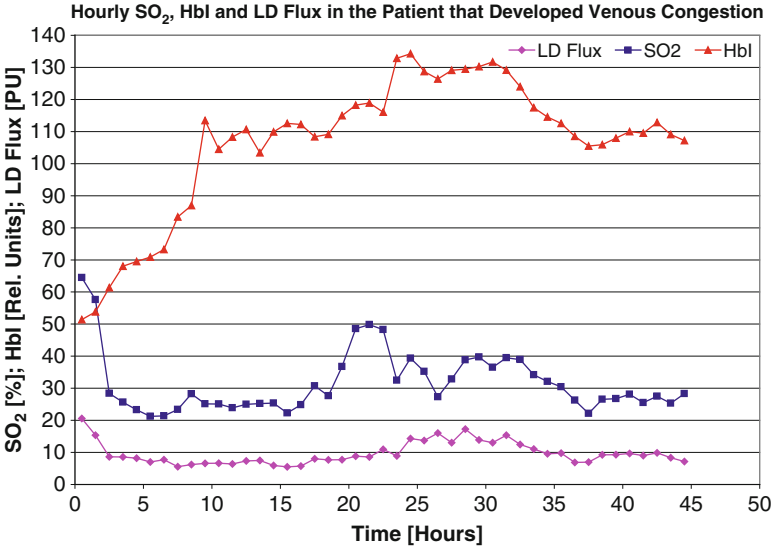

Fig. 28.2 Hourly averaged LD flux (*filled diamond*), S_tO_2 (*filled square*) and HbI (*filled triangle*) in a patient who developed venous congestion 2 h post-operatively. The rapid fall in S_tO_2 accompanied by a simultaneous rise in HbI indicates that accumulation of blood (venous congestion) is the cause of the flap failure. The fall in LD flux in this early post-operative period is much less dramatic

The equipment was well tolerated by all patients and ward staff. Tissue oxygen saturation accurately reflected clinical outcome and compared favourably with LD. Furthermore, the HbI appears to offer the potential to differentiate between arterial and venous vascular occlusion. While a critical alarm value for S_tO_2 has yet to be established, the results show an encouraging correlation between the tissue S_tO_2 readings and both clinical outcome and laser Doppler. The increased sensitivity of the S_tO_2 measurement at low flow when compared with LD [6] reflects the improved potential this instrument may have for free flap monitoring. Indeed, the technique was adopted for routine clinical monitoring of TRAM flaps at the University Hospital of North Durham as a result of these studies.

4 Surgical Site Infection

Wound infections (surgical site infections, SSIs) are common, occurring in up to 30% of operations for abdominal surgery, and are estimated to cost the UK National Health Service up to £65 million per year. Previously, studies by Hopf et al. 1997 [8] had indicated that subcutaneous pO_2 measured post-operatively in a surrogate wound in the arm of patients having undergone abdominal surgery correlated with the subsequent occurrence of SSI. However, the technique was highly invasive and the aim of our study was to determine whether the use of non-invasive subcutaneous tissue $S_{sct}O_2$ measurements adjacent to the surgical wound could be predictive of SSI. The results of this study have been presented elsewhere [9, 10].

Patients undergoing major abdominal surgery were invited to participate. Subcutaneous tissue SO_2 ($S_{sct}O_2$) was measured adjacent to the wound site pre-operatively and then at 12, 24 and 48 h post-operatively using an Inspectra® model 325 (Hutchinson Technology, Minnesota, USA) NIR $S_{sct}O_2$ monitor. Signs of infection were assessed independently for up to 1 month post-operatively. Two groups were then classified retrospectively: those who healed uneventfully (Group A) and those who developed SSI (Group B).

Of 61 patients, 42 healed uneventfully, 17 developed SSI and 2 were lost to follow-up. The overall infection rate was 28.8%. There were no significant differences in sex, age, skinfold thickness or body mass index (BMI) between the two groups.

At 12 h there was a significant difference between the two groups with respect to mean wound $S_{sct}O_2$ (± standard deviation) (A = 58.3 ± 21.6%, B = 42.2 ± 16.6%, $p = 0.005$, 95% confidence interval = 5.26, 26.98). A receiver operating characteristic curve showed that the sensitivity and specificity were maximal (71% and 73%, respectively; chi-squared test: $p = 0.002$) when a wound $S_{sct}O_2$ of 53% was chosen as the threshold to classify potential infection. The commonly used National Nosocomial Infection Score (NNIS) for predicting SSIs had a specificity of 95% and a sensitivity of 0% for the same patients; two patients predicted by the NNIS to develop SSI healed uneventfully and all of the 17 patients who developed SSI were predicted to heal uneventfully.

The study showed that the wound $S_{sct}O_2$ in the early post-operative period was significantly lower in the groups that developed SSI than in those who healed successfully and is a better prediction tool for wound infection than the NNIS risk score.

5 Bowel Ischaemia

Diagnosis of bowel ischaemia is difficult because of its non-specific presentations and the lack of simple diagnostic tests. Visible light spectrophotometry is a new technique for assessment of bowel tissue oxygenation. The aim of the study was to explore the use of VLS in assessing bowel S_tO_2 in the basal and ischaemic states and compare it with Laser Doppler flowmetry.

Nine patients undergoing elective left-sided colon resections were included in this study. Tissue S_tO_2 values were measured perioperatively within the serosal and the mucosal layers of the descending colon, sigmoid colon and the rectum on four occasions: at the beginning of the operation (baseline), after mobilisation of the sigmoid, after ligation of the inferior mesenteric artery (IMA) and after complete devascularisation of the sigmoid. The mucosal measurements were carried out using a catheter probe (Moor Instruments DP6a, Axminster, UK) through a flexible sigmoidoscope. LD flow was also measured on all these occasions.

The results showed no significant difference in the baseline S_tO_2 and flux between the different parts of the bowel. There was a significant decrease in the mean mucosal S_tO_2 in the sigmoid after ligation of the IMA and after complete devascularisation. The mean (± SD) mucosal S_tO_2 in the sigmoid decreased from a baseline value of $74\% \pm 5\%$ to $57\% \pm 12\%$ ($P = 0.012$) after ligation of the IMA and to $36\% \pm 15\%$ ($P = 0.012$) after complete devascularisation. The serosal S_tO_2 in the sigmoid decreased from a baseline value of $88\% \pm 8$ to $80\% \pm 9\%$ after complete devascularisation. There was a significant drop in the LD flux in the serosal and the mucosal layer of the sigmoid following ligation of the IMA and complete devascularisation but the flux values had high variability.

Mucosal S_tO_2 measurements using VLS can accurately diagnose an ischaemic state of the colon and therefore may be a useful investigation in patients with suspected colonic ischaemia. If serosal measurements are required, VLS is not reliable and laser Doppler might be more useful. Further details of this study can be found elsewhere [11].

6 Summary

It has not been possible to cover all areas of application here. However, one emerging area is the monitoring of trauma patients using the thenar eminence as the site of NIRS tissue oxygen measurements and the reader is referred to a review article by Santora and Moore, 2009 [12] for further information.

The above clinical applications of tissue oxygen saturation measurements are just a few examples where these non-invasive techniques, whether VLS or NIRS, can provide valuable real-time information to the clinician which may influence the course of treatment and may ultimately result in a better clinical outcome for the patient.

Acknowledgments It is not possible here to list everyone who has helped in some way with the above projects. However, the author is most grateful for the collaboration of many clinical colleagues in facilitating the studies and, in particular, to former Surgical Research Fellows Charlotte Ives and Daya Singh for carrying them out.

References

1. Newton DJ, Harrison DK, Hanna GB et al (1997) Microvascular blood flow and oxygen supply in ulcerated skin of the lower limb. Adv Exp Med Biol 428:21–26
2. Harrison DK, McCollum PT, Newton DJ et al (1995) Amputation level assessment using lightguide spectrophotometry. Prosthet Orthot Int 19:139–147
3. Hanson JM, Harrison DK and Hawthorn IE (2002) Tissue spectrophotometry and thermographic imaging applied to routine clinical prediction of amputation level viability. In: Müller GJ, Kessler M (eds) Progress in biomedical optics and imaging: functional monitoring and drug-tissue interaction. Spie Proc Series 4623, pp 187–194
4. Harrison DK, Hawthorn IE (2005) Amputation level viability in critical limb ischaemia: setting new standards. Adv Exp Med Biol 566:325–332
5. Harrison DK, Gaylard LG, Singh DB (2007) Thermographic imaging for amputation level viability assessment: just a pretty picture or a quantitative tool? Thermology Int 17:79–80
6. Caddick J, Raine C, Harrison D et al (2006) Lightguide spectrophotometry to monitor free TRAM flaps. Adv Exp Med Biol 578:351–356
7. Harrison DK, Evans SD, Abbot NC et al (1992) Spectrophotometric measurements of haemoglobin saturation and concentration in skin during the tuberculin reaction in normal human subjects. Clin Phys Physiol Meas 13:349–363
8. Hopf HW, Hunt TK, West JM et al (1997) Wound tissue oxygen tension predicts the risk of wound infection in surgical patients. Arch Surg 132:997–1004
9. Ives CL, Harrison DK, Stansby G (2006) Prediction of surgical site infections using spectrophotometry: preliminary results. Adv Exp Med Biol 578:149–154
10. Ives CL, Harrison DK, Stansby G (2007) Tissue oxygen saturation, measured by near-infrared spectroscopy, and its relationship to surgical-site infections. Br J Surg 94:87–91
11. Singh DB, Stansby G, Bain I, Harrison DK (2009) Intraoperative measurement of colonic oxygenation during bowel resection. Adv Exp Med Biol 645:261–266
12. Santora RJ, Moore FA (2009) Monitoring trauma and intensive care unit resuscitation with tissue hemoglobin oxygen saturation. Crit Care 13(Suppl 5):S10

Chapter 29
Oscillations in Cardiac Output in Hypoxia with Periodic Breathing and Constant End-Tidal PCO_2 at High Altitude (5,000 m)

C.B. Wolff, M. Bell, C.D. Thake, and D.J. Collier

1 Introduction

At sea level arterial oxygen content (CaO_2) varies little with even quite large changes in ventilation because, for normal oxygen tension (PO_2), the subject exists on the near flat part of the oxygen haemoglobin (Hb) dissociation curve. However, $PetCO_2$ will change inversely as ventilation changes, a "washout" effect; despite oxygen delivery (DO_2) staying virtually constant at any given metabolic rate. DO_2 change will only depend upon variations in cardiac output (CO). With a low arterial PO_2 at high altitude even quite small changes in ventilation will alter CaO_2 so that arterial oxygen delivery will vary, additionally, as a result of changes in ventilation. It is known that in the steady state, within the physiological range, there is very good matching of DO_2 to oxygen consumption (VO_2) in most organs; hence, DO_2 tends to be sustained at an appropriate level in the face of steady state changes in CaO_2 [1]. If there is sufficiently large change in respiration to alter CaO_2 significantly at altitude then we might expect reciprocal change in CO, providing compensation, such that DO_2 does not change. It is not known whether such acute CaO_2 changes result in such compensatory changes in CO. If they do then hyper-ventilatory episodes noted in 1994 should result in oscillating SaO_2 (and CaO_2). Only if there is a

C.B. Wolff (✉)
Clinical Pharmacology and Anaesthetics, William Harvey Research Institute, Barts and The London, London, UK
e-mail: chriswolff@doctors.org.uk

M. Bell
Stapleton Road Resource Centre, Doncaster, UK

C.D. Thake
School of Life and Health Sciences, Coventry University, Priory Street, Coventry, CV1 5FB, UK

D.J. Collier
Division Clinical Pharmacology and Anaesthetics Organization William Harvey Research Institute, Barts and The London, London, UK

M. Wolf et al. (eds.), *Oxygen Transport to Tissue XXXIII*, Advances in Experimental Medicine and Biology 737, DOI 10.1007/978-1-4614-1566-4_29,

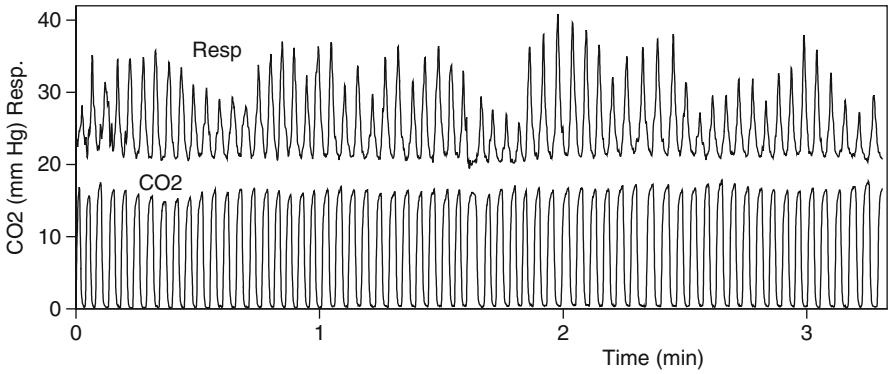

Fig. 29.1 In subject 04 end-tidal PCO_2 hardly varied, whereas the stethograph record (Resp.) shows large, near periodic, ventilatory changes. If CO_2 was arriving at the lung at a constant rate one would expect the respiratory variation to result in large reciprocal changes in end-tidal PCO_2. The hypothesis is that there must be an oscillating rate of CO_2 arrival at the lungs as a result of oscillations in cardiac output [time 0 here was at 11 min 43.8 s of the original record, during mild exercise]. *Note*: The stethograph record is non-linearly related to breathing – non-parametric – and so does not have units though larger and smaller magnitudes are correctly indicated

sufficiently rapid response of the tissues to such CaO_2 oscillations will there be compensatory oscillations in CO. The hypothesis here is that such changes in CO result in changes in CO_2 arrival at the lung with a ventilatory response to match. This would explain the bouts of hyper-ventilation. Constancy of PCO_2 is then sustained by rapid and complete responsiveness of respiratory control.

Figure 29.1, recorded during the current high altitude expedition, illustrates the phenomenon of hyper-ventilatory episodes with little change in end-tidal PCO_2.

2 Methods

Each normal subject was studied at rest and during mild exercise (approximately 35 W). The sea level studies at rest included, first air breathing then exposure to 12% oxygen and have been reported earlier [2]. The sea level studies also included moderate exercise and were controls for rest and exercise at altitude; methods were reported in detail and are here described in outline. Four data channels were recorded (CED, Spike2): airway PCO_2, respiration (stethograph), arterial oxygen saturation (SaO_2) and non-invasive arterial blood pressure (Finapress BP). CO was derived from the BP record (PulseCO™, patented algorithm of LiDCO, UK). The stethograph record depends on chest circumference, non-linearly related to ventilation. It therefore does not have a simple unit of measurement but gives a general indication of ventilatory change and precise timing of each breath. Eight subjects were studied at sea level and eight at 5,000 m (in the Hidden Valley in West Central Nepal); ethical permission came from the Kings College Hospital Research Ethics Committee for sea level and the "Nepal Health Research Council" for the altitude work. (Contacts: http://www.nhrc.org.np/for the Hidden Valley; Official mail: nhrc@nhrc.org.np).

2.1 Analytical Methods

The time delays have been examined between recordings showing oscillations in respiration and CO and, where SaO_2 oscillates, the time delay from respiratory troughs and peaks to those of SaO_2.

3 Results

Table 29.1 shows the values of SaO_2, Hb, CaO_2, CO and DO_2 for both sea level and altitude studies where there is a single representative value. On occasion values were changing but an attempt has been made to use a representative value.

The recording shown in Fig. 29.1 was one of the three situations where there was striking periodic breathing and little or no change in end-tidal PCO_2. However, the arterial blood pressure record was faulty so that only a short length of record could be used to give mean CO. The two subjects exhibiting periodic breathing with adequate BP records (01 and 09) also had demonstrable, CO oscillations with corresponding periodicity. For subject 01 SaO_2 also oscillated as a result of the periodic breathing. Figure 29.2 shows the stethograph (breathing) and SaO_2 records for exercise in subject 01 at altitude (hidden valley) with the concurrent CO values (derived from the arterial blood pressure).

This analysis examines the functional relationships between respiration, recorded SaO_2 and CO, initially on the basis of timing of events – peaks and troughs in particular. Some quantitative aspects follow with assessment from an approximate derivation of DO_2.

1. Do SaO_2 oscillations follow and correspond with respiratory oscillations (indicated by the stethograph record)?
2. Do CO oscillations correspond with respiratory oscillations?
3. Are the CO oscillations the inverse of the SaO_2 oscillations?

Figure 29.3 shows, on the left, the time intervals between the respiratory peaks and, both SaO_2 peaks and CO troughs. On the right the time intervals are between respiratory troughs and both SaO_2 troughs and CO peaks. The time intervals between the respiratory events (peaks and troughs) and corresponding (inverse) CO events (troughs and peaks) shorten successively, compatible with the increasing CO as exercise progresses. By contrast the delays between respiration and SaO_2 are each made up of firstly, passage of blood from lung to aorta then, passage down the arm to the oximeter and finally, an additional oximeter instrumentation delay. Most delay (arm and oximeter) is therefore independent of CO which explains the much more constant delays from respiratory to SaO_2 events.

As a result of the differences in timing of SaO_2 and CO the product (putative DO_2 related value) is not quite constant (Fig. 29.4). However, the result is entirely compatible with a tissue response regulating DO_2 partially compensating for large swings in SaO_2 resulting from the periodic breathing.

Table 29.1 Hb, SaO_2, CO and calculated CaO_2 and DO_2 for rest and exercise on air and 12% O_2 at sea level (**a**) and on air at rest and in exercise at high altitude (HV, Hidden Valley, **b**)

(a) Sea level		On air				On 12% O_2				Exercise			
Subject	Hb	SaO_2	CaO_2	CO	DO_2	SaO_2	CaO_2	CO	DO_2	SaO_2	CaO_2	CO	DO_2
01	11.4	97.7	15.24	8.93	1,361	85.2	13.17	10.99	1,447	86.3	13.5	12.6	1,689
02	13.6	98.3	18.31	3.39	621	92.5	17.05	4.46	760	92.5	17.2	5.6	956
03	14.4	97.5	19.14	7.11	1,361	85.0	16.56	10.30	1,705	80.3	15.8	13.4	2,119
04	12.9	96.8	16.97	5.46	926	92.9	16.26	5.25	853	75	13.2	11.6	1,522
05	12.5	96.0	16.38	5.99	981	90.7	15.38	5.86	901	87	14.9	10.0	1,489
06	13.7	98.5	18.43	4.52	833	87.4	16.20	5.94	962	79.1	14.7	10.5	1,551
07	12.4	97.3	16.46	5.88	968	87.1	14.64	7.19	1,053	79.2	13.4	11.8	1,583
08	15.6	96.2	20.37	5.33	1,086	87.4	18.43	5.25	968	81.9	17.4	14.3	2,478

(b) HV		Rest				Exercise			
Subject	Hb	SaO_2	CaO_2	CO	DO_2	SaO_2	CaO_2	CO	DO_2
01	12.9	85.3	15.1	8.99	1,355	83.2	14.69	12.02	1,765
02	13.0								
03	15.9	83.2	18.0	4.06	732	79.5	17.23	7.45	1,284
04	14.9	85.2	17.3	6.40	1,110	83.3	16.95	14.78	2,505
05									
06	15.7	84.1	18.0	6.97	1,252				
07	12.9	82.7	14.5	4.71	684	78.0	13.69	8.52	1,166
08	18.4			5.03				8.80	
09	15.3	81.7	17.0	6.22	1,057	78.7	16.35	8.30	1,358
10	13.2	65.5	11.8	3.74	442	60.5	10.91	5.83	635

Units: Hb g dl^{-1}, SaO_2 (%), CaO_2 ml dl^{-1}, CO l min^{-1} and DO_2 ml min^{-1}

Boxes for CO and SaO_2 values indicate strong oscillations in subjects 01 and 09 with strongly periodic respiration. For subject 04 showing strongly periodic breathing in exercise CO derivation was prevented by an insufficient length of adequate BP record. The exercise SaO_2 values at sea level for subjects 01 and 02 followed recovery from an initial fall; to under 75% for subject 01 but only to 88% for subject 2

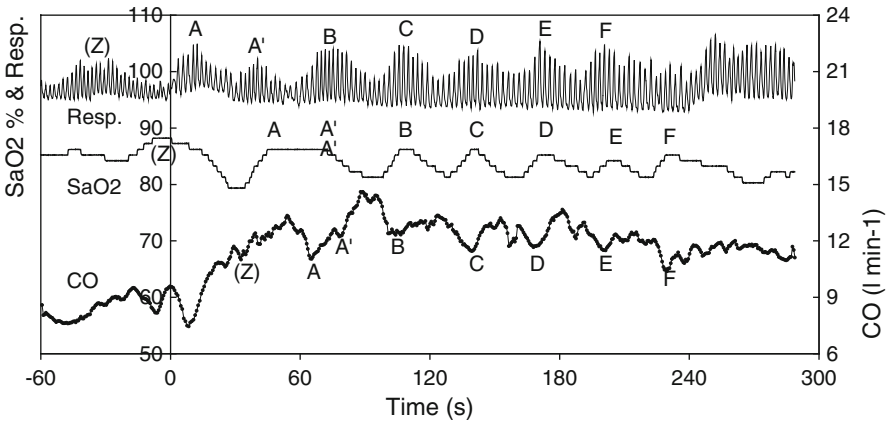

Fig. 29.2 Recording from subject 01 at altitude, the last minute of rest and four minutes mild exercise; stethograph (Resp.), SaO_2 and CO oscillations. The respiratory maxima during exercise are lettered A to F as are the corresponding points on SaO_2. Troughs in the CO recording are indicated which putatively correspond to the SaO_2 peaks (see text). Resp. is non-parametric, timing is correctly indicated

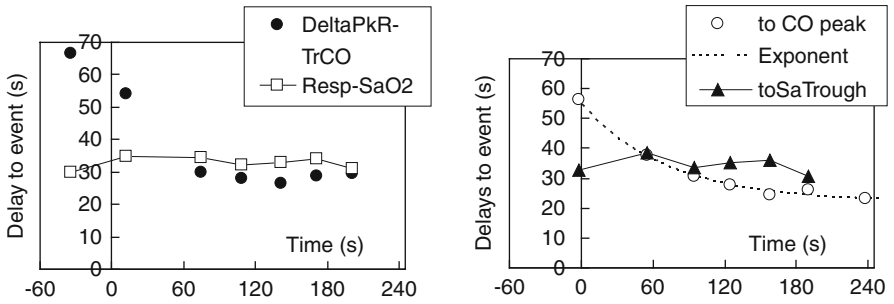

Fig. 29.3 This shows delays for the record of Fig. 29.2. On the *left*, the time intervals are from respiratory peaks to SaO_2 peaks and to CO troughs; on the *right*, from respiratory troughs to SaO_2 troughs and to CO peaks. The exponential in the right-hand panel plateaus at 22 s; the curve is: de lay = 32.636 × [EXP(−0.0138 × time)] + 22 s

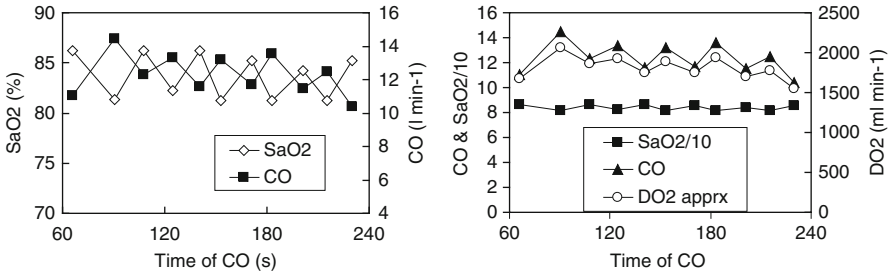

Fig. 29.4 Corresponding values of SaO_2 and cardiac output are plotted against the timing of the CO event (peak or trough) on the *left*. On the *right* DO_2 has been added. DO_2 still oscillates though less so than SaO_2, when scaled similarly, suggesting DO_2 compensation is partial

The CO oscillations ranged in amplitude from 1.4 to 2.8 $l min^{-1}$ (average 1.84 $l min^{-1}$) and constituted 11–21% of the average CO for the cycle concerned (average 12.5 $l min^{-1} \pm 0.5\ l min^{-1}$ sd).

4. Does the oscillating CO with accompanying higher CO_2 flow into the lungs perpetuate the periodic breathing (sustaining a feedback loop)?

If so there should be a relationship between some points on each CO oscillation corresponding with the simultaneous respiratory record.

There is correspondence of peaks in the stethograph record, A to E and a point a short way up the upslope of the cardiac oscillation but this does not apply to respiratory peak F which coincides with trough E.

In Fig. 29.5 we have respiration, heart rate (HR), CO and airway PCO_2 for the third subject (09) showing clearly periodic events in the respiratory record. In this case there are gasps, usually single, and a very steady end-tidal PCO_2 ($PetCO_2$) value.

The large swings in CO in subject 09 at rest at high altitude should follow the gasps at a near constant time interval since the subject is at rest. In Fig. 29.6 the

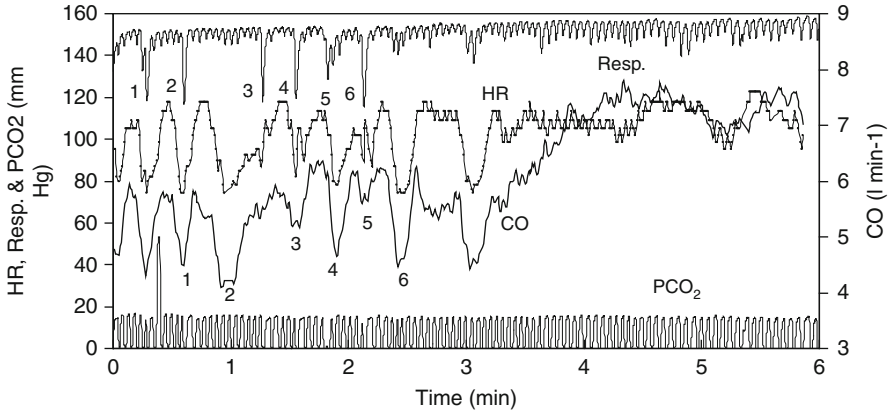

Fig. 29.5 This shows the recording in the resting subject 09 at high altitude in which repeated gasps occurred during the first half of the record, events numbered 1–6 near the downward deflections of the stethograph record (Resp.). Corresponding troughs in the heart rate and CO records suggest compensatory change towards constancy of DO_2. $PetCO_2$ remained constant despite respiratory and circulatory changes (tall spike, 7% calibration, 53.2 mmHg)

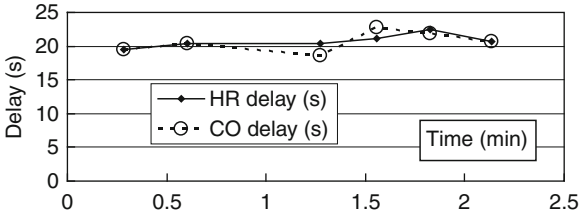

Fig. 29.6 This shows the delays between each gasp and the subsequent minimum in the cardiac output record for subject 09 at high altitude. For this recording, at rest, the delays are near constant, in contrast to the progressive fall seen early in exercise in subject 01 as cardiac output increased (see Fig. 29.3)

times between each gasp and putative corresponding CO trough have been plotted for both the heart rate and CO records.

As one would expect for the resting state, there is no significant trend for the lung to tissue delay (mean values for heart rate and CO 20.8 ± 0.4 s and 20.6 ± 0.6 SEM s).

The period of the oscillations is: mean 24.9 ± 4.1 SEM; median 19.0 s, rather shorter than for subject 01 (mean 32.1 ± 4.1 sd). This may be the reason for the absence of oscillations in SaO_2, a highly damped recording.

4 Discussion

The puzzle, periodic breathing during steady metabolism with constant end-tidal PCO_2, has been shown to be associated with oscillating CO in two of the three subjects exhibiting strong episodes of periodic breathing. End-tidal PCO_2 constancy in

the illustrated records of subject 04 (Fig. 29.1) and subject 09 (Fig. 29.5) was not quite matched for subject 01. For subject 01 $PetCO_2$ did oscillate a little in response to respiration but much less than would be expected with a constant rate of arrival of lung CO_2. There is a reason why PCO_2 oscillations will, for a given degree of respiratory oscillation, be less than at sea level. This is because of the far lower PCO_2 at altitude. The rate of change of PCO_2, determining PCO_2 oscillation amplitudes, is directly related to the mean value for a given rate of CO_2 production (VCO_2). However, the complete absence of end-tidal PCO_2 oscillation and the presence of the hypothesized CO oscillations confirm the oscillatory CO as the likeliest explanation for the gross respiratory changes sustaining $PetCO_2$ constancy. The CO oscillations for subject 01 (derived from the recorded arterial blood pressure) appear to be imperfect and yet there is good correspondence of respiratory events with the putative corresponding, compensatory, events in the CO record (peak respiration with CO troughs and respiratory troughs with CO peaks). There is also close correspondence between respiratory and SaO_2 events (peaks with peaks and troughs with troughs).

The lack of recorded SaO_2 change, where gasps occurred, in the record of subject 09, relate to the damped nature of the oximeter, adequate to show the slower oscillations of subject 01. The very precise correspondence of the respiratory gasps of subject 09 with the clear CO (and heart rate) troughs following, as they do, after a near constant interval, suggests a strong response to a quick rise in actual SaO_2. Certainly, the swings in CO are compatible with an indirect response to the respiratory events.

The events depicted in Fig. 29.1 (subject 04), Fig. 29.2 (subject 01) and Fig. 29.5 (subject 09) all occurred at altitude, involved respiratory periodicity and constant or near constant end-tidal PCO_2 at high altitude.

The results here support the original hypothesis that oscillatory CO accounts for the respiratory periodicity which then sustains a constant $PetCO_2$. The coupled hypothesis, that the ventilatory periodicity is, in turn, caused by the fluctuation in the rate of arrival of CO_2 at the lung seems partially supported by finding a near constant relation of the peak respiratory values in subject 01 (Fig. 29.2) with a rising section of the CO record. However, the detail awaits both augmentation and further modelling since the relationship is not a simple one where breathing follows CO. The precise events at the tissues, speeding up and slowing down, will influence the CO_2 content of the blood leaving the tissues. It does seem that the appearance of the phenomenon in exercise may relate to the fact that the predominant blood flow is at a particular single part of the body, the exercising muscle. By contrast, at rest the brain, gastro-intestinal tract and liver, kidney and muscle are all significant contributors functioning at different time intervals away from the lung, so the much more mixed picture probably militates against a single wave of varying CO_2 flux arriving at the lung.

It seems to be a straightforward matter of physics that there must be a large variation in the rate of arrival of CO_2 at the lung in the situation of periodic breathing and constant $PetCO_2$. The very fact that $PetCO_2$ is held constant in the face of varying CO_2 arrival at the lung illustrates the presence of powerful respiratory control

sustaining isocapnia. Studies on modification of CO_2 oscillations of respiratory frequency suggest they are somehow involved in this feature of respiratory control [3]. There is a further puzzle in the case of the resting record of subject 09 (Fig. 29.5). The gasps appear to correspond in timing with the troughs of the CO oscillations and the fact that the periodic breathing involves gasps rather than crescendo–decrescendo changes suggests there may be some other reason for the respiratory phenomenon, rather than a response to a fluctuating rate of arrival of CO_2 at the lung. Hence, we may have complete control loops with delays for subjects 01 and 04 and some other reason for the respiratory gasps for subject 09.

4.1 Background Measurements

It is not easy to see further with regard to the mechanisms involved in periodic breathing than the present speculation from the data recorded here but it is worth exploring aspects and implications of the measurements available in Table 29.1.

(a) *Haemoglobin* (Hb) rose from the sea level mean of 13.4 $g\,dl^{-1}$ (range: 11.4–15.6, 7 subjects; subject 05, 12.5 at sea level not included) to 14.7 $g\,dl^{-1}$ (range 12.9–18.4 for 9 subjects) at the Hidden Valley or for the 5 sea level subjects with measurements also at high altitude the mean is 14.8 (range the same). On paired *t* testing Hb had risen by 1.4 $g\,dl^{-1}$ ($p<0.01$, one tail). This was in the face of sub-acute acclimatization, subjects having been at 5,000 m for less than 1 week.

(b) *Arterial content* (CaO_2) at rest (on air) mean of all eight subjects 17.7 ml dl^{-1} at sea level and 16.0 for seven subjects at altitude. For five subjects measured at both sites mean values were 17.2 ml d^{-1} at sea level 16.6 ml dl^{-1} at altitude, mean difference −0.6 ml dl^{-1} not significantly different ($p=0.085$, paired *t* testing). The increased Hb had largely compensated for the low SaO_2 at altitude (mean for the same subjects $81.4\% \pm 0.5\%$, an average fall of 13.4%).

(c) *Oxygen delivery* (DO_2) for all eight subjects at sea level, mean value 1,078 ml min^{-1} and seven subjects at altitude mean DO_2 was 934 ml min^{-1}, 13% less; comparison of five subjects at both levels gave mean DO_2 at sea level 1,187 ml min^{-1} and at altitude 1,008 ml min^{-1}, again only a 15% reduction on average which was not significant ($p=0.195$, paired *t* test, one tail). For DO_2 to be similar, at least, some compensation had occurred for low SaO_2 and could be partly from the increase in Hb and partly CO.

(d) *Examination of CO data* shows mean values that barely differ, however. For all sea level subjects ($n=8$) CO was 5.83 $l\,min^{-1}$ at sea level and for HV 5.77 $l\,min^{-1}$ (eight subjects, two were different) a difference of only 1%. On paired *t* testing six subjects' mean values were 6.21 and 6.03 $l\,min^{-1}$, still very similar (only a 3% fall). Therefore, on average, near compensation was achieved from the increase in Hb.

That air breathing DO_2 was sustained at rest on exposure to 12% oxygen at sea level has already been shown by Bell et al. [2]. However, the effect of exercise on SaO_2 in hypoxic subjects is illustrated by the recorded values.

(e) *Exercise in hypoxia almost always caused a fall in SaO_2* though there were occasions where a fall was followed by recovery. SaO_2 for subject 01 at sea level fell on exercise initially well below the resting value on 12% O_2 but ended up higher. Mean SaO_2 fall at sea level from rest to exercise was $5.85\% \pm 2.09\%$ (SEM), $p = 0.012$ (from 88.5% to 82.7%). For the Hidden valley the fall in SaO_2 was $3.40\% \pm 0.53\%$ (SEM), $p << 0.001$ (from 80.6% to 77.2%). The fall with exercise was therefore usual in both acute and sub-acute hypoxia.

(f) *Mean DO_2 in exercise* for sea level (on 12% oxygen) for eight subjects was $1{,}673 \pm 160$ $l\,min^{-1}$ (SEM) and $1{,}452 \pm 258$ for eight subjects at altitude. However, only four subjects' measurements were common to both altitudes (01, 03, 04 and 07) and the means were $1{,}728 \pm 135\,l\,min^{-1}$ and $1{,}680 \pm 304\,l\,min^{-1}$. Neither unpaired nor paired *t* tests showed the differences as significant but the work rate may not have been quite the same. Also, individual differences were large and in both directions.

In summary, the strikingly significant aspects of this background data (Table 29.1) were:

1. Increased Hb on ascent to the Hidden Valley (5,000 m)
2. Fall in SaO_2 at rest
3. Drop in SaO_2 from hypoxic rest to exercise both at sea level and at altitude

Non-significant changes were:

1. CaO_2 between sea level and high altitude while breathing ambient air.
2. DO_2 values at sea level and at high altitude, both comparing rest and comparing exercise. However, individual differences were present.
3. Average CO at rest was the same at sea level and altitude but, again, there were individual differences.

5 In Conclusion

The idea that periodic breathing accompanied by constant end-tidal PCO_2 must be accompanied by periodic, or oscillatory, CO has been confirmed in two subjects. A third subject's recordings manifested the phenomenon but the blood pressure record was inadequate for derivation of the concurrent CO. The CO changes appear to act towards sustaining oxygen delivery.

Acknowledgments Thanks are due to Professor CJ Hinds (anaesthetics) for providing the hypoxic gas mixture (William Harvey Institute, Queen Mary College, London, UK). Also, Medical Expeditions – Medex, for the provision of Laboratory Facilities in collaboration with the Department of Health and Exercise Sciences, School of Sport, Bangor, Wales, UK.

References

1. Wolff CB (2007) Normal cardiac output, oxygen delivery and oxygen extraction. Adv Exp Med Biol 599:169–182
2. Bell M, Thake CD, Wolff CB (2011) Effect of inspiration of 12% O_2 (balance N_2) on cardiac output, respiration, oxygen saturation and oxygen delivery. Adv Exp Med Biol 701:327–332, Ch. 44
3. Collier DJ, Nickol AH, Milledge JS, van Ruiten HJA, Collier CJ, Swenson ER, Datta A, Wolff CB (2008) Alveolar PCO_2 oscillations and ventilation at sea level and at high altitude. J Appl Physiol 104:404–415

Chapter 30
The Relationship of Acute Mountain Sickness to Arterial Oxygen Saturation at Altitudes of 3,324 to 5,176 m

G. Brierley, T. Parks, and C.B. Wolff

1 Introduction

Acute mountain sickness (AMS) is a recognised complication of exposure to hypobaric hypoxia. There are few factors predictive of the condition whose complications can include pulmonary oedema and death. The Lake Louise Consensus Scoring System [1] has been verified as a method of accurately recording AMS symptoms.

Compensation for hypobaric hypoxia at altitude through increased blood flow and oxygen delivery is a recognised phenomenon. However, its relationship to AMS is not yet understood. Previous studies include that of Kazanobu et al. of an 11-day trek to 3,650 m from 2,350 m which showed AMS correlating with SaO_2 [2] and that of Burgess et al. who found a significant association between AMS and minimum sleep and exercise SaO_2 values up to and including 5,050 m [3]. Burgess et al. were unable to show a relationship between AMS at altitude and sea level hypoxic ventilatory response. In a study by Roach et al. [4] resting SaO_2 in 102 asymptomatic subjects at 4,200 m were largely predictive of subsequent AMS on a climb towards a higher altitude summit (6,194 m). Those with the lowest SaO_2 values had the highest incidence of AMS during the further ascent.

We therefore hypothesised that individuals who did not increase their oxygen delivery appropriately would suffer more symptoms of AMS than those who did.

G. Brierley • T. Parks
Oxford Radcliffe Hospitals NHS Trust, Headley Way, Headington, Oxford, UK

W. C.B. (✉)
Clinical Pharmacology and Anaesthetics, William Harvey Research Institute,
Barts and The London, Queen Mary College, London University, 52 Victoria Park CB4 3EL,
Cambridge, London, UK
e-mail: chriswolff@doctors.org.uk

M. Wolf et al. (eds.), *Oxygen Transport to Tissue XXXIII*, Advances in Experimental Medicine and Biology 737, DOI 10.1007/978-1-4614-1566-4_30,

2 Methods

During a 28-day expedition in the Peruvian Andes, measurements were taken from a willing team of seven UK residents and, for 20 days only, one sea-level dwelling Peruvian resident (subject 9). Subject 6 joined the group late and gave up after 3 days. For subject 8 data were incomplete so have not been included in analysis. All participants (two female, subjects 1 and 2) had participated in sport at a high level apart from subject 5 who showed no signs of fatigue during the expedition. Age ranged from 18 to 26 years. Resting HR and SaO_2 were measured twice daily (Nellcor, Pulse Oximeters, Model N20, Rochester, USA). Rest measurement followed at least 5 min sitting quietly. Subjects also scored their AMS symptoms twice daily according to the Lake Louise Consensus Scoring System [1].

Following resting measurements, subjects carried out a 2-min period of exercise (stepping on and off a 22 cm step). During this period of exercise, SaO_2 and HR were recorded at 30-s intervals. The altitude at each recording was measured using a Global Positioning Satellite System (Garmin eTrex, Kansas, USA).

3 Results

All but one subject (04, with the highest mean SaO_2rest) showed a highly significant negative HRrest/SaO_2rest correlation. Examples are shown in Fig. 30.1: subject 04 (non-significant) on the left and subject 09 (highly significant, 20-day subject) on the right. The slope, intercept, *r* value, *n*, level of significance and mean SaO_2rest for each individual are given in Table 30.1.

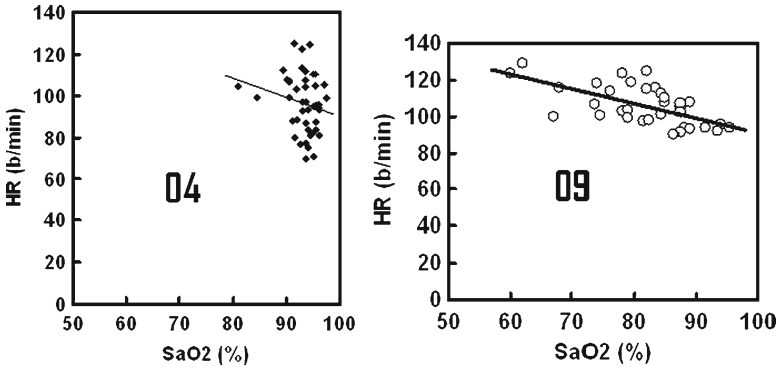

Fig. 30.1 Subject 04 had the highest mean SaO_2rest and was the only subject in whom HRrest failed to correlate with SaO_2rest when all twice daily recorded values were plotted (*left*). Subject 09 (20-day) HRrest versus SaO_2rest values show the strongest correlation and lowest mean SaO_2 (*right*)

Table 30.1 Regression relationships of heart rate to SaO_2rest (y=HR, x=SaO_2) for each individual subject

	Slopes	Intercepts	"r="	*n*	*P* values	SaO_2,means
01	−1.061	186.2	0.695	45	<0.001	84.7
02	−0.659	131.6	0.377	45	0.01	89.3
03	−0.758	147.5	0.516	45	<0.001	85.7
04	−0.896	179.8	0.200	45	ns	93.2
05	−1.555	230.3	0.559	45	<0.001	90.6
07	−0.695	131.1	0.390	45	0.01	88.4
10	−1.213	195.6	0.477	45	0.001	89.0
09	−0.800	171.2	0.633	35	<0.001	81.9

Subject 09 (20-day)

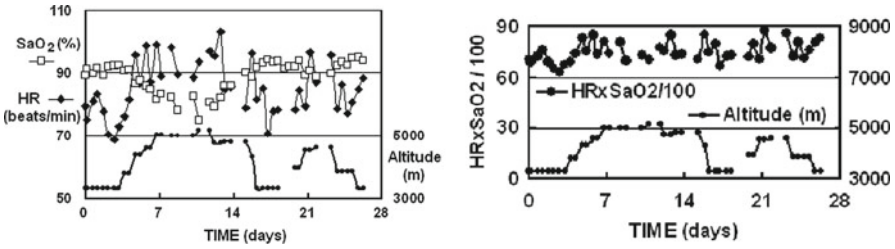

Fig. 30.2 Mean values for each time point of, on the *left*, HRrest and SaO_2rest and, on the *right*, HR × SaO_2 (DO_2). The corresponding altitudes are also shown (both plots). HRrest tends to be high when SaO_2rest is low at the higher altitudes. After the initial 5 days, there is little change in HR × SaO_2

SaO_2rest, HRrest and HR × SaO_2 (DO_2 surrogate for oxygen delivery) were plotted for each subject individually. All subjects showed a small increase in DO_2 after 5 days then, with some variation, a near constant value for the rest of the trip (data not shown). Values of SaO_2rest, HRrest and DO_2 for all individuals who completed the 28-day trek were averaged (mean) for each time point. Figure 30.2 shows, on the left, mean values of HRrest and SaO_2rest for each time point plotted with altitude for the 28-day expedition and mean values for DO_2 on the right, again with altitude. The approximately opposite movement of HR and SaO_2 is apparent, as is the near constant DO_2, which, having risen as the subjects gain altitude on day 5 and 6 shows no obvious further trend.

The opposing changes in HRrest and SaO_2rest are consistent with compensation for hypoxia, compatible with the observed, near constant DO_2. However, a wide range of values for individual mean SaO_2rest was noted; the values for each subject (for the whole expedition) are plotted in Fig. 30.3 (x-axis) with mean HRrest (y-axis). As expected, HRrest does not correlate with SaO_2rest here since subjects differed in weight and stature.

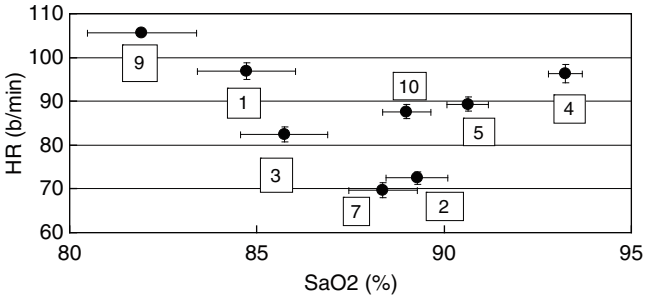

Fig. 30.3 Here individual mean values for HRrest and SaO_2rest have been plotted for the whole trip, with standard error bars. Mean SaO_2rest values cover a wide range

Table 30.2 SaO_2 and HR means are given for rest and exercise for each subject completing 28 days, with rest/exercise differences

Subject	SaO_2 ex	SaO_2 rest	Diff SaO_2	HR ex	HR rest	Diff HR	AMS mean
01	78.7	84.7	6.0	108.6	96.9	11.7	3.56
02	86.3	89.3	3.0	88.6	72.5	16.1	1.63
03	80.3	85.7	5.5	89.7	82.5	7.1	2.32
04	89.9	93.2	3.3	107.0	96.2	10.7	0.30
05	86.9	90.6	3.7	98.5	89.4	9.2	0.22
07	85.1	88.4	3.3	81.7	69.7	12.0	1.86
10	86.4	89.0	2.6	96.3	87.6	8.7	1.12

Mean AMS scores are also given

All exercise values for each subject who completed 28 days were averaged (mean) to give individual mean values for HRex and SaO_2ex. These are shown in Table 30.2. Resting values and the differences (exercise minus rest) are included. Mean AMS scores are also given for each individual subject.

Individual mean SaO_2rest and SaO_2ex appear in Fig. 30.4; SaO_2ex versus SaO_2rest (left panel with a line of identity); mean AMS score against mean SaO_2, separately for rest and exercise (right panel). Regression line equations: $AMSmean = -0.3778 \times SaO_2rest + 35.086$ ($r = 0.926$, $p = 0.002$) and $AMSmean = -0.273 \times SaO_2ex + 24.726$ ($r = 0.927$, $p = 0.003$). Hence, individual mean AMS scores are highly significantly related to mean SaO_2. The Peruvian subject (09, 20-day) did not undertake the exercise protocol; his AMS score is much lower than expected given his SaO_2rest value but he did complete less time at altitude (Fig. 30.4).

4 Discussion

In the present study, the surrogate for oxygen delivery ($DO_2 = HR \times SaO_2$) remained near constant once the expedition climbed above 3,324 m. There was a highly significant correlation between HRrest and SaO_2rest in all but the subject with the

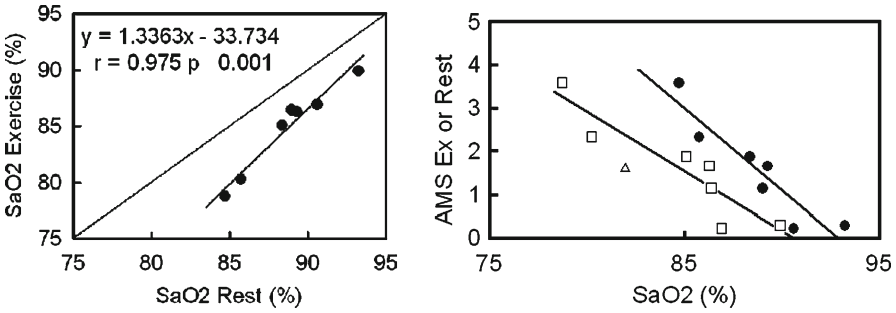

Fig. 30.4 On the *left* are shown individual mean SaO_2 values for exercise and rest for all seven 28-day subjects with a line of identity. On the *right* are shown the relationship of mean AMS score to mean SaO_2 either for rest (*solid circles*) or for exercise (*open squares*). The triangle represents AMS score against SaO_2rest for subject 09 (20-day)

highest mean SaO_2rest. The wide ranging individual mean SaO_2rest shows variation in respiratory compensation, but the HRrest/SaO_2rest correlations are evidence of circulatory compensation. Those subjects with more pronounced respiratory compensation, that is higher mean SaO_2rest, appear the more successful in sustaining lower AMS scores. However, the sustainability of appropriate DO_2 would probably not continue with higher altitudes, more rapid ascent or even mild exercise. There was no bias from gender differences (SaO_2 values for subjects 1 and 2 – female – are part of an even spread, Fig. 30.3).

The original hypothesis, that DO_2 would be reduced in those with the highest AMS scores, turns out to be wrong for this altitude profile. In a recent study DO_2 was also sustained on acute exposure to moderate hypoxia (12% oxygen), also showing a range of ventilatory and cardiac output responses [5]. It is possible that PCO_2 at sea level may predict the response to hypobaric hypoxia since low SaO_2 will go with a high PCO_2 as shown by Reeves et al. [6]. It is of interest that double insertion of the ACE gene gives individuals an advantage where extreme ascents are concerned [7]. Whether the ACE gene advantage is coupled to the more pronounced respiratory compensation found here and by [6] awaits future studies.

Acknowledgments Thanks are due for advice from David Collier and for the loan of pulse oximeters to G Douglas Thake. Also, for Grants given by Cambridge University Expeditions Fund, the Wellington College Bevir Memorial Trust and the Selwyn College Cott Fund.

References

1. Hackett PH, Oeltz O (1992) The Lake Louis Consensus on the definition and quantification of altitude illness. In: Sutton JR, Coates G, Houston CS (eds) Hypoxia and mountain medicine. Queen City Printers, Burlington, pp 327–330
2. Kazunobu O, Hiroshi E, Yumiko E, Katsumi A (2001) Acute mountain sickness and arterial oxygen saturation during altitude trekking. Comparisons between high school adolescents, young adults and middle-older adults. Jpn J Mt Med 21(1):83–88

3. Burgess KR, Johnson P, Edwards N, Cooper J (2004) Acute mountain sickness is associated with sleep desaturation at high altitude. Respirology 9:485–492
4. Roach RC, Greene ER, Schoene RB, Hackett PH (1998) Arterial oxygen saturation for prediction of acute mountain sickness. Aviat Space Environ Med 69(12):1182–1185
5. Bell M, Thake CD, Wolff CB (2011) Effect of inspiration of 12% O_2 (balance N_2) on cardiac output, respiration, oxygen saturation and oxygen delivery. Adv Exp Med Biol 701:327–332, Ch 44
6. Reeves JT, McCullough RE, Moore LG, Cymerman A, Weil JV (1993) Sea-level PCO_2 relates to ventilatory acclimatization at 4,300 m. J Appl Physiol 75(3):1117–1122
7. Montgomery HE, Marshall RM, Hemingway H, Myerson S, Clarkson P, Dollery C et al (1998) Human gene for physical performance. Nature (London) 393:221–222
8. Wolff CB (2007) Normal cardiac output, oxygen delivery and oxygen extraction. Adv Exp Med Biol 599:169–182
9. Parks T, Brierley G, Wilson C, Wolff C (2009) Arterial blood oxygen saturation and heart rate and their relationship to acute mountain sickness at altitude. A field study (abstract). Proc Physiol Soc 14:PC2

Chapter 31
Effects of Acute Anemia and Hyperoxia on Oxygen Distribution

Catalina Messmer, Pedro Cabrales, and Marcos Intaglietta

1 Introduction

Hyperoxic ventilation (HV) is used clinically as a means to augment tissue oxygenation through the increase of arterial oxygen content in conditions of anemia. Since hemoglobin is saturated with oxygen when arterialized blood leaves the lung, the increase in oxygen delivery attained by HV is restricted to the increase in the amount of oxygen dissolved in plasma [1]. It is generally perceived that oxygen supplementation is beneficial; however, there is no compelling evidence that it yields a positive clinical effect. This could be the consequence of increased tissue pO_2 due to increased FiO_2 lowering tissue perfusion due to vasoconstriction, as demonstrated in the vasculature of the brain, heart, and limbs. Exposure of the tissue to hyperoxic conditions causes vasoconstriction, as shown by Lindbom and Arfors [2], in the microcirculation of the rabbit tenuissimus muscle where exposure of the preparation to high oxygen content superfusion solution decreased functional capillary density (FCD: number of capillaries with RBC transit per unit volume of tissue). Thorborg et al. [3] showed that mean tissue pO_2 on the surface of skeletal muscle increases when FiO_2 is progressively increased from normal to 0.70; however, as the average tissue pO_2 increased, so did the dispersion of the data, i.e., the number of tissue regions with low and high pO_2. Whalen and Nair [4] showed a fall in deep tissue pO_2 in cat skeletal muscle when the surface of the tissue was exposed to elevated oxygen levels, an effect also found by Duling [5] in the arterioles of the hamster cheek pouch. Experimental studies tend to show that hyperoxia does not provide a uniform benefit for tissue oxygenation [6, 7] since vasoconstriction interferes with capillary oxygen delivery when blood oxygen content and pO_2 are increased in the tissue. This may be due to an oversupply of oxygen resulting from the extra oxygen

C. Messmer (✉) • P. Cabrales • M. Intaglietta
Department of Bioengineering, University of California San Diego,
9500 Gilman Drive, La Jolla, CA 92093, USA
e-mail: c_messmer@gmx.de

M. Wolf et al. (eds.), *Oxygen Transport to Tissue XXXIII*, Advances in Experimental Medicine and Biology 737, DOI 10.1007/978-1-4614-1566-4_31,

carried by plasma in combination with the oxygen transported by RBCs. This oversupply of oxygen may not be present in conditions of hemodilution when the intrinsic oxygen-carrying capacity of blood is diminished. The present study was carried out to determine the functional effects of normobaric HV (FiO_2 1.00) in the microcirculation in the unanesthetized hamster window chamber model in conditions of isovolumic hemodilution and to determine if vasoconstriction interferes with tissue oxygenation.

2 Materials and Methods

Animal preparation. Investigations were performed in Golden Syrian hamsters of 55–65 g BW. The hamster window chamber model is often used for microvascular studies in unanesthetized hamsters. Surgical technique and preparation is described in detail elsewhere [8]. *Inclusion criteria*. MAP > 80 mmHg, HR > 320 bpm, Hct > 45%, and systemic arterial pO_2 > 50 mmHg. *Study protocol*. Acute hemodilution was induced by exchanging 40% of the animals blood volume with dextran 70 kDa (B. Braun, Irvine, CA). *Functional capillary density*. Functional capillaries are defined as capillary segments that have RBC transit in a 30-s period. Observation was done systematically by displacing the microscopic field of view by a field width across the window chamber in 10–15 successive steps. The first field was chosen by some distinctive anatomic landmark (i.e., large bifurcation) to easily and quickly reestablish the same fields throughout the experiment. *Microvascular pO_2 distribution*. PO_2 measurements were made using the Pd-phosphorescence quenching method developed by Wilson [9], adapted for microcirculatory studies [10] based on the oxygen-dependent quenching of phosphorescence emitted by albumin-bound metalloporphyrin complex after pulsed light excitation. *Cardiac Output (CO) measurements*. CO was measured by a modified thermodilution technique [11] on a different group of animals. Measurements were done under normoxic conditions and hyperoxic conditions after an adaptation period of 5 min. *Statistical analysis*. Comparisons were made with the Mann-Whitney rank sum test (GraphPad Prism 4). Changes are considered statistically significant if $p < 0.05$. Calculations that are not directly measurable in our model are based on mean values of measured parameters. *Experimental setup*. Systemic parameters, blood gas analysis, vascular diameter [12], RBC velocity [13, 14], and FCD measurements were recorded 5 min after the animal had become accustomed to the restraining tube and to the tent air-flow system under an inverted microscope equipped with a water immersion ×40 objective. Six arterioles and six venules in each animal were chosen for investigation. The same sites of study were followed throughout the experiment. After microvascular and systemic baseline characterization, the inlet gas to the plastic tent was switched to 100% O_2 to induce hyperoxia. After 5 min of exposure, systemic parameters and blood gas analysis were evaluated, as well as FCD. The Pd-porphyrin dye was injected over 1 min intravenously and allowed 10 min to distribute. Intravascular oxygen tension in the vessels and tissue was measured.

3 Results

The microvascular study was performed using 20 animals. All assigned animals tolerated the hemodilution protocol without visible signs of discomfort. The animals were assigned randomly to the experimental groups: 43% Hct, FiO_2 0.21 ($n=5$), 43% Hct, FiO_2 1.00 ($n=5$), 25% Hct, FiO_2 0.21 ($n=5$), and 25% Hct, FiO_2 1.00 ($n=5$). Additional animals were used for the separate cardiac output measurements. Systemic conditions of the different groups are given in Table 31.1. These results show that inspired gas (FiO_2 1.00) did not statistically modify MAP, HR, Hb, Hct, pH, pCO2, BE, and FCD. However, CO changed significantly during hyperventilation; CO was reduced (values relative to baseline 1.00 at 43% Hct and FiO_2 0.21) to 0.71 for 43% Hct by the increase of FiO_2 to 1.00, hemodilution increased CO to 1.36 for 25% Hct FiO_2 0.21 and decreased to 0.94 for 25% Hct, FiO_2 1.00. FiO_2 of 1.00 caused a significant increase in arterial pO_2 of 620% increase at 43% Hct and 700% increase at 25% Hct. Animals were able to maintain their blood pH and pCO_2. The changes in arteriolar and venular diameters are shown in Fig. 31.1; changes were not significantly different from baseline. Figure 31.2 shows the change of the RBC flow velocity in arterioles and venules following FiO_2 1.00. Inhalation of high oxygen levels increased flow velocity at normal conditions and decreased flow velocity at Hct 25%. The diameter and RBC velocity data were used to compute microvascular blood flow in the vessels resulting from this calculation. Arteriolar and venular flow after exposure to hyperoxia was increased at normal Hct and decreased at Hct 25%. The tissue pO_2 measured by scanning the tissue along set paths without regard to microvascular structures have a Gaussian distribution (mean ± SD, mmHg): 29.6 ± 5.7 (43% Hct, FiO_2 0.21); 32.0 ± 10.5 (43% Hct, FiO_2 1.00); 31.12 ± 8.0 (25% Hct, FiO_2 0.21); 26.0 ± 11.3 (25% Hct, FiO_2 1.00) (Table 31.2). All changes are significant relative to baseline measurements at FiO_2 0.21, $p<0.05$. Oxygen tensions in the microvascular network in hyperoxic and normal conditions were 36.4 ± 3.8 (43% Hct, FiO_2 0.21); 45.0 ± 7.6 (43% Hct, FiO_2 1.00); 41.3 ± 85

Table 31.1 Systemic and blood gas parameters

Parameters	43% Hct, FiO_2 0.21	43% Hct, FiO_2 1.00	25% Hct, FiO_2 0.21	25% Hct, FiO_2 1.00
Blood pressure (mmHg)	122.1 ± 8.2	127.1 ± 6.3	115 ± 7.1	109.5 ± 11.9
Heart rate (beats/min)	447 ± 39	436 ± 43	401 ± 61	424 ± 63
Cardiac output (ml/min)	17.9 ± 3.3	12.7 ± 2.7	24.3 ± 4.3	16.9
Cardiac index [ml/(min kg)]	203.4 ± 16.2	144 ± 31	277.3 ± 39.5	192.8
Hematocrit (%)	42.8 ± 3.0	42 ± 3.4	27.2 ± 1.8	30.8 ± 4.6
Hemoglobin (g/dl blood)	14.6 ± 0.8	14.6 ± 0.8	9.4 ± 0.5	10.4 ± 1.5
PH	7.393 ± 0.02	7.354 ± 0.02	7.340 ± 0.04	7.523 ± 0.02
pCo_2 (mmHg)	51.4 ± 3.9	56.96 ± 5.4	60.36 ± 5.8	60.3 ± 3.4
pO_2 (mmHg)	66.5 ± 7.1	412.5 ± 26.8	64.5 ± 7.9	451.8 ± 10.2
Base excess (mmol/l)	4.36 ± 0.7	3.8 ± 1.1	4.1 ± 1.8	3 ± 2.3
FCD	90 ± 19	91 ± 26	88 ± 31	83 ± 16

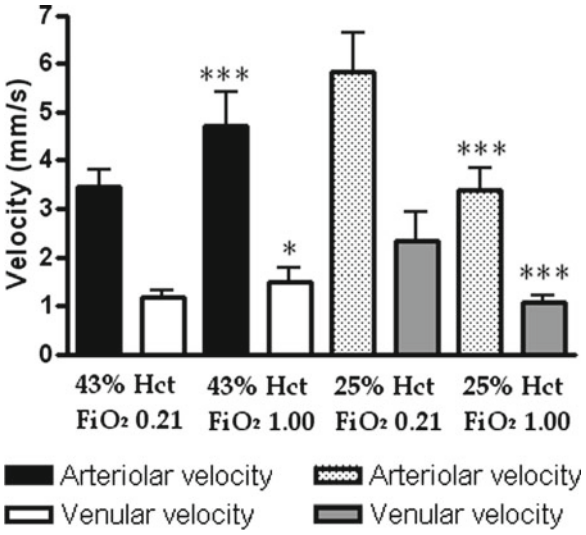

Fig. 31.1 Changes of blood flow as a result of 100% oxygen inspiration

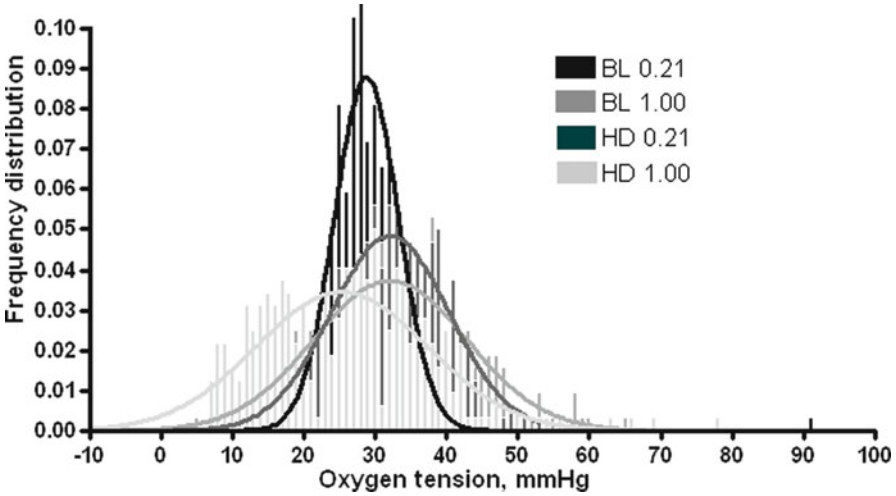

Fig. 31.2 Distribution of oxygen tension during normoxia and normobaric hyperoxia

(25% Hct, FiO_2 0.21); 51.2 ± 14.2 (25% Hct, FiO_2 1.00) in arterioles and 27.3 ± 4.9 (43% Hct, FiO_2 0.21); 35.5 ± 10.7 (43% Hct, FiO_2 1.00); 26.3 ± 9.8 (43% Hct, FiO_2 0.21); 23.1 ± 8.1 (25% Hct, FiO_2 1.00) in venules. During hyperoxia they were significantly different from the corresponding order in normoxia. Table 31.2 shows data on oxygen delivery and consumption in the microcirculation.

Table 31.2 Oxygen delivery and consumption in the microcirculation of the hamster window model

	43% Hct, FiO_2 0.21	43% Hct, FiO_2 1.00	25% Hct, FiO_2 0.21	25% Hct, FiO_2 1.00
Microvascular arterial flow (nL/s)	1	1.07	1	0.6
Microvascular venular flow (nL/s)	1	1.6	1	0.43
Arteriolar PO_2 (mmHg)	36.4 ± 3.8	45.0 ± 7.6	41.3 ± 85	51.2 ± 14.2
Arteriolar saturation (%)	0.59	0.73	0.68	0.8
Venular PO_2 (mmHg)	27.3 ± 4.9	35.5 ± 10.7	26.3 ± 9.8	23.1 ± 8.1
Venular saturation (%)	0.39	0.57	0.36	0.28
Oxygen delivery (ml O_2/dl blood min)	19.47	32.41	13.11	28.05
Relative oxygen consumption (ml O_2/dl)	94.25	90.1	127.29	118.17

4 Discussion

The principal finding of the study was that HV with 100% oxygen has a limited effect on microvascular pO_2 at physiological hematocrit but leads to diminuition of oxygen tension in the tissue and a decrease of blood flow velocity after moderate hemodilution. HV increases the amount of oxygen physically dissolved in plasma and by that CaO_2 (arterial oxygen content). Although at physiologic hemoglobin concentrations the percent contribution of plasma oxygen to VO_2 (oxygen consumption) may be considered negligible (approx. 5%), the situation changes after moderate acute normovolemic hemodilution; because of the loss of erythrocytes as oxygen transporters, the percent contribution of physically dissolved oxygen to VO_2 increases to 47% (hemoglobin 7 g/dl) [1]. In the hemodilution group the vasodilatation due to anemia seems to be compensated by the vasoconstrictive component of HV, therefore we do not see any significant difference in vessel diameters between the groups. At physiological Hct, blood flow velocity was significantly increased by HV, while it was decreased at anemic conditions, which might be due to the loss of erythrocytes which can act like an oxygen puffer in order to protect the tissue from harm by HV, so that the organism reacts with a reduction of blood flow velocity as compensating mechanism. Moreover, hyperoxia initiated after moderate hemodilution partially reversed the compensatory mechanisms for moderate anemia where blood flow normally increases and created a margin of safety for tissue oxygenation and organ function. However, the oxygen frequency distribution in the hyperventilated 25% Hct group in our study was significantly lower compared to the other groups, which could be due to lower blood flow velocity.

We conclude in our study that at normal Hct values and during moderate hemodilution hyperoxia-induced vasoconstriction impairs microvascular oxygen transport and tissue oxygenation in the peripheral microcirculation.

Acknowledgments The authors thank F. Barra and C. Walser for technical assistance with the animal preparation.

References

1. Habler OP, Kleen MS, Hutter JW et al (1998) Effects of hyperoxic ventilation on hemodilution-induced changes in anesthetized dogs. Transfusion 38:135–144
2. Lindbom L, Arfors KE (1985) Mechanism and site of control for variation in the number of perfused capillaries in skeletal muscle. Int J Microcirc Clin Exp 4:121–127
3. Thorborg P, Malmqvist LA, Lund N (1988) Surface oxygen pressure distribution in rabbit skeletal muscle: dependence on arterial pO_2. Microcirc Endothelium Lymphatics 4:169–192
4. Whalen WJ, Nair P (1970) Skeletal muscle pO_2: effect of inhaled and topically applied O_2 and CO_2. Am J Physiol 218:973–980
5. Duling BR (1972) Microvascular responses to alterations in oxygen tension. Circ Res 31:481–489
6. Bertuglia S, Colantuoni A, Coppini G et al (1991) Hypoxia- or hyperoxia-induced changes in arteriolar vasomotion in skeletal muscle microcirculation. Am J Physiol 260:H362–H372
7. Sullivan SM, Johnson PC (1981) Effect of oxygen on arteriolar dimensions and blood flow in cat sartorius muscle. Am J Physiol 241:H547–H556
8. Endrich B, Asaishi K, Götz A et al (1980) Technical report: a new chamber technique for microvascular studies in unanaesthetized hamsters. Res Exp Med 177:125–134
9. Wilson DF (1993) Measuring oxygen using oxygen dependent quenching of phosphorescence: a status report. Adv Exp Med Biol 333:225–232
10. Torres Filho IP, Intaglietta M (1993) Microvessel PO_2 measurements by phosphorescence decay method. Am J Physiol Heart Circ Physiol 265:H1434–H1438
11. Cabrales P, Acero C, Intaglietta M et al (2003) Measurement of the cardiac output in small animals by thermodilution. Microvasc Res 66:77–82
12. Intaglietta M, Tompkins W (1973) Microvascular measurements by video image shearing and splitting. Microvasc Res 5:309–312
13. Intaglietta M, Silverman NR, Tompkins WR (1975) Capillary flow velocity measurements in vivo and in situ by television methods. Microvasc Res 10:165–179
14. Lipowsky HH, Zweifach BW (1978) Application of the “two-slit” photometric technique to the measurement of microvascular volumetric flow rates. Microvasc Res 15:93–101

Part IV
Oxygenation of Various Organs

Chapter 32
Monitoring Cardiopulmonary Function and Progression Toward Shock: Oxygen Micro-sensor for Peripheral Tissue

David F. Wilson, Sergei A. Vinogradov, Gregory J. Schears, Tatiana V. Esipova, and Anna Pastuszko

1 Introduction

According to the Center for Disease Control, trauma is the leading cause of death between the ages of 1 and 44, of both civilians and military personnel. Hemorrhage is responsible for over 35% of pre-hospital deaths and over 40% of deaths within the first 24 h of arrival to a trauma facility [1]. In the military environment, this can reach up to 90% [2]. Onset of shock occurs when loss of blood leads to insufficient delivery of oxygen to critical central organs. This depresses essential energy metabolism and increases carbon dioxide and other acids in the cells of these tissues and the organs begin to fail.

Recognizing and rapidly treating inadequate oxygen delivery to tissues is a cornerstone of critical care management, but standard methods for objectively quantifying and monitoring deficient oxygen delivery are recognized to be inadequate (see [3]). First, responders must identify which patients have insufficient blood volume, and therefore require perfusion, and which patients do not, avoiding fluid overloading of the latter. Early-stage shock due to insufficient blood volume is often difficult to recognize due to compensatory mechanisms in the body that shutdown flow to low-priority tissues, such as peripheral muscle, in order to maintain flow to the essential central organs such as the brain, heart, and lungs [4]. Infusing fluids into all patients regardless of whether they are deficient in blood volume is not a

D.F. Wilson (✉) • S.A. Vinogradov • T.V. Esipova • A. Pastuszko
Department of Biochemistry and Biophysics, University of Pennsylvania, 422 Curie Boulevard, 915 S-C Building, Philadelphia, PA 19104, USA
e-mail: wilsondf@mail.med.upenn.edu

G.J. Schears
Department of Anesthesiology, Mayo Clinic, Rochester, MN 55905, USA

M. Wolf et al. (eds.), *Oxygen Transport to Tissue XXXIII*, Advances in Experimental Medicine and Biology 737, DOI 10.1007/978-1-4614-1566-4_32,

viable solution because volume overload can cause life-threatening pathology. Dilution of the blood due to infusion of resuscitation products can also cause dysfunction in coagulation and this is associated with a 3.5- to 5-fold increase in mortality [5].

We describe a new, minimally invasive, sensor for accurate continuous monitoring of tissue oxygenation that is suitable for clinical use and should provide objective and quantitative measure of the oxygen delivery to tissue.

2 Methods

Measuring oxygen by phosphorescence quenching. Phosphorescence arises when a phosphor is excited to the triplet state by absorption of a photon of light and then returns to the ground state with emission of light (phosphorescence). The excited triplet state may also return to the ground state by colliding with, and transferring energy to, another molecule (quencher) in the environment. The rate of decay of the excited triplet state, phosphorescence lifetime, depends on the concentration of the quenching molecules in the solution. These properties have been used to develop a highly sensitive and accurate method for oxygen measurement by determining the extent of quenching of a phosphorescent probe [6–9]. The phosphorescence lifetime or intensity may be converted to oxygen pressure using the Stern–Volmer relationship:

$$\frac{I^0}{I} = \frac{T^0}{T} = 1 + k_Q T^0 \left[\mathrm{pO}_2\right], \tag{32.1}$$

where I^0 and T^0 are the Intensity and lifetime in the absence of oxygen, respectively, I and T are the intensity and lifetime, respectively, at a given value of oxygen pressure (pO_2), and k_Q is a constant describing the frequency of quenching collisions between the phosphor molecules in the triplet state and molecular oxygen. k_Q is a function of the diffusion constants for phosphor and oxygen, temperature and phosphor environment (see [8] for calibration). A frequency domain phosphorescence lifetime measurement instrument [9] with a 635-nm laser diode as the light source and an avalanche photodiode detector was used in the present studies to determine phosphorescence lifetimes and thereby oxygen concentrations.

Phosphorescent oxygen sensors (Oxyphors). A number of phosphorescent oxygen probes have been described [10–15]. Oxyphor G3, the one chosen for this application, is based on Pd-tetrabenzoporphyrin [16] (Fig. 32.1). Oxyphor G3 is a Pd tetrabenzoporphyrin (PdTBP) modified with generation-3 polyarylglycine dendrons and coated with a layer of peripheral polyethylene glycol (PEG) residues. The dendrimer in G3 folds tightly around the PdTBP core in aqueous media and controls its exposure to oxygen. The phosphorescence quantum yield of G3 is about 2% and the lifetime T^0 is about 270 μs. The Oxyphor G3 has absorption bands with maxima at 445 and 635 nm and the phosphorescence emission maximum is near 810 nm.

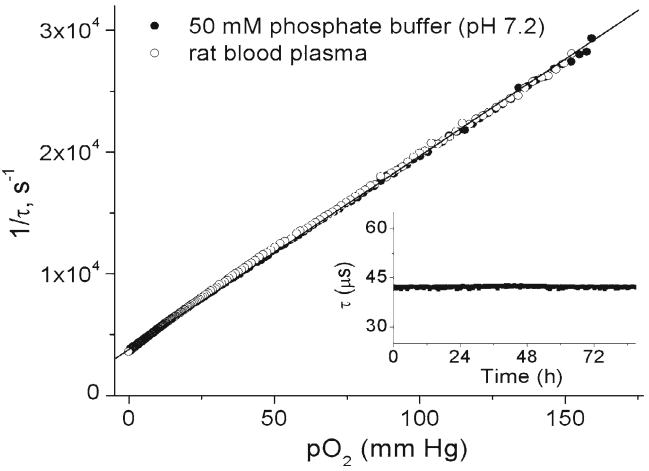

Fig 32.1 Calibration of Oxyphor G3. The measurements are of the phosphorescence lifetime of Oxyphor G3 as a function of the oxygen pressure when it is dissolved in phosphate buffer and in blood plasma at 23°C. The straight line is the best fit to the Stern–Volmer equation. The inset shows measurements of the Oxyphor G3 lifetime in air-saturated phosphate buffer measured over a >72-h period

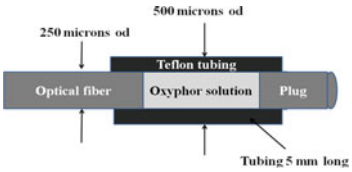

Fig. 32.2 A schematic drawing of the prototype oxygen sensor on the end of a 250 μm outside diameter plastic optical fiber

Oxygen micro-sensors. In order to facilitate use of the sensors in the clinics, it is important that the Oxyphor is not in direct contact with the body. To accomplish this we have chosen to sequester the solution of Oxyphor in a sealed Teflon AF chamber. This chamber has been made very small and placed on the end of an optical fiber (Fig. 32.2). The optical fiber conducts the excitation light from a 635-nm laser diode to the sample and returns the emitted phosphorescence to the detector. The current prototype chamber uses Teflon tubing with an outside diameter of 500 μm and an inside diameter of 250 μm, placed on the end of a 250-micron plastic optical fiber.

All animal procedures strictly followed the NIH Guide for the Care and Use of Laboratory Animals and have been approved by the Institutional Animal Care and Use Committee of the University of Pennsylvania.

3 Results

The oxygen micro-sensors have been extensively tested in vitro. The response time measured when sensors are moved between two solutions with different oxygen pressures (such as air saturated and about 15 torr) is slightly less than 1 min. This is sufficiently rapid to measure most physiological changes in oxygen pressure in tissues. The in vitro stability has been measured by placing micro-sensors in air-saturated media and measuring the internal oxygen pressure each 15 s over periods of up to 16 h. The measurement to measurement variability was typically less than ±2%. The signal to noise was initially near 40 and declined over the 16 h to about 20. Individual sensors have been constructed and stored for many days without change in sensitivity as long as they are kept from drying out.

The micro-sensors are intended for measuring oxygen in tissue in vivo. Preliminary measurements have been made by "piggy backing" them to experiments studying the effects of hypoxic hypoxia and ischemic hypoxia on brain in a newborn piglet model. The sensors were inserted into the tissue while within a thin-walled 21-gauge needle and then the needle withdrawn. Figure 32.3 shows the measurements obtained when the sensor was placed in the striatum of the brain while Fig. 32.4 shows oxygen measurements placed in peripheral muscle (leg). In both cases, measurements were made for 4–6 h without significant increase in the noise level of the measurements.

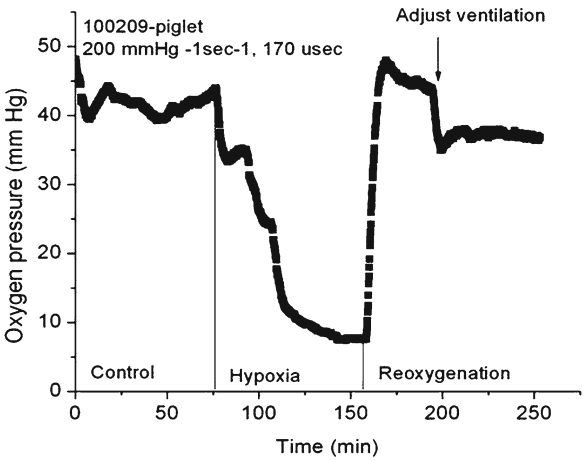

Fig. 32.3 Oxygen measurements in the striatum of the brain of anesthetized piglets. The sensors were inserted into the tissue inside 20-gauge needles and then the needles withdrawn. Measurements were begun within 1 min of insertion and continued at 15 s intervals. During the period labeled hypoxia, oxygen in the inspired air was stepwise lowered over a period of 20 min until the oxygen pressure in the brain decreased to 6–8 torr. The brain oxygen level was maintained at that level for 1 h and then the oxygen in the inspired gas was returned to 21%

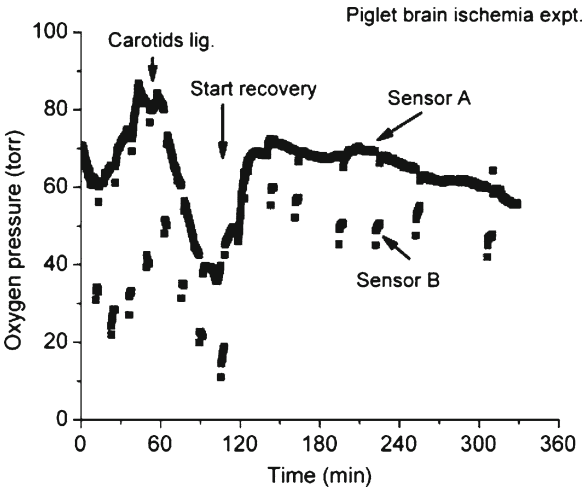

Fig 32.4 Oxygen measurements in the peripheral muscle of anesthetized piglets. The sensors were inserted into the tissue inside 20 gauge needles and then the needles withdrawn. Measurements were begun within 1 min of insertion and continued at 15 s intervals. Two sensors were inserted, one in the back leg (sensor A) and the other in the fore leg (sensor B). Ischemic hypoxia was induced in the brain by ligating both carotid arteries then lowering the oxygen in the inspired gas over a 20-min period to achieve a brain tissue oxygen pressure of 6–8 torr. This was maintained for 1 h, the ligations removed, and O_2 in the inspired gas raised to 21%. At about 15-min intervals, sensor (A) was disconnected and sensor (B) connected. After 4–6 measurements, B was disconnected and A was reconnected

4 Discussion

The first generation of oxygen micro-sensors for measurements in peripheral tissue have very good oxygen measurement capabilities. Their function appears well suited for monitoring the status of trauma patients, particularly by first response teams. Because the Oxyphor is in solution, the calibration is absolute, eliminating any need for on-site calibration and making the sensors fully interchangeable. Insertion requires minimal technical expertise and can be accomplished in less than 1 min. Measurements can begin as soon as the sensor is inserted into the tissue. The sensors are stable under measurement conditions and functioned reliably for periods of at least 4–6 h after insertion into the tissue. The initial oxygen sensors have outside diameters of 500 μm and response times of about 1 min, but it is expected that the size will be reduced to about 400 μm outside diameter, allowing insertion through 22-gauge needles and providing response times of 30 s or less. The phosphorescence lifetime reader used with the micro-oxygen sensors can be made small, less than $12 \times 10 \times 4$ cm, light weight, and battery powered, and therefore convenient and flexible enough for use in the field. The data can also be transmitted to a central computer system by building in an appropriate wireless transmitter, although this function has not been implemented in the prototype instruments.

Because there is a great need for better monitoring of trauma patients and generally for patients requiring critical care, extensive efforts are underway to try to fill this need. Much of the effort focuses on using near infrared light to measure hemoglobin saturation (NIR). This is a very attractive approach because the measurements are non-invasive and readily translated into the clinics. The weakness is that the measurements are of small differences in absorption in highly scattering media containing other chromophors. There are several NIR instruments in use or being tested in the clinics, but their predictive value in clinical applications remains to be established. In the case of trauma patients, clinical trials suggest the current generation of instruments provide data about as predictive of multi-organ failure as the base deficit [3, 17, 18].

The oxygen micro-sensors described in the present paper measure with high accuracy, even at the low oxygen concentrations expected to exist in tissue under conditions of compromised blood flow. They are, however, more invasive than NIR. Whether the higher accuracy will provide sufficient predictive advantage to justify the greater invasiveness remains to be established.

Acknowledgments Supported in part by grants NS-31465, HL-58669, HL081273, and 1R43HL103358. DFW, GJS, and SAV have patents issued and pending related to the described oxygen sensors.

References

1. Kauvar DS, Holcomb JB, Norris GC, Hess JR (2006) Fresh whole blood transfusion: a controversial military practice. J Trauma Inj Infect Crit Care 61(1):181–184
2. Cooke WH, Salinas J, Convertino VA et al (2006) Heart rate variability and its association with mortality in prehospital trauma patients. J Trauma Inj Infect Crit Care 60(2):363–370
3. Convertino VA, Ryan KL, Rickards CA et al (2008) Physiological and medical monitoring for en route care of combat casualties. J Trauma Inj Infect Crit Care 64(4 Suppl):S342–S353
4. Finch CA, Lenfant C (1972) Oxygen transport in man. New Engl J Med 286:407–415
5. Malone DL, Dunne J, Tracy JK et al (2003) Blood transfusion, independent of shock severity, is associated with worse outcome in trauma. J Trauma Inj Infect Crit Care 54(5):898–907
6. Vanderkooi JM, Maniara G, Green TJ, Wilson DF (1987) An optical method for measurement of dioxygen concentration based on quenching of phosphorescence. J Biol Chem 262:5476–5482
7. Wilson DF, Rumsey WL, Green TJ, Vanderkooi JM (1998) The oxygen dependence of mitochondrial oxidative phosphorylation measured by a new optical method for measuring oxygen. J Biol Chem 263:2712–2718
8. Dunphy I, Vinogradov SA, Wilson DF (2002) Oxyphor R2 and G2: phosphors for measuring oxygen by oxygen dependent quenching of phosphorescence. Anal Biochem 310:191–198
9. Vinogradov SA, Fernandez-Seara MA, Dugan BW, Wilson DF (2001) Frequency domain instrument for measuring phosphorescence lifetime distributions in heterogeneous samples. Rev Sci Instrum 72:3396–3406
10. Rozhkov V, Wilson DF, Vinogradov SA (2001) Tuning oxygen quenching constants using dendritic encapsulation of phosphorescent Pd-porphyrins. Polym Mater Sci Eng 85:601–603

11. Rozhkov V, Wilson DF, Vinogradov SA (2002) Phosphorescent Pd porphyrin-dendrimers: tuning core accessibility by varying the hydrophobicity of the dendritic matrix. Macromolecules 35:1991–1993
12. Finikova OS, Cheprakov AV, Beletskaya IP, Vinogradov SA (2001) An expedient synthesis of substituted tetraaryltetrabenzoporphyrins. Chem Commun 3:261–262
13. Finikova OS, Cheprakov AV, Beletskaya IP et al (2004) Novel versatile synthesis of substituted tetrabenzoporphyrins. J Org Chem 69(2):522–535
14. Rietveld IB, Kim E, Vinogradov SA (2003) Dendrimers with tetrabenzoporphyrin cores: near infrared phosphors for in vivo oxygen imaging. Tetrahedron 59:3821–3831
15. Vinogradov SA, Wilson DF (1994) Metallotetrabenzoporphyrins. New phosphorescent probes for oxygen measurements. J Chem Soc Perkin Trans II 2:103–111
16. Lebedev AY, Cheprakov AV, Sakadzic S et al (2009) Dendritic phosphorescent probes for oxygen imaging in biological systems. ACS Appl Mater Interfaces 1:1292–1304
17. Cohn SM, Nathens A, Moore FA et al (2007) The StO_2 in trauma patients trial investigators: tissue oxygen saturation predicts the development of organ dysfunction during traumatic shock resuscitation. J Trauma 62:44–55
18. Moore FA, Nelson T, McKinley BA (2008) Massive transfusion in trauma patients: tissue hemoglobin oxygen saturation predicts poor outcome. J Trauma 64:1010–1023

Chapter 33
Whole Body Oxygen Delivery and Consumption During Cardiopulmonary Bypass Surgery

J. Ashmore, J. Pickett, J. Alder, R. Marks, and M. Thorniley

1 Introduction

Maintenance of adequate perfusion during cardiopulmonary bypass (CPB) is vital for the preservation of organ function. A balance between oxygen demand and supply is required in order to prevent tissue ischaemia. Hypothermic conditions during CPB are known to be cerebrally protective by slowing the rate of metabolism and reducing demand for oxygen [1]. This can extend the safety margins of perfusion practice during surgery resulting in the possibility of lower pump flow rates and reduced haematocrit [2, 3]. Despite the clear benefits from the application of hypothermia during surgery, the incidence of neurological injury following CPB still remains a major concern. One landmark study has shown that 42% of patients develop long-term cognitive impairment 5 years post-operatively [4]. The aim of this study is to investigate the limits of this hypothermic protection by direct measurement of oxygen delivery and consumption, during full flow bypass and for periods of hypoperfusion.

J. Ashmore (✉) • J. Pickett
Department of Clinical Physics, The Royal London Hospital, Barts and The London NHS Trust, 56-76 Ashfield Street, Whitechapel, London E1 2BL, UK
e-mail: jonathan.ashmore@nhs.net

J. Alder • M. Thorniley
Medical School, University of Manchester, Sheffield S5 7AU, UK

R. Marks
Department of Anaesthesia, Northern General Hospital, Herries Road, Sheffield S5 7AU, UK

M. Wolf et al. (eds.), *Oxygen Transport to Tissue XXXIII*, Advances in Experimental Medicine and Biology 737, DOI 10.1007/978-1-4614-1566-4_33,

2 Methods

Measurements of total oxygen consumption and delivery were made from 12 patients undergoing CPB performed by the same surgeon. A standardized anaesthetic technique was applied and the oxygen consumption and delivery measurements were derived from in-line oximetry and bypass pump flow rate recordings [5]. Each recording contained a period of hypothermia (32°C) followed by a period of re-warming returning the patient to normothermic temperatures (37.5°C) prior to weaning off CPB. The patient temperature was determined through their blood temperature obtained from the heat exchange unit in the extracorporeal circuit. During recordings of both hypothermic and normothermic periods, hypoperfusion events were identified where the pump flow rate had been markedly reduced at surgical request.

To examine differences in O_2 consumption during hypothermia compared to normothermia an average was taken of the oxygen consumption before (hypothermic) and after re-warming (normothermic). In order to exclude any periods of hypoperfusion from the average, the O_2 consumption curve was filtered by removing the flow downs after which a box-type smoothing function was applied to the data. The true average in O_2 consumption during the normothermic and hypothermic periods was then calculated through averaging the smoothed oxygen consumption data prior to re-warming where the patient temperature was less than 32.5°C. This typically was a period of 1 h. The normothermic oxygen consumption data were calculated from the smoothed data following the re-warming period when the temperature was greater than 37°C. This typically was a period of 20 min.

During a hypoperfusion event (flow down) there is a build up of oxygen debt due to the O_2 consumption being reduced below the baseline level seen prior to the flow down. When the flow has returned to normal the O_2 consumption initially exceeds baseline but eventually returns to normal, as illustrated in Fig. 33.1. The O_2 debt is calculated as the area between the O_2 consumption curve and the pre-flow down baseline, which was extrapolated to predict the nominal consumption during the

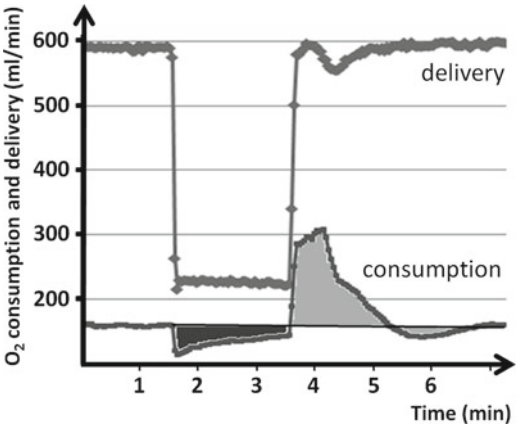

Fig. 33.1 Oxygen delivery and consumption curves during a typical flow down period. The region of oxygen debt is highlighted by the *dark grey area* and oxygen repayment by the *light grey area*

flow down period. This extrapolation consisted of fitting a linear curve between the pre-flow down baseline and the value to which the consumption returned following the hyperaemic response. The O_2 repayment is calculated by numerically integrating the area between the O_2 consumption curve and the extrapolated baseline following restoration of full flow (Fig. 33.1 indicates dark grey and light grey areas for oxygen debt and repayment, respectively). The O_2 repayment ratio is calculated from the ratio of this O_2 repayment to the O_2 debt. This analysis was performed on flow downs which were categorised as either hypothermic or normothermic. A paired *t* test was then used to test for a difference between the hypothermic and normothermic repayment ratios. For this reason the analysis was only performed on patients that had suitable flow downs in both the hypothermic ($n=18$) and the normothermic ($n=9$) regions. It was found that 5 of the 12 patients satisfied this condition, with flow down times ranging from 21 to 201 s.

3 Results

All patients survived with no post-operative complications. A typical recording over the course of an operation is shown in Fig. 33.2. The oxygen delivery and consumption curves are shown, together with the smoothed consumption and temperature curves. An increase in consumption with temperature during re-warming can be clearly seen. Figure 33.3 shows the average O_2 consumption during the hypothermic (before re-warming) and normothermic (after re-warming) periods for each patient. Also shown is the average consumption for all patients combined during hypothermia and normothermia. From this average it was found that the effect of hypothermia was to reduce O_2 consumption by $43 \pm 10\%$ (mean ± SD) compared to normothermia.

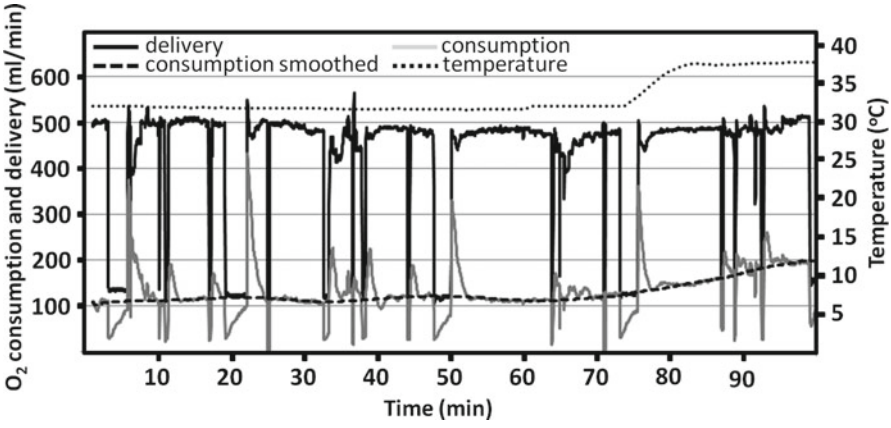

Fig. 33.2 Timeline of measurements during surgery. Overlaid on the O_2 consumption curve (*grey curve*) is the same consumption data with flow downs filtered out and the data smoothed (*dashed*, *black curve*)

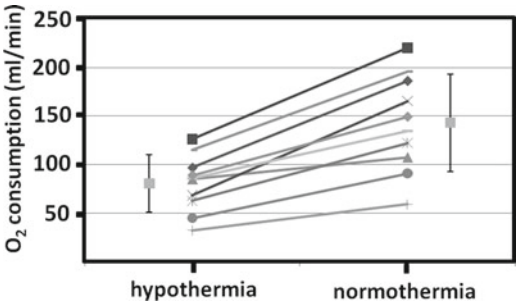

Fig. 33.3 Oxygen consumption data during hypothermia compared to normothermia. Lines indicate the results for each patient. *Isolated squares* indicate averaged results over all patients (±SD)

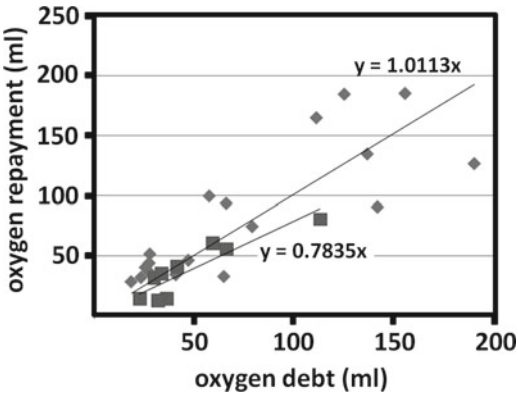

Fig. 33.4 Oxygen debt vs. repayment analysis. Data points correspond to single flow down events categorised as either normothermic (*squares*) or hypothermic (*diamonds*). Linear fits are indicated and equations shown

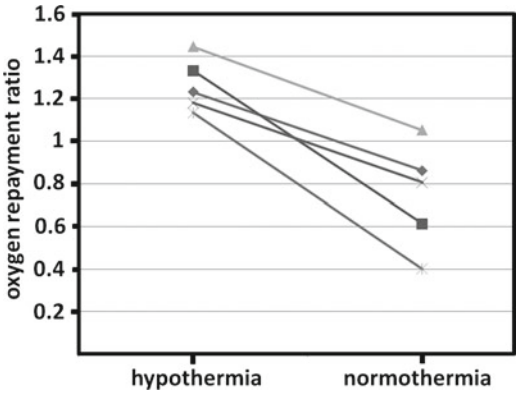

Fig. 33.5 Oxygen repayment ratios between hypothermia and normothermia for five patients. Each line connects the average values for the hypothermic and normothermic repayment ratios for each patient

A *t* test showed a significant difference between the average hypothermic and normothermic O_2 consumptions ($P<0.003$).

Figure 33.4 shows the results of plotting oxygen repayment vs. oxygen debt for each flow down. The gradient obtained from the linear fit to the data in Fig. 33.4 is a measure of the oxygen repayment ratio. It was found that the oxygen repayment ratio during hypothermia was 101 ± 8% whilst during normothermia the repayment ratio was reduced to 78 ± 6%. Figure 33.5 shows the results of the repayment ratio

for the five patients with measurable flow downs in both the hypothermic and normothermic regions. The plot clearly demonstrates a lower repayment ratio following return to normothermia. A paired *t* test showed a significant difference between the average hypothermic and normothermic repayment ratios ($P < 0.003$).

4 Conclusions

These results indicate clear differences in the metabolism of CPB patients during hypothermia compared to normothermia. All patients studied exhibited a 43% reduction in baseline O_2 consumption during hypothermia, in agreement with the well-known effect of hypothermia on the metabolic rate. In previous studies the cerebral metabolic rate of oxygen consumption (V02′) has been reported to follow the empirical relationship $V02' = 0.021e^{(0.11477T)}$, where T is the temperature [6]. Applying the temperature change for mild hypothermia used in our study the expected reduction in oxygen consumption can be calculated from this relationship to be 47%, a value which is within the 10% error range of our data suggesting that cerebral and whole body O_2 consumption may vary with temperature in a similar fashion. It was observed that the oxygen repayment ratio for a flow down event was on average 78 ± 6% during normothermia and 101 ± 8% in hypothermia. This difference in the repayment ratios can be due to several physiological and metabolic reasons. It has been reported that the magnitude and duration of luxury perfusion observed following restoration of flow is dependent upon the duration of the flow down [7]. Shoemaker et al. reported the role of the O_2 debt in high-risk surgical patients and that a strong relationship exists between outcome and the duration and magnitude of the O_2 debt [8]. Similarly Cook et al. showed that in patients undergoing CPB there is an uncoupling of the relationship between cerebral blood flow and metabolism both during cooling to and re-warming from hypothermic temperatures [9]. Mortillaro et al. and Fahey et al. reported similar observations to ours where in normothermic animal models oxygen repayment was found to be less than 100% [10, 11]. They attributed this to a reduction in oxygen demand during the flow down period. Further analysis is currently underway investigating repayment ratios in a group of 47 patients.

Acknowledgments J.A. is funded by the NHS London clinical scientist training scheme.

References

1. Kirklin JW, Barrat-Boyes BG (1993) Hypothermia, circulatory arrest and cardiopulmonary bypass. In: Kirklin JW, Barrat-Boyes BG (eds) Cardiac surgery. Livingstone, New York, pp 61–128
2. Fox LS, Blackstone EH, Kirklin JW et al (1984) Relationship of brain blood flow and oxygen consumption to perfusion flow rate during profoundly hypothermic cardiopulmonary bypass. An experimental study. J Thorac Cardiovasc Surg 87:658–664

3. Slater JM, Orszulak TA, Cook DJ (2001) Distribution and hierarchy of regional blood flow during hypothermic cardiopulmonary bypass. Ann Thorac Surg 72:542–547
4. Newman MF, Kirchner JL, Phillips-Bute B et al (2001) Longitudinal assessment of neurocognitive function after coronary-artery bypass surgery. N Engl J Med 344:395–402
5. A. Crerar-Gilbert, H. Bishop, J.A. Pickett et al (2001) Continuous arteriovenous oximetry as a measure of perfusion during hypothermic cardiopulmonary bypass. Br J Anaesth 87: 660P
6. Croughwell ND, Smith LR, Quill T (1992) The effect of temperature on cerebral metabolism and blood flow in adults during cardiopulmonary bypass. J Thorac Cardiovasc Surg 103:549–554
7. McCullough JN, Zhang N, Reich DL et al (1999) Cerebral metabolic suppression during hypothermic circulatory arrest in Humans. Ann Thorac Surg 67:1895–1899
8. Shoemaker WC, Appel PL, Kram HB (1992) Role of oxygen debt in the development of organ failure sepsis, and death in high-risk surgical patients. Chest 102:208–215
9. Cook DJ, Oliver WC, Orszulak TA et al (1995) Cardiopulmonary bypass temperature, hematocrit, and cerebral oxygen delivery in humans. Ann Thorac Surg 60:1671–1677
10. Mortillaro NA, Granger HJ (1977) Reactive hyperemia and oxygen extraction in the feline small intestine. Circ Res 41:859–864
11. Fahey JT, Lister G et al (1989) Response to low cardiac output: developmental differences in metabolism during oxygen deficit and recovery in lambs. Pediatr Res 26:180–187

Chapter 34
Pharmacologic Interventions to Improve Splanchnic Oxygenation During Ventilation with Positive End-Expiratory Pressure

A. Fournell, T.W.L. Scheeren, O. Picker, and L.A. Schwarte

1 Introduction

Mechanical ventilation (MV) to preserve or improve systemic oxygenation is a mainstay in the management of critically ill patients [1]. The art of MV has contributed enormously to improving the outcome of these patients [2]. Furthermore, ever since the first report about its usefulness in patients with the adult respiratory distress syndrome (ARDS) [3], the application of PEEP resides in a core position in the ventilator settings in MV.

However, as these patients are frequently also prone to the development of a MSOF, it is mandatory to not only consider the impact of MV on systemic hemodynamic and oxygenation variables but to also be aware of possible side effects, for example, on end-organ oxygenation [4]. This applies especially to the splanchnic region, a site usually referred to as the *motor* of MSOF [5], as there is increasing evidence of microvascular blood flow alterations in MSOF [6–8].

In a pilot study we demonstrated a profound and sustained reduction in the oxygen saturation in gastric mucosa (μHbO_2) which remained depressed despite the normalization of cardiac output (CO) and mean arterial pressure (MAP) following the restoration of preload [9]. These results were confirmed by our

A. Fournell (✉) • O. Picker
Department of Anesthesiology, Heinrich Heine University Düsseldorf,
Himmelgeister Landstraße 92, 40589 Düsseldorf, Germany
e-mail: Fournell@uni-duesseldorf.de

T.W.L. Scheeren
Department of Anesthesiology, University Medical Center Groningen,
Groningen, The Netherlands

L.A. Schwarte
Department of Anesthesiology, VU University Medical Center,
Amsterdam, The Netherlands

M. Wolf et al. (eds.), *Oxygen Transport to Tissue XXXIII*, Advances in Experimental Medicine and Biology 737, DOI 10.1007/978-1-4614-1566-4_34,

findings in volunteers breathing continuous positive airway pressure (CPAP): We demonstrated that CPAP attenuates μHbO_2 pressure-level dependently despite uncompromised systemic hemodynamics and oxygenation [10].

Given the obvious disparity between the persistent attenuation in μHbO_2 and normalized systemic variables, we sought for further therapeutic options to augment μHbO_2. Therefore, we developed a canine model of compromised systemic circulation by ventilation with PEEP to decrease CO dose dependently. Simultaneously μHbO_2 was assessed continuously by reflectance spectrophotometry [11]. Using this model chronically instrumented dogs for the measurement of CO (transit-time flowmeters implanted around the pulmonary artery) were repeatedly studied during general anesthesia to evaluate the effects of different interventions on μHbO_2.

2 Modulation of Splanchnic-Catecholamine Receptor Activity

Catecholamines may both increase or decrease splanchnic perfusion and thus oxygenation, depending on their affinity to different receptors, dosage, and condition of application (healthy condition or pathologic state). Dopamine failed to consistently improve μHbO_2 both under unstressed and compromised circulatory conditions, that is, reduced CO due to the application of PEEP, regardless of markedly improved systemic hemodynamics and systemic oxygen delivery [12].

Besides activating dopamine receptors, the stimulation of β-adrenergic receptors is increasingly considered to regulate splanchnic blood flow and herein, in particular the β_2-receptor appears to be involved. Especially the synthetic catecholamine dopexamine (both a dopamine and β_2-receptor agonist) has been recommended for the augmentation of splanchnic perfusion. In our canine model dopexamine increased μHbO_2 both under unstressed and compromised hemodynamic conditions [12]. Further support for the concept that β_2-stimulation is essential to induce the beneficial regional effects of dopexamine can be derived from our findings that the selective blockade of the β_2-receptor blunted markedly the dopexamine-induced increase in μHbO_2 [12].

We attributed the failure of dopamine to increase μHbO_2 to the unique receptor affinity of dopamine, that is, even at low doses dopamine may not only activate dopaminergic receptors but α- and β-receptors as well. Since an activation of α_1-receptors may lead to splanchnic vasoconstriction, thus counteracting the vasodilation by stimulation of dopaminergic receptors, we hypothesized that the selective blockade of the α_1-receptors may unveil the vasodilatory effects of dopamine. Consequently we studied the effect of dopamine during a selective blockade of α_1-receptors on μHbO_2. The combined effect of both measures resulted in an increase in μHbO_2 even at low doses of dopamine [13].

This is in full accordance with our study on the selective dopamine receptor agonist fenoldopam, which preferentially increased μHbO_2 [14]. Additional measurements with a selective DA_1-receptor antagonist confirmed our hypothesis that the DA_1-receptor is responsible for the beneficial effects of fenoldopam. In this setting the dopamine receptor blockade nullified the beneficial effects of fenoldopam [14].

3 Effects of Inodilators

Cardiac failure increases the risk of splanchnic hypoperfusion. In this condition levosimendan, a drug possessing both inotropic and vasodilatory potential should be useful to increase CO and to decrease mesenteric arterial resistance. Therefore, we tested the hypothesis that levosimendan increases μHbO_2 and compared its effects to the established inotropes milrinone and dobutamine. In contrast to milrinone (showing no significant regional effects) and dobutamine (marked systemic effects) levosimendan augmented μHbO_2 selectively, that is, at only moderately increased oxygen delivery (DO_2) in the uncompromised state [15].

4 Thoracic Epidural Anesthesia

Since the sympathetic nervous system is involved in the regulation of gastrointestinal perfusion and predominantly releases the vasoconstrictive α_1-agonist norepinephrine, we assumed that an extended thoracic epidural anesthesia (TEA) should preserve μHbO_2. Our results during TEA demonstrated a well-maintained μHbO_2 despite significant depression of CO, DO_2, and MAP during ventilation without PEEP. Moreover, and more important: Although TEA worsened the response to ventilation with PEEP, and elicited a profound decrease in μHbO_2, restoring DO_2 by volume loading completely normalized μHbO_2 [16].

5 Conclusions

From our results in the catecholamine studies [12–14] we conclude that some vasodilatory action of the drugs could be responsible for their effect on the augmentation of μHbO_2, for example, dopamine under α_1-blockade, thus unveiling the vasodilatory potential of the drug, but not dopamine alone improved splanchnic oxygenation [13].

Further support for the view that vasodilation is a key factor to augment splanchnic oxygenation is provided in the levosimendan study [16]. As levosimendan only slightly increased DO_2 its action in augmenting μHbO_2 should not be attributed to a mainly systemic inotropic effect of the drug, but to the peripheral stimulation of vascular adenosine triphosphate (ATP)-sensitive potassium channels, thus causing vasodilation.

Moreover in the TEA study [15], contrasting our results in earlier studies [9, 12–14], restoring preload and thus DO_2 sufficed to restore splanchnic oxygenation. As splanchnic vessels present a dense sympathetic innervation, the extended sympathetic block could have prevented vasoconstriction or promoted splanchnic vasodilation by inhibiting the release of catecholamines.

Acknowledgments The above-mentioned studies have been funded by a grant from the Research Commission, Medical Faculty, Heinrich-Heine-University Düsseldorf and departmental funds.

References

1. Slutsky AS, Imai Y (2003) Ventilator-induced lung injury, cytokines, PEEP, and mortality: implications for practice and for clinical trials. Intensive Care Med 29:1218–1221
2. Plötz FB, Slutsky AS, van Vught AJ et al (2004) Ventilator-induced lung injury and multiple system organ failure: a critical review of facts and hypotheses. Intensive Care Med 30:1865–1872
3. Ashbaugh DG, Petty TL, Bigelow DB et al (1969) Continuous positive-pressure breathing (CPPB) in adult respiratory distress syndrome. J Thorac Cardiovasc Surg 57:31–41
4. De Backer D (2000) The effects of positive end-expiratory pressure on the splanchnic circulation. Intensive Care Med 26:361–363
5. Carrico CJ, Meakins JL, Marshall et al (1986) Multiple-organ-failure syndrome. Arch Surg 121:196–208
6. Parrillo JE (1993) Pathogenetic mechanisms of septic shock. N Engl J Med 328:1471–1477
7. Hinshaw LB (1996) Sepsis/septic shock: participation of the microcirculation: an abbreviated review. Crit Care Med 24:1072–1078
8. De Backer D, Creteur J, Preiser J-C et al (2002) Microvascular blood flow is altered in patients with sepsis. Am J Respir Crit Care Med 166:98–104
9. Fournell A, Scheeren TW, Schwarte LA (1998) PEEP decreases oxygenation of the intestinal mucosa despite normalization of cardiac output. Adv Exp Med Biol 454:435–440
10. Fournell A, Schwarte LA, Kindgen-Milles D et al (2003) Assessment of microvascular oxygen saturation in gastric mucosa in volunteers breathing continuous positive airway pressure. Crit Care Med 31:1705–1710
11. Frank KH, Kessler M, Appelbaum K et al (1989) The Erlangen micro-lightguide spectrophotometer EMPHO I. Phys Med Biol 34:1883–1900
12. Scheeren TW, Schwarte LA, Loer SA et al (2002) Dopexamine but not dopamine increases gastric mucosal oxygenation during mechanical ventilation in dogs. Crit Care Med 30:881–887
13. Schwarte LA, Picker O, Schindler A et al (2004) Dopamine under alpha$_1$-blockade, but not dopamine alone or fenoldopam, increases depressed gastric mucosal oxygenation. Crit Care Med 32:150–156
14. Schwarte LA, Picker O, Schindler AW et al (2003) Fenoldopam: but not dopamine – selectively increases gastric mucosal oxygenation in dogs. Crit Care Med 31:1999–2005
15. Schwarte LA, Picker O, Bornstein SR et al (2005) Levosimendan is superior to milrinone and dobutamine in selectively increasing microvascular gastric mucosal oxygenation in dogs. Crit Care Med 33:135–142
16. Schwarte LA, Picker O, Hohne C et al (2004) Effects of thoracic epidural anaesthesia on microvascular gastric mucosal oxygenation in physiological and compromised circulatory conditions in dogs. Br J Anaesth 93:552–559

Chapter 35
Effect of Pneumoperitoneum on Functional Residual Capacity

Akira Matsunaga, Katsuhiro Ohse, Yasuyuki Kakihana, Mina Masuda, Kanako Ikoma, and Yuichi Kanmura

1 Introduction

Laparoscopic surgery is usually performed using the intra-abdominal insufflation of carbon dioxide, that is, pneumoperitoneum (PP). PP increases the intra-abdominal-pressure (IAP) and leads to an abdominal expansion. This expansion causes a cranial shift of the diaphragm, reducing the functional residual capacity (FRC) [1]. PP may reduce the FRC below the closing volume, which predisposes the airway to closure and atelectasis, resulting in decreased arterial oxygenation. An Engström Carestation ventilator with a built-in modified nitrogen washout/washin technique has been reported to be useful for measuring the FRC in mechanically ventilated patients [2]. The aim of this study was to evaluate the adverse effect of PP on FRC and the improvement of the degraded FRC using a positive end-expiratory pressure (PEEP).

2 Methods

2.1 Patients and Anesthesia

After obtaining IRB approval and patient consent, 16 patients who were scheduled for elective abdominal laparoscopic surgery to be performed under a general anesthesia with endotracheal intubation were studied. The operations consisted of gastric resections in six patients, bowel resections in four patients, gynecological surgeries in three patients, and other operations in three patients. The patients comprised 11

A. Matsunaga (✉) • K. Ohse • Y. Kakihana • M. Masuda • K. Ikoma • Y. Kanmura
Department of Anesthesiology & Critical Care Medicine, Graduate School of Medical and Dental Sciences, Kagoshima University, 8-35-1 Sakuragaoka, Kagoshima 890-8520, Japan
e-mail: matunaga@m3.kufm.kagoshima-u.ac.jp

M. Wolf et al. (eds.), *Oxygen Transport to Tissue XXXIII*, Advances in Experimental Medicine and Biology 737, DOI 10.1007/978-1-4614-1566-4_35,

Table 35.1 Data before PP and during PP and PP with PEEP

	Before PP	During PP	During PP with PEEP	Friedman test
FRC (mL)	1,833	1,573*	1,861#	$p<0.01$
$n=16$	(1,300–2,112)	(1,302–2,022)	(1,578–2,273)	
PaO_2 (mmHg)	173	151*	179#	$p<0.01$
$n=12$	(155–191)	(135–165)	(146–169)	
PIP (cmH_2O)	11	17*	20*#	$p<0.01$
$n=16$	(10–13)	(15–18)	(19–22)	
IAP (mmHg)	0	9*	9*	$p<0.01$
$n=16$	(0–0)	(7–9)	(9–9)	

Data are the medians (interquartile range)

*$p<0.05$ versus before PP, #$p<0.05$ versus during PP (Wilcoxon signed-rank test with Bonferroni correction). Before PP = just before PP, During PP = 30 min after the induction of PP, During PP with PEEP = 30 min after the application of a PEEP of 5 cmH_2O under PP

FRC functional residual capacity, *PP* pneumoperitoneum, *PIP* peak inspiratory pressure, *IAP* intra-abdominal pressure

men and 5 women, with an age (median (interquartile range)) of 52 (36–59) years. Their body weights, body heights, and body mass indices were 57 (51–64) kg, 159 (157–160) cm, and 23.2 (19.8–24.4) kg/m^2, respectively. Patients with a reduced left ventricular function (EF < 50%) or a reduced respiratory function (%VC < 80% or $FEV_{1.0\%}$ < 70%) were excluded. General anesthesia was induced and maintained with propofol and remifentanil. All the patients receiving rocuronium as a muscle relaxant were ventilated with a tidal volume of 8 mL/kg, an FiO_2 of 40%, and a respiratory rate of 10–15 breaths/min using an Engström Carestation (GE Healthcare) to maintain an end-tidal CO_2 of between 35 and 40 mmHg.

2.2 FRC Measurement

The Engström Carestation measures the FRC using a modified nitrogen washout/washin technique that requires inspiratory and expiratory analyzes of oxygen and carbon dioxide with just a 10% change in the oxygen level. A single procedure requires two measurements of approximately 20 breaths each. The algorithm for the nitrogen washout/washin technique used by the Engström Carestation has been described in detail by Olegård et al. [3].

2.3 Study Protocol

The FRC, peak inspiratory pressure (PIP), and IAP were recorded just before PP, 30 min after the induction of PP (during PP), and 30 min after the application of a PEEP of 5 cmH_2O under PP (during PP with PEEP). In 12 of 16 patients, partial pressure of arterial oxygen (PaO_2) was measured simultaneously (Table 35.1).

2.4 Statistical Analysis

Data were expressed as the median values and the interquartile range (25–75%). Changes in variables were tested using the Friedman test; if significant, pairwise *post-hoc* comparisons were performed using the Wilcoxon signed-rank test with Bonferroni correction. Correlations between the changes in the FRC and PaO_2 were analyzed using the Spearman rank correlation test. A p value of <0.05 was considered statistically significant.

3 Results

The data obtained before PP, during PP, and during PP with a PEEP of 5 cmH_2O are shown in Figs. 35.1–35.3. PP increased the IAP from 0 mmHg to 9 (7–9) mmHg in all the patients. PP increased the PIP from 11 (10–13) cmH_2O to 17 (15–18) cmH_2O,

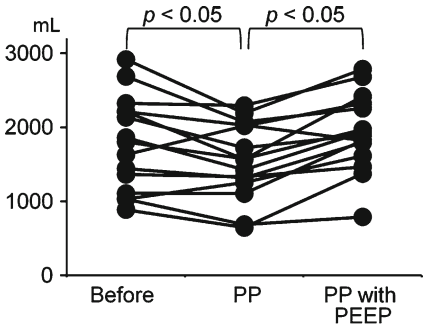

Fig. 35.1 Changes in FRC before and during PP, and during PP with PEEP ($n=16$). The FRC was recorded just before PP (Before), 30 min after the induction of PP (PP), and 30 min after the application of a PEEP of 5 cmH_2O under PP (PP with PEEP). *FRC* functional residual capacity, *PP* pneumoperitoneum

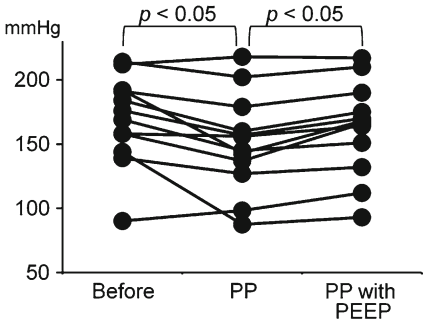

Fig. 35.2 Changes in PaO_2 before and during PP, and during PP with PEEP ($n=12$). The PaO_2 was recorded just before PP (Before), 30 min after the induction of PP (PP), and 30 min after the application of a PEEP of 5 cmH_2O under PP (PP with PEEP). *PP* pneumoperitoneum

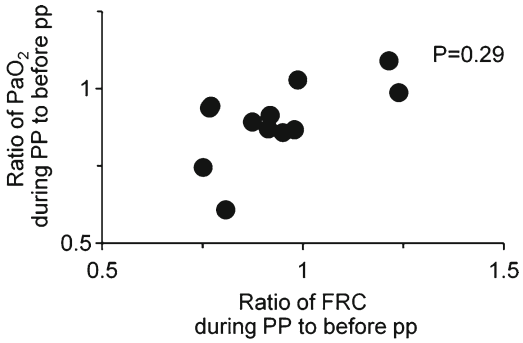

Fig. 35.3 Correlation between the changes in the FRC and the PaO_2 before and during PP ($n=12$). The changes in the FRC and the PaO_2 are the ratio of the FRC and the PaO_2 during PP to before PP, respectively. *FRC* functional residual capacity, *PP* pneumoperitoneum

while a PEEP of 5 cmH_2O increased the PIP to 20 (19–22) cmH_2O. PP significantly ($p<0.05$) decreased the FRC and PaO_2 from 1,833 (1,300–2,112) mL to 1,573 (1,302–2,022) mL and from 173 (155–191) mmHg to 151 (135–165) mmHg, respectively. In contrast, a PEEP of 5 cmH_2O significantly ($p<0.05$) increased the FRC and PaO_2 to 1,861 (1,578–2,273) mL and 165 (137–170) mmHg, respectively. No correlation ($p=0.29$) between the changes in the FRC and the PaO_2 were observed before and during PP (Table 35.1).

4 Discussion

Positive pressure ventilation under general anesthesia with muscle paralysis has been reported to cause a cranial shift in the diaphragm that reduces the FRC [4] and can lead to atelectasis in dependent lung regions within minutes [5]. Furthermore, a correlation between an increased atelectatic area and an increased shunting of pulmonary blood flow, resulting in a reduction in arterial oxygenation, was observed using CT during general anesthesia [6]. PP causes an additional cranial shift in the diaphragm that could further reduce the FRC and increase the mismatch between ventilation and perfusion. In this study, the FRC decreased significantly after the induction of PP: the mean decrease was 220 mL, which was almost the same as the value measured using spiral CT in patients who underwent a laparoscopic cholecystectomy [1]. Chiumello et al. [2] also showed the accuracy of FRC measurements using an Engström Carestation, compared with CT data, in ICU patients requiring ventilatory support. The application of a PEEP of 5 cmH_2O significantly improved the decreased FRC to the level before the PP in the present study; the mean increase was 307 mL. Neumann et al. [7] used the original nitrogen washout technique to measure the FRC in ventilated patients with or without lung disease at three PEEP levels, that is 0, 5, and 10 cmH_2O. The application of a PEEP of 5 cmH_2O increased the FRC in patients with normal respiratory function, acute lung injury, and chronic obstructive pulmonary disease by 297, 201, and 204 mL, respectively.

In the present study, the induction of PP caused a decrease in arterial oxygenation, which was improved by the application of a PEEP of 5 cmH_2O; no correlation was observed between the decrease in the FRC and the decrease in arterial oxygenation. However, previous studies in anesthetized patients with normal lung function have shown no adverse effect of PP on arterial oxygenation; instead, arterial oxygenation during PP has been reported to increase [8]. Furthermore, Strang et al. [9] demonstrated in a porcine model that the aggravation of atelectasis caused by the induction of PP was not paralleled by an increased pulmonary shunt or impaired arterial oxygenation using spiral CT. The reason why the induction of PP decreased pulmonary oxygenation in the present study may be that the patients were not in the same position during the study. Several patients were placed in the Trendelenburg position to facilitate a laparoscopic surgical procedure. A combination of PP and the Trendelenburg position has been reported to decrease arterial oxygenation in patients undergoing laparoscopic gynecological surgery [10].

In conclusion, the results of the present study indicate that the induction of PP caused a significant decrease in the FRC, which was improved by the application of a PEEP, and no correlation was observed between the reduction in the FRC and the decrease in arterial oxygenation during PP.

References

1. Andersson LE, Bååth M, Thörne A et al (2005) Effect of carbon dioxide pneumoperitoneum on development of atelectasis during anesthesia, examined by spiral computed tomography. Anesthesiology 102:293–299
2. Chiumello D, Cressoni M, Chierichetti M et al (2008) Nitrogen washout/washin, helium dilution and computed tomography in the assessment of end expiratory lung volume. Crit Care 12:R150
3. Olegård C, Söndergaard S, Houltz E et al (2005) Estimation of functional residual capacity at the bedside using standard monitoring equipment: a modified nitrogen washout/washin technique requiring a small change of the inspired oxygen fraction. Anesth Analg 101:206–212
4. Hedenstierna G, Strandberg A, Brismar B et al (1985) Functional residual capacity, thoracoabdominal dimensions, and central blood volume during general anesthesia with muscle paralysis and mechanical ventilation. Anesthesiology 62:247–254
5. Hedenstierna G, Tokics L, Strandberg A et al (1986) Correlation of gas exchange impairment to development of atelectasis during anaesthesia and muscle paralysis. Acta Anaesthesiol Scand 30:183–191
6. Tokics L, Hedenstierna G, Strandberg A et al (1987) Lung collapse and gas exchange during general anesthesia: effects of spontaneous breathing, muscle paralysis, and positive end-expiratory pressure. Anesthesiology 66:157–167
7. Neumann P, Zinserling J, Haase C et al (1998) Evaluation of respiratory inductive plethysmography in controlled ventilation: measurement of tidal volume and PEEP-induced changes of end-expiratory lung volume. Chest 113:443–451
8. Odeberg S, Sollevi A (1995) Pneumoperitoneum for laparoscopic surgery does not increase venous admixture. Eur J Anaesthesiol 12:541–548
9. Strang CM, Hachenberg T, Fredén F et al (2009) Development of atelectasis and arterial to end-tidal PCO_2-difference in a porcine model of pneumoperitoneum. Br J Anaesth 103:298–303
10. Nishio I, Noguchi J, Konishi M et al (1993) The effects of anesthetic techniques and insufflating gases on ventilation during laparoscopy. Masui 42:862–866

Chapter 36
Estimation of Molecular Hydrogen Consumption in the Human Whole Body After the Ingestion of Hydrogen-Rich Water

Akito Shimouchi, Kazutoshi Nose, Mikiyasu Shirai, and Takaharu Kondo

1 Introduction

The estimation of oxygen radical content is clinically important because oxygen radicals are closely associated with many diseases. There is a growing body of evidence to suggest that hydrogen gas (H_2) plays an important role in inactivating oxidative stressors such as hydroxyl radicals in animal models of cerebral infarction [1], hepatic injury [2], and myocardial ischemia–reperfusion injury [3]. Very recently, it has been reported that continuous consumption of H_2-rich water reduces oxidative stress in the brain and prevents stress-induced decline in learning and memory caused by chronic physical restraint [4]. These reports suggested that exogenous H_2 could be partially trapped by oxygen radicals. In fact, Ohsawa et al. [1] demonstrated an arterial–venous difference in H_2 concentration during the inhalation of H_2 in rats and suggested that the H_2 had been incorporated into tissues. Thereafter, we estimated H_2 consumption occurring after the ingestion of H_2-rich water, but without measurement of ventilation volumes [5]. However, very few studies have reported direct evidence as to whether exogenous H_2 is consumed in the human body. We hypothesized that H_2 consumption after the ingestion of H_2-rich water may be associated with oxygen radical production in the body. In the present study, we determined the exact amount of exhaled H_2 by simultaneous measurements of ventilation volume and breath H_2 before and after the ingestion of the H_2-rich water. We then estimated the amount of oxygen radicals produced in the body in terms of H_2 consumption, based on the assumptions that leakage of H_2

A. Shimouchi, M.D., Ph.D. (✉) • K. Nose • M. Shirai
Department of Cardiac Physiology, National Cerebral and Cardiovascular Center Research Institute, 5-7-1, Fujishiro-dai, Suita, Osaka, 565-8565, Japan
e-mail: ashimouc@res.ncvc.go.jp

T. Kondo
College of Life and Health Sciences, Chubu University, Kasugai, Aichi, Japan

M. Wolf et al. (eds.), *Oxygen Transport to Tissue XXXIII*, Advances in Experimental Medicine and Biology 737, DOI 10.1007/978-1-4614-1566-4_36,

molecules from the experimental procedures, H_2 release from the skin surface, and consumption of H_2 by bacterial flora in the colon were almost negligible. These assumptions were initially demonstrated in healthy subjects and are described in the discussion section.

2 Materials and Methods

H_2-rich water was made by dissolving H_2 into water under high pressure by Blue Mercury Inc. (Tokyo, Japan) [4]. The H_2-rich water contained very low levels of electrolytes and no protein, carbohydrates, or lipids (total energy: 0 kcal). Fresh packed H_2-rich water in 500 ml aluminum pouches was purchased from the company and used for the experiments within 3 days. As cold stimulation [6] enhances colonic motility and increases the H_2 content of breath, the room temperature and the water being ingested were kept at 25°C. Just before ingestion, 50 μl of H_2-rich water were quickly sampled, transferred into a 22 ml vial tube, sealed, and shaken for 60 min. Using a gas-tight glass syringe, 1 ml of the head space was injected into the gas chromatograph with a semiconductor detector (TRIlyzer mB-3000, Taiyo Instruments Inc., Osaka, Japan) to measure its H_2 content. The H_2 content of the H_2-rich water in the aluminum pouch was calculated from the H_2 concentration and a solubility value of 0.0176 vol gas STP/vol liquid at 1 atom partial pressure [7].

Subjects: Seven adult volunteers (five men and two women; mean age: 36 ± 12 years) participated in this study. The subjects refrained from consuming food, supplements, and drugs (they were allowed to drink water) for at least 15 h before the experiments in order to decrease colonic fermentation. On the experimental day, the subjects rested in a sitting position, wore a nose-clip and mouthpiece, and breathed highly purified artificial air (21% O_2 balanced with nitrogen) for 19 min in order to measure the baseline H_2 concentrations of their breath. After removing the nose-clip and mouthpiece, they drank 500 ml of H_2-rich water from an aluminum pouch within 1 min in order to minimize H_2 leakage from the bag. Except during the ingestion of H_2-rich water, their expiratory minute volume was continuously measured using a respiromonitor (Respiromonitor RS330, Minato, Co., Ltd., Osaka, Japan). Every 2 min, exhaled breath was collected for 30 s in a Douglas bag, and a breath sample was immediately transferred to a gas-tight glass syringe so that H_2 analysis could be performed using the same sensor as mentioned above. The total amount of exhaled H_2 (TAE_{H_2} (mol)) after the ingestion of the H_2-rich water was given as:

$$\mathrm{TAE}_{\mathrm{H}_2} = \frac{\Delta t}{22.4} \times \left(\frac{1}{2} F(t_0)\mathrm{VE}(t_0) + \sum_{n=1}^{29} F(t_{2n})\mathrm{VE}(t_{2n}) + \frac{1}{2} F(t_{60})\mathrm{VE}(t_{60}) \right),$$

$$\text{where } F(t_{2n}) = F_{\mathrm{EH}_2}(t_{2n}) - \text{baseline } F_{\mathrm{EH}_2}(t_{2n}),$$

where $F_{\mathrm{EH}_2}(t_{2n})$ denotes the fractional concentration of expired breath H_2 at time t_{2n} ($n = 0, 1, 2, \ldots 30$), $\mathrm{VE}(t_{2n})$ is expiratory minute volume (l/min) at time t_{2n}, and the

time interval Δt is 2 min. Baseline $F_{EH_2}(t_{2n})$ was obtained from the linear regression line for the data (t_{2n}, $F_{EH_2}(t_{2n})$) between −18 and −2 min, and the data at 60 min. All volumes were measured under standard pressure, temperature, and dry conditions.

3 Results

Drinking H_2-rich water increased the H_2 content of the subjects' exhaled breath, as illustrated in Fig. 36.1. The mean baseline level of breath H_2 from −18 to −2 min was 6.9 ± 0.7 ppm. The ingestion of H_2-rich water rapidly increased the subjects' breath H_2 content to its maximal level of 35.6 ± 12.3 ppm at 10 min after ingestion, and thereafter, breath H_2 content gradually decreased to the baseline level within 60 min.

The total amounts of ingested and exhaled H_2 after the ingestion of the H_2-rich water are listed in Table 36.1. The latter values were always lower than the former. The total amount of exhaled H_2 was 59 ± 10% of ingested H_2. Therefore, approximately 41% of ingested H_2 was consumed or lost.

4 Discussion

This study confirmed that the ingestion of H_2-rich water rapidly increased breath H_2 content to its peak level within 10 min of ingestion. The peak breath H_2 value was slightly lower than that found in our previous report, possibly because end-expiratory

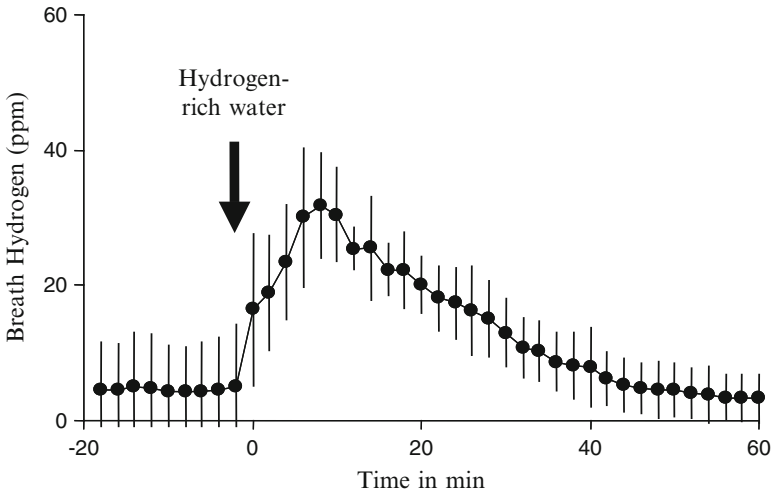

Fig. 36.1 Changes in breath H_2 (ppm) after the ingestion of H_2-rich water. The subjects ingested the H_2-rich water from −1 to 0 min

Table 36.1 Characteristic parameters related to exhaled/ingested H_2

Subject	Sex (F/M)	Age (y.o.)	Height (cm)	BW (Kg)	BSA (m^2)	BMI	VE (l/min)	Ingested H_2 (μmol)	Exhaled H_2 (μmol)	Exh/Ing H_2 (%)	Consumed H_2 (nmol/kg/min)	Consumed H_2 (μmol/m^2/min)
1	M	55	180	92	2.12	28.4	6.76	262	171	65	17	0.7
2	F	23	170	56	1.65	19.5	5.64	243	145	60	29	1.0
3	M	27	183	76	1.98	22.9	5.94	301	184	61	25	1.0
4	M	40	169	65	1.75	22.6	5.25	292	167	57	32	1.2
5	F	35	156	45	1.41	18.3	4.17	281	143	51	51	1.6
6	M	47	174	71	1.84	23.4	6.76	266	200	75	16	0.6
7	M	26	175	64	1.77	20.9	4.99	230	103	45	33	1.2
Mean		36	172	67	1.79	22.3	5.64	268	159	59	29	1.0
SD		12	9	15	0.23	3.3	0.94	26	32	10	12	0.3

BW body weight, *BSA* body surface area, *BMI* body mass index, *VE* expired minute ventilation volume (STPD), *Exh/Ing H_2* exhaled H_2/ingested H_2 ratio

breath was sampled in our previous study [5], whereas exhaled breath was obtained as total expiratory ventilation volume in the present study.

In our previous report [5], we roughly estimated that 72% of the H_2 ingested from H_2-rich water was exhaled in breath. This calculation was performed using the end-tidal H_2 concentration and the minute volume ventilation derived from a mean body weight. We considered that higher levels of end-tidal breath H_2 led to the higher estimation of exhaled volumes of H_2 molecules than the present ones.

Prior to the present study, we confirmed that 2–5% of the H_2 poured into a cup was lost during the first 3 min. To prevent the loss of H_2 as much as possible, the subjects drank the H_2-rich water directly from an aluminum pouch in this study. Furthermore, in our recent study, we found that approximately 0.1% of H_2 was released from the body surface as a skin gas after the ingestion of H_2-rich water. Therefore, the H_2 release from the skin was negligible.

On the other hand, H_2 produced by colonic fermentation is partially consumed by bacterial flora in the colon [8]. However, breath H_2 release had almost ended 60 min after the ingestion of H_2-rich water, possibly because the H_2 was unable to reach the colon. Otherwise, some of the ingested H_2 in the upper alimentary tract might have diffused into the colon. To exclude the effects of H_2-utilizing bacteria, we confirmed that pretreatment with antibiotics did not change H_2 consumption in a healthy subject.

H_2 molecules are not involved in the metabolic pathway in the human body, except for when they are consumed by bacterial flora in the colon. A recent report has clarified that the H_2 molecule is a weak scavenger of hydroxyl radicals and is not effective against superoxide or hydrogen peroxide [1]. Therefore, assuming that the H_2 molecule only scavenged hydroxyl radicals and that bacterial consumption in the alimentary tract and on the skin surface could be excluded, it was considered that most of the H_2 remaining in the body reacted with chemicals with a high affinity for H_2.

Taking the above considerations together, it is likely that H_2 consumption is associated with the production rate of oxygen radicals such as hydroxyl radicals. Therefore, we estimated that the production rate of hydroxyl radicals was at least 29 nmol/kgBW/min or 1.0 μmol/min/m^2 as shown in Table 36.1.

5 Conclusion

H_2 enriched water caused a rapid increase in breath H_2 content. Sixty percent of the ingested H_2 was exhaled, and approximately 40% was consumed in the body, which is closely associated with the production of oxygen radicals in the body.

Acknowledgments This work was supported by the Japan Society for the Promotion of Science (Grant-in-Aid 16209020, 21240057, 21659211, 19–1063) and the Intramural Research Fund of the National Cerebral and Cardiovascular Center (22-4-5). The authors have no conflicts of interest to report. We thank all the volunteers who participated in this study.

References

1. Ohsawa I, Ishikawa M, Takahashi K et al (2007) Hydrogen acts as a therapeutic antioxidant by selectively reducing cytotoxic oxygen radicals. Nat Med 13:688–694
2. Fukuda K, Asoh S, Ishikawa M et al (2007) Inhalation of hydrogen gas suppresses hepatic injury caused by ischemia/reperfusion through reducing oxidative stress. Biochem Biophys Res Commun 361:670–674
3. Hayashida K, Sano M, Ohsawa I et al (2008) Inhalation of hydrogen gas reduces infarct size in the rat model of myocardial ischemia-reperfusion injury. Biochem Biophys Res Commun 373:30–35
4. Nagata K, Nakashima-Kamimura N, Mikami T et al (2009) Consumption of molecular hydrogen prevents the stress-induced impairments in hippocampus-dependent learning tasks during chronic physical restraint in mice. Neuropsychopharmacology 34(2):501–508
5. Shimouchi A, Nose K, Yamaguchi M et al (2009) Breath hydrogen produced by ingestion of commercial hydrogen water and milk. Biomarker Insights 4:27–32
6. O'Brien JD, Thompson DG, Burnham WR et al (1987) Action of centrally mediated autonomic stimulation on human upper gastrointestinal transit: a comparative study of two stimuli. Gut 28:960–969
7. Young CL (ed) (1981) Hydrogen and deuterium. In: IUPAC solubility data series, vol 5/6, Pergamon, Oxford
8. Levitt MD, Bond JH, Levitt DG (1981) Gastrointestinal gas. In: Johnson LR (ed) Physiology of the gastrointestinal tracts. Raven, New York, pp 1301–1315

Chapter 37
Prenylated Acylphloroglucinol Derivatives: Isoprenomics-Based Design, Syntheses and Antioxidative Activities

Ryo Tanaka, Yoshihiro Uto, Kenta Ohnaka, Yuki Ohta, Kazufumi Yazaki, Naoyuki Umemoto, Eiji Nakata, and Hitoshi Hori

1 Introduction

Low-density lipoprotein (LDL) is a major cholesterol carrier in the blood, and its oxidized LDL (OxLDL) has an important role in the development of atherosclerosis [1, 2]. The developments of effective antioxidants are, therefore, desirable to prevent the oxidation of LDL. Hops are used primarily as flavoring and stability agents in beer, to which they impart a bitter, tangy flavor, and are reported to also have various medicinal activities such as antibacterial [3], anti-allergic [4], and anti-inflammatory activities [5]. Major hop components, humulones and lupulones, are poly-prenylated acylphloroglucinol derivatives, were shown to have potent antioxidative activity [6], and the structures of which are very interesting from the standpoint of isoprenomics [7, 8]. Deoxyhumulone and Deoxycohumulone are key intermediates in the biosynthesis of humulones and lupulones (Fig. 37.1) [9]; however, there is no report concerning their biological activity at all. We, therefore, designed isoprenomics-based prenylated biosynthetic intermediates of cohumulone and colupulone as LDL-targeting antioxidants.

R. Tanaka (✉) • Y. Uto • K. Ohnaka • Y. Ohta • E. Nakata • H. Hori
Department of Life System, Institute of Technology and Science, Graduate School, The University of Tokushima, Minamijosanjimacho-2, Tokushima, 770-8506, Japan
e-mail: hori@bio.tokushima-u.ac.jp

K. Yazaki
Laboratory of Plant Gene Expression, Research Institute for Sustainable Humanosphere, Kyoto University, Uji, 611-0011, Japan

N. Umemoto
Central Laboratories for Frontier Technology, Kirin Holdings Co., Ltd., Tochigi, 329-1414, Japan

M. Wolf et al. (eds.), *Oxygen Transport to Tissue XXXIII*, Advances in Experimental Medicine and Biology 737, DOI 10.1007/978-1-4614-1566-4_37,

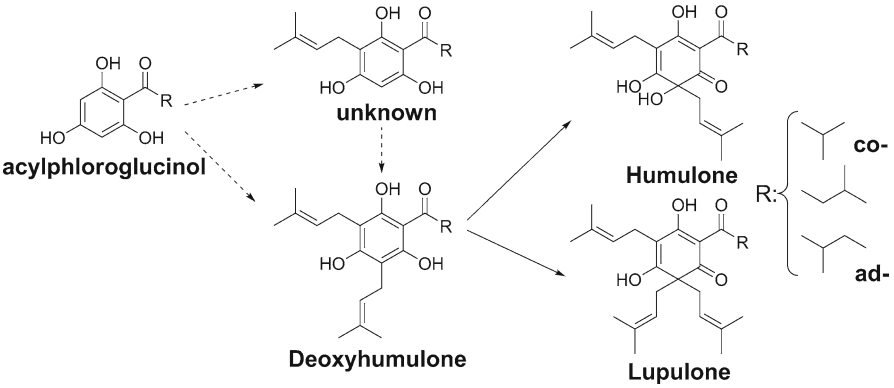

Fig. 37.1 Predicted biosynthetic pathways of humulones and lupulones

2 Materials and Methods

2.1 Chemicals

Phloroglucinol and nitrobenzene were purchased from Sigma-Aldrich, Tokyo, Japan. Linoleic acid, 2-methylpropanoyl chloride, and carbon disulfide were obtained from Tokyo Chemical Industry Co., Ltd, Tokyo, Japan. Aluminium chloride, 2,2′-azobis(2-aminopropane) dihydrochloride (AAPH), 2-thiobarbituric acid (TBA), and 1,1-diphenyl-2-picrylhydrazyl (DPPH) were purchased from Wako Pure Chemical Industries Ltd., Osaka, Japan. Sodium methoxide and 3,3-dimethylallyl bromide were synthesized in our laboratory. All the other chemicals were of reagent grade.

2.2 Synthesis of 2-Methyl-1-(2,4,6-Trihydroxyphenyl)-1-Propanone (UTX-52)

Phloroglucinol (18.4 mmol) and aluminium chloride (3 eq.) were dissolved in nitrobenzene (4.4 ml) and carbon disulfide (7.3 ml), and then 2-methylpropanoyl chloride (1 eq.) was added with stirring. The reaction mixture was stirred at room temperature for 20 h. The mixture was poured into water and the mixture was extracted with Et_2O, and then washed with saturated aqueous $NaHCO_3$ followed by saturated aqueous NaCl. The Et_2O layer was dried (anhydrous $MgSO_4$) and evaporated under reduced pressure. Residues were purified by silica gel column chromatography with hexanes and ethyl acetate to give the product as yellow oil. UTX-52: yield 63%; ^{1}H NMR [400 MHz, $(CD_3)_2CO$] δ 5.92 (s, 1H), 5.92 (s, 1H), 3.99–3.92 (m, 1H), 1.12 (d, 6H, J = 6.4 Hz); EI-MS m/z: 196 (M^+).

2.3 Synthesis of 2-Methyl-1-[2,4,6-Trihydroxy-3-(3-Methyl-2-Butenyl)Phenyl]-1-Propanone (UTX-53) and 2-Methyl-1-[2,4,6-Trihydroxy-3,5-Di(3-Methyl-2-Butenyl) Phenyl]-1-Propanone (UTX-54)

UTX-52 (2.0 mmol) was dissolved in toluene (10 ml) and methanol (1.0 ml). Sodium methoxide [2.1 eq. (UTX-53) or 3.0 eq. (UTX-54)] was added with stirring on ice bath, and then 3,3-Dimethylallyl bromide [2.1 eq. (UTX-53) or 3.0 eq. (UTX-54)] was dropped slowly. The reaction mixture was stirred at room temperature for 1.5 h. The mixture was acidified with 2 N HCl and the mixture was extracted with Et_2O. The Et_2O layer was washed with saturated aqueous NaCl followed by Na_2SO_4. The Et_2O layer was evaporated under reduced pressure. Residues were purified by silica gel column chromatography with hexanes and ethyl acetate to give the product as yellow oil. UTX-53: yield 6.6%; ^{1}H NMR [400 MHz, $(CD_3)_2CO$] δ 5.93 (s, 1H), 5.23–5.19 (m, 1H), 3.87–3.84 (m, 1H), 3.11 (d, 2H, J = 6.6 Hz), 1.61 (s, 3H), 1.49 (s, 3H), 1.00 (d, 6H, J = 6.3 Hz); EI-MS *m/z* 264 (M^+). UTX-54: yield 6.4%; ^{1}H NMR [400 MHz, $(CD_3)_2CO$] δ 4.79–4.76 (m, 2H), 3.95–3.87 (m, 1H), 2.53 (d, 2H, J = 7.8 Hz), 2.42 (d, 2H, J = 7.8 Hz), 1.45 (s, 3H), 1.43 (s, 3H), 0.93 (d, 6H, J = 6.9 Hz); EI-MS *m/z* 332 (M^+).

2.4 Assay of Free Radical Scavenging Activity

Free radical scavenging activity was determined using DPPH at 517 nm according to the method of Blois [10] with some modifications. About 3.0 ml of 100 μM DPPH ethanol solution (60%), containing 40 mM MES (pH 5.5), was added with 30 μl of different concentrations of antioxidants tested. The radical scavenging activity of the test compounds was expressed as IC_{50} value.

2.5 Assay of Linoleic Acid and LDL Oxidation

Inhibitory activities of antioxidants on linoleic acid oxidation were performed by the conjugated diene formation assay [11].

An LDL (density, 1.006–1.063 g/ml) was fractionated from human plasma by ultracentrifugation (80,000 rpm, 1.0 h) using the CS120 ultracentrifuge equipped with a RP80AT rotor (Hitachi Koki Co., Ltd), dialyzed at 4°C against three changes of phosphate-buffered saline (PBS; pH 7.35). The LDL solution was flushed with nitrogen, stored in the dark at 4°C, and used within 5 days from the time of the preparation. Protein was measured by the Bradford method using bovine serum albumin as standard.

The effects of antioxidants on lipid oxidation of human LDL (50 μg protein/ml) were evaluated by measurement of thiobarbituric acid reactive substances (TBARS)

by the method of Yagi [12] during copper-induced oxidation (5 μM $CuSO_4$, 10 mM PBS). The concentration (IC_{50}) leading to 50% decrease of the amount of TBARS was estimated by linear regression analyses from three individual measurements.

3 Results and Discussion

3.1 Design and Synthesis

We designed isoprenomics-based prenylated biosynthetic intermediates of cohumulone and colupulone as LDL-targeting antioxidants. A synthesis of acylphloroglucinol (UTX-52) was performed with Friedel–Crafts acylation. Second, prenylation of UTX-52 was performed according to our established aromatic prenylation method [7], we obtained mono-prenylated acylphloroglucinol UTX-53, and di-prenylated acylphloroglucinol UTX-54 with low yield (Scheme 37.1).

3.2 DPPH Free Radical Scavenging Activity

Free radical reactivities were determined by DPPH assay. The free radical scavenging activity of UTX-53 (IC_{50} = 25.3 μM) was highest among all compounds tested and its potency was about twice as International Calibration Extract (ICE-2, IC_{50} = 49.3 μM) as a hop extract. The scavenging activity of UTX-54 (IC_{50} = 50.5 μM) showed almost the same as that of ICE-2, while UTX-52 showed very weak activity (IC_{50} = 197 μM) (Table 37.1). The stoichiometry ratio of the reaction to DPPH was UTX-53:DPPH = 2:1 and that of UTX-54:DPPH = 1:1.

3.3 Inhibitory Activity Against Linoleic Acid or LDL Oxidation

Inhibitory activities of linoleic acid oxidation were measured by the conjugated-diene formation assay. The inhibitory activity of UTX-53 (4.91 min/μM) on linoleic

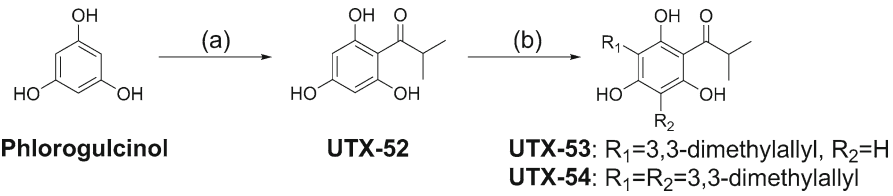

Scheme 37.1 Synthesis of acylphloroglucinol UTX-52 and prenylated acylphloroglucinol UTX-53, UTX-54. Reagents and conditions (**a**) isobutyryl chloride, $AlCl_3$, nitrobenzene, CS2, r.t., 20 h, 63%; (**b**) 3,3-dimethylallyl bromide, NaOMe, toluene, MeOH, r.t., 1.5 h, UTX-53 (6.6%); UTX-54 (6.4%)

Table 37.1 Antioxidant activities of the acylphloroglucinol and prenylated acylphloroglucinols

Compound	DPPH (IC_{50}, μM)	Linoleic acid (min/μM)	Human LDL (IC_{50}, μM)	clog*P*
UTX-52	197 ± 15.3	0.17 ± 0.13	63.5 ± 14.8	1.51
UTX-53	25.3 ± 1.98	4.91 ± 0.30	50.1 ± 10.0	3.44
UTX-54	50.5 ± 3.96	1.21 ± 0.16	60.5 ± 11.8	5.38
ICE-2	49.3 ± 8.19	1.22 ± 0.10	6.5 ± 0.75	–

Value represent mean ± SD of three experiments. clog*P* was calculated by the program Pallas 3.0 (CompuDrug International Inc., Arizona, USA)

acid oxidation showed about four times higher than ICE-2 (1.22 min/μM). UTX-54 (1.21 min/μM) showed the same inhibitory activity as ICE-2, while UTX-52 (0.17 min/μM) showed lower inhibitory activity than other compounds tested (Table 37.1). Because the radical scavenging activity and the inhibitory activity on linoleic acid oxidation show a good correlation, we suggested that the antioxidative activity of prenylated acylphloroglucinols strongly depend on the radical reactivity.

The inhibitory activity of UTX-52 (IC_{50} = 63.5 μM), UTX-53 (IC_{50} = 50.1 μM), and UTX-54 (IC_{50} = 60.5 μM) on human LDL oxidation showed almost the same inhibitory activity, and these compounds were weaker than that of ICE-2 (IC_{50} = 6.46 μM) (Table 37.1). Higher inhibitory activity of ICE-2 was supported according to the chelate formation (not shown). These results were not similar to those of our results obtained on artepillin C isoprenomics [7, 8], where there is a positive correlation between the inhibitory activity of lipid oxidation and the relative hydrophobicity.

4 Conclusions

According to these results, we suggest that the antioxidative activity of prenylated acylphloroglucinols strongly depends on the radical reactivity, not on the hydrophobicity of, e.g., artepillin C analogues.

Acknowledgments We thank Ms. Maki Nakamura, Ms. Emiko Okayama and the staff of our faculty for measurement of NMR and elemental analyses.

References

1. Steinberg D (1995) Role of oxidized LDL and antioxidant in atherosclerosis. Adv Exp Med Biol 369:39–48
2. Witztum JL, Steinberg D (1991) Role of oxidized low density lipoprotein in atherogenesis. J Clin Invest 88:1785–1792
3. Larson AE, Yu RR, Lee OA et al (1996) Antimicrobial activity of hop extracts against Listeria monocytogenes in media and in food. Int J Food Microbiol 33:195–207

4. Segawa S, Takata Y, Kaneda H et al (2007) Effects of a hop water extract on the compound 48/80-stimulated vascular permeability in ICR mice and histamine release from OVA-sensitized BALB/c mice. Biosci Biotechnol Biochem 71:1577–1581
5. Hougee S, Faber J, Sanders A et al (2006) Selective inhibition of COX-2 by a standardized CO_2 extract of *Humulus lupulus* in vitro and its activity in a mouse model of zymosan-induced arthritis. Planta Med 72:228–233
6. Tagashira M, Watanabe M, Uemitsu N (1995) Antioxidative activity of hop bitter acids and their analogues. Biosci Biotechnol Biochem 59:740–742
7. Uto Y, Ae S, Koyama D et al (2006) Artepillin C isoprenomics: design and synthesis of artepillin C isoprene analogues as lipid peroxidation inhibitor having low mitochondrial toxicity. Bioorg Med Chem 14:5721–5728
8. Uto Y, Ae S, Hotta A et al (2006) Artepillin C isoprenomics: design and synthesis of artepillin C analogues as antiatherogenic antioxidants. Adv Exp Med Biol 578:113–118
9. Zuurbier KWM, Fung SY, Scheffer JJC et al (1998) In-vitro prenylation of aromatic intermediates in the biosynthesis of bitter acids in *Humulus lupulus*. Phytochemistry 49:2315–2322
10. Blois MS (1958) Antioxidant determinations by the use of a stable free radical. Nature 181:1199
11. Liégeois C, Lermusieau G, Collin S (2000) Measuring antioxidant efficiency of wort, malt, and hops against the 2,2′-azobis(2-amidinopropane) dihydrochloride-induced oxidation of an aqueous dispersion of linoleic acid. J Agric Food Chem 48:1129–1134
12. Yagi K (1998) Simple assay for the level of total lipid peroxides in serum or plasma. Methods Mol Biol 108:101–106

Part V
Muscle Oxygenation

Chapter 38
Retrograde Perfusion of the Hind Leg in Diabetic Patients Suffering from Arteriosclerosis Obliterans: Theoretical Considerations of Oxygen Supply and Lymphatic Flow Based on Rat Models

Tomiyasu Koyama and Tadahiro Sasajima

1 Introduction

Arteriosclerosis obliterans leads to the total closure of arterial vessels, loss of toes or even the leg itself. To prevent the need for amputation, Sasajima and colleagues [1] refined the surgical grafting technique whereby a distal vein is arterialized (DVA) [2, 3].

When, after destruction of the valves, a branch of a still healthy artery (posterior tibialis) was grafted onto the vena plantaris, the edema in the foot dispersed rapidly and the skin became warm and pink. Cineangiography after 4 months confirmed the development of microvessels in the peripheral tissue. These clinical observations indicated that sufficient blood and oxygen can be transported to resting skeletal muscle through the bypass graft. To establish the physiological basis for the success of the present surgical technique, the venular network was studied and evaluated with Krogh's tissue cylinder model [4]. The density of the venular network suggested a tissue domain area small enough for oxygen delivery in keeping with the success of vascular surgery in the patients.

The question of lymphatic outflow was not, however, considered. Since the lymphatic flow depends linearly on perfusion pressure, the application of arterial blood pressure to the vein seems likely to induce a high outflow, resulting in tissue edema. In an attempt to estimate the lymphatic outflow in the hind limb subjected to DVA, we have combined data on the permeability of venules in rats with data on the geometry of the venular network.

T. Koyama (✉)
Hokkaido University, N-1 W-25 2-7-16, Sapporo, 064-0821, Japan
e-mail: tomkoyamajp@yahoo.co.jp

T. Sasajima
Department of Surgery, Asahikawa Medical University, Asahikawa, Japan
e-mail: sasajima@asahikawa-med.ac.jp

M. Wolf et al. (eds.), *Oxygen Transport to Tissue XXXIII*, Advances in Experimental Medicine and Biology 737, DOI 10.1007/978-1-4614-1566-4_38,

2 Methods

Since the density of venules in a unit volume of rat skeletal muscle is available [5], the venular network can be considered as a single straight tube surrounded by a tissue cylinder [4]. The lymphatic fluid from the perfusing blood is expelled across the total surface area of the venular tube into the surrounding tissue cylinder, depending on the pressure gradient. Using the reported filterability in the venule, the lymphatic outflow could be calculated. The numerical values shown below were recalculated where necessary and expressed in cm, min and mmHg to allow easier comparison with available data.

3 Results

The lymphatic outflow per unit volume of tissue depends on the filterability, total surface area of the blood vessel and pressure gradient between the blood vessel and tissue. The filterability of coronary venules is reported to be 265.2×10^{-7} cm^3 cm^{-2} min^{-1} mmHg [6]. Assuming the tissue pressure to be small and the density of the tissue to be 1 g cm^{-3}, the lymphatic outflow per unit volume of tissue can be estimated by a simple calculation. As in our previous paper [4], we assumed a straight venular tube ($\phi = 30$ μm) with a circumference of 9.4×10^{-3} cm and a length of 4.43×10^2 cm cm^{-3} in a unit volume of tissue; this gives a total surface area of 4.16 cm^2 cm^{-3}. Using these values, the lymphatic outflow is given by:

$$\begin{aligned}\text{Lymphatic outflow} &= \text{Filterability} \cdot \text{ Surface area} \cdot \text{ Blood pressure} \\ &= 0.011\text{ml} \cdot \ 100\text{g}^{-1}\,\text{min}^{-1}\ \text{mmHg}^{-1}.\end{aligned}$$

When the venular perfusion pressure is increased to 100 mmHg by the arterial blood pressure, it would be 1.1 ml × 100 g^{-1} min^{-1}.

4 Discussion

The rate of lymphatic outflow in the normal rat lower limb including both the capillary and venular networks was studied by Kamiya et al. [7]. Using a gravity method they reported a value of 0.03 ml × 100 g^{-1} min^{-1} mmHg^{-1}. Assuming 15 mmHg [8] for the venular blood pressure, the lymphatic outflow rate will be 0.45 ml × 100 g^{-1} min^{-1}. The above value estimated for DVA perfusion is only 2.44 times bigger than the one expected in the normal vascular network. This increase in lymphatic outflow appears somewhat small considering the size of the increase in pressure.

This relatively small increase in flow despite the sudden rise in perfusion pressure in the distal vein graft probably reflects the well-known reserve capacity of the lymphatic system. A rise in the interstitial pressure from the normal value −6.5 to

0 mmHg causes a 10- to 50-fold increase in the lymphatics [9]. A similarly marked five- to tenfold increase in lymph flow through the thoracic duct occurs in rats following an administration of a half ml of olive oil by mouth [10]. It seems probable that a similar reserve capacity also exists in the lymphatic system of the lower limb.

Additionally, the partial recovery of the contraction of the skeletal muscle resulting from DVA will accelerate venous flow and decrease the lymphatic outflow.

Finally, it should be mentioned that the difference between the value reported in the whole hind limb [7] and the above estimate may be partially due to the broad approximations, including omission of the effects of capillary net made in the present study. If the capillary surface area could be added to the venular surface area in the estimation of distal vein arterialisation, the total surface area relevant to lymphatic outflow would be bigger than the present estimation. In the lower limb study [7] the lymphatic flow was given as 0.03 ml × 100 g^{-1} $mmHg^{-1}$, i.e., 3.0 ml × 100 g^{-1} $mmHg^{-1}$ × 100 $mmHg^{-1}$. Using the present estimation obtained from the hypothetical venular cylinder the values would be 1.1 ml × 100 g^{-1} × 100 $mmHg^{-1}$. If the surface area of capillary networks was added to the venular surface area, the value for the lymphatic outflow should be a little larger. Thus, the difference between the two studies would be smaller.

5 Conclusion

These estimations suggest there would be only a moderate increase in the lymphatic outflow from the venular network following surgical arterialisation of a distal vein in the lower limb. Together with the results of our previous study we conclude that DVA surgery is physiologically useful, improving oxygen supply without greatly increasing lymphatic outflow.

Acknowledgments The authors wish to express their thanks to Prof. Dr. K. Messmer, Munich University, for his valuable advice and Dr. A. Silver, Physiological Institute, Cambridge University, for her kind suggestions.

References

1. Azuma N, Inaba M, Akasaka N, Haga M, Uchida H, Asada H, Goh K, Sasajima T (2005) Foot salvage achieved by free flap transfer with bypass surgery. Jpn J Vasc Surg 14:151–158
2. François-Franck M (1896) Note a propos de la communication de M. Raymond Petit, sur la suture arterio-veineuse. Compt Rend Hebd Soc Biol 48:150–151
3. Taylor RS, Belli A-M, Hacob S (1999) Distal venous arterialisation for salvage of critically ischemic inoperable limbs. Lancet 354:1962–1965
4. Koyama T, Sasajima T (2011) Sufficient oxygen can be transported to resting skeletal muscle via arterialization of the vein: theoretical considerations in a rat model. Adv Exp Med Biol 701:335–339

5. Engelson ET, Schmid-Schoenbein GW, Zweifach BW (1985) The micro-vasculature in skeletal muscle. III. Venous network anatomy in normotensive and spontaneously hypertensive rats. Int J Microcirc Clin Exp 4(3):229–248
6. Yuan Y, Chilian WM, Granger HJ, Zawieja DC (1993) Permeability to albumin in isolated coronary venules. Am J Physiol 265(2 Pt 2):H543–H552
7. Kamiya A, Rippe B, Folkow B (1979) Volume of capillary exchange vessels measured with a gravimetric method in rat hindquarters. Microvasc Res 17:142–157
8. Widmaier EP, Raff H, Strary KT (2004) Vander, Sherman, Luciano's human physiology. McGraw-Hill, New York, p416
9. Guyton AC (1974) Integrative hemodynamics. In: Sodeman WA Jr, Sodeman WA Sr (eds) Pathologic physiology. W.B. Saunders Co., New York
10. Yoffery JM, Courtice FC (1956) Lymph flow during absorption of food. Edward Arnold Publisher Ltd., London

Chapter 39
Triplet Imaging of Oxygen Consumption During the Contraction of a Single Smooth Muscle Cell (A7r5)

Matthias Geissbuehler, Thiemo Spielmann, Aurélie Formey, Iwan Märki, Marcel Leutenegger, Boris Hinz, Kai Johnsson, Dimitri Van De Ville, and Theo Lasser

1 Introduction

We have recently demonstrated a novel technique [1] that enables monitoring of oxygen kinetics at the cellular and sub-cellular level. The method was based on quenching by oxygen of the triplet state of a standard fluorescent compound.

Many other methods enabling oxygen sensing at the cell level exist. Previous work on this topic includes methods based on fluorescence intensity quenching [2], phosphorescence lifetime based methods [3], luminescence based methods [4], and methods working with delayed fluorescence [5].

However, most of these methods are based on low-intensity signals, which does not allow for both high-spatial and high-temporal resolution. Our method is based on a modulated excitation [6] of a standard fluorescent molecule. The resulting

M. Geissbuehler (✉) • I. Märki • T. Lasser
Laboratoire d'Optique Biomédicale LOB, École Polytechnique Fédérale de Lausanne (EPFL), BM 5.138, Station 17, Lausanne, 1015, Switzerland
e-mail: matthias.geissbuehler@epfl.ch

T. Spielmann
Laboratoire d'Optique Biomédicale LOB, École Polytechnique Fédérale de Lausanne (EPFL), BM 5.138, Station 17, Lausanne, 1015, Switzerland

Experimental Biomolecular Physics, Department of Applied Physics, Royal Institute of Technology, AlbaNova University Center, Stockholm, 106 91, Sweden

A. Formey
Laboratory of Cell Biophysics LCB, École Polytechnique Fédérale de Lausanne (EPFL), Lausanne, 1015, Switzerland

M. Leutenegger
Laboratoire d'Optique Biomédicale LOB, École Polytechnique Fédérale de Lausanne (EPFL), BM 5.138, Station 17, Lausanne, 1015, Switzerland

Department of NanoBiophotonics, Max Planck Institute for Biophysical Chemistry, Göttingen, 37077, Germany

M. Wolf et al. (eds.), *Oxygen Transport to Tissue XXXIII*, Advances in Experimental Medicine and Biology 737, DOI 10.1007/978-1-4614-1566-4_39,

signal can be detected with a standard integrating charge coupled device camera. This method is compatible with almost any fluorophore with a (non-radiative) triplet state that can be quenched by dissolved molecular oxygen. Further on, since a multitude of fluorophores can be used, a number of standard labeling protocols exist that can be used with our technique.

2 Oxygen Sensing by Triplet State Quenching

More than 60 years ago, German scientists discovered that molecular oxygen interacts with fluorescent compounds and quenches their luminescence [7]. This strong interaction is related to the particular electronic configuration of the ground state of molecular oxygen. The molecule resides in a triplet configuration, which enables it as an acceptor for energy transfers from the excited triplet state of a fluorescent molecule as described in Fig. 39.1. The relationship between the quencher (oxygen) and the triplet state lifetime can be described by the Stern–Volmer equation (see [1] for further details). Inside a cell, the molecule is exposed to varying micro-environments,

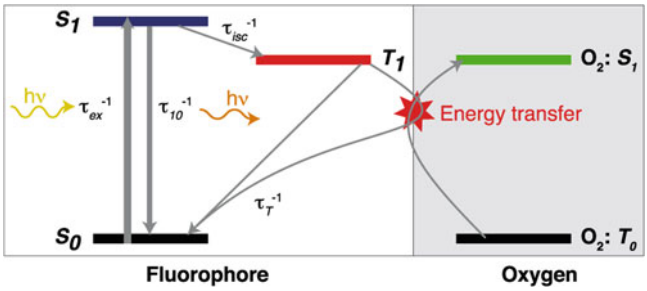

Fig. 39.1 Jablonski diagram of a fluorescent molecule illustrating the three basic energy states of the molecule. Molecular oxygen exhibits a triplet configuration in its ground state which allows it to accept energy transfers from the triplet state of the fluorescent molecule. Reprint from [1]

B. Hinz
Laboratory of Tissue Repair and Regeneration, CIHR Group in Matrix Dynamics, University of Toronto, Toronto, ON, Canada, M5S 3E2

K. Johnsson
Laboratory of Protein Engineering LIP1, École Polytechnique Fédérale de Lausanne (EPFL), Lausanne, 1015, Switzerland

D. Van De Ville
Medical Image Processing Laboratory MIP, École Polytechnique Fédérale de Lausanne (EPFL), Lausanne, 1015, Switzerland

Medical Image Processing Laboratory MIP, University of Geneva, Geneva, 1211, Switzerland

which modify locally both the diffusion time as well as the triplet lifetime in the absence of the quencher because of additional relaxation pathways [8]. This makes it difficult to map oxygen concentrations to measured triplet lifetimes. But nevertheless *variations* in oxygen concentrations are directly proportional to *variations* in triplet lifetimes (see [1] for derivation of formalism). It is hence possible to look at the kinetics of oxygen consumption at the cellular and sub-cellular levels using the described quenching mechanism.

3 Triplet Imaging by Modulated Excitation

The method is based on a modulated excitation scheme, which leads to characteristic population of the triplet as well as singlet states. The resultant fluorescent signal shows a distinctive decrease in intensity for longer pulse widths of excitation. This decrease is related to the increasing population on the triplet state.

We built a custom-made excitation setup where the emission of a Millenia Pro laser ($\lambda = 532$ nm; Newport Spectra Physics) was switched with an acousto-optic modulator (rise-time of ~10 ns; Gooch and Housego). This source was used to illuminate the sample observed on a standard upright microscope (Axiovert 200, Objective: Plan-Neofluar 40×/0.75 Ph2; Carl Zeiss). The image acquisition was done with an electromagnetic charge-coupled device camera (Luca, Andor Technology). Further details can be found in [1].

A typical image of a smooth muscle cell A7r5 with good triplet state lifetime contrast can be seen in Fig. 39.2. Many sub-cellular compartments can be distinguished on the triplet lifetime image (red and yellow spots). As described in Sect. 39.2, these are most likely linked to different micro-environments and not different oxygen concentrations.

3.1 Calibration by Oxygen Scavenging System

In order to relate the triplet lifetime to oxygen concentrations, we have calibrated and validated the oxygen sensitivity of our setup, using the enzyme ascorbase (Sigma-Aldrich) for catalyzing the oxidation of L-ascorbic acid (Sigma-Aldrich) as proposed by Lo [9]. In parallel to the triplet imaging measurement, we monitored the oxygen content of the solution using a dissolved oxygen probe (SG6 Seven Go Pro with InLab 605 sensor; Mettler-Toledo). As shown in Fig. 39.3a the probe reveals the linear decrease of dissolved oxygen. The graph of the triplet state relaxation rate $k_T = 1/\tau_T$ in Fig. 39.3b also demonstrates a linear relationship, which suggests that the molecules' response to oxygen can indeed be described by the Stern–Volmer model.

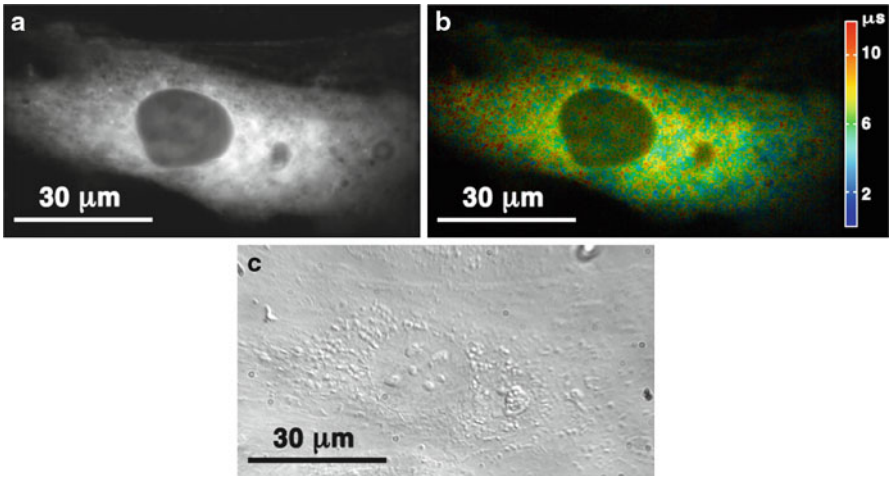

Fig. 39.2 Triplet state image of a smooth muscle cells A7r5 with transient transfection of the cytosolic fusion protein β-galactosidase (SNAP-β-gal) employed for the labeling with TMR. (**a**) Fluorescence intensity image. (**b**) Triplet lifetime image with color encoded lifetime. (**c**) Differential interference contrast (DIC) image. The acquisition settings for this image were optimized for best triplet lifetime contrast resulting in peak intensities at the center of the image of ~4 mW/mm^2. This cell has been labeled using the standard covalys labeling protocol (incubation with TMR-Star at 5 µM for 30 min)

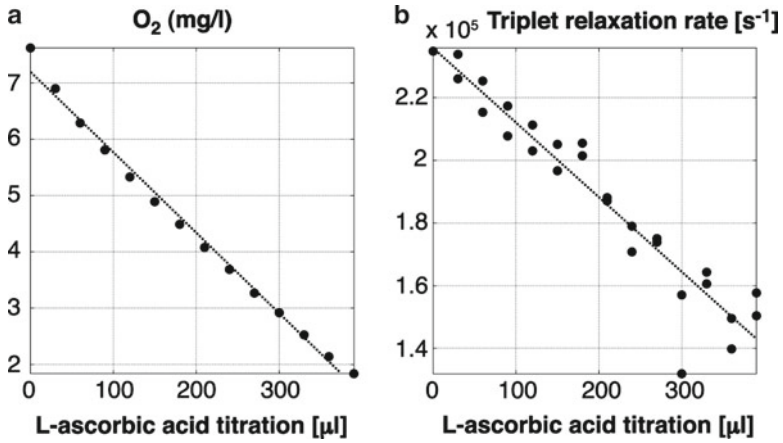

Fig. 39.3 Observation of TMR adhering to a glass cover slide in a flow cell. Titration of 25.5 mM L-ascorbic acid removes the oxygen in controlled discrete steps. (**a**) Dissolved oxygen as measured by a commercial probe. (**b**) Triplet state relaxation rate $k_T = 1/\tau_T$. Reprinted from [1]

4 Triplet Imaging of Single Smooth Muscle Cells A7r5

In a more applied experiment, we assessed the oxygen consumption of a single rat thoracic aorta smooth muscle cell A7r5 (Promochem; CRL-1444) during a [Arg^8]-vasopressin acetate salt (AVP; Sigma; V9879) stimulated contraction experiment [10]. The cells have been labeled using the SNAP-tag technique [11]. We transfected A7r5 with the SNAP-tag-β-galactosidase which is a cytosolic protein linked to a tag. Labeling the tag allowed attaching tetramethylrhodamine (TMR) as fluorophore. Further details on the experimental methods can be found in [1].

The results of three AVP stimulation experiments are shown in Fig. 39.4a. The displayed curves stem from a selected area inside the cells (usually about one-third of the whole cell size, see [1] for the corresponding images). As mentioned above, the variation in $k_T = 1/\tau_T$ is proportional to the variation in the oxygen concentration. After global stimulation with 500 nM AVP the cells undergo a contraction. This leads to an oxygen consumption inside the cell, which can be observed on the temporal evolution of the triplet relaxation rate. In Fig. 39.4b the temporal evolutions are normalized with respect to their initial and final steady states. For the negative controls, we used a factor of 0.4×10^{-5} for the normalization corresponding to a typical difference between the steady state values before and after adding AVP. The intracellular oxygen concentration shows a mono-exponential decay upon contraction. This is in good agreement with previously measured results in skeletal muscle fibers [12].

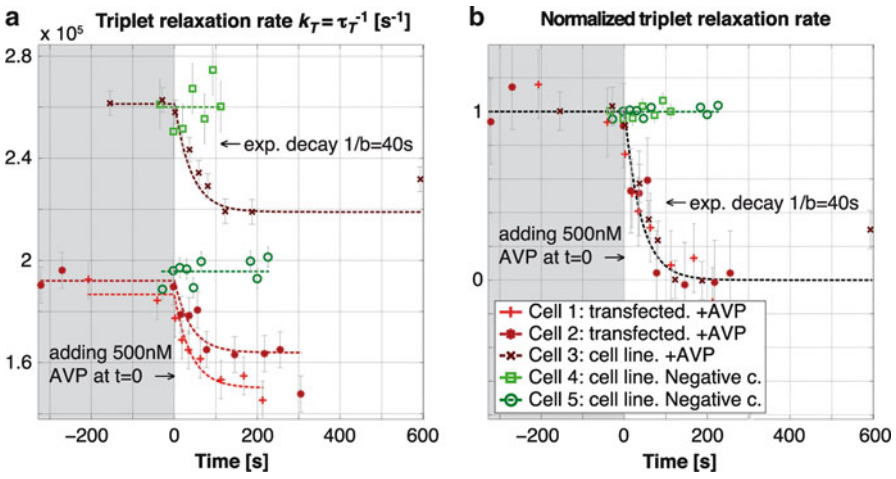

Fig. 39.4 Three experiments on [Arg8]-vasopressin (AVP) induced contraction of smooth muscle cells A7r5 with transient transfections of the cytosolic fusion protein β-galactosidase (SNAP-β-gal) employed for the labeling with TMR. Comparison with negative control (no AVP-stimulation). Reprinted from [1]

5 Conclusion

We have demonstrated a novel concept for functional wide-field microscopy that allows monitoring of oxygen kinetics with both high spatial and temporal resolutions. In a calibration experiment, the system demonstrated a linear response to the removal of oxygen following the Stern–Volmer model. In a second step we have measured the oxygen consumption of a single smooth muscle cell A7r5 upon induced contraction. The intracellular oxygen concentration shows a mono-exponential decay upon contraction.

In conclusion, our proposed triplet-state imaging concept is a novel method for investigating oxygen concentration variations at the cellular and sub-cellular levels with time resolutions in the order of a second.

References

1. Geissbuehler M et al (2010) Triplet imaging of oxygen consumption during the contraction of a single smooth muscle cell (A7r5). Biophys J 98(2):339–349
2. Knopp JA, Longmuir IS (1972) Intracellular measurement of oxygen by quenching of fluorescence of pyrenebutyric acid. Biochim Biophys Acta – Gen Sub 279(2):393–397
3. Vanderkooi JM et al (1987) An optical method for measurement of dioxygen concentration based upon quenching of phosphorescence. J Biol Chem 262(12):5476–5482
4. Hartmann P et al (1995) Luminescence quenching behavior of an oxygen sensor based on a Ru(II) complex dissolved in polystyrene. Anal Chem 67(1):88–93
5. Mik EG et al (2006) Mitochondrial PO_2 measured by delayed fluorescence of endogenous protoporphyrin IX. Nat Methods 3(11):939–945
6. Sandén T et al (2007) Monitoring kinetics of highly environment sensitive states of fluorescent molecules by modulated excitation and time-averaged fluorescence intensity recording. Anal Chem 79(9):3330–3341
7. Kautsky H, Müller G (1947) Luminescenzumwandlung durch Sauerstoff – Nachweis geringster Sauerstoffmengen. Z Naturforsch A 2(3):167–172
8. Rehm D, Weller A (1970) Kinetics of fluorescence quenching by electron and H-atom transfer. Isr J Chem 8(2):259–271
9. Lo LW (1996) Calibration of oxygen-dependent quenching of the phosphorescence of Pd-meso-tetra (4-carboxyphenyl) porphine: a phosphor with general application for measuring oxygen concentration in biological systems. Anal Biochem 236(1):153–160
10. Renterghem CV (1988) Vasopressin modulates the spontaneous electrical activity in aortic cells (line A7r5) by acting on three different types of ionic channels. Proc Natl Acad Sci USA 85(23):9365–9369
11. Keppler A et al (2003) A general method for the covalent labeling of fusion proteins with small molecules in vivo. Nat Biotechnol 21(1):86–89
12. Hogan MC (2001) Fall in intracellular PO_2 at the onset of contractions in Xenopus single skeletal muscle fibers. J Appl Physiol 90(5):1871–1876

Chapter 40
Relationship Between Submaximal Handgrip Muscle Force and NIRS-Measured Motor Cortical Activation

Gérard Derosiere and Stéphane Perrey

1 Introduction

As humans, generation of muscle force is a central part of our daily motor tasks. When producing movement, the force output required to manipulate hand-held objects can be changed over a large range. Few studies have carried out a detailed investigation into the relationship between brain activation and muscle force, owing to methodological difficulties in evaluating in vivo brain activation. In recent years, Dettmers et al. [1] during a positron emission tomography (PET) study showed a logarithmic relationship between the index finger flexion force and brain activation whereas others (finger flexor muscles in Dai et al. [2]; isometric index finger abduction in van Duinen et al. [3]) found a linear relationship using functional magnetic resonance imaging (fMRI). These findings suggest that brain activity is positively correlated to voluntary effort, as a higher level of effort is required for exerting greater muscle force. However, the nature of the relationship between brain activity and submaximal generated force remains to be clarified. The present study aimed to elucidate the nature of the relationship between muscle handgrip force and oxygenated hemoglobin (oxy-Hb) levels as an indicator of brain activity in the primary motor cortex area with near-infrared spectroscopy (NIRS). NIRS is one of the non-invasive emerging neuroimaging techniques, which allows measurement of human brain activity for a wide range of daily motor tasks [4].

G. Derosiere • S. Perrey (✉)
Movement to Health, University Montpellier 1. Euromov,
700 Avenue du Pic Saint Loup, 34090 Montpellier, France
e-mail: stephane.perrey@univ-montp1.fr

M. Wolf et al. (eds.), *Oxygen Transport to Tissue XXXIII*, Advances in Experimental Medicine and Biology 737, DOI 10.1007/978-1-4614-1566-4_40,

2 Methods

2.1 Subjects

Nine healthy subjects participated in the study (eight men and one woman, all right-handed, age 32 ± 8 years). All subjects had no known neuromuscular disorders. The procedure of the experiment was explained to the subjects and all subjects gave informed consent prior to their participation.

2.2 Motor Tasks

The subjects sat in a comfortable chair with their right elbow angle set at 110° and wrist supported by an adjustable table. The left arm rested naturally by the side of the body. The subject's right hand was placed under restraining straps in order to facilitate isometric exercise during the trials. Motor tasks were isometric handgrip contractions by the right hand at 10, 20, 30, 40, and 50% of maximum voluntary contraction (MVC) in a 30 s exertion with a 60 s recovery, pseudo-randomly assigned in one block design (Fig. 40.1). Each subject was required to perform the

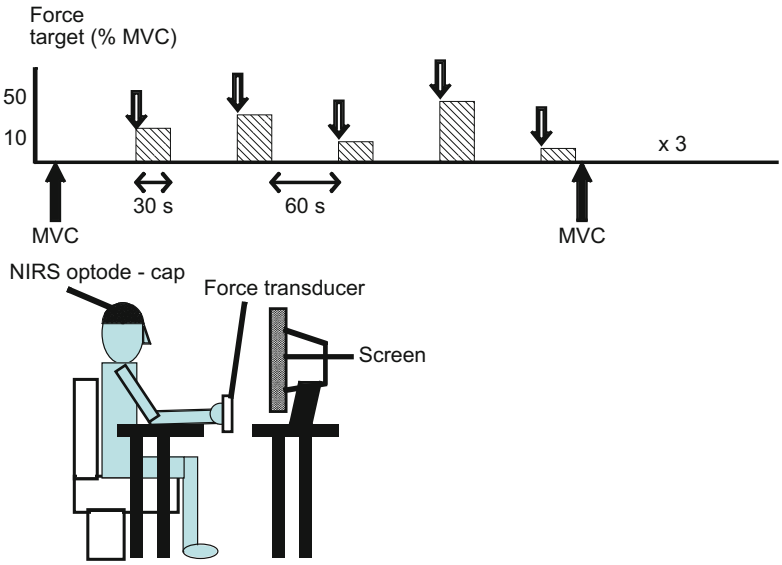

Fig. 40.1 Illustration of the experimental sequencing (*top*) and setup (*bottom*). *Shaded boxes* are motor task periods assigned pseudo-randomly. *MVC* maximal voluntary contraction. See text for further details

block three times at each of the set intensities. To prevent the effects of possible fatigue, the pseudo-random order prevented immediate repetition of relatively high force levels; furthermore after each block, a brief MVC (5 s) was performed to ensure that muscle fatigue did not occur over time. During the experiment, the subjects squeezed the handgrip to match the target force provided by a visual feedback system. On the computer monitor in front of the subjects, the force output and the target line were displayed in real-time (Fig. 40.1).

2.3 Near-Infrared Spectroscopy

We used four wavelengths (775, 810, 850, and 910 nm) of NIRS (NIRO-300, Hamamatsu Photonics, Japan) to analyze motor cortex oxygenation. The optical probe consisted of one emitter and one detector (comprising three separate sensors). The distance between the transmitting and receiving probe was 4 cm. The NIRS probe was guided on the subjects' heads through glass fiber bundles. The NIRS probe was positioned over the subjects' left motor cortex area enclosing C3 according to the international EEG 10-20 system, and was fixed with a cap on the head and elastic bandages. The positioning of the probe on the motor area for the hand was checked during a pinching task of the right hand to induce functional oxygenation. To reduce artifacts, the subjects were asked to minimize head and body movements and were given instructions to breathe gently and regularly. Hair was parted under the probes for both the source and detector to leave ample hair-free scalp. The NIRS data were collected at a sample frequency of 2 Hz. The change (Δ) in total-Hb (μM cm), defined as the sum of the changes in oxy-Hb (μM cm) and deoxy-hemoglobin, can be used as a measure of blood volume changes.

2.4 Data Analysis

Changes in total-Hb and oxy-Hb data were calculated as the average of the last 10 s during the exercise subtracting from a baseline defined as the average value over the 10-s period just before the start of the motor task (Fig. 40.2). For each force, the ΔOxy-Hb and Δtotal-Hb data were averaged between the three repetitions in each subject. To test whether the brain activity differed significantly between the five target force levels (within-subject factor), an ANOVA for repeated measures was used. When the main analysis indicated a significant effect for force, post-hoc (Bonferroni) analysis was performed. Polynomial stepwise regression was used to test whether the relationship between brain activity and force was linear or nonlinear. Significance level was set at $P<0.05$. All data are presented as mean ± standard deviation (SD).

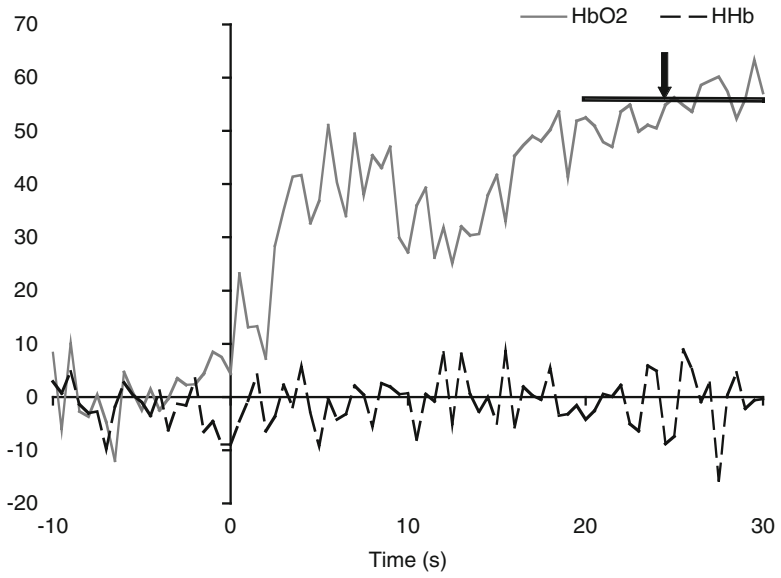

Fig. 40.2 Hemodynamic time course plot, illustrating for one typical subject the changes in oxygenated hemoglobin (HbO_2) and deoxy-hemoglobin (HHb) in response to motor stimulation (50% MVC for 30 s). The *black arrow* indicates the last 10 s for the calculation of changes above the baseline value

3 Results

The mean target force level ranged from 36.49 (10% MVC) to 182.56 N (50% MVC). For all force levels, the subjects performed the force task according to the instructions. There were no significant differences between MVCs (mean value of 365.12 ± 87.70) during the total duration of the study. Oxy-Hb level changed significantly according to the force intensity ($F = 26.28$, $P < 0.01$) and was linearly correlated ($R^2 = 0.968$, $P < 0.01$). Similar response patterns were found for total-Hb ($R^2 = 0.958$, $P < 0.01$). Post-hoc analyses revealed that significant increases in both Oxy-Hb and total-Hb were present from 30% MVC. Entering a quadratic term led to a significantly stronger relationship ($R^2 = 0.998$, $P < 0.01$, Fig. 40.3) between force and brain activity (as evaluated by Oxy-Hb response) for the whole group. However, for the individual subjects, this relationship was more often better fitted by a linear term (eight subjects vs. five subjects with a quadratic term, respectively). A small but not significant change in deoxy-hemoglobin was found.

4 Discussion

This pilot study aimed to determine motor cortical activation using the NIRS technique in response to force modulation (varying submaximal levels of force production) of a handgrip motor task. We found strong correlations between these measurements

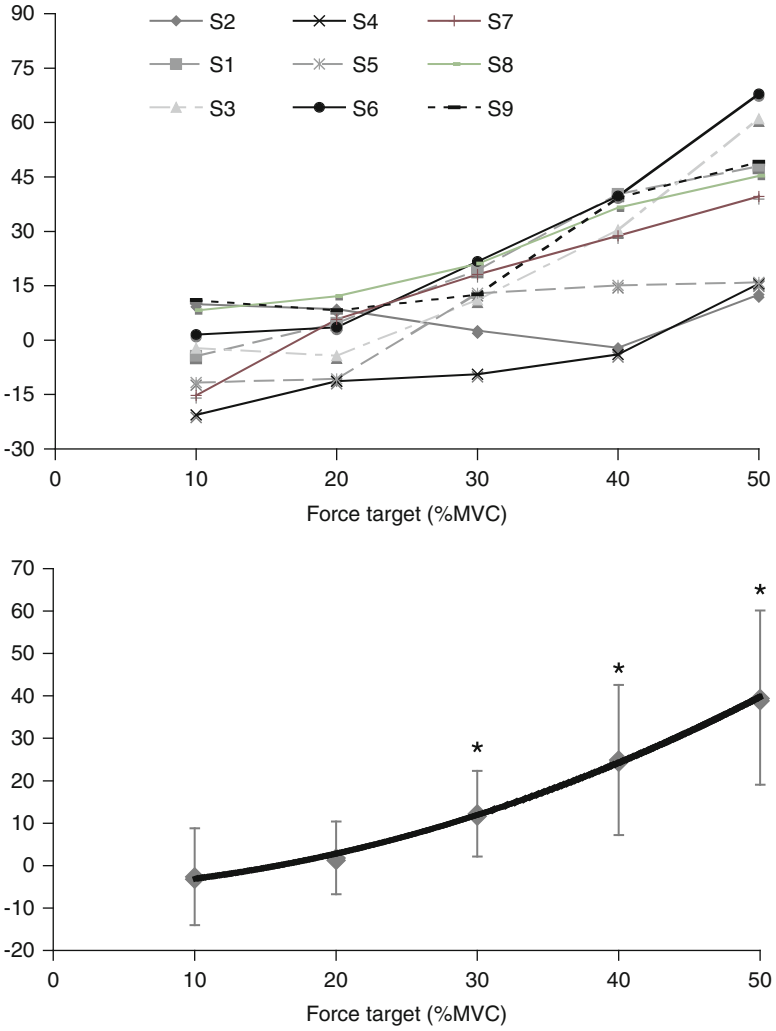

Fig. 40.3 The correlation between muscle force and brain activation estimated by NIRS during right-hand contractions. The mean amplitude of the three contractions at each force level (% MVC) is plotted against the mean amplitude of the accompanying brain activation changes (Oxy-Hb) for each individual subject (*top*) and for the whole group (*bottom*). *Significantly different from 10% MVC, $P<0.05$

both at a group and at an individual level. Our data measured by NIRS confirm similar brain activation patterns (i.e., increase of Oxy-Hb and total-Hb responses) as a function of force production as described in some previous fMRI [2, 3] and PET [1] studies. Activation response characterized by a marked increase in Oxy-Hb and total-Hb and a roughly constant level of deoxy-hemoglobin could have resulted from an increase in the regional cerebral metabolic rate for oxygen, compensated by

an increase in the regional cerebral blood flow over the activated cortical area. Our data strengthen the previous findings [1], as linear correlation performed on data in different subject does not necessarily imply a linear correlation within a single subject (Fig. 40.3). Indeed for some subjects, we found that the relationship between NIRS measured brain activation and submaximal force for isometric contractions up to 50% MVC was better described by a curvilinear equation (5 out of 13 subjects). This implies that it is important to control individually the levels of motor output activation during a NIRS task. These results are valuable for investigating, e.g., motor fatigue (e.g., [5]) or investigations on therapeutic intervention with brain computer interfaces driven by NIRS signals derived directly from the motor cortical areas [6]. As a subject for further research, it is necessary to examine the relationship between locomotion speed and the extent of the region activated in the brain with the multichannel NIRS system.

Acknowledgments This study was supported by research funds of both the Languedoc-Roussillon Region Council and the French University Institute. The authors would like to acknowledge the contribution of François Alexandre for his assistance in collecting the data.

References

1. Dettmers C, Fink GR, Lemon RN et al (1995) Relation between cerebral activity and force in motor areas of the human brain. J Neurophysiol 74:802–815
2. Dai TH, Liu JZ, Sahgal V (2001) Relationship between muscle output and functional MRI-measured brain activation. Exp Brain Res 140:290–300
3. van Duinen H, Renken R, Maurits NM et al (2008) Relation between muscle and brain activity during isometric contractions of the fist dorsal interosseus. Hum Brain Mapp 29:281–299
4. Perrey S (2008) Non-invasive NIR spectroscopy of human brain function during exercise. Methods 45:289–299
5. Rupp T, Perrey S (2008) Prefrontal cortex oxygenation and neuromuscular responses to exhaustive exercise. Eur J Appl Physiol 102:153–163
6. Coyle S, Ward T, Markham C et al (2004) On the suitability of near-infrared (NIR) systems for next-generation brain-computer interfaces. Physiol Meas 25:815–822

Part VI
Methodology for O_2 Measurement

Chapter 41
Feasibility Study of Non-invasive Oxygenation Measurement in a Deep Blood Vessel Using Acousto-Optics and Microbubbles

Jack E. Honeysett, Eleanor Stride, and Terence S. Leung

1 Introduction

Here we investigate the potential for performing non-invasive oxygen saturation (SO_2) measurements in deep blood vessels such as the pulmonary artery. Measures of mixed venous oxygen saturation (S_vO_2) from the pulmonary artery are used in intensive care monitoring as an early-warning indicator of cardiac failure. This currently requires an invasive intravenous catheter: a procedure which is both costly and carries significant patient risk [1].

This in silico model of a deep blood vessel is used to test the feasibility of performing non-invasive SO_2 measurements in the pulmonary artery. We propose to use acousto-optics (AO) with microbubble signal enhancement [2]. The cylindrical vessel (as shown in Fig. 41.1) contains two distinct populations of optical scatterers: one population with the scattering and absorption properties of venous blood, and the other with the optical and acoustic properties of microbubbles. The surrounding volume has the optical properties of generic biological tissue. Here SO_2 is defined as the proportion of haemoglobin molecules in the tissue which are oxygenated.

Microbubbles have been shown to be an effective contrast agent for diagnostic ultrasound (US) imaging [3]. Under applied US pressure, the gas undergoes volumetric oscillations [4]. The presence of microbubbles in the blood will significantly alter its optical properties, in particular the refractive index and optical scattering of the blood. In addition, the optical properties of microbubbles are expected to vary with the applied US pressure: as the microbubble oscillates, its cross-sectional

J.E. Honeysett (✉) • T.S. Leung
Biomedical Optics Research Laboratory, Department of Medical Physics and Bioengineering, University College London, Malet Place Engineering Building, WC1E 6BT, London, UK
e-mail: j.honeysett@ucl.ac.uk

E. Stride
Department of Mechanical Engineering, University College London, Malet Place Engineering Building, WC1E 6BT, London, UK

M. Wolf et al. (eds.), *Oxygen Transport to Tissue XXXIII*, Advances in Experimental Medicine and Biology 737, DOI 10.1007/978-1-4614-1566-4_41,

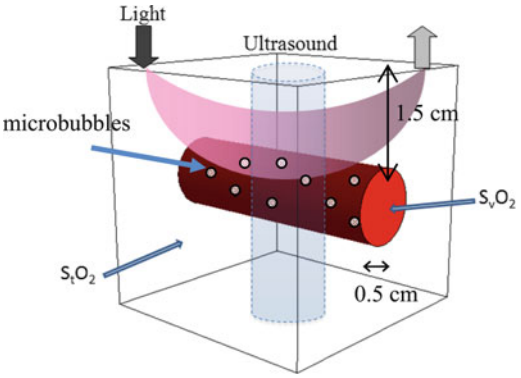

Fig. 41.1 An applied US field modulates the optical properties of the medium, as well as the optical properties of the microbubbles in the blood [2]. The oxygen saturations inside the blood vessel and tissue are defined as S_vO_2 and S_tO_2, respectively

area and hence optical scattering coefficient will vary. This variation in optical properties is expected to be greater than the variation of the biological tissue under US, since gas-filled microbubbles are highly compressible. This is proposed as a means of amplifying the AO modulation of light in the focal region, by perturbing the partial pathlengths (PPLs) of photons. A change in optical PPLs will result in a change in observed attenuation on the surface of the tissue, which will also be dependent on the distribution of optical absorbers in the tissue.

2 Monte Carlo Methods

The implementation of the Monte Carlo model of light propagation is based on graphics-processing unit (GPU) accelerated software developed previously at UCL [5]. This tracks the phase (and hence optical pathlength) of individual photon packets as they pass through a scattering and absorbing medium. The model was extended to include a cylindrical blood vessel containing microbubbles, with radius 0.5 cm and central axis 1.5 cm below the surface, embedded in homogeneous surrounding tissue. The absorption coefficients μ_a can be independently specified for the external tissue ($\mu_{a,t}$) and blood vessel ($\mu_{a,v}$) to model various oxygen saturations (S_vO_2 in the vessel and S_tO_2 in the tissue). In the case of blood, a haemoglobin concentration of 14 g/dl was assumed; for tissue, optical properties used for modelling the extracerebral layer of the head were employed [6], including background absorption due to water. US is assumed to propagate as infinite planar wavefronts with a frequency of 2 MHz, peak pressure of 0.28 MPa and focal region encompassing the whole blood vessel (in the optical field of view). Full simulation parameters are given in Table 41.1.

Radial oscillations of microbubbles under US are described by the Rayleigh–Plesset equation [4]. These oscillations are non-linear at high acoustic pressures (such as those used here), but by limiting radial changes to second order [7] an analytical solution was derived. The radius of a microbubble, $R(t)$, depends on the acoustic phase at that point. The optical scattering coefficient for microbubbles [8] is expected to be proportional to R^2, and hence will also vary spatially and temporally.

Table 41.1 Parameters for blood and surrounding tissue (for an optical wavelength of 830 nm) used in the simulations

	μ_s (cm^{-1})	Anisotropy (g)	Hb concentration (μM)	SO_2 (%)	Hb μ_a (cm^{-1})	Background μ_a (cm^{-1})
Tissue	20	0.9	11	[65, 85]	[0.165, 0.167]	0.032
Blood	20	0.9	2200	[65, 85]	[5.135, 5.350]	–

SO_2 is varied in intervals of 5%

Parameters for SonoVue™ microbubbles have been measured experimentally [4], and are used in this simulation. The concentration of microbubbles within the vessel is 10^5 mm^{-3}.

We present the results as a comparison between the AO signal and a purely optical technique. The optical signal is calculated as the change in optical attenuation ΔA relative to the intensity at a reference level I_{ref} (75% S_vO_2 and 75% S_tO_2), i.e. $\Delta A = \ln(I_{ref} / I)$

The AO-modulated signal (AOM), is defined as the difference in light attenuation on the surface of the tissue resulting from the interaction of the US field with the microbubbles:

$$\Delta\mathrm{AOM} = \Delta A_{US} - \Delta A \tag{41.1}$$

where ΔA_{US} indicates that the US field is turned on.

The sensitivity of purely optical techniques (reliant on changes in ΔA) to changes in oxygen saturation is compared with the sensitivity of AO techniques (which measure changes in ΔAOM). Here sensitivity is defined as the rate of change of the measured signal with respect to the change in S_vO_2 or S_tO_2:

$$\Sigma_{AO,v} = \frac{\partial(\Delta\mathrm{AOM})}{\partial(S_vO_2)} : \Sigma_{AO,v} = \frac{\partial(\Delta\mathrm{AOM})}{\partial(S_vO_2)} \tag{41.2}$$

where $\Sigma_{O,v}$ is the sensitivity of optical techniques to vessel SO_2 changes, and $\Sigma_{AO,v}$ is the sensitivity of AO techniques to vessel SO_2 changes. This is valid for small changes in S_vO_2, assuming no change in photon pathlengths.

3 Results

The relative sensitivities of these two techniques to changes in blood vessel oxygenation S_vO_2 and tissue oxygenation S_tO_2 are investigated, relative to the baseline levels of S_vO_2=75% and S_tO_2=75%. Figure 41.2 shows the changes in ΔA and ΔAOM with varying S_vO_2 and S_tO_2.

The sensitivities $\Sigma_{O,v}$, $\Sigma_{O,t}$, $\Sigma_{AO,v}$ and $\Sigma_{AO,t}$ are calculated numerically by linear regression (see Fig. 41.2). The relative sensitivities of both measures to blood vessel SO_2 are found to be: $\Sigma_{O,v}/\Sigma_{O,t}$=0.10 and $\Sigma_{AO,v}/\Sigma_{AO,t}$=7.4. A relative sensitivity greater than one indicates that such a signal is more sensitive to vessel SO_2 than to tissue SO_2.

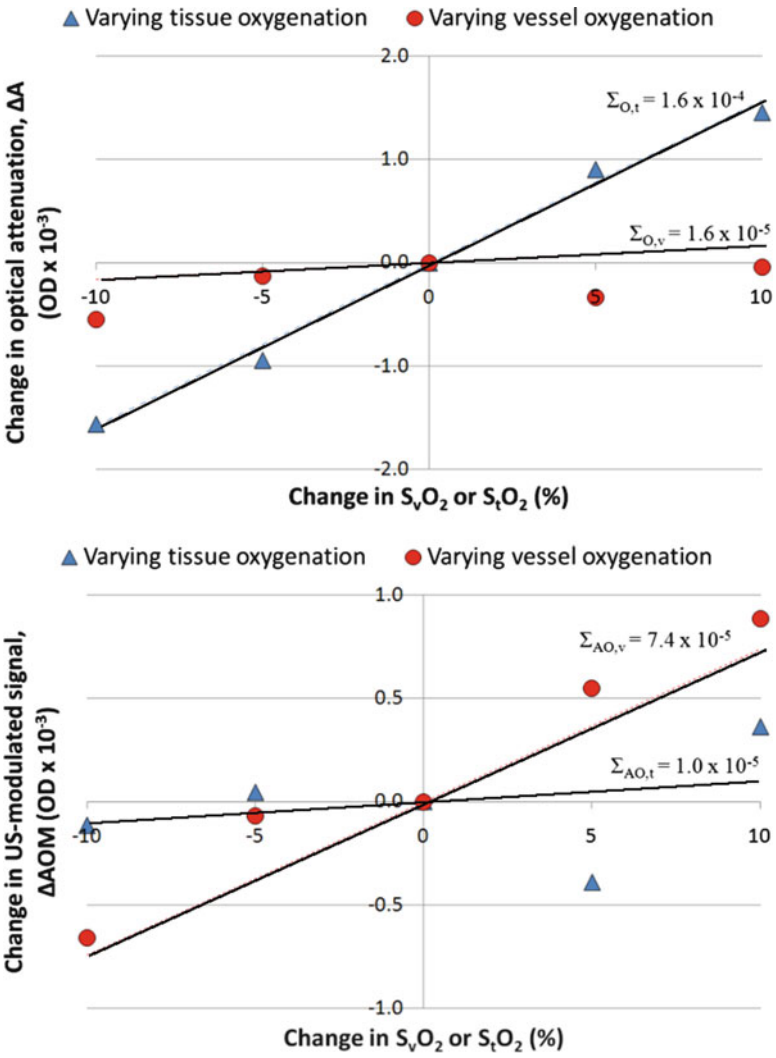

Fig. 41.2 *Top*: Change in optical signal with changing vessel/tissue SO_2. *Bottom*: Change in AO signal. (*Bold lines* indicate the results of linear regression fits to each data set)

The Monte Carlo model also tracks the total pathlength of each individual photon, and distinguishes between the PPL spent in the tissue and the PPL spent inside the blood vessel. Therefore, we can analyse the effect of US on these PPLs separately. In order to do this we calculate the difference in the mean pathlength, Δl, induced by the US.

Table 41.2 Mean PPLs (and associated standard errors) in the vessel and tissue, and the difference in PPL as a result of US

	PPL without US (mm)		Change in PPL induced by US, Δl (mm)	
	Mean	Standard error	Mean	Standard error
PPL in vessel, l_v	0.160	0.004	0.013	0.006
PPL in tissue, l_t	70.1	0.02	0.36	0.03

Here S_vO_2 and S_tO_2 are 75%

Table 41.2 shows the mean PPLs in the vessel and tissue, and the change in PPL induced by US.

4 Discussion

Figure 41.2 shows that purely optical techniques, based on measuring changes in attenuation, are not sensitive to variations in deep blood vessel SO_2. This is known and has been described by analytical and Monte Carlo models [9]. This result can be explained in our case by considering a simplified model of light attenuation, based on the modified Beer–Lambert law applied to an inhomogeneous medium [10]. In the case where the total haemoglobin concentration is constant, ΔA can be expressed in terms of changes in SO_2:

$$\Delta A = \left\{ l_v c_v \Delta S_v O_2 + l_t c_t \Delta S_t O_2 \right\} (\varepsilon_{HbO} - \varepsilon_{HHb}) \tag{41.3}$$

where $l_{v/t}$ is the PPL in the vessel/tissue, $c_{v/t}$ is the absolute total haemoglobin concentration in the vessel/tissue and $\varepsilon_{HbO/HHb}$ is the specific extinction coefficients of oxy/deoxyhemoglobin.

Table 41.2 shows that the PPL for photons in the tissue is at least 400 times longer than the PPL in the vessel. According to this model, the sensitivity is proportional to the product of the pathlength with the total haemoglobin concentration ($l_v c_v$ and $l_t c_t$): for the vessel and tissue, respectively, these products are $l_v c_v \approx 350$ mm μM and $l_t c_t \approx 770$ mm μM. In agreement with the measured sensitivities in Sect. 3, this predicts that near infrared spectroscopy (NIRS) is at least twice as sensitive to changes in surrounding tissue S_tO_2 compared with changes in vessel S_vO_2.

The AO-modulated signal ΔAOM is however dependent on the change in pathlength Δl induced by US-modulation:

$$\Delta AOM = \left\{ \Delta l_v c_v \Delta S_v O_2 + \Delta l_t c_t \Delta S_t O_2 \right\} (\varepsilon_{HbO} - \varepsilon_{HHb}) \tag{41.4}$$

In this simulation US-induced changes in the optical attenuation are purely a result of changes in microbubble scattering. The optical scattering coefficient of microbubbles ($\mu_{s,b}$) is modulated by the presence of an US field. This in turn alters

Table 41.3 Relative sensitivities of optical and AO signals to vessel SO_2

	Relative sensitivity to vessel SO_2	Predicted by linear model (41.3) and (41.4)	Simulation results (Fig. 41.2)
Optical signal	$\Sigma_{O,v}/\Sigma_{O,t}$	0.45	0.10
AO signal	$\Sigma_{AO,v}/\Sigma_{AO,t}$	7.3	7.4

the optical field, modulating the PPLs of photons both within the blood vessel (where the microbubbles are localised) and in the tissue.

In (41.4) the sensitivity of the AO signal is predicted to be proportional to the product of the change in PPL due to US with the Hb concentration. In this case these products are: $\Delta l_v c_v \approx 29$ mm μM and $\Delta l_t c_t \approx 4$ mm μM. Therefore, we would expect the AO signal to be more sensitive to changes in blood vessel SO_2 by at least a factor of 7. This is in agreement with the results of the simulation (see Table 41.3).

5 Conclusions

These results suggest that AO techniques are sensitive to deep blood vessels, whereas purely optical measurements are confounded by absorption in the surrounding tissue bed. Microbubbles in the blood vessel, when driven to oscillate by applied US, have an optical scattering coefficient which varies with bubble size. These changes in scattering properties lead to an US-induced change in PPL for photons in the blood vessel: this will cause the overall attenuation of photon paths to change significantly as a result of the US field. AO techniques are therefore a promising candidate for non-invasive SO_2 measurements in a deep blood vessel, such as the pulmonary artery. The next challenge is to extract accurate SO_2 measurements from the AO signal.

Acknowledgements The authors would like to thank Samuel Powell for assistance in implementing the GPU-based simulations and Dr. Jing Deng for useful discussions. This work was funded by the Centre for Mathematics and Physics in the Life Sciences and Experimental Biology (CoMPLEX) Doctoral Training Centre at UCL, through a studentship, the British Heart Foundation, the Medical Research Council and the Engineering and Physical Sciences Research Council (Grant Code EP/G005036/1).

References

1. Reinhart K, Kuhn HJ, Hartog C et al (2004) Continuous central venous and pulmonary artery oxygen saturation monitoring in the critically ill. Intens Care Med 30:1572–1578
2. Honeysett J, Stride E, Leung T (2010) Monte Carlo simulations of acousto-optics with microbubbles. Proc SPIE 7564:75640K
3. Lindner JR (2004) Microbubbles in medical imaging: current applications and future directions. Nat Rev Drug Discov 3(6):527533

4. Stride E, Tang MX, Eckersley RJ (2009) Physical phenomena affecting quantitative imaging of ultrasound contrast agents. Appl Acoust 70(10):1352
5. Leung TS, Powell S (2010) Fast Monte Carlo simulations of ultrasound modulated light using a graphics processing unit. J Biomed Opt 15(5):055007
6. Leung TS, Tachtsidis I, Tisdall M et al (2007) Theoretical investigation of measuring cerebral blood flow in the adult human head using bolus indocyanine green injection and near-infrared spectroscopy. Appl Opt 46(10):1604–1614
7. Church CC (1995) The effects of an elastic solid surface layer on the radial pulsations of gas bubbles. J Acoust Soc Am 97:1510
8. Dean CE, Marston PL (1991) Critical angle light scattering from bubbles: an asymptotic series approximation. Appl Opt 30(33):4764–4776
9. Firbank M, Okada E, Delpy DT (1997) Investigation of the effect of discrete absorbers upon the measurement of blood volume with near-infrared spectroscopy. Phys Med Biol 42:465
10. Hiraoka M, Firbank M, Essenpreis M et al (1993) A Monte Carlo investigation of optical pathlength in inhomogeneous tissue and its application to near-infrared spectroscopy. Phys Med Biol 38:1859

Chapter 42
Sensitivity Enhancement of NIR Fluorescence Contrast Agent Utilizing Gold Nanoparticles

Kyung A. Kang, Jianting Wang, Martin G. O'Toole, Michael Nantz, Joseph D. Moore, Sebastien Laulhe, and Samuel Achilefu

1 Introduction

Indocyanine green (ICG) is one of a few, if not the only, near infrared (NIR) contrast agents that can be used for humans. The quantum yield of this fluorophore is only 0.0028 and 0.012, in water and plasma [1], respectively, and, therefore, artificially enhancing its quantum yield is highly desired. Since fluorescence of a fluorophore is initiated by optically exciting its electrons, one way of changing the fluorescence level is by placing it near an electric field. Gold nanoparticles (GNPs) generate a strong electric (plasmon) field on and around them upon receiving light [2, 3]. Therefore, they can be good candidates for influencing the electron status of a fluorophore [3]. Gold has been used extensively in bio-applications because of its chemical inertness.

The strength of the plasmon field generated by a GNP is the highest on its surface and decays rapidly with the distance from the GNP surface [4, 5]. If the field strength that increases the fluorescence of a fluorophore is known, then one can achieve a higher fluorescence by placing the fluorophore at the distance from a GNP with this particular field strength.

Here, we present the relationship between the plasmon field strength on/around a GNP and fluorescence of Cypate [6] (an ICG-based NIR fluorophore), which may be helpful for developing more effective and safe NIR optical contrast agents.

K.A. Kang (✉) • J. Wang • M.G. O'Toole
Department of Chemical Engineering, University of Louisville, Louisville, KY 40292, USA
e-mail: kyung.kang@louisville.edu

M. Nantz • J.D. Moore • S. Laulhe
Chemistry Departments, University of Louisville, Louisville, KY, USA

S. Achilefu
Radiology Department, Washington University, St. Louis, MO, USA

M. Wolf et al. (eds.), *Oxygen Transport to Tissue XXXIII*, Advances in Experimental Medicine and Biology 737, DOI 10.1007/978-1-4614-1566-4_42,

2 Methods

For placing Cypate (Cy) at a constant distance from a GNP, first 10 nm GNP colloids (Ted Pella; Redding, CA) were coated with poly (allylamine hydrochloride) (PAH; Sigma Aldrich; St. Louis, MO) and poly(sodium-4-styrene sulfonate) (PSS; Polymer Standard Service; Mainz, Germany) as described by Schneider et al. [7]. PAH is a cationic and PSS is an anionic polymer, and they form a strong and stable two-layer structure. The bi-layer is coated on GNP layer-by-layer, forming GNP-$(PAH/PSS)_i$, where *i* is the number of the layers. Cypate was produced and supplied by Achilefu's group. It was placed on the PAH/PSS bi-layers coated GNPs in the form of Cy-conjugated PAH (PAH-Cy). Conjugation of Cy to PAH was done via COOH and NH_2 reaction by using 1-Ethyl-3-[3-dimethylaminopropyl]carbodiimide hydrochloride (EDC; Thermo Scientific, Rockford, IL). For coating PAH-Cy onto the outermost layer of GNP-$(PAH/PSS)_i$, GNP-$(PAH/PSS)_i$ solution was added drop-wise into the PAH-Cy solution (DI water) and stirred for 12 h. The GNP-$(PAH/PSS)_i$-(PAH-Cy) was then purified by dialysis (20 kD MW cut-off) and centrifugation (11,000 rpm).

To link Cypate to GNPs via spacers, the two –COOH endings of Cypate were first replaced with –CHO to modify Cypate (m-Cypate). The spacers were HS-$(CH_2)_{12}$-poly$(EG)_n$-ONH_2, where EG is ethylene glycol. In our study, *n* was 4, 6, or 8 to vary the spacer length. m-Cypate is first mixed with blocking agent IN-$(CH_2)_2$-ONH_2 at a 1:1 ratio to block one of the two –CHO sites. The spacer was then reacted with GNP (GNP-Sp) and GNP-Sp was purified as described above. GNP-Sp was reacted with m-Cypate. The resulting GNP-Sp-Cy was purified.

3 Results and Discussion

3.1 Effect of GNP Plasmon Field Strength on Fluorescence Level: Theoretical Analysis

An electric field near a fluorophore affects the fluorescence in two different ways. It enhances the fluorescence emission rate by enhancing the excitation decay rate and also changes (mainly reduces) the quantum yield of the fluorophore [5, 8]. For a known electric field strength, the enhancement of the excitation decay rate and the change in the quantum yield of a fluorophore can be theoretically estimated. The main parameters affecting the field strength are the GNP size and the wavelength of the light applied [4]. The field strength is the highest on the GNP surface. It decays rapidly with the distance from the surface and the rate of the decay is faster for smaller particles [8]. For biological application, the particle size should be large enough to increase the circulation time in blood but small enough not to get accumulated in excretory organs. The size of 10–100 nm appears to be an appropriate range [9, 10]. Another important factor in the use of nanoparticles for biomedical

purposes is the surface charge, and a neutral charge is known to be the best [9]. Since each fluorophore has a particular excitation wavelength, changing the wavelength is usually not practical. Therefore, the plasmon field strength for a desired fluorescence manipulation may be achieved by selecting an appropriate GNP size and by placing the fluorophore at a proper distance from the GNP.

In the theoretical study for computing the plasmon field strength (E_p), we used a model developed by Neeves and Birnboim [4]. This model is useful because it includes the shells of various materials (e.g., bio-compatible polymer) on the particle. The excitation decay rate γ_{exc} has a relationship with E_p as in (42.1).

$$\frac{\gamma_{\text{exc}}}{\gamma_{\text{exc}}^{\text{o}}} = \left(\frac{E_{\text{p}}}{E_{\text{p}}^{\text{o}}} \right)^2, \tag{42.1}$$

where the superscript 'o' denotes the values without a GNP.

The field strength also affects the fluorescence by changing the quantum yield (q) of a fluorophore, in a relationship shown in (42.2) [5].

$$q = \frac{\gamma_{\text{r}} / \gamma_{\text{r}}^{\text{o}}}{\gamma_{\text{r}} / \gamma_{\text{r}}^{\text{o}} + \gamma_{\text{abs}} / \gamma_{\text{abs}}^{\text{o}} + (1 - q^{\text{o}}) / q^{\text{o}}}, \tag{42.2}$$

where γ_r and γ_{abs} are the radiative rate and the additional non-radiative rate due to the absorption of the radiated energy, respectively. The first term [γ_r / γ_r^o] is the same as [$\gamma_{exc} / \gamma_{exc}^o$] for a spherical particle with a quasi-static polarizibility. The second term becomes large, i.e., q becomes small (quenching), when the fluorescence emission wavelength is close to the GNP absorption peak (~520 nm). The third term becomes important if the fluorophore has a low intrinsic quantum yield (q^o). The resulting fluorescence change (ϕ) is the combination of the two values in (42.1) and (42.2) and can be expressed as:

$$\phi = \frac{\gamma_{\text{exc}}}{\gamma_{\text{exc}}^{\text{o}}} \frac{q}{q^{\text{o}}}. \tag{42.3}$$

Using the relationship described above, the change in Cypate fluorescence by GNPs was theoretically estimated. The system studied was: (1) 10 nm GNPs; (2) polymer bi-layer(s) PAH/PSS on the GNP surface; and (3) fluorophore, Cypate on the polymer layer. Assuming that the quantum yield of Cypate is similar to ICG, we used the ICG intrinsic quantum yield value 0.012 [1] in our computation.

Figure 42.1a shows the normalized plasmon field strength distribution on and around a 10 nm GNP. The field strength rapidly decays with the distance from the surface. This plasmon field distribution enhances the excitation decay rate as shown in Fig. 42.1b. The enhancement is very high when the distance from the GNP surface is less than 3 nm. As in (42.2), the field strength also affects the quantum yield of a fluorophore. Figure 42.1c shows the changes in the Cypate quantum yield (Fig. 42.1c). At the GNP surface, the quantum yield is zero and it remains very low within 1 nm from the GNP surface. The resulting fluorescence of Cypate is the

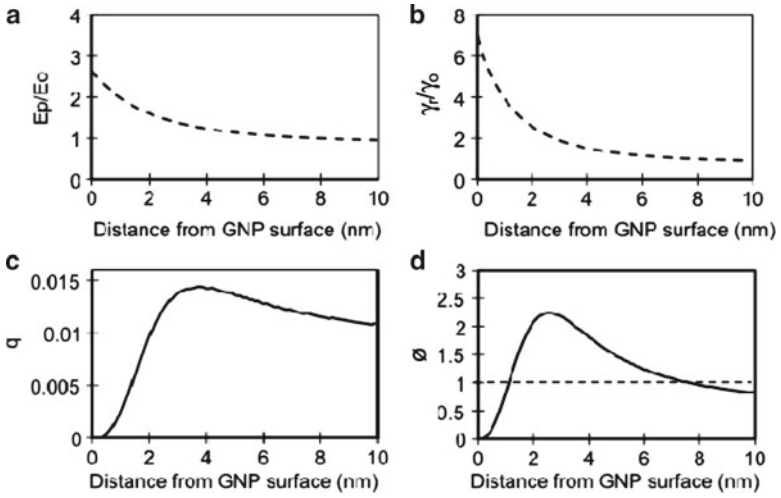

Fig. 42.1 Theoretical estimation of (**a**) the plasmon field distribution around a polymer-coated 10 nm GNP, (**b**) enhancement of the excitation decay rate by the plasmon field, (**c**) quantum yield of Cypate influenced by the plasmon field, and (**d**) resulting fluorescence

combination of the enhancement of the excitation decay rate and the Cypate quantum yield (Fig. 42.1d). Cypate within 1.5 nm from the surface shows quenching and between 1.5 and 3 nm it shows the enhancement up to 2.3 times.

3.2 Changes in Cypate Fluorescence by GNP: Experimental

3.2.1 Fluorophore Placed Outside Polymer Layer on GNP

To experimentally study the effect of a GNP on Cypate fluorescence, we placed polymer layer(s) between Cypate and the GNP. The distance between Cypate and a GNP was varied by varying the numbers of the PAH/PSS bi-layer on a GNP and then placing Cypate-conjugated PAH on the bi-layer(s). Unlike the system used in the theory (Fig. 42.2a), there were multiple Cypate molecules in the PAH-Cy layer. Also, PAH-Cy has a thickness ~1 nm (Fig. 42.2b). However, the Cypate concentration in each sample was constant. The average bi-layer thickness was 2.1 nm, measured by the transmission electron microscope and the particle size analyzer. To observe the Cypate fluorescence on the GNP surface, Cypate was also adsorbed directly onto the GNP. Figure 42.3 shows the Cypate fluorescence change with the change in the PAH/PSS bi-layer number. The control was the PAH-Cy without GNPs at the same Cypate concentration. Fluorescence from the Cypate adsorbed on the GNP surface was completely quenched. For the GNP with PAH-Cy layer alone (no PAH/PSS), the fluorescence is still significantly quenched. This GNP property of fluorescence quenching can be utilized in the molecular beacon [11] construction

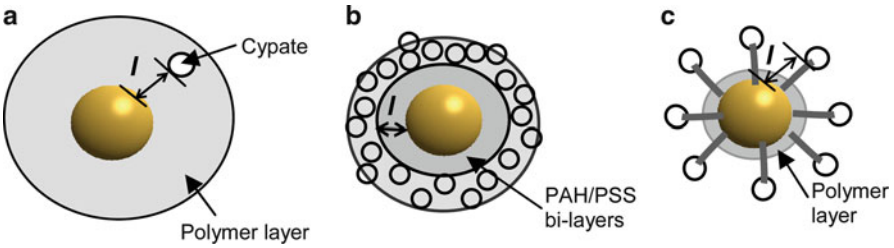

Fig. 42.2 Arrangements of a GNP and Cypate molecule(s) in the study: (**a**) Cypate is placed at a distance of *l* from the GNP surface – system for the theoretical analysis, (**b**) a PHA-Cy layer placed on PHA/PSS bi-layer(s) of a thickness of *l*, coated GNP, (**c**) Cypate placement near a biopolymer-coated GNP via spacers

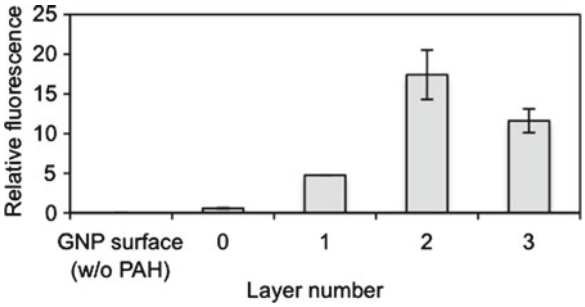

Fig. 42.3 Relative fluorescence emission level when Cypate is placed outside the PHA/PSS bi-layer polymer at various layer numbers (GNP size, 10 nm; constant Cypate concentration; the average PHA/PSS layer thickness, 2.1 nm)

with little restriction in the absorption wavelength of quenchers. The fluorescence increases as the layer number increases: When Cypate was placed on the two bi-layers, the fluorescence is enhanced up to 17 times. For the particles with three layers, fluorescence is still enhanced but not as much as for the two layers. The trend of the fluorescence level is similar to the theoretical estimation (Fig. 42.1d) but the level of enhancement in the experiment was much greater. This may be due to the differences in the system (Fig. 42.2a, b).

3.2.2 Fluorophore-Connected GNP via Spacers

For most nano-contrast agents, fluorophores are usually linked via spacers outside a polymer-coated GNP, as in Fig. 42.2c. We studied the changes in the Cypate when it is connected to GNPs by the spacers at three different lengths (Fig. 42.4a; length estimated by molecular simulation). Each spacer is composed of a carbon chain with –SH ending (for stable coating on GNP) and a PEG (for hydrophilicity). Figure 42.4b shows the changes in the fluorescence of Cypate separated from a

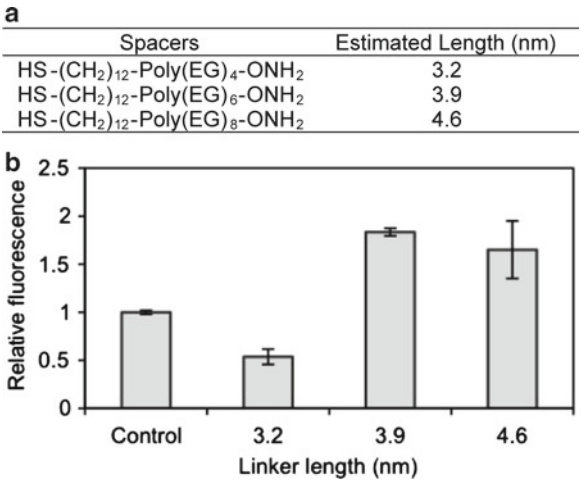

Fig. 42.4 (**a**) Spacers used for Cypate linkage on GNP at various lengths and (**b**) fluorescence emission when Cypate is linked to a GNP via the spacers

GNP by the spacers. The spacer at a length 3.1 nm shows a slight reduction in the fluorescence. The one at the 3.9 nm shows the highest enhancement (~2 times) and the one at 4.9 nm shows 1.5 times. The result confirms that the Cypate fluorescence can be enhanced by GNPs, improving its sensitivity.

4 Conclusions

The fluorescence of an ICG-based NIR fluorophore, Cypate, was enhanced by GNPs, which can be used for increasing sensitivity of optical sensing/imaging. Artificially controlling fluorescence by GNPs (both quenching and enhancement) can be used for developing molecular beacon or Förster resonance energy transfer (FRET) in a new but easier way.

Acknowledgment The authors acknowledge the financial support from the U.S. Army Breast Cancer Program.

References

1. Benson RC, Kues HA (1978) Fluorescence properties of indocyanine green as related to angiography. Phys Med Biol 23:159–163
2. Kang KA, Hong B (2006) Biocompatible nano-metal particle fluorescence enhancers. Crit Rev Eukaryot Gene Expr 16:45–60
3. Wang J, Nantz MH, Achilefu S, Kang KA (2010) FRET-like fluorophore-nanoparticle complex for highly specific cancer localization. Adv Exp Med Biol 662:407–414
4. Neeves AE, Birnboim MH (1989) Composite structures for the enhancement of nonlinear-optical susceptibility. J Opt Soc Am B 6:787–796

5. Bharadwaj P, Anger P, Novotny L (2007) Nanoplasmonic enhancement of single-molecule fluorescence. Nanotechnology 18:044017
6. Achilefu S, Dorshow R, Bugaj J, Rajagopalan R (2000) Novel receptor-targeted fluorescent contrast agents for in vivo tumor imaging. Invest Radiol 35:479–485
7. Schneider G, Decher G, Nerambourg N, Praho R, Werts MHV, Blanchard-Desce M (2006) Distance-dependent fluorescence quenching on gold nanoparticles ensheathed with layer-by-layer assembled polyelectrolytes. Nano Lett 6:530–536
8. Anger P, Bharadwaj P, Novotny L (2006) Enhancement and quenching of single-molecule fluorescence. Phys Rev Lett 96:113002
9. Davis ME, Chen Z, Shin DM (2008) Nanoparticle therapeutics: an emerging treatment modality for cancer. Nat Rev Drug Discov 7:771–782
10. Jiang W, Kim BYS, Rutka JT, Chan WCW (2008) Nanoparticle-mediated cellular response is size-dependent. Nat Nanotechnol 3:145–150
11. Tyagi S, Kramer FR (1996) Molecular beacons: probes that fluoresce upon hybridization. Nat Biotechnol 14:303–308

Chapter 43
Development of a Model to Aid NIRS Data Interpretation: Results from a Hypercapnia Study in Healthy Adults

Tracy Moroz, Murad Banaji, Martin Tisdall, Chris E. Cooper, Clare E. Elwell, and Ilias Tachtsidis

1 Introduction

Changes in carbon dioxide levels are known to alter cerebral blood flow [1]. Hypercapnia studies have been carried out in healthy volunteers to characterise brain tissue oxygenation and blood flow changes, measured with near-infrared spectroscopy (NIRS) and transcranial Doppler (TCD) [2].

Here we apply the BrainSignals model [3], a physiological model of brain circulation and metabolism, to data from a hypercapnia study in healthy adults [4]. The model predicts several physiological variables, including those which can be measured with NIRS and TCD. It has previously been used successfully to describe the effects of hypoxia, also in healthy adults. We aimed to reproduce the experimental results as closely as possible with the model, and in doing so, enhance our understanding of the measurements, and the effects of hypercapnia.

2 The BrainSignals Model

The structure of the model is illustrated in Fig. 43.1. The circulatory part of the model comprises three compartments: arteries and aterioles, capillaries and veins. The venous and capillary volumes are fixed, but the arterial/arteriolar compartment

T. Moroz • M. Banaji • M. Tisdall • C.E. Elwell • I. Tachtsidis (✉)
Biomedical Optics Research Laboratory, Department of Medical Physics and Bioengineering, University College London, Malet Place Engineering Building, Gower Street, London WC1E 6BT, UK
e-mail: iliastac@medphys.ucl.ac.uk

C.E. Cooper
Department of Biological Sciences, University of Essex, Wivenhoe Park, Colchester CO4 3SQ, UK

M. Wolf et al. (eds.), *Oxygen Transport to Tissue XXXIII*, Advances in Experimental Medicine and Biology 737, DOI 10.1007/978-1-4614-1566-4_43,

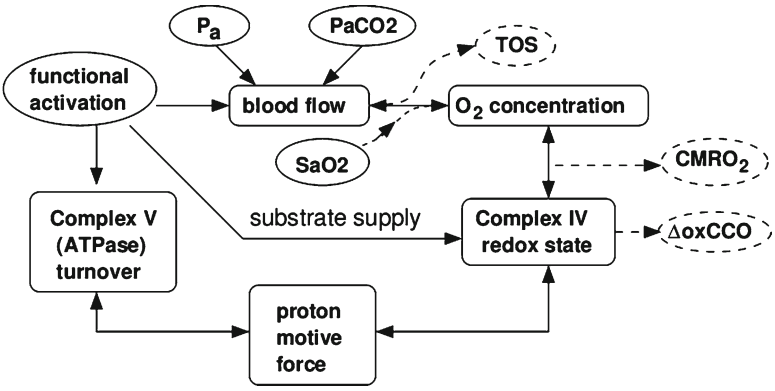

Fig. 43.1 A diagram of the BrainSignals model. Inputs are shown in *solid ovals* and outputs in *dashed ovals*. Model processes are shown in *rectangles*. Figure reproduced from Banaji et al. [3]

has variable resistance which is sensitive to four input variables: the arterial pressure of carbon dioxide ($PaCO_2$), the arterial oxygen saturation, the mean arterial blood pressure (MBP) and a parameter representing neuronal activation. $PaCO_2$ affects the resistance via the following equations.

$$\frac{d\nu}{dt} = \frac{1}{\tau}(PaCO_2 - \nu) \tag{43.1}$$

$$\eta = R_C\left(\frac{\nu}{\nu_n} - 1\right) + \ldots \tag{43.2}$$

Here, τ is a time constant, and ν represents a low-pass filtered version of $PaCO_2$ with normal value ν_n. R_C is a parameter controlling the magnitude of the response to $PaCO_2$ changes and has a default value of 2.2. The muscular tension in the arterial wall depends on η, which is the sum of the $PaCO_2$ term shown and three similar terms for the other input variables listed above. An average vessel radius is calculated from the balance of pressures and tensions in the vessel wall. This in turn determines the resistance of the arterial/arteriolar tree via Poiseuille's law. An increase in vessel radius leads to an increase in blood volume and blood flow. The model output of velocity of blood in the middle cerebral artery (Vmca) is proportional to cerebral blood flow.

All blood compartments have a fixed haemoglobin concentration [Hb] whose default value in the model is 2.275 mM. In each compartment, a fraction of this haemoglobin is oxygenated. These fractions are determined from the arterial oxygen saturation (a model input), and from the rate of oxygen transport to the mitochondria for respiration. The tissue oxygen saturation (TOS) is the overall percentage of oxygenated haemoglobin in the arteries and veins. The steady state changes of Vmca and TOS with default model parameters and varying $PaCO_2$ are shown in Fig. 43.2.

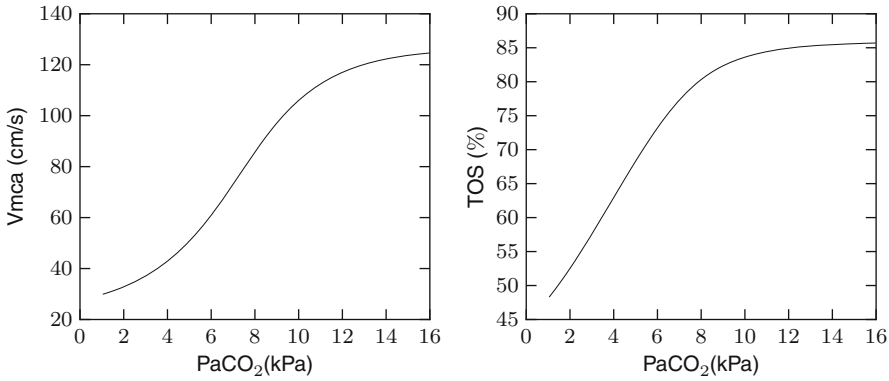

Fig. 43.2 Prediction of Vmca and TOS by the model at different $PaCO_2$ values

3 Methods

Data were analysed from a hypercapnia study of 14 healthy adult volunteers [4]. This involved a 1.5 kPa increase in end tidal CO_2 ($EtCO_2$) for 10 min, with 5 min at baseline before and after. Throughout the study, the subjects' heart rate, mean blood pressure (MBP) and arterial oxygen saturation (SaO_2) were monitored. The blood velocity in the middle cerebral artery (Vmca) was also monitored using TCD. The TOS, a measure of the percentage of oxygenated haemoglobin, was obtained using the NIRO 300 (Hamamatsu Photonics KK). All signals were smoothed and filtered, and any periods with obvious instrumentation noise were identified by inspection and replaced by a linear interpolation. SaO_2, $EtCO_2$ and MBP were input to the model, and its outputs compared with the measured Vmca and TOS.

Parameter optimisation was carried out using a version of Powell's method implemented in SciPy [5]. The rms difference between a measured and simulated signal was calculated by a numerical integration of the squared difference between the two signals, over all time points. The aim of optimisation was to minimise this rms difference for each subject, using TOS, Vmca or a weighted combination of the two. For Vmca, the simulated data from each parameter set was rescaled so that its average value matched that of the measured data, prior to error calculation. Initially, two model parameters were optimised: blood haemoglobin concentration [Hb] (or haematocrit), chosen for its influence on the absolute TOS value, and R_C, which represents the sensitivity of the flow response to $PaCO_2$ changes.

The success of a simulated dataset was judged by its rms difference, and also by comparing its response with that of the measured data. To calculate the response, a period of hypercapnia and a subsequent baseline period were identified by inspection of the $EtCO_2$ trace for each subject. The response was then calculated from the means during these periods, after resampling to 1 Hz, as follows:

$$\text{TOS response} = \text{TOS}(\text{hypercapnia}) - \text{TOS}(\text{baseline}) \tag{43.3}$$

$$\text{Vmca response} = \frac{\text{Vmca(hypercapnia)} - \text{Vmca(baseline)}}{\text{Vmca(baseline)}} \times 100\% \quad (43.4)$$

After analysing the results, three new mechanisms were added to the model in turn. Firstly, to simulate an extracerebral contribution to TOS, TOS(corrected) was calculated as the weighted sum of intra and extracerebral compartments

$$\text{TOS(corrected)} = (1-t)\text{TOS}(i) + t.\text{TOS}(e) \quad (43.5)$$

where t is the fractional contribution of the extracerebral compartment, and TOS(e) its fixed TOS value. TOS(i), the intracerebral TOS, was calculated as before. TOS(e) and t were optimised together with R_C. Secondly, venous volume was varied with CO_2 levels. Previously, it was fixed at 0.75 of the normal total blood volume ($V_{blood,n}$). This was changed to

$$\text{Venous volume} = (0.75 + v(\text{PaCO}_2 - \text{PaCO}_{2,n}))V_{blood,n} \quad (43.6)$$

where $PaCO_{2,n}$ is the model's normal value of $PaCO_2$. The constant v was included as an optimisation parameter. Finally, a change linking metabolic rate to CO_2 levels was introduced, via a parameter representing the demand. This was varied in a similar way to venous volume

$$\text{Venous volume} = (0.75 + v(\text{PaCO}_2 - \text{PaCO}_{2,n}))V_{blood,n} \quad (43.7)$$

and d was optimised. Changes in demand also have a direct effect on the blood flow; but this was removed here by setting the relevant parameter R_u to zero.

4 Results

The measured data are summarised in Table 43.1. The mean (±SD) TOS and Vmca responses were 1.1 ± 0.8% and 26 ± 11%, respectively.

The six differently optimised datasets are summarised in Table 43.2. Parameter values not given in the table were set at their defaults, except for [Hb]. In optimisations 2 and 4–6, [Hb] was fixed at its value from optimisation 1. The errors in TOS and Vmca response for each subject in each of these optimisation sets, and for no optimisation, are shown in Fig. 43.3. With no optimisation, mean simulated TOS response was 7.1 ± 1.1%. Vmca was better predicted, with a mean response of 32 ± 6%. The response of each signal could be matched well when optimising to that

Table 43.1 Summary of the measured data, mean (SD) across the 14 subjects

	Normocapnia	Hypercapnia
Duration (s)	240 (20)	500 (50)
$EtCO_2$ (kPa)	5.2 (0.3)	6.9 (0.3)
TOS (%)	69 (6)	70 (6)
Vmca (cms^{-1})	42 (11)	52 (13)

Table 43.2 Details of the optimisation methods and results

Optimisation		1	2	3	4	5	6
Parameters optimised	R_C	0.3 (0.2)	1.5 (0.6)	1.1 (0.4)	1.6 (0.6)	1.4 (0.6)	1.2 (0.4)
	[Hb] (mM)	2.1 (0.7)	–	2.0 (0.7)	–	–	–
	t	–	–	–	0.79 (.13)	–	–
	TOS(e) (%)	–	–	–	69 (6)	–	–
	v (mmHg)$^{-1}$	–	–	–	–	0.06 (0.05)	–
	d (mmHg)$^{-1}$	–	–	–	–	–	0.16 (0.05)
Signals optimised to	TOS	x	–	x	x	x	x
	Vmca	–	x	x	x	x	x

The first row contains the mean (SD) across 14 subjects of the optimised parameter values. No value given indicates that a parameter was fixed

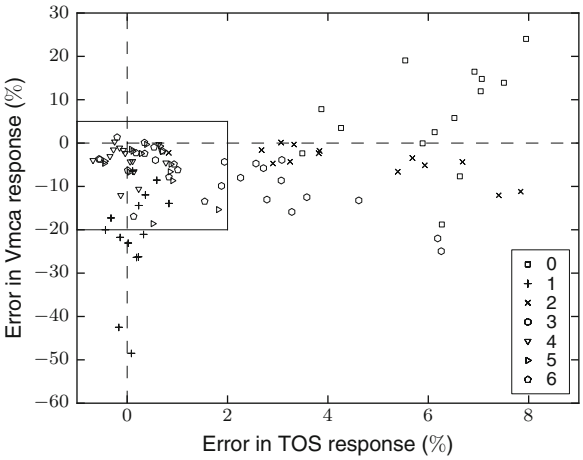

Fig. 43.3 Modelled response minus measured response for TOS vs. Vmca. The response is the difference (TOS) or percentage change (Vmca) of the mean at hypercapnia from the mean at baseline. The legend refers to the six optimisation methods described in Table 43.2. Series 0 represents no optimisation. Each point within a series represents a subject. The *box* at the origin surrounds all the points from optimisations 4–6, where new mechanisms were introduced

signal alone. The parameter [Hb] was not included in the Vmca optimisation since it only had a small effect on the response. The mean value of R_C resulting from optimisation 2 was significantly larger than that from optimisation 1; i.e., a greater sensitivity of blood flow to CO_2 was required to explain the changes measured in Vmca, than that required to explain the changes measured in TOS. Consequently, optimisation 3, which attempted to match both signals, was less successful: in every subject, simulated TOS response was too large, whilst simulated Vmca response was too small.

All three new model mechanisms reduced this discrepancy. The additional compartment for TOS was the most successful, leading to simulated TOS and Vmca responses of $1.1 \pm 0.6\%$ and $22 \pm 6\%$. The mean optimum weight of the extracerebral compartment was 0.8 (range 0.45–0.95). With a varying venous volume, simulated response was reduced to $1.6 \pm 0.9\%$ for TOS and $20 \pm 7\%$, for Vmca, and therefore

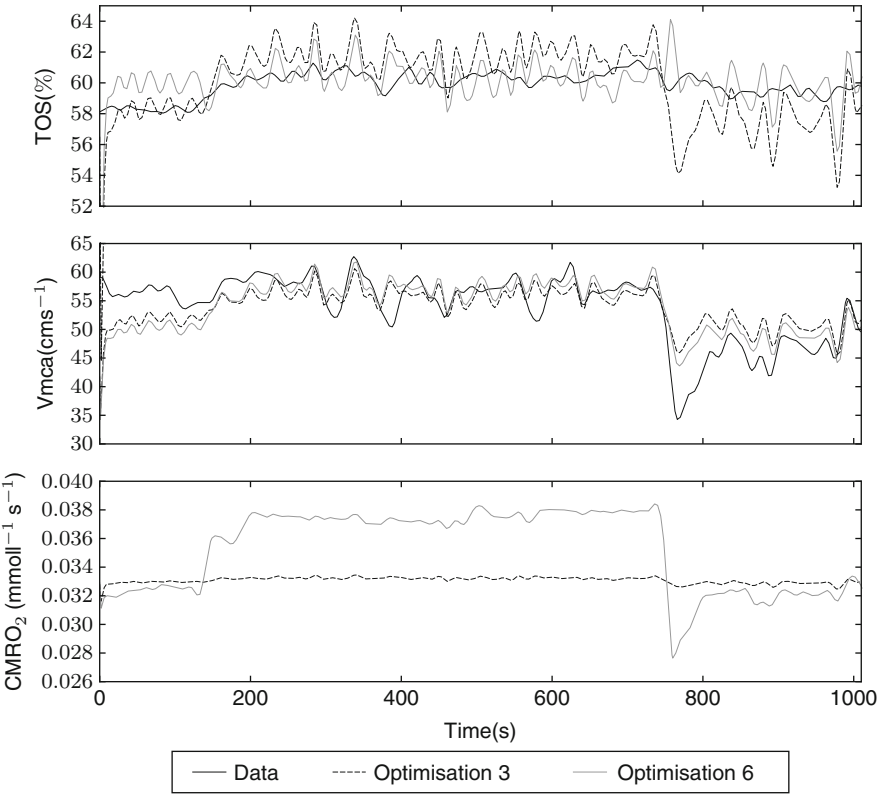

Fig. 43.4 Examples of TOS, Vmca and $CMRO_2$ from one volunteer. The graphs show the measured signal (*solid black*), the modelled signal after optimisation 3 (*dashed*) and the modelled signal after optimisation 6 (*solid grey*)

matched better the measured signals. However, this corresponded to a mean venous volume change of 100% (range 20–230%). When optimising the change in oxygen metabolism, the mean resulting cerebral metabolic rate of oxygen consumption ($CMRO_2$) increase was $18 \pm 8.5\%$. Simulated TOS and Vmca responses were $1.5 \pm 0.9\%$ and $21 \pm 8\%$ which matched well with the measured signals. An example of the $CMRO_2$ change in one subject, along with the measured and modelled TOS and Vmca, is shown in Fig. 43.4.

5 Discussion

As expected, Vmca and TOS increased during hypercapnia. The model behaviour was qualitatively correct, but consistently overestimated the ratio of TOS response to Vmca response. All three additional mechanisms reduced this discrepancy;

however, the magnitude of the changes required for optimum fitting suggested that no single mechanism is likely to be successful in its own right.

TOS has been shown to have a high sensitivity and specificity to intracerebral changes [6]. It is surprising therefore, that an 80:20 extracerebral to intracerebral weighting was required to optimise the fitting of the TOS data.

The method of changing venous volume was very simplistic. A more realistic method could be incorporated, as in other models [7]. However, a large change in venous volume would still be required to fit TOS response accurately. Evidence from PET studies indicates that the cerebral blood volume changes seen during hypercapnia are caused primarily by arterial volume changes [8]. Our optimisation suggests a doubling of the venous volume during the hypercapnia challenge, which seems unlikely.

Finally, linking of $CMRO_2$ to CO_2 levels allowed improved simulations of Vmca and TOS. But as before, the 18% increase was unexpectedly large. Changes in brain blood flow and oxygenation during CO_2 challenges are well documented; however, there are still open questions regarding the changes in metabolism [9]. CO_2 is usually assumed to be metabolically neutral. For example, in fMRI studies, hypercapnia is often used with this assumption to estimate oxygen metabolism changes from the BOLD signal [10]. However, recently Tachtsidis and colleagues have analysed the NIRS measured change in concentration of cytochrome c oxidase (CCO), and reported an increase in the CCO redox state in healthy volunteers during hypercapnia, that cannot be exclusively attributed to the increase in oxygen delivery [4]. We are currently exploring whether CCO measurements can provide additional data to help discriminate between the different hypotheses presented above.

In conclusion, there is an anomalous (small) change of TOS in response to hypercapnia that cannot be explained by optimisation of a single parameter in our model. We are currently attempting to optimise to a combination of factors simultaneously. If this does not prove possible it will suggest that TOS as measured optically does not report on the cerebral oxygen saturation as defined in our model.

Acknowledgments The authors would like to thank the Wellcome Trust (088429/Z/09/Z) and the Centre for Mathematics and Physics in the Life Sciences and Experimental Biology for the financial support of this work. This work was undertaken at University College London Hospitals and partially funded by the UK Department of Health's National Institute for Health Research Centres funding scheme.

References

1. Reivich M (1964) Arterial PCO_2 and cerebral hemodynamics. Am J Physiol 206:25–35
2. Tisdall M, Taylor C, Tachtsidis I et al (2009) The effect on cerebral tissue oxygenation index of changes in the concentrations of inspired oxygen and end-tidal carbon dioxide in healthy adult volunteers. Anesth Analg 109(3):906–913
3. Banaji M, Mallet A, Elwell C et al (2008) A model of brain circulation and metabolism: NIRS signal changes during physiological challenges. PloS Comput Biol 4:e1000212

4. Tachtsidis M, Tisdall M, Leung T et al (2009) Relationship between brain tissue haemodynamics, oxygenation and metabolism in the healthy human adult brain during hyperoxia and hypercapnea. Adv Exp Med Biol 645:315–320
5. Jones E, Oliphant T, Peterson P, et al. (2001) SciPy Open source scientific tools for Python. http://www.scipy.org. Accessed Aug 2010
6. Al-Rawi P, Smielewski P, Kirkpatrick P (2001) Evaluation of a near-infrared spectrometer (NIRO 300) for the detection of intracranial oxygenation changes in the adult head. Stroke 32:2492–2500
7. Ursino M, Lodi C (1998) Interaction among autoregulation, CO_2 reactivity, and intracranial pressure: a mathematical model. Am J Physiol 274:H1 715–H1 728
8. Ito H, Ibaraki M, Kanno I et al (2005) Changes in the arterial fraction of human cerebral blood volume during hypercapnia and hypocapnia measured by positron emission tomography. J Cereb Blood Flow Metab 25:852–857
9. Siesjo B (1980) Cerebral metabolic rate in hypercarbia – a controversy. Anesthesiology 52:461–465
10. Davis T, Kwong K, Weisskoff R et al (1998) Calibrated functional MRI: mapping the dynamics of oxidative metabolism. Proc Natl Acad Sci USA 95:1834–1839

Chapter 44
Boron Tracedrug: Design, Synthesis, and Pharmacological Activity of Phenolic BODIPY-Containing Antioxidants as Traceable Next-Generation Drug Model

Eiji Nakata, Masato Koizumi, Yohei Yamashita, Yoshihiro Uto, and Hitoshi Hori

1 Introduction

In early stages of the drug discovery and developing process, medicinal chemistry- and pharmaceutical-researchers make a great effort to evaluate the pharmacokinetics (PK) of drug candidates. Recently, increased needs for this PK have stimulated medicinal chemistry researchers to develop drugs with their own superior traceability. Traditionally, the radiolabeled compounds have been studied for their purposes. However, they have two inherent problems, their half-life and specific regulations for the experimental facilities. These problems increase the need for medicinal chemists to develop the traceable drugs themselves without their radioisotope labeling. We had the idea of boron tracedrug embedded boron atoms in their scaffold [1]. This idea is based on our previous drug design studies on the development of hypoxia-targeting boron-10 (^{10}B) carrier compounds for boron neutron capture therapy (BNCT) [2]. ^{10}B, a naturally occurring and stable isotope (19.9%), possesses neutron capture activity to produce a prompt γ-ray when being irradiated by thermal neutron. We can measure ^{10}B concentration by neutron induced prompt γ-ray spectroscopy (NIPS) to detect the localization of the boron tracedrugs actually whenever they are required to be.

We discuss here as our boron tracedrug approach the design and synthesis of the phenolic BODIPY-containing antioxidants, UTX-42, UTX-43, and UTX-44 (Fig. 44.1). Their antioxidant activities are evaluated by spectroscopic analysis with 2,2′-azinobis(3-ethylbenzothiazoline-6-sulfonate) (ABTS) radical cation and their inhibitory activities on lipid peroxidation of rat liver mitochondria (RLM).

E. Nakata • M. Koizumi • Y. Yamashita • Y. Uto • H. Hori (✉)
Department of Life System, Institute of Technology and Science, Graduate School, The University of Tokushima, Minamijosanjimacho-2, Tokushima 770-8506, Japan
e-mail: hori@bio.tokushima-u.ac.jp

M. Wolf et al. (eds.), *Oxygen Transport to Tissue XXXIII*, Advances in Experimental Medicine and Biology 737, DOI 10.1007/978-1-4614-1566-4_44,

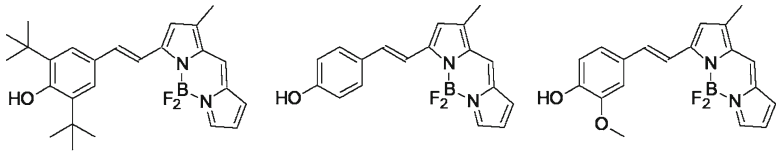

Fig. 44.1 Structures of the phenolic BODIPY-containing antioxidants, UTX-42 (**1**), UTX-43 (**2**), and UTX-44 (**3**)

2 Materials and Methods

2.1 Chemicals and Molecular Orbital Calculations

Phenolic BODIPY-containing antioxidants were synthesized according to the previous method with slight modification [3]. All chemicals were purchased from Tokyo Chemical Industry Co., Ltd., Wako Pure Chemical Industries, Ltd., and Sigma-Aldrich. The ab initio MO calculation was performed with B3LYP hybrid density functional in conjugation with the 3-21G(d) basis set using the Gaussian 03 suite programs [4]. Visualization of the molecular geometries calculated by Gaussian 03 was carried out with GaussView 3.0 [5].

2.2 General Procedure for Synthesis of UTX-42, UTX-43, and UTX-44

1,3-Dimethyl-BODIPY (**4**) (0.1 mmol) and the corresponding benzaldehyde (3,5-di-*tert*-butyl-4-hydroxybenzaldehyde (**5**), *p*-hydroxybenzaldehyde (**6**) and vanillin (**7**)) (0.1 mmol) were dissolved in ethanol. Pyrrolidine (10 mmol) and acetic acid (10 mmol) were added with stirring. The reaction mixture was stirred at reflux temperature for 3 h. The solvent was evaporated under reduced pressure. The residue was purified by silica gel column chromatography (the eluents were dichloromethane: hexane = 1:1 for UTX-42, hexane:ethyl acetate = 2:1 for UTX-43, and dichloromethane only for UTX-44).

2.2.1 2,6-Di-tert-butyl-4-[2-(1-methyl-4,4-difluoro-4-bora-3*a*-4*a*-d-iaza-*s*-indacen-3-yl)-vinyl]-phenol (UTX-42)

Yield 22.8%. ^{1}H NMR (400 MHz, CD_3OD) δ 7.42–7.60 (m, 8H), 6.95–6.97 (m, 2H), 6.44–6.45 (m, 1H), 2.35 (s, 3H), 1.48 (s, 18H); HRMS(FAB$^+$) calcd for $C_{26}H_{31}BF_2N_2O$ (M^+) *m*/*z* 436.2497. Found 436.2527; Anal. Calcd for $C_{26}H_{31}BF_2N_2O$: C, 71.57; H, 7.16; N, 6.42. Found: C, 71.32; H, 7.04; N, 6.39.

2.2.2 4-[2-(1-Methyl-4,4-difluoro-4-bora-3*a*-4*a*-diaza-*s*-indacen-3-yl)-vinyl]-phenol (UTX-43)

Yield 56.2%. ^{1}H NMR (400 MHz, CD_3OD) δ 7.42–7.50 (m, 4H), 7.38–7.42 (m, 2H), 6.93–6.95 (m, 2H) 6.83–6.85 (m, 2H). 6.44 (s, 1H), 2.33 (s, 3H); HRMS(FAB$^+$) calcd for $C_{18}H_{15}BF_2N_2O$ (M^+) *m*/*z* 324.1245. Found 324.1251.

2.2.3 2-Methoxy-4-[2-(1-methyl-4,4-difluoro-4-bora-3*a*-4*a*-diaz-a-*s*-indacen-3-yl)-vinyl]-phenol (UTX-44)

Yield 41.6%. ^{1}H NMR (400 MHz, CD_3OD) δ 7.43–7.46 (m, 2H), 7.28–7.34 (m, 2H), 7.04–6.12 (m, 2H) 6.74–6.76 (m, 2H). 6.34–6.36 (m, 1H), 3.84 (s, 3H), 2.25 (s, 3H); HRMS(FAB$^+$) calcd for $C_{19}H_{17}BF_2N_2O$ (M^+) *m*/*z* 354.1351. Found 324.1335; Anal. Calcd for $C_{19}H_{17}BF_2N_2O$: C, 64.44; H, 4.84; N, 7.91. Found: C, 64.30; H, 4.88; N, 7.80.

2.3 Antioxidant Activity

The reactivity of the drug with ABTS radical cation was measured according to the method of Re et al. [6]. The preprepared stock solution of ABTS radical cation (7 mM ABTS in 2.54 mM potassium persulfate buffer) was diluted with ethanol to the absorbance of about 0.70 at 734 nm. The decolorization assay was started by mixing 2 ml of the diluted ABTS solution with 20 μl of the test compound (ethanol solution) in a cuvette. After 6 min mixing, the absorbance of 734 nm was measured. In a control experiment, the test compound solution was replaced with ethanol, and the radical scavenging activity of the test compounds was expressed as the IC_{50} value.

2.4 Inhibition Activity of RLM Lipid Peroxidation

RLM were isolated from male Wistar rats (140–260 g) as reported previously [7]. The mitochondrial protein content was determined by the Biuret method using bovine serum albumin as a standard. Lipid peroxidation in RLM was performed and IC_{50} in the RLM lipid peroxidation reaction was determined as reported previously [8].

3 Results and Discussion

3.1 Design and Synthesis

We designed phenolic BODIPY-containing antioxidants, UTX-42, UTX-43, and UTX-44. Their molecular orbitals, thus eigenvalues and coefficients of Frontier

Table 44.1 Molecular orbitals and their energy levels of the phenolic BODIPY-containing antioxidants

Compounds	LUMO	HOMO
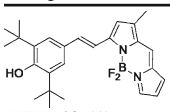 UTX-42 (1)	 E_{LUMO} = −2.6843 eV	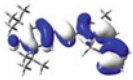 E_{HOMO} = −5.1873 eV
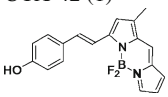 UTX-43 (2)	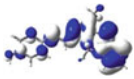 E_{LUMO} = −2.7477 eV	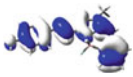 E_{HOMO} = −5.2722 eV
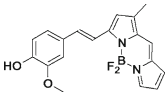 UTX-44 (3)	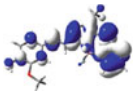 E_{LUMO} = −2.7355 eV	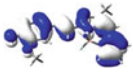 E_{HOMO} = −5.1740 eV

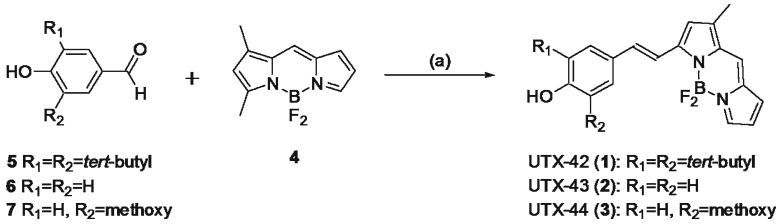

Scheme 44.1 Synthesis of the phenolic BODIPY-containing antioxidants. Reagents and conditions: (a) **4**, corresponding benzaldehydes **5**, **6**, **7**, EtOH, reflux, 3 h, UTX-42 (**1**); 22.8%, UTX-43 (**2**); 56.2% ,UTX-44 (**3**); 41.6%

orbitals (HOMO and LUMO), were given in Table 44.1. 1,3-Dimethyl-BODIPY **4** was prepared according to the previous method with slight modification [3]. Second, Knoevenagel condensation reactions were performed between 1,3-dimethyl-BODIPY and their corresponding benzaldehydes derivatives **5**, **6**, **7**, giving UTX-42, UTX-43, and UTX-44, respectively. They were purified by silica gel column chromatography obtained in satisfactory yields (Scheme 44.1).

3.2 Antioxidant Activity

The antioxidant activities of the phenolic BODIPY-containing antioxidants were evaluated by their spectroscopic analysis with ABTS radical cation. The IC_{50} value of UTX-42, UTX-43, and UTX-44 were almost the same in the range of 5.40–9.51 μM. They showed slightly higher reactivity than trolox (Table 44.2).

Table 44.2 Antioxidant activities of the phenolic BODIPY-containing antioxidants

Compound	ABTS (IC_{50}, μM)	RLM lipid (IC_{50}, μM)	clog*P*
UTX-42	6.80 ± 0.65	0.95 ± 0.20	9.49
UTX-43	9.51 ± 0.19	0.63 ± 0.01	6.46
UTX-44	5.40 ± 0.41	0.34 ± 0.19	6.36
Trolox	12.2 ± 0.24	10.5	2.51

Values represent means ± SD of three experiments. clog*P* was calculated by OSIRIS [9]

3.3 Inhibitory Activity on RLM Lipid Peroxidation

We further investigated the activities of them against RLM lipid peroxidation. ADP and Fe^{2+} were used as initiator of a radical reaction, and then IC_{50} was estimated from O_2 consumption in the presence or absence of phenolic BODIPY-containing antioxidants. We found that the inhibitory activities of the drugs were much higher than that of trolox by one to two orders of magnitude (Table 44.2). This result suggests that the phenolic BODIPY-containing antioxidants are much more potent than trolox as inhibitors of RLM lipid peroxidation. Among them, UTX-44 has the highest potent antioxidant.

4 Conclusions

The phenolic BODIPY-containing antioxidants UTX-42, UTX-43, and UTX-44 were synthesized. Their reactivities with ABTS radical cation were slightly higher than trolox. They, especially UTX-44, also showed much higher inhibitory activity than trolox against RLM lipid peroxidation. These results demonstrated that UTX-44 had the most potent boron-containing antioxidant among them. These drugs would be boron tracedrugs possessing powerful antioxidant potency. Now we plan to evaluate their in vitro and in vivo toxicity and traceability by NIPS.

Acknowledgments We thank Ms. Maki Nakamura, Ms. Emiko Okayama, and the staff of our faculty for measurement of NMR and elemental analyses. We also thank Prof. Toshihiro Hashimoto and Ms. Yasuko Okamoto for measurement of FAB-MS.

References

1. Hori H, Uto Y, Nakata E (2010) Medicinal electronomics bricolage design of hypoxia-targeting antineoplastic drugs and invention of boron tracedrugs as innovative future-architectural drugs. Anticancer Res 30:3233–3242
2. Nagasawa H, Uto Y, Kirk KL et al (2006) Design of hypoxia-targeting drugs as new cancer chemotherapeutics. Biol Pharm Bull 29:2335–2342

3. Lee JS, Kang NY, Kim YK et al (2009) Synthesis of a BODIPY library and its application to the development of live cell glucagon imaging probe. J Am Chem Soc 131:10077–10082
4. Frisch MJ, Trucks GW, Schlegel HB, et al. Gaussian, Inc., Wallingford CT, Gaussian 03, Revision B.04, 2004
5. Flükiger HP, Lüthi S, Portmann J (2000) Weber. Swiss National Supercomputing Centre CSCS, Manno, Switzerland
6. Re R, Pellegrini N, Proteggente A, Pannala A et al (1999) Antioxidant activity applying an improved ABTS radical cation decolorization assay. Free Radic Biol Med 26:1231–1237
7. Myers DK, Slater EC (1957) The enzymatic hydrolysis of adenosine triphosphate by liver mitochondria I. Activities at different pH values. Biochem J 67:558–572
8. Uto Y, Ae S, Koyama D et al (2006) Artepillin C isoprenomics: design and synthesis of artepillin C isoprene analogues as lipid peroxidation inhibitor having low mitochondrial toxicity. Bioorg Med Chem 14:5721–5728
9. Muller R. The organic chemistry portal home page, chemistry tools, The OSIRIS Property Explorer. http://www.organic-chemistry.org/prog/peo/

Chapter 45
Modelling and Filtering of Physiological Oscillations in Near-Infrared Spectroscopy by Time-Varying Fourier Series

Ivo Trajkovic, Christoph Reller, and Martin Wolf

1 Introduction

We have developed and implemented a method for modeling and adaptive filtering of oscillatory components, in particular the ones caused by (1) the cardiac activity, called "heartbeat," and (2) the low frequency oscillations (also Mayer waves), called "LFO," in signals measured with near-infrared spectroscopy (NIRS), called "raw NIRS signals," Examples of the latter are the gray curves in Fig. 45.1a, c. The overall aim is to extract each pure signal component, since (1) one disturbs the detection of another, for example, hemodynamic brain activity and LFO, (2) then the interrelation between several components can be assessed, and (3) characterizing each component separately could yield new understandings of underlying biological processes.

A traditional band-pass filter [1] will not do, since (1) to include the typical sharp peaks in the heartbeat (gray curve in Fig. 45.1c), the high cutoff frequency must be rather high; thus, high-frequency noise survives the filtering, (2) the physiology fluctuates, for example, the heart rate doubles quickly after starting a physical exercise, and window-based processing allows the harmonics of one or more components, for example, heartbeat and fast neuronal activity, to spectrally overlap in a window.

Our method has not been tested yet with the breathing component, thus only the heartbeat and the LFO are addressed in this chapter.

I. Trajkovic (✉) • M. Wolf
Biomedical Optics Research Laboratory, Division of Neonatology,
Department of Obstetrics and Gynecology, University Hospital Zurich,
Frauenklinikstrasse 10, 8091 Zurich, Switzerland

Institute for Biomedical Engineering, University of Zurich and ETH Zurich,
8093 Zurich, Switzerland
e-mail: ivot@alumni.ethz.ch

C. Reller
Signal and Information Processing Laboratory (ISI), ETH Zurich,
8092 Zurich, Switzerland

M. Wolf et al. (eds.), *Oxygen Transport to Tissue XXXIII*, Advances in Experimental Medicine and Biology 737, DOI 10.1007/978-1-4614-1566-4_45,

Strictly periodic signals can be efficiently represented by Fourier series. Let $x_1, x_2, \ldots$ be the equidistantly sampled version of a strictly periodic real-valued signal, let n be the discrete time index, and let k be the harmonic index. Then

$$x_n = \mathrm{Re}\left(\sum_{k=0}^{\infty} A_k e^{jkn\Omega} \right), \tag{45.1}$$

with real-valued coefficient A_0, complex-valued coefficients $A_1, A_2, \ldots \in \mathbb{C}$ and fundamental frequency $\Omega \in [0, 2\pi]$.

We classify the oscillatory components as "almost periodic," since their period lengths and signal shapes drift over time [2]. We propose to describe such a component by a "Fourier series" with time-variant fundamental frequency (related to the

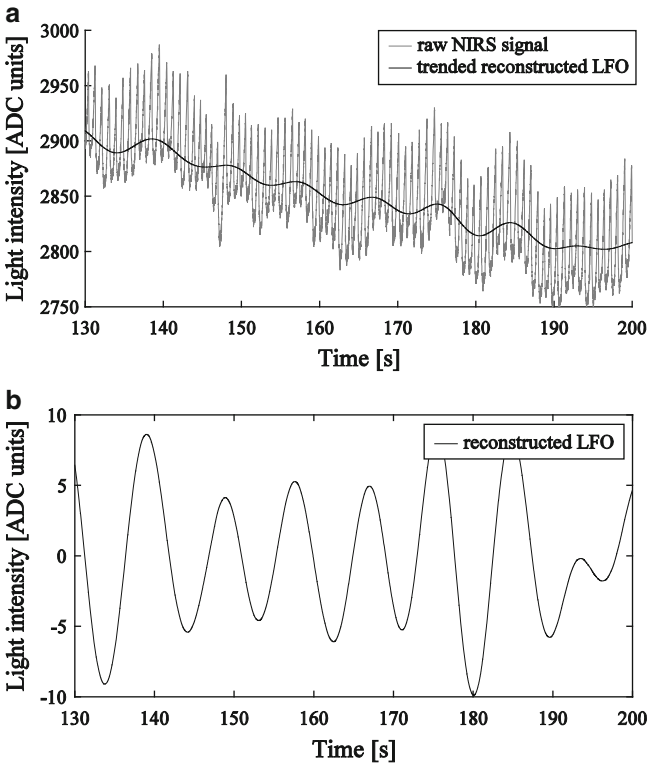

Fig. 45.1 The *gray curves* in (**a**) and (**c**) are raw NIRS signals sampled at 100 Hz. The *black curve* in (**c**) is the reconstructed heartbeat including the estimated slow trend $\hat{\mathbf{A}}_{0,-}$; the *black curve* in (**a**) is the same for the LFO; (**b**) is the LFO without $\hat{\mathbf{A}}_{0,-}$; (**d**) is the heartbeat without $\hat{\mathbf{A}}_{0,-}$. The heartbeat is also recognizable in (**a**) (spikes in the *gray curve*). The signal values are given in "ADC units" since the NIRS instrumentation uses an Analog-to-Digital Converter (ADC) to digitize light intensity values

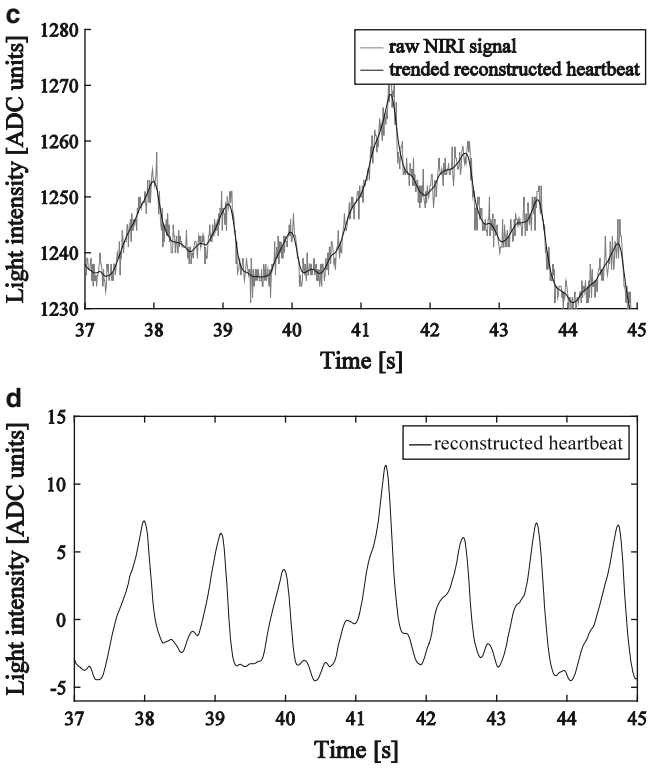

Fig. 45.1 (continued)

varying period length) and time-variant coefficients (related to the varying signal shape), that is, we change (45.1) into

$$x_n = \mathrm{Re}\left(\sum_{k=1}^{K} A_{k,n} e^{jk\theta_n} \right), \tag{45.2}$$

with

$$\begin{aligned} A_{k,n} &\approx A_{k,n+1}, \\ \theta_{n+1} &= \left(\theta_n + \Omega_n\right)_{\mathrm{mod}2\pi}, \end{aligned} \tag{45.3}$$

and

$$\Omega_n \approx \Omega_{n+1}. \tag{45.4}$$

In this chapter, we present an algorithm for estimating the model parameters θ_n which is considerably faster than the algorithm in [2].

When modelling the heartbeat, the magnitude of the coefficients $A_{k,n}$ in (45.2) typically decays with increasing harmonic index k. Consequently, for $k \geq K$, the harmonics of the heartbeat cannot be distinguished from the noise. The noise energy in raw NIRS signals, and thus K, varies depending on the data channel, NIRS instrumentation and subject; typically $3 \leq K \leq 7$ whereas $K = 1$ suffices for modelling the LFO. In [2], K was chosen manually (for each subject and data channel); if K is chosen too high, the reconstructed heartbeat will contain noise; if K is chosen too low, high-frequency parts of the heartbeat will not be modeled. At the the end of the next section, we show an intuitive procedure for estimating K from the measured signal.

2 Estimating the Model Parameters

Let the raw NIRS signal $\mathbf{y} = (y_1, \ldots, y_N)$ be a noisy, trended version of the signal $\mathbf{x} = (x_1, \ldots, x_N)$ in (45.2) where N is the signal length. Specifically,

$$\mathbf{y} = \mathbf{A}_{0,-} + \mathbf{x} + \mathbf{Z}, \tag{45.5}$$

where $\mathbf{Z} = (Z_1, \ldots, Z_N)$ is discrete time white Gaussian noise, and the trend $\mathbf{A}_{0,-} = (A_{0,1}, \ldots, A_{0,N})$ models changes slower than the heartbeat, or the LFO respectively, and thus is omitted in (45.2). We will use the vectors $\mathbf{A}_{k,-} = (A_{k,1}, \ldots, A_{k,N})$ for $k = 0, \ldots, K$ and decorate estimates with a hat (e.g., $\hat{\mathbf{C}}$ is an estimate of $\mathbf{C}$).

Given $\mathbf{y}$, the objective is to estimate the phases $\boldsymbol{\theta} = (\theta_1, \ldots, \theta_N)$, K and the coefficient vectors $\mathbf{A}_{0,-}, \ldots, \mathbf{A}_{K,-}$ such that $\left\| \mathbf{y} - \hat{\mathbf{x}} - \hat{\mathbf{A}}_{0,-} \right\|^2$ is minimal, where $\hat{\mathbf{x}}$ is the reconstructed signal by applying the estimates in (45.2).

The estimation algorithm consists of several building blocks (see Fig. 45.2).

Initially, the "A_0 estimator" estimates the slow trend $\mathbf{A}_{0,-}$ by a one-time procedure similar to low pass filtering and based on $\mathbf{y}$ only.

In the heartbeat and the LFO, most of the energy, apart from the noise, lies in the fundamental frequency coefficient $\mathbf{A}_{1,-}$. Thus, a first rough estimate of such an

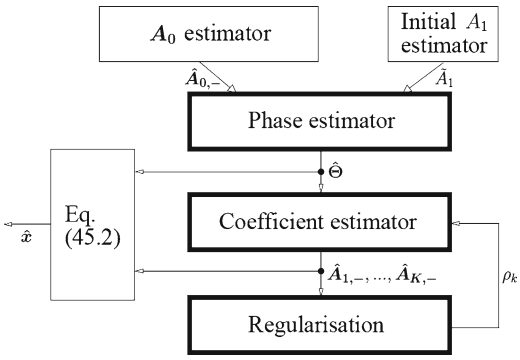

Fig. 45.2 The building blocks of the proposed algorithm

oscillatory component is a complex sinusoid with constant complex magnitude. The "initial A_1 estimator" block makes an estimate $\tilde{A}_1$ of this magnitude such that the sinusoid has approximately the same energy as $\mathbf{y} - \hat{\mathbf{A}}_{0,-}$.

The "phase estimator" calculates the final estimate $\hat{\boldsymbol{\theta}}$ of $\boldsymbol{\theta}$ based on estimates $\hat{\mathbf{A}}_{0,-}$ and $\tilde{A}_1$ and (45.2) with $K = 1$ parameterised as

$$x_n = \mathrm{Re}\left(\tilde{A}_1 e^{jx_n}\right) = \mathrm{Re}\left(\tilde{A}_1\right)\cos\left(\theta_n\right) - \mathrm{Im}\left(\tilde{A}_1\right)\sin\left(\theta_n\right) = \hat{\mathbf{A}}_1\mathbf{C}_n, \tag{45.6}$$

with constant vector $\hat{\mathbf{A}}_1 \hat{=} \left(\mathrm{Re}(\tilde{A}_1) - \mathrm{Im}(\tilde{A}_1)\right)$. We introduce a state vector $\mathbf{C}_n \hat{=} (\cos(\theta_n) \quad \sin(\theta_n))^{\mathrm{T}}$ and define a state transition

$$\mathbf{C}_n = \mathrm{rot}(\hat{\boldsymbol{\Omega}})\mathbf{C}_{n-1} + \mathbf{U}_n, \tag{45.7}$$

where

$$\mathrm{rot}(\hat{\Omega}) = \begin{pmatrix} \cos(\hat{\Omega}) & -\sin(\hat{\Omega}) \\ \sin(\hat{\Omega}) & \cos(\hat{\Omega}) \end{pmatrix},$$

is a rotation matrix and $\hat{\Omega}$ is a prior estimate of Ω_n in (45.3). $\hat{\Omega}$ is derived by using the formula in [2], Sect. 3.3, paragraph 4 and assuming a typical heart rate depending on the subject, for example, $H \hat{=} 80$ bpm for adults. Since $\hat{\Omega}$ is fixed, despite the fact that the heart rate varies considerably depending on various factors, uncertainty, that is, two-dimensional zero-mean white Gaussian noise $\mathbf{U}_n$ with diagonal covariance matrix $\mathbf{V}$, is added to the rotated state in (45.7). This addition of noise defines (45.4). The frequency and its variability (and thus $\hat{\Omega}$ and $\mathbf{V}$) in the LFO are smaller than in the heartbeat.

The estimate $\hat{\mathbf{C}}_n$ of $\mathbf{C}_n$ is made as

$$\hat{\mathbf{C}}_n = \arg\max_{\mathbf{C}_n} f(\mathbf{C}_n \mid \hat{\mathbf{A}}_{0,-}, \tilde{A}_1, \mathbf{y}) \tag{45.8}$$

The function f in (45.8) comprises (45.5), (45.6) and (45.7).

Each estimate $\hat{\theta}_n$ in $\hat{\boldsymbol{\theta}}$ is made as

$$\hat{\theta}_n = \tan^{-1}\left(\frac{\hat{\mathbf{C}}_n(2)}{\hat{\mathbf{C}}_n(1)}\right), \tag{45.9}$$

with $\hat{\mathbf{C}}_n(i)$ denoting the i-th entry of the vector $\hat{\mathbf{C}}_n$.

In this chapter, a node in the factor graph is either (1) the relationship between two or more variables, defined through an equation, or (2) a prior probability density. Edges are variables.

The "phase estimator" uses a factor graph containing N consecutive sections one of which is depicted in Fig. 45.3, that is, the outgoing edge $\mathbf{C}_{n+1}$ of the graph in the figure is at the same time the incoming edge of its right neighbor.

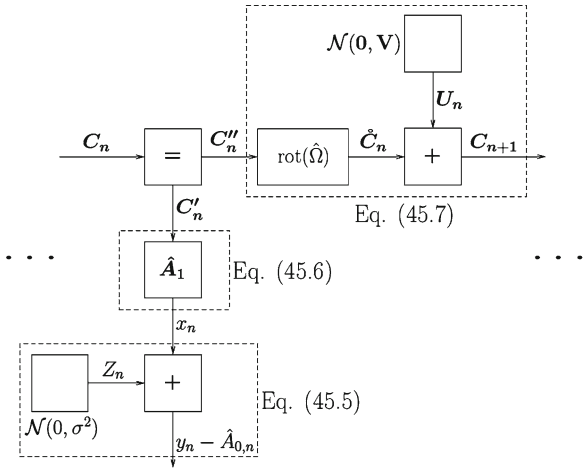

Fig. 45.3 Factor graph used for estimating $\mathbf{C}_n$

In Fig. 45.3, the "="-node clones $\mathbf{C}_n$: $\mathbf{C}'_n \triangleq \mathbf{C}_n$ and $\mathbf{C}''_n \triangleq \mathbf{C}_n$; the "$\hat{\mathbf{A}}_1$"-node represents (45.6); the section of the graph with the incoming edge x_n is (45.5); the section of the graph with the incoming edge $\mathbf{C}''_n$ is (45.7). The sum-product algorithm for Gaussian messages [3] is applied on the factor graph in Fig. 45.3 to derive f in (45.8).

A message (1) is a scaled conditional probability density of the underlying edge, (2) can traverse the edge in both directions, and (3) is named μ including an arrow, which indicates the forward ($\vec{\mu}$) or backward ($\overleftarrow{\mu}$) direction with respect to the edge direction, and the name of the underlying edge as a subscript (e.g., $\vec{\mu}_X$).

The schedule of the message passing algorithm on the factor graph in Fig. 45.3 is:

1. For $n = 1,\ldots,N$, calculate $\overleftarrow{\mu}_{X_n}$ from the measured sample y_n, estimate of the slow trend $\hat{A}_{0,n}$ and the prior probability density $\vec{\mu}_{Z_n}$ represented by the "$N(0,\sigma^2)$"-node.
2. For $n = 1,\ldots,N$, calculate $\overleftarrow{\mu}_{\mathbf{C}'_n}$ from $\overleftarrow{\mu}_{X_n}$ by means of ([3], Table 3).
3. For $n = 1,\ldots,N$, calculate in sequence (1) $\vec{\mu}_{\mathbf{C}''_n}$ from $\overleftarrow{\mu}_{\mathbf{C}'_n}$ and $\vec{\mu}_{\mathbf{C}_n}$ by means of ([3], Table 2) ($\vec{\mu}_{\mathbf{C}_1}$ is neutral: $\vec{\mu}_{\mathbf{C}_1} = 1$), (2) $\vec{\mu}_{\mathring{\mathbf{C}}_n}$ from $\vec{\mu}_{\mathbf{C}''_n}$ by means of ([3], Table 3), since the rotation of the state $\mathbf{C}_n$ can be expressed as a matrix multiplication (45.7), (3) $\vec{\mu}_{\mathbf{C}_{n+1}}$ from $\vec{\mu}_{\mathring{\mathbf{C}}_n}$ ([3], Table 2).
4. For $n = N,\ldots,1$, calculate in sequence (1) $\overleftarrow{\mu}_{\mathring{\mathbf{C}}_n}$ from $\overleftarrow{\mu}_{\mathbf{C}_{n+1}}$ ([3], Table 2), (2) $\overleftarrow{\mu}_{\mathbf{C}''_n}$ from $\overleftarrow{\mu}_{\mathring{\mathbf{C}}_n}$ ([3], Table 3), and (3) $\overleftarrow{\mu}_{\mathbf{C}_n}$ from $\overleftarrow{\mu}_{\mathbf{C}''_n}$ and $\overleftarrow{\mu}_{\mathbf{C}'_n}$ ([3], Table 2). $\overleftarrow{\mu}_{\mathbf{C}_N}$ is neutral: $\overleftarrow{\mu}_{\mathbf{C}_N} = 1$.
5. For $n = 1,\ldots,N$, calculate the marginal $\tilde{\mu}_{\mathbf{C}_n} = \vec{\mu}_{\mathbf{C}_n} \cdot \overleftarrow{\mu}_{\mathbf{C}_n}$ and then the estimate $\hat{\theta}_n$ according to (45.8) and (45.9) with $f \triangleq \tilde{\mu}_{\mathbf{C}_n}$ in (45.8).

The "coefficient estimator" uses $\hat{\theta}$ to calculate the full set of coefficient estimates $\hat{\mathbf{A}}_{1,-},\ldots,\hat{\mathbf{A}}_{K,-}$. The used factor graph and message passing algorithms correspond with the ones in [2], Sect. 3.4, with a slight modification.

To derive K in (45.2), in each iteration step in the "regularisation"–"coefficient estimator" loop, the "regularisation" block calculates for $1 \le k \le K_{\max}$ the noise-to-coefficient ratio $\rho_k \triangleq \| \mathbf{y} - \hat{\mathbf{x}} \|^2 / \| \hat{\mathbf{A}}_{k,-} \|^2$ based on the estimate $\hat{\mathbf{A}}_{k,-}$ and the reconstructed signal $\hat{\mathbf{x}}$ from the previous iteration step. The higher ρ_k, the more the "coefficient estimator" damps $\hat{\mathbf{A}}_{k,-}$ in the next iteration step. This procedure requires slight modifications in the factor graph of the "coefficient estimator" which are described in detail in [4]. The estimate of K is the largest $k \in [1, K_{\max}]$ for which $\| \hat{\mathbf{A}}_{k,-} \| > \tau$, where τ is a threshold.

"Equation (45.2)" block reconstructs the heartbeat, or the LFO respectively, by applying the estimates $\hat{\boldsymbol{\theta}}$ and $\hat{\mathbf{A}}_{1,-}, \ldots, \hat{\mathbf{A}}_{K,-}$ in (45.2).

3 Results and Conclusions

The resulting (trended) heartbeat estimate (black curve in Fig. 45.1c) highly agrees with a corresponding estimate computed with the algorithm in [2] ($r = 0.999518$).

Compared to the algorithm in [2], the algorithm proposed in this chapter is (1) faster, (2) able to estimate K from the measured signal, (3) able to estimate the LFO, and (4) confirmed through many more results from functional studies [4].

References

1. Katura T, Tanaka N, Obata A, Sato H, Maki A (2006) Quantitative evaluation of interrelations between spontaneous low-frequency oscillations in cerebral hemodynamics and systemic cardiovascular dynamics. Neuroimage 31:1592–1600
2. Trajkovic I, Reller C, Wolf M, Loeliger H-A (2009) Modelling and filtering almost periodic signals by time-varying Fourier series with application to near-infrared spectroscopy. Proc. 17th European Signal Proc. Conf. (EUSIPCO), pp. 632–636
3. Loeliger H-A, Justin Dauwels, Junli Hu, Sascha Korl, Li Ping, Kschischang FR (2007) The factor graph approach to model-based signal processing. Proc IEEE 95:1295–1322
4. Trajkovic I (2010) Modelling and filtering almost periodic signals by time-varying Fourier series with application to near-infrared spectroscopy. Ph.D. thesis, ETH Zurich

Index

M. Wolf et al. (eds.), *Oxygen Transport to Tissue XXXIII*, Advances in Experimental Medicine and Biology 737, DOI 10.1007/978-1-4614-1566-4,